UNIVERSITEIT VAN PRETORIA
UNIVERSITY OF PRETORIA
YUNIBESITHI YA PRETORIA

PERFORMANCE ENHANCEMENT IN PROTON EXCHANGE MEMBRANE FUEL CELL - NUMERICAL MODELING AND OPTIMISATION

by

Surajudeen Olanrewaju Obayopo

Submitted in partial fulfilment of the requirements for the degree

PHILOSOPHIAE DOCTOR in Mechanical Engineering

in the

Faculty of Engineering, Built Environment and Information Technology
University of Pretoria
Pretoria

Supervisor: Prof. T. Bello-Ochende
Co-Supervisor: Prof. J.P. Meyer

2012

ABSTRACT

TITLE: **PERFORMANCE ENHANCEMENT IN PROTON EXCHANGE MEMBRANE FUEL CELL - NUMERICAL MODELING AND OPTIMISATION**

AUTHOR: **S.O. Obayopo**

SUPERVISOR: **Prof. T. Bello-Ochende**

CO-SUPERVISOR: **Prof. J.P. Meyer**

DEPARTMENT: **Mechanical and Aeronautical Engineering**

UNIVERSITY: **University of Pretoria**

DEGREE: **Philosophiae Doctor (Mechanical Engineering)**

Sustainable growth and development in a society requires energy supply that is efficient, affordable, readily available and, in the long term, sustainable without causing negative societal impacts, such as environmental pollution and its attendant consequences. In this respect, proton exchange membrane (PEM) fuel cells offer a promising alternative to existing conventional fossil fuel sources for transport and stationary applications due to its high efficiency, low-temperature operation, high power density, fast start-up and its portability for mobile applications. However, to fully harness the potential of PEM fuel cells, there is a need for improvement in the operational performance, durability and reliability during usage. There is also a need to reduce the cost of production to achieve commercialisation and thus compete with

existing energy sources. The present study has therefore focused on developing novel approaches aimed at improving output performance for this class of fuel cell.

In this study, an innovative combined numerical computation and optimisation techniques, which could serve as alternative to the laborious and time-consuming trial-and-error approach to fuel cell design, is presented. In this novel approach, the limitation to the optimal design of a fuel cell was overcome by the search algorithm (Dynamic-Q) which is robust at finding optimal design parameters. The methodology involves integrating the computational fluid dynamics equations with a gradient-based optimiser (Dynamic-Q) which uses the successive objective and constraint function approximations to obtain the optimum design parameters. Specifically, using this methodology, we optimised the PEM fuel cell internal structures, such as the gas channels, gas diffusion layer (GDL) - relative thickness and porosity - and reactant gas transport, with the aim of maximising the net power output. Thermal-cooling modelling technique was also conducted to maximise the system performance at elevated working temperatures.

The study started with a steady-state three-dimensional computational model to study the performance of a single channel proton exchange membrane fuel cell under varying operating conditions and combined effect of these operating conditions was also investigated. From the results, temperature, gas diffusion layer porosity, cathode gas mass flow rate and species flow orientation significantly affect the performance of the fuel cell. The effect of the operating and design parameters on PEM fuel cell performance is also more dominant at low operating cell voltages than at higher operating fuel cell voltages. In addition, this study establishes the need to match the PEM fuel cell parameters such as porosity, species reactant mass flow rates and fuel gas channels geometry in the system design for maximum power output.

This study also presents a novel design, using pin fins, to enhance the performance of the PEM fuel cell through optimised reactant gas transport at a reduced pumping power requirement for the reactant gases. The results obtained indicated that the flow

Reynolds number had a significant effect on the flow field and the diffusion of the reactant gas through the GDL medium. In addition, an enhanced fuel cell performance was achieved using pin fins in a fuel cell gas channel, which ensured high performance and low fuel channel pressure drop of the fuel cell system. It should be noted that this study is the first attempt at enhancing the oxygen mass transfer through the PEM fuel cell GDL at reduced pressure drop, using pin fin.

Finally, the impact of cooling channel geometric configuration (in combination with stoichiometry ratio, relative humidity and coolant Reynolds number) on effective thermal heat transfer and performance in the fuel cell system was investigated. This is with a view to determine effective thermal management designs for this class of fuel cell. Numerical results shows that operating parameters such as stoichiometry ratio, relative humidity and cooling channel aspect ratio have significant effect on fuel cell performance, primarily by determining the level of membrane dehydration of the PEM fuel cell. The result showed the possibility of operating a PEM fuel cell beyond the critical temperature ($\leq 80^{\circ}$C), using the combined optimised stoichiometry ratio, relative humidity and cooling channel geometry without the need for special temperature resistant materials for the PEM fuel cell which are very expensive.

In summary, the results from this study demonstrate the potential of optimisation technique in improving PEM fuel cell design. Overall, this study will add to the knowledge base needed to produce generic design information for fuel cell systems, which can be applied to better designs of fuel cell stacks.

Keywords: PEM fuel cell; Computational fluid dynamics; Optimisation algorithm; Design parameters; Reactant gas transport; Pin fin; Cooling channel; Higher temperatures; Optimal performance.

ACKNOWLEDGEMENTS

First, I thank the almighty God for His mercies and protection during the planning and execution of this research work.

I would like to express my sincere gratitude to my supervisor, Professor Tunde Bello-Ochende, for his guidance, encouragement and support from the beginning to the final stage of this thesis. I thank him for teaching me how to be independent and remain focused when facing research challenges.

Special thanks go to my co-supervisor, Professor Josua Petrus Meyer, for affording me the opportunity to be part of their research group, and for his constant support and encouragement during the course of my study. He is a memorable mentor to younger researchers.

I also express my appreciation to Prof. J. A. Snyman for his encouragement and support on the Dynamic-Q optimisation algorihm used in part of this study.

My special thanks are due to all academic staff of the Department of Mechanical and Aeronautical Engineering, University of Pretoria. They have made my stay a successful one. The kind gestures of Dr. Dirker, Prof. Slabbert and the rest of the staff are highly acknowledged. Thank you all for your constant advice and guidance through the journey.

My special thanks go to the departmental administrative staff members for their support: Tersia Evans and Elizabe Pieterse.

My gratitude also extends to my colleagues who helped me during the research and writing of this thesis: Bode Olakoyejo, Seun Ogunronbi, Fervent Ighalo, Oke Adekola, Darshik, Low Cotz, Willem le Roux, Loyd, Mehdi, Aggrie, Ernest,

Adewunmi and other members of the thermofluid research group at the University of Pretoria. Appreciation is further extended to my friends in South Africa and abroad for their love, affection and support: Dr & Mrs Adebesin, Dr & Mrs Oboirien, Dr & Mrs Adeleke, Mr & Mrs Aregbesola, Dr & Mrs Raji, Dr Odusote, Dr & Mrs Musodiq Bello, Alhaji & Alhaja Oyekunle, Dr & Mrs Oseni, Prof. M.A. Rahaman, Prof. A.A. Asere, Dr A. Sanusi, Alhaji N. Adegun, Akeem Jimoh, Tajudeen Ogunmola, Sirajudeen Aderoju, Moshood Adelani, Leasu Ismail, Sulaiman Yahya and Rasheed Dauda.

I thank my parents Mr and Mrs Obayopo, for their invaluable support, love and prayers. I thank my brothers and sister for their constant prayers. My profound gratitude goes to my wife, Rofiat Omolola and our kids (Abdul-Rahman, Mar'yam and Ibrahim) for their emotional support, patience, encouragement and love through the journey. Words cannot express my gratitude and appreciation to them during the period of this study.

Finally, I would like to acknowledge the financial support of the Advanced Engineering Centre of Excellence at the University of Pretoria, NRF, TESP, NAC, the SOLAR Hub with the Stellenbosch University, EEDSM Hub and the CSIR.

PUBLICATIONS IN JOURNALS AND CONFERENCES

Articles in refereed journals

1. S.O. Obayopo, T. Bello-Ochende, J.P. Meyer. Three-dimensional optimisation of a fuel gas channel of a PEM fuel cell for maximum current density. *International Journal of Energy Research*: DOI:10.1002/er.1935. Accepted for publication on 4 August 2011.

2. S.O. Obayopo, T. Bello-Ochende, J.P. Meyer. Modelling and optimisation of reactant gas transport in PEM fuel cell with transverse pin fin insert in channel flow. *International Journal of Hydrogen Energy*: doi:10.1016/j.ijhydene.2012.03.150. Accepted for publication on 27 March 2012.

Journal article submitted for publication

1. T. Bello-Ochende, S.O. Obayopo, J.P. Meyer. Numerical Modeling and Optimisation of Cooling Channel Geometric Configuration for Optimal Performance of High-temperature PEM Fuel Cell System. Submitted to International Journal of Hydrogen Energy.

Papers in refereed conference proceedings

1. S.O. Obayopo**,** T. Bello-Ochende, J.P. Meyer. Numerical Optimization of a Single PEM Fuel Cell under Variable Operating Conditions. *Proceedings of the 7th International Conference on Heat Transfer, Fluid Mechanics and Thermodynamics,* HEFAT 2010, pp. 667-672. Antalya, Turkey, 19-21 July 2010.

2. S.O. Obayopo, T. Bello-Ochende, J.P. Meyer. Thermodynamic Optimization of PEM Fuel Cell Stack Gas Channel for Optimal Thermal Performance. *Proceedings of the 14th International Heat Transfer Conference (ASME),*

IHTC-14, paper no. IHTC14-22233, Washington DC, USA, 8-13 August 2010.

3. S.O. Obayopo, T. Bello-Ochende, J.P. Meyer. Numerical Study of effect of design and physical parameters on a PEM fuel cell performance. *Proceedings of the 8th International Conference on Heat Transfer, Fluid Mechanics and Thermodynamics,* HEFAT 2011, pp. 567, Pointe Aux Piments, Mauritius, 11-13 July 2011.

4. S.O. Obayopo, T. Bello-Ochende, J.P. Meyer. Optmising the Performance of a PEM Fuel Cell with Transverse Fins Insert in the Channel Flow using Mathematical Algorithm. *Proceedings of the ASME 2012 6th International Conference on Energy Sustainability & 10th Fuel Cell Science, Engineering and Technology Conference ESFuelCell2012*, San Diego, CA, USA, 23-26 July 2012.

5. S.O. Obayopo, T. Bello-Ochende, J.P. Meyer. Numerical Study and Optimisation of Channel Geometry and Gas Diffusion Layer of a PEM Fuel Cell. *Proceedings of the ASME 2012 6th International Conference on Energy Sustainability & 10th Fuel Cell Science, Engineering and Technology Conference ESFuelCell2012*, San Diego, CA, USA, 23-26 July 2012.

6. S.O. Obayopo, T. Bello-Ochende, J.P. Meyer. Impact of Cooling Channel Geometry on Thermal Management and Performance of a Proton Exchange Membrane Fuel Cell. *Proceedings of the 9th International Conference on Heat Transfer, Fluid Mechanics and Thermodynamics,* HEFAT 2012, Malta, 16-18 July 2012.

Papers in non-refereed conference proceedings

1. S.O. Obayopo, T. Bello-Ochende, J.P. Meyer. Thermodynamic Optimization of Proton Exchange Membrane Fuel Cell System. *Proceedings of the First Postgraduate Renewable Energy Symposium,* NCRS2010, Paper no. NCRS017. pp. 1-15. Stellenbosch, South Africa, 11-12 November 2010.

2. S.O. Obayopo, T. Bello-Ochende, J.P. Meyer. Performance enhancement of PEM fuel cell through reactant gas channel and gas diffusion layer optimization. *Proceedings of the Second Postgraduate Renewable Energy Symposium,* NCRS2011, Paper no. NCRS010. pp. 1-15. Stellenbosch, South Africa, 17-18 November 2011.

TABLE OF CONTENTS

LIST OF FIGURES

LIST OF TABLES

NOMENCLATURE

A	Channel width (m)
$\boldsymbol{A}$	Hessian matrix of the objective function
A_{ch}	Cross-sectional area of channel (m^2)
A^c	Fin cross-sectional area (m^2)
B	Channel depth (m)
$\boldsymbol{B}_i$	Hessian matrix of the inequality function
C	Constant
a, b, c	Diagonals of Hessian matrices $\boldsymbol{A}, \boldsymbol{B}, \boldsymbol{C}$
$\boldsymbol{C}_j$	Hessian matrix of the equality function
C_F	Quadratic drag factor
C_p	Specific heat capacity ($J\ kg^{-1}$)
c_r	Condensation rate constant
D	Gas diffusivity ($m^2\ s^{-1}$)
D_{ch}	Channel diameter (m)
D_f	Diameter of pin fin (m)
D_{eff}	Effective diffusivity ($m^2\ s^{-1}$)
D_h	Hydraulic diameter (m)
E	Electrolyte
E_{OCV}	Open-circuit voltage (V)
e^-	Electron
F	Faraday constant (96, 487 $C\ mol^{-1}$)

F	Friction factor
$f(\mathbf{x})$	Objective function
$\tilde{f}(\mathbf{x})$	Objective approximate function
G	Computational domain width (m)
$g_j(\mathbf{x})$	j-th equality constraint function
$\tilde{g}_j(\mathbf{x})$	j-th inequality constraint approximate function
h	Enthalpy (J kg^{-1})
H	Computational domain height (m)
$h_k(\mathbf{x})$	k-th equality constraint function
$\tilde{h}_k(\mathbf{x})$	k-th equality constraint approximate function
h_L	Enthalpy of condensation/vaporisation of water (J kg^{-1})
I	Exchange current density (A m^{-2})
i_o	Local current density (Am^{-2})
j	Volumetric transfer current
k	Thermal conductivity (W m^{-1} K^{-1})
K	Permeability
L	Channel axial length (m)
MW	Molecular weight
M	Molar mass (g/mol)
$\dot{m}$	Channel mass flow rate (kg/s)
n	Electron number

n_d	Electro-osmotic drag coefficient
P	Pressure (Pa)
P^*	Wetted perimeter
P_c	Capillary pressure (Pa)
P_o	Poiseuille constant
P_{pump}	Pumping power (W)
$P[k]$	Successive sub-problem
Q	Volume flow rate (m^3/s)
r_p	Mean pore radius
r_w	Water condensation rate (s^{-1})
R	Universal gas constant (8.314 J mol^{-1} K^{-1})
Re	Reynolds number
R_f	Dimensionless flow resistance
R_{ohm}	Resistance of proton transfer through electrolyte membrane (Ωm^2)
RH	Relative humidity
S	Liquid saturation or source term
S	Pin spacing (m)
Sh	Sherwood number
S_h	Volumetric heat source term
s_w	Water saturation
$\mathbb{R}^n$	n-dimensional real space

T	Time (s)
T	Temperature (K)
U	Overall heat transfer coefficient
U_o	Average velocity at inlet (m/s)
U_0	Thermodynamic equilibrium potential
u, v	Velocities in the x- and y- directions (m/s)
$\mathbf{u}$	Velocity vector [ms^{-1}]
V	Volume (m^3)
V	Cell potential (V)
V_{avg}	Mass-averaged velocity (m/s)
V_d	Volume ratio in diffusion layer
V_s	Surface ratio in diffusion layer
x, y, z	Cartesian coordinate (m)
w	Water
w	Mean velocity (m/s)
W	Molar mass fraction of oxygen
V_w	Convective velocity
$\boldsymbol{x}^*$	Design variables
$\boldsymbol{x}^k$	Design points
j,k, m,n,r	Positive integer

Greek

Δ	Difference operator
β	Permeability (m^2)
ε	Porosity
υ	Viscosity of flow [kg m^{-1} s^{-1}]
μ	Fluid viscosity (kg m^{-1} s^{-1})
μ	Penalty parameter value
α_{an}	Electrical transfer coefficient (anode)
α_{cat}	Electrical transfer coefficient (cathode)
λ	Membrane water content
λ	Tip clearance ratio
V	Kinematic viscosity [m^2 s^{-1}]
κ	Ionic conductivity [S/m]
ζ	Pitch
φ	Solid fraction
η	Over-potential (V)
Φ	Phase potential function (V)
ρ	Density (kg m^{-3})
τ	Tortuosity
σ	Electrical conductivity

Subscripts

a	Air
an	Anode
avg	Average
c	Capillary
cat	Cathode
ch	Channel
D	Porous diffusion layer
e	Electrolyte
eff	Effective
f	Fuel
G	Gas
H	Hydraulic
k	species
L	Liquid water
m	Mass moment source
m	Membrane
max	Maximum
min	Minimum
opt	Optimum
px, *py, pz*	Momentum source terms

react	Electrochemical reaction
ref	Reference value
s	Electronic conductive solid matrix
sat	Saturation
T	Energy source term
w	Liquid water source
v	Vapor phase
x,y,z	Components in the *x-*, *y-* and *z-* directions

AC	Alternating current
BPP	Bipolar plate
BTU	British thermal unit
CESFF	Convection-enhanced serpentine flow field
CL	Catalyst layer
CO	Carbon monoxide
CO_2	Carbon dioxide
CFD	Computational fluid dynamics
CHP	Combined heat and power
DC	Direct current
EMF	Electromotive force
FEM	Finite element method
GDL	Gas diffusion layer

H_2	Hydrogen gas
HOR	Hydrogen oxidation reaction
HT	Higher temperature
ICE	Internal combustion engine
LFOPC	Leapfrog optimization program for constrained problems
MEA	Membrane electrode assembly
MFPM	Multi-facilitated proton membrane
NO_x	Nitrogen oxides
O_2	Oxygen
ORR	Oxygen reduction reaction
PEM	Proton exchange membrane
PEMFC	Proton exchange membrane fuel cells
Pt	Platinum
SQP	Sequential quadratic programming

1

CHAPTER 1: INTRODUCTION

1.1 BACKGROUND AND MOTIVATION

Energy is becoming an issue of serious concern in the world today. It is inevitable for human life and a secure supply of energy is required for sustainability of human societies [1]. The need to satisfy world energy demand, which actually determines the living standard of the populace, is increasing. This energy is utilised to generate the electricity we need for our homes, businesses, schools and factories. It energises our computers, lights, refrigerators, washing machines and air conditioners, to mention only a few. Also, the quantity of energy required in the industrial sector of the economy for its production activities is ever-increasing. This energy is mostly obtained from fossil fuel stock combustion processes and great deals of pollutant gases (CO_2, NO_X, etc.) are emitted to the atmosphere [2, 3]. Some of these gases, especially CO_2, are a major contributor to global warming and its attendant consequences, such as rise in global average temperatures, rise in sea levels, flooding and deforestation. Therefore, the effects of global warming have become an issue of major concern to goverments, policy makers and environmentalists. Hence, in recent times, numerous researches and commissioned studies have focused on the development of carbon-free energy sources that are environment-friendly, sustainable and cheaply available so as to minimise the amount of pollutant gases emitted into the atmosphere as a result of energy consumption [4].

The available energy sources in the world today are divided into two groups: renewable and non-renewable sources. Renewable energies are those that come from natural resources and are replenished naturally. Non-renewable energies are those that

are not replenished or only replenished very slowly. The available renewable energy systems range from solar power systems, wind power systems, geothermal power systems, fuel cells, etc. Renewable systems have different comparative advantages which usually determine their applications. Both renewable and non-renewable energy sources can be used to produce secondary energy sources, including electricity and hydrogen. However, most of our energy sources today are from non-renewable sources, which include the fossil fuels, i.e. oil, natural gas and coal [3]. Renewable energy resources become an important option to fossil fuel as the negative environmental consequences of fossil fuel increases and its utility cost (electricity) climbs. The quality of renewable energy technologies, that makes it a viable substitute to fossil fuel, includes its modular nature, lower operating cost and its flexibility and adaptability. These energy sources are considered by many as a direct replacement of existing fossil fuel technologies and this has made the evaluation of its benefit in terms of cost to be rated low when compared to traditional fossil technologies. The baseline is to view these renewable technologies as a complementary modular addition to existing energy systems with short lead-times [1]. This will adequately reduce the pressure on the national grids and ensure availability of energy to people in remote areas. Moreover, it will help reduce the amount of pollutant gases released into the atmosphere as a result of fossil fuel usage.

The world energy consumption projection by 2030 is estimated at about 700 Quadrillion British thermal unit (BTU) [5]. This figure equates to two-thirds more energy than the present usage. Fossil fuels will remain the dominant sources of energy, accounting for more than 90% of the projected increase in demand [5]. Problems associated with energy supply and demand are much more than global warming threats, but environmental concerns such as ozone layer depletion, pollution, deforestation and radioactive emission are increasing today [1]. These environmental problems need to be addressed quickly if the world is to achieve a sustainable energy future. The drive today is to seek for sustainable development through the utilisation of energy sources that has little or no adverse impact on the environment [6, 7]. These

energy sources (i.e. solar, wind, etc.) are easily replenished once consumed, as compared to finite fossil fuels (oil, coal and natural gas).

Hydrogen, a clean and renewable fuel source, is generally available in abundance and is a safe energy source [8, 9]. This fuel type can be generated from different kinds of sources, including most renewable sources and fossil fuels (natural gases and coal gasification). Figure 1.1 illustrates a typical comparison of utilising gasoline and hydrogen as fuel for transportation and mobile applications in the service sector [10]. The figure illustrates that hydrogen sources are diverse on the energy sector side and that the emission characteristics are quite limited on the service sector side, making hydrogen a key candidate for future energy currency.

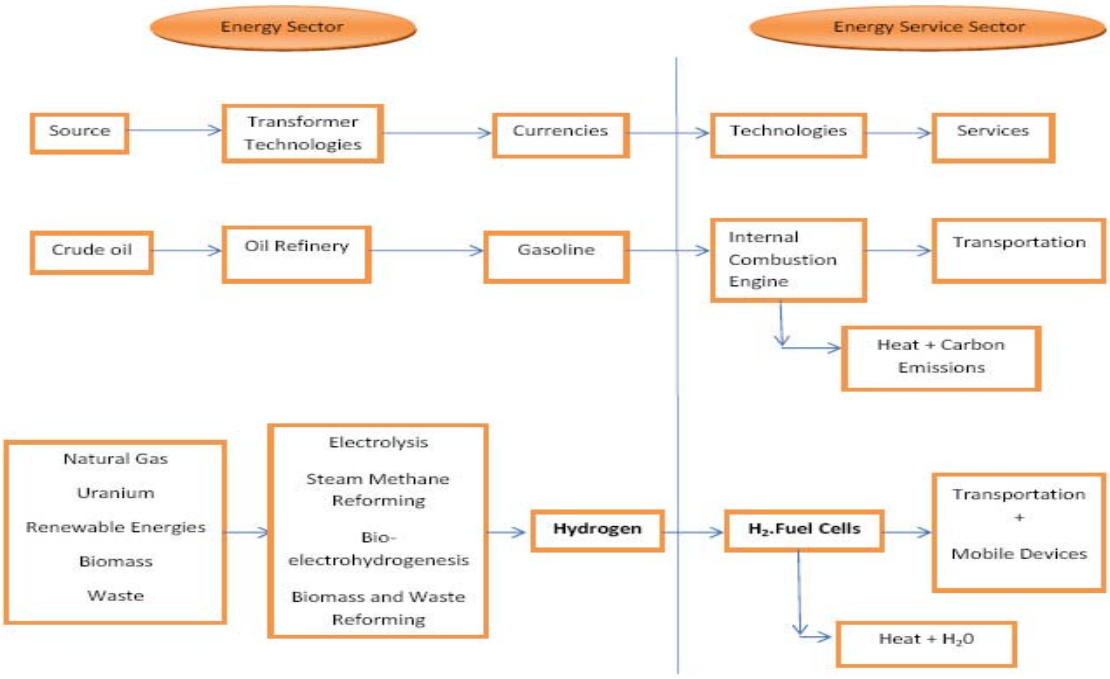

Figure 1.1 Comparison between hydrogen and gasoline as energy currency on service delivery chain [10]

Hydrogen has long been recognised as a potential fuel source for application in engines due to some unique and desirable properties [11]. These properties include its combustion in oxygen that produces only water as a waste, though, when combusted

in air, could generate some oxides of nitrogen. Table 1.1 is a comparison of combustion properties of hydrogen with other fuels. The table shows the outstanding properties of hydrogen in terms of performance when compared with other conventional fuels.

Recent studies [12-14] have shown the importance of hydrogen energy to sustainable development and in resolving the prevalent global environmental issues. The transition to hydrogen-based economy, where the main energy carrier is hydrogen and the main non-chemical energy form is electricity, is being made gradually and interest in this area is growing rapidly. However, generating electricity directly from hydrogen requires specific energy technologies such as the *fuel cell*. Fuel cell is a thermodynamic system that generates power by a direct conversion of the chemical energy in fuel into electrical power through electrochemical reaction [15].

Table 1.1 Combustion properties of hydrogen compared with other fuels [4]

Property	Hydrogen	Methane	Gasoline
Flammability limits (% by volume)	4-75	5.3-15.0	1.2-6.0
Minimum ignition energy (mJ)	0.02	0.28	0.25
Laminar flame speed at NTP (m/s)	1.90	0.38	0.37-0.43
Adiabatic temperature (°k)	2318	2190	~2470
Autoignition temperature (°k)	858	813	~500-750
Quenching gap at NTP (mm)	0.64	2.03	~2.0

Recent advancements in fuel cells have been driven by the demand for highly efficient power generation devices. Current fuel cell investments are mainly made by automotive industries to increase fuel efficiency and/or to use hydrogen as an alternative fuel. There are also opportunities of its application in power and electronic industries. The main reason for using fuel cells in power generation is the need for pollution reduction, back-up power, diversification of energy supply, as well as reduction in foreign energy dependency. Fuel cells are very useful as power sources in remote locations, such as spacecraft, remote weather stations, large parks, rural

locations and in certain military applications. A fuel cell running on hydrogen can be compact and lightweight, and have no major moving parts. A new application is micro combined heat and power (CHP), which is cogeneration for family homes, office buildings and factories [16].

Among the various types of fuel cells, *proton exchange membrane fuel cells* (PEMFCs), also termed "proton exchange membrane fuel cell" system, has attracted much interest as a convenient and viable alternative source of power, with promising potential to reduce the excess consumption of fossil fuel and discharge of carbon-dioxide [14]. The PEMFC has a high power density and a relatively low operating temperature (ranging from 60 to 80 degrees Celsius). The low operating temperature means that it does not take very long for the fuel cell to warm up and start generating electricity. Hence, PEMFC may most likely power automobiles and even residential houses in the nearest future.

Despite the potential of fuel cells to serve as clean alternative energy sources, a lot of issues still need to be addressed, mainly its cost of production and technical issues relating to optimal operating performance. The costs of components required to make fuel cells are prohibitive. For PEMFC systems, costly components such as proton exchange membranes, precious metal catalysts (usually platinum), gas diffusion layers and bipolar plates constitute up to 70% of the cost of a typical module [15]. Also, stationary fuel cell application typically require more than 40,000 hours of reliable operation at temperatures of -35°C to 40°C, while automotive fuel cells require a 5,000-hour lifespan (equivalent of 150,000 miles) under extreme temperatures. Automotive engines must also be able to start reliably at -30^{o}C and have high power to volume ratio (typically 2.5 KW per liter). Thus, there is the need to develop fuel cells that are durable and can operate at temperatures greater than 100°C and yet function well at sub-zero ambient temperatures. In addition, the cell membranes also tend to degrade while the fuel cell system cycles on and off, particularly as operating temperatures rises. Hence, it is important for the membrane

to remain stable under cycling conditions. Also, PEMFC membranes must be hydrated in order to transfer hydrogen protons. This is necessary because, if water in the system evaporates too quickly, the membranes dry up and resistance across it increases. It will eventually crack, creating a gas "short circuit" where hydrogen and oxygen combine directly, generating heat that will damage the fuel cell. This condition necessitates that the fuel cell continues to operate in sub-zero temperatures, low humidity environments and high operating temperatures. Furthermore, when a fuel cell is in operation, the temperature must be maintained throughout the cell in order to prevent destruction of the cell through thermal loading. This is particularly challenging, since the reaction in the fuel cell is highly exothermic (heat releasing) and thus, large quantities of heat is generated within the fuel cell. Maintaining a uniform operating cell temperature in the fuel cell is thus not a trivial task.

The technical issues highlighted above, have hindered the commercialisation of PEMFC, hence there is need for in-depth research to understand and proffer solutions aimed at improving the performance of this class of fuel cell, so as to meet the market competitiveness compared to fossil-fuel based energy systems. One of the main objectives of the present fuel cell research in the industry today is the need to improve the performance of fuel cells. This can be done by better design and enhancing its capability so as to increase its production at low cost in order for it to compete favourably with fossil fuel-based systems. There are two primary approaches to achieving this, that is:

- Design, build and experimentally test approach to evaluate its performance

- Simulate by numerical modelling approach

The first approach usually yields useful and physical representative information of the phenomenon in the real system but is costly and time-consuming [10]. This becomes more difficult when looking into the vast number of working parts involved in a fuel

cell system and the limited experimental techniques available. The modelling approach can provide the much needed insight into the phenomena that characterise fuel cell systems at a reduced cost and time [10]. Optimal design of the system can thus be achieved and subsequently help at achieving the goal of fuel cell commercialisation. Performance improvement in the proton exchange membrane (PEM) fuel cell system is still an open research. More design models are being developed with the aim of enriching the knowledge base on generic information needed for a better design of PEM fuel cell systems. This research is one of the efforts channelled in that direction by introducing a more novel modelling approach coupled with optimisation techniques to improve the performance of PEM fuel cell systems.

1.2 REVIEW OF RELATED LITERATURE

A significant amount of research studies have been devoted to the study of PEM fuel cells, ranging from theoretical to experimental studies. With regards to the former, several empirical and mathematical models, which are aimed at understanding and predicting PEM fuel cell performance, have been proposed. Giner and Hunter [17] and Cutlip *et al.* [18, 19] have proposed the first of such models taking into consideration diffusion and reaction in the gas-diffusion electrodes. More attention subsequently spring up towards experimental studies [20-22] using simple 0-D models to analyse data on PEM fuel cells. These models normally fit the experimental data with a single equation. Although these models demonstrate good fits and are quick and easy to implement, they are less accurate and reliable in predicting the PEM fuel cell behaviour. More fundamental models were developed thereafter to simulate performance and gain deeper understanding of the underlying fundamental transport processes. Two main works in this regard are those of Bernadi and Verbrugge [23] (hereafter referred to as B&V) and Springer *et al.* [24]. Both studies included the membrane, diffusion media and catalyst layers in their respective models. B&V's model assumes a fully hydrated membrane and incorporates porous-electrode

equations and Stefan-Maxwell diffusion in the diffusion media and catalyst layers. The model of Springer *et al.* [24] does not use porous-electrode equations but changing water content in the membrane. This changing water content allows for variable properties in the membrane such as conductivity and the water diffusion coefficient. Most models today can conveniently trace their roots back to B&V studies [25].

The advances in digital computer technology have spurred the progress in the area of fuel cell development, especially in the application of numerical methods for fuel cell optimisation. The advancement in computational fluid dynamics (CFD) allows for effective design and optimisation of the fuel cell systems, with reduced reliance on hardware prototyping and reduction in development cycles. CFD provides a platform for understanding the variety of complex multi-physics transport processes characterised by a broad spectrum of length and time scales in the fuel cell structure. These processes include phenomena which involve fluidic, ionic, electronic and thermal transport in concert with electrochemical reactions. B&V's model forms the basis for almost all the CFD models in fuel cells today [25]. The incorporated electrochemical effects stem from the developed equations of B&V, such as their kinetic source terms in the catalyst layers and the use of Schlogl's equation for water transport in the membrane. The following sections (1.2.1-1.2.4) deal with specific literature relevant to this thesis, in which related studies addressing the design, optmisation and performance analysis of PEM fuel cells are discussed.

1.2.1 OPTIMAL OPERATING CONDITIONS FOR PEM FUEL CELL

Fuel cell operation involves the specification of a range of operating conditions such as temperature, pressure, stoichiometry ratio of reactant gases, porosity of the diffusion layers, etc. Accurate specification of this range of operating conditions will assist in predicting the fuel cell performance under these specified conditions and

could be used to optimise the design of a fuel cell system. Appropriate operating conditions are also required for a PEM fuel cell system to achieve and maintain stable operational performance. Effects of the gas hydrodynamics on the performance of the air cathode of a PEMFC with an interdigitated gas distributor has been studied by Yi and Nguyen [26]. In addition, pressure drop between the inlet and outlet channels, electrode height and shoulder width on the average current density were studied. They discovered that, with the forced flow-through condition created by the interdigitated gas distributor design, the diffusion layer thickness is greatly reduced. However, even with a much thinner diffusion layer, diffusion still plays a significant role in the transportation of oxygen to the reaction surface. In addition, the average current density generated at an air cathode increases with higher gas flowrates, thinner electrodes and narrower shoulder widths between the inlet and outlet channels of the interdigitated gas distributor.

Chan and Tun [27] conducted an investigation to determine the effects of the different parameters such as catalyst layer porosity, catalyst layer thickness and ionic conductivity on the performance of PEM fuel cells. The model showed that catalyst layer porosity and catalyst layer thickness has a significant effect on the limiting current density for the fuel cell. However, the ionic conductivity has no effect on the limiting current density. Furthermore, Jaouen *et al.* [28] used a one-dimensional, steady-state agglomerate model to determine the nature of mass transport limitations in the PEM fuel cell cathode. Effects of the active layer thickness, oxygen concentration and relative humidity of the oxygen stream were investigated. The result of the model shows that limitation by proton migration in the active layer, or by oxygen diffusion in the agglomerates leads to a doubling of the Tafel slope at higher current densities. For those two types of transport limitations, the dependence of the reaction rate on the active-layer thickness, oxygen partial pressure and relative humidity of the specie gas were shown. When additional limitation, due to slow gas phase diffusion, appears, the double Tafel slope is distorted. A mathematical

expression for the limiting current density, due to this process, was presented for use in correcting the polarisation curves for slow gas phase diffusion.

Studies on the effects of various operational parameters such as temperature, pressure, stoichiometric ratio, porosity and gas diffusion layer (GDL) thickness on the fuel cell performance was performed by Berning *et al.* [29]. They observed that temperature, pressure, stoichiometry ratio, GDL thickness and porosity, all have an impact on the limiting current density at a varying degree for the fuel cell. They also observed the need to estimate the extent of contact resistance inside the fuel cell in order to properly assess the impact of porosity and channel width on fuel cell performance. Kazim *et al.* [30] presented a two-dimensional mathematical model in which they investigated the effects of cathode porosity, inlet oxygen mole fraction, operating temperature and pressure on the performance of PEM fuel cells with the interdigitated flow field. The obtained result illustrated the positive impact of an increase in the GDL porosity on the fuel cell performance. Furthermore, it was observed that an increase in the mole fraction, operating pressure, or temperature of the oxygen entering the cathode GDL leads to higher fuel cell performance.

Chu *et al.* [31] studied the effect of variability in the porosity size of the GDL on the performance of PEM fuel cell. They observed that a fuel cell embedded in a GDL with a larger averaged porosity consumes a greater amount of oxygen, such that a higher current density is generated and a better fuel cell performance of the fuel cell is obtained. This explains partly why fuel cell performance deteriorates significantly as the cathode is flooded with water (i.e. to give a lower effective porosity in the GDL). In terms of the system performance, a change in GDL porosity has virtually no influence on the level of polarisation when the current density is medium or lower, but exerts a significant influence when the current density is high. The investigations of Jeng *et al.* [32] focused on the effects of the change in the porosity of the GDL on the performance characteristics of a PEMFC. Their results also showed that the existence of ribs causes the GDL to be used only partly in the mass transfer process.

The GDL's effectiveness decreases with the cell current density and increases with the width of the gas flow channels. The PEM fuel cell performance decreased with an increase in the GDL thickness when the GDL porosity is low. However, when a high-porosity GDL is used, the optimal thickness becomes an indicator which determines the maximal PEM fuel cell performance.

Wang *et al.* [33] conducted a study aimed at verifying the mechanisms of parameter effects and their interrelationship by comparing modelling results with experimental data. They observed that, when adequate humidification is provided, the performance of the PEM fuel cell improves with the increase in fuel cell temperature. The result also showed that anode and cathode humidification has significant effects on the performance of the PEM fuel cell. Lee *et al.* [34] conducted a numerical simulation of the species gas in the fuel channel and the diffusion layer to investigate the effects of GDL thickness, porosity and distribution of the pore size on the PEM fuel cell performance. The PEM electrodes were prepared by applying different porous GDLs onto each face of a carbon cloth support. They discovered that a GDL with a more porous structure performed better. More importantly, it was shown that a GDL's geometric characteristics (thickness, porosity and distribution of pore size) greatly affect the performance of the PEM fuel cell.

Hwang *et al.* [35] presented a three-dimensional numerical model to simulate the transport phenomena on the cathode air-side of a PEMFC. They compared the polarisation curves of the interdigitated flow field and parallel flow field for a typical PEM fuel cell. Their study ascertained the fact that an interdigitated flow field gives a higher average current density on the catalyst layer surface than with parallel flow field under similar mass flow rate and cathode overpotential. Effects of electron transport through the GDL of the PEM fuel cell was investigated by Meng and Wang [36]. They discovered that the lateral electronic resistance of the GDL, which is affected by the electronic conductivity, GDL thickness and gas channel width played a critical role in determining the current distribution and cell performance. It was further

observed that, under fully-humidified gas feed in the anode and cathode, both oxygen and lateral electron transport in the GDL dictated the current distribution. The lateral electronic resistance dominated the current distribution at high cell voltages, while the oxygen concentration played a more decisive role at low cell voltages. With reduced GDL thickness, the effect of the lateral electronic resistance on the current distribution and cell performance became even stronger, because the cross-sectional area of the GDL for lateral electron transport was smaller.

Du *et al.* [37] proposed a theoretical model to investigate the effective protonic and electronic conductivity of the catalyst layers in PEM fuel cells. The model showed that effective protonic conductivity increased with an increase in the Nafion volume fraction in the catalyst layers of the PEM fuel cells. The study also showed that effective protonic conductivity increased almost linearly with an increase in the operating temperature for a given water activity. Pasaogullari and Wang [38] conducted an investigation on the two-phase flow characteristics in the cathode GDL of a PEMFC. They revealed that an onset of flooding of the porous cathode hinders the rate of oxygen mass transport to the cathode catalyst layer. In addition, their result showed that the rate of cell humidification and mass flow rate of the reactant gas species are important parameters determining PEMFC two-phase flow transport characteristics and performance.

Lu and McGurick [39] presented a model of the PEMFC cathode with an interdigitated gas distributor to investigate the effects of various parameters such as electrode permeability, thickness and shoulder width on the cell performance. It was observed that changes in permeability, ranging from 10^{-8} to 10^{-13} m^2, has little impact on the cell performance. Increasing the electrode thickness and the shoulder width resulted in poorer performance due to greater resistance to flow. In addition, their results showed that liquid water tends to form near the outlet of the electrode when the current density is greater than 1.0×10^4 A m^{-2}. Sun *et al.* [40] developed a two-dimensional model to investigate the influence of the GDL property and flow-field

geometry, such as diffusion layer diffusivity, diffusion layer conductivity, channel width-to-area ratio and diffusion layer thickness on the local reaction rate in the PEMFC cathode catalyst layer. Their work showed that, when the PEMFC is operated using reformate hydrogen, the performance drops dramatically due to carbon monoxide (CO) poisoning as the anode gas flow rate increases. More research on the CO poisoning effect on PEMFC performance are reported in the literature [41-43].

Mawardi and Pitchumani [44] studied the effect of parameter uncertainty on the variability in performance of PEM fuel cells and optimisation of different operating parameters that affects fuel cell performance. They developed a sampling-based stochastic model to measure the performance of PEM fuel cells. The results further provided a valuable tool for the design of fuel cells under uncertainty in material and operating parameters.

Hsieh *et al.* [45] investigated the effects of the operating temperature and backpressure on the performance of micro PEM fuel cells using different flow fields. Their study concluded that cell performance increases with an increase in cell operating temperature until a limiting or threshold level is reached. In addition, they observed that the higher the flow-back pressure, the better the performance of the single micro PEMFC at a fixed cell operating temperature. The interdigitated flow field showed better performance, while lower pressure was obtained using mesh-type flow field at a fixed active area of the membrane electrode assembly (MEA).

Yan *et al.* [46] investigated the steady and transient response on performance in both single fuel cell and stack configuration under a variety of loading cycles and operating conditions. They discovered that different feed gas humidity, operating temperature, feed gas stoichiometry, air pressure, fuel cell size and gas flow pattern affect both the steady-state and dynamic response of fuel cells. They experimentally confirmed that a decrease in the cathode humidity has a detrimental effect on the fuel cell steady state and dynamic performance of the fuel cell. Temperature variation also significantly

affects fuel cell performance through its effect on membrane conductivity and water transport in the GDL and the catalyst layer. Amirinejad *et al.* [47] conducted experiments to study the effects of operating parameters on PEM fuel cell performance by using dry and humidified hydrogen and oxygen as reactant and oxidant gases, respectively. The result of their experiment showed that the most important factor affecting the PEMFC performance is the mass transport limitation. This limitation included the transport of reactant and oxidant gases to active sites of the catalyst, the transport of the proton from the anode side to the cathode side through the membrane, and the transport of produced water from the cathode side to the anode side by back-diffusion mechanism. Fuel cell operating parameters such as temperature, pressures and humidity of reactant gases could decrease the mass transport limitation and improve the performance of the fuel cell.

Zhou *et al.* [48] developed a steady-state, two-dimensional model to illustrate the inlet humidification and pressure effects on PEM fuel cell performance. Their model asserts the fact that humidification of both the anode and the cathode is very important for fuel cell performance. Also, the pressure drop in the PEM fuel cell flow channels increases the pumping power requirement and attention must be paid to this pressure situation when designing the fuel cell. Yan *et al.* [49] determined the electrical characteristics of a PEMFC stack under varying operating conditions, using AC impedance measurement technique. They documented the fact that the air humidity and cell temperature greatly impact on the charge transfer resistance of the PEM fuel cell stack. Similar to Yan *et al.*'s work is studies by Zhang *et al.* [50]. They investigated the effect of reactant gas relative humidity on fuel cell performance using the AC impedance and cyclic voltammetry methods. This study affirmed that a reduction in the relative humidity of a fuel cell can depress the electrode kinetics, including electron reaction and mass diffusion rates, and the proton conductivity of the membrane, resulting in a dramatic degradation of the fuel cell performance.

Hung *et al.* [51] developed a theoretical model to investigate the effects of operating parameters (e.g. temperature, humidification temperature, pressure, gas stoichiometry ratios) on cell performance. Design and modelling parameters were obtained using a regression analysis of experimental data and validating it as these operating parameters changes. Hwang *et al.* [52] presented a non-isothermal model of PEMFC in contact with an interdigitated flow field to study the effect of flow orientation on thermal-electrochemical transport in a PEM fuel cell. The study revealed that both the solid-matrix and fluid-phase temperatures are increased with the increase of the total overpotential of the fuel cell. In addition, the fluid-phase and solid-matrix temperature distributions are significantly affected by the flow orientation of the species reactant in the PEM fuel cell.

Yuan *et al.* [53] proposed a three-dimensional multi-phased model of a PEM fuel cell to predict the effects of operating parameters on the performance of PEM fuel cells. The study revealed that fuel cell performance is enhanced with an increase in operating pressure, temperature and air stoichiometry ratio. The study asserts the fact that anode humidification has more significant effects on the PEM fuel cell performance than cathode humidification. It was also documented that best performance occurred at low air relative humidity and high hydrogen relative humidity.

In summary, most theoretical studies on fuel cells in the literature focus on the numerical simulation of the transport phenomenon and parametric study of the effects of physical variables. The main objectives of the reported models are to investigate the performance of fuel cells under various operating conditions, with a view to find optimal performance parameters.

1.2.2 FUEL GAS CHANNEL OPTIMISATION FOR PEM FUEL CELLS

One of the critical issues in proton exchange membrane fuel cell design is the efficient design of the flow channels to ensure uniform distribution of the reactant gases in the fuel cell stack. The flow field geometry and pattern has great influence on the reactant gas transport, water management and the efficient utilisation of the fuel gases, since efficient species gas transport and water removal from the fuel cell system is enabled by proper flow field design. The flow field design for fuel cells is thus one of the important technical challenges for PEM fuel cell design and operation and impacts on system performance and life-span [54].

Kumar and Reddy [55] studied the effect of the dimensions and shape of the flow channels in the flow-field of a PEMFC. The flow field used for the study was the single-path serpentine design. They concluded from their study that optimum channel width, land width and channel depth for optimal fuel cell performance are close to values of 1.5, 0.5 and 1.5 mm, respectively. In addition, it was found that reducing the channel land width, increases the hydrogen consumption at the anode section of the fuel cell. A hydrodynamic model to study flow distribution and pressure drop in parallel-channel configurations of a planar fuel cell was developed by Maharudrayya *et al.* [56]. They considered Z-type and U-type configuration channels in their study. The obtained result shows that for a fuel cell distributor plate, low and high flow maldistribution could occur for both the Z-type and U-type configuration. The extent of this maldistribution is a function of the geometric factors of the parallel-channel configuration and these factors could be manipulated to achieve a uniform flow distribution in the fuel cell system.

Shimpalee *et al.* [57] investigated the impact of channel path length on a PEMFC system. They concluded from their work that better uniformity in local temperature, water content and current density distribution in the serpentine flow-field design of the PEM fuel cell system is obtained by using a shorter path length rather than a

longer path. Hence, reducing the PEM flow-field path length is a prospective variable for improving the performance and efficiency of the PEMFC system. Inoue *et al.* [58] conducted a study to investigate the effect of gas channel depth on current density distribution of PEM fuel cell using computational fluid dynamics, including gas flow through a GDL. They found that output current density of the fuel cell system increases with the decrease in the depth of the separator channel and corresponding increase in pressure drop and current density distribution.

A model similar to that of Inoue [58], was employed by Ahmed and Sung [59] to investigate the effect of channel geometric configuration at high operating current density of the fuel cell. Their result demonstrated the fact that a rectangular channel cross-section produces higher cell voltages compared with trapezoidal and parallelogram channel cross-sections. However, the trapezoidal cross-section proves more effective at ensuring uniform reactant and local current density distribution over the reactant area of the fuel cell. The results further ascertain the fact that shoulder width impacts great on fuel cell performance when compared with other geometric factors. Also, Cheng *et al.* [60] conducted a study to optimise the geometrical parameters of the PEMFC, by using a numerical approach coupled with an optimiser. The result of their study shows that the gas channel width fraction, the gas channel height and the thickness of the GDL all influenced the performance of the fuel cell system. In addition, their study shows that, using the coupled optimiser at channel width fraction of 0.3925, gas channel height of 1.2034 mm and GDL thickness of 0.176 mm, an optimal power density of 1857 W m^{-2} is obtained when compared with the original fuel cell design.

Xu and Zhao [61] developed a novel flow-field for polymer electrolyte-based fuel cell systems by re-pattering conventional single serpentine flow fields. Their studies confirmed the effectiveness of this new design at inducing larger pressure difference between adjacent flow channels over the electrode surface area of the fuel cell. The effect of such large difference is that mass transport of the reactant gases and products

are enhanced to and from the catalyst layer. Furthermore, water clogging within the electrode in greatly reduced.

Li *et al.* [62] proposed a flow-field design procedure to effectively eliminate resident water flooding in the PEM fuel cells. They employed a design based on specifying appropriate pressure drop along the flow channel that will ensure evaporation or drift force removal by the gas stream in the flow channel width, therefore, dehydrating the fuel cell membrane. They reported that the designed flow-field procedure is effective for water removal in the fuel cell. Their claims were validated experimentally, by using a neutron imaging technique measurement of liquid water content in the fuel cell system. Shimpalee and van Zee [63] numerically investigated the effect of rib and channel dimension of the reactant flow-field on the performance of PEMFC under automotive and stationary conditions. The obtained result revealed that, for stationary applications, employing a narrower channel with widened rib spacing produces higher fuel cell performance, with the reverse being a case of automotive application.

Owejan *et al.* [64] studied the effects of flow field and GDL properties on water accumulation in the PEMFC. They documented that flow field channels with hydrophobic coating retain more water in the fuel system, but the spread of a higher number of smaller water slugs improves the fuel cell performance at high current density. The result further demonstrated the fact that cells made by using diffusion media with lower in-plane gas permeability shows lower water accumulation capacity in the fuel cell system. Peng *et al.* [65] developed a model to optimise the flow channel design and at the same time balance the fuel cell stack performance and formability. Their optimisation result shows that optimum dimensional values for channel depth, channel width, rib width and transitional radius of 0.5, 1.0, 1.6 and 0.5 mm, respectively, were obtained at highest reaction efficiency of 79% and formability of 1.0 of the fuel cell used for their study.

Sinha *et al.* [66] presented a three-dimensional, non-isothermal PEMFC model to investigate the effect of flow field design on the performance of the system at elevated temperatures. They compared the fuel cell performance with serpentine and parallel flow field design when the fuel cell is operated at 95ºC under various inlet humidity conditions. They concluded that the parallel flow field design ensure better and uniform distributed performance on the entire cell active area when compared to the serpentine flow field at low inlet relative humidity and elevated temperatures. Hsieh and Chu [67] conducted a study on channel and rib geometric scale effects of flow-field plates on the performance and transient thermal characteristics of micro-PEM fuel cell system. They found that optimum channel-to-rib width ratio for the range considered in their study to be 0.67, considering the net power gain of the system. In addition, they documented the fact that channel and rib geometric effect has no significant effect on the cell system transient temperature distribution.

Ferng *et al.* [68] performed a numerical and experimental investigation into the effects of flow channel patterns on the performance of PEM fuel cell by using parallel and serpentine flow channels with the single path of uniform depth and four paths of step-wise depth, respectively. They documented in their study that the serpentine flow channel is better when compared with the parallel flow channel. Their result further shows that different depth of the flow channel significantly affect the performance of the parallel design but have no significant effect on the serpentine channel design performance. Wang *et al.* [69] studied the local transport phenomena and PEM fuel cell performance with various serpentine flow field designs. The study considered single, double and triple serpentine flow field designs. The predicted results was confirmed, i.e. that the single serpentine flow field has better performance when compared with double and triple serpentine designs and the performance of the single serpentine flow field increases as the number of the channel bend is increased. It was also found that the performance of the fuel cell increases slowly as fuel channel width increases.

Finally, a comprehensive review on flow field design in the bipolar plates of PEM fuel cells has been published by Li and Sabir [70]. They presented reviews on various flow-field layouts developed by different companies and research groups. Furthermore, they enumerated and evaluated the pros and cons in those various designs. In addition, the review concluded that improvement on flow-field design for fuel cells can greatly improve the goal of cost reduction and performance enhancement for the commercialisation of PEM fuel cell. However, flow-field design is still an open ended on-going research and more novel designs, that will be suitable for different and specific applications, are required.

1.2.3 REACTANT GAS TRANSPORT IN PEM FUEL CELLS

Flow distribution in PEMFC impacts greatly on the performance and efficiency of the system. The efficient distribution of species reactant to ensure homogenous spread on the GDL at reasonable pressure drop along the flow channel distributor is crucial to both effective utilisation of fuel gases and PEMFC performance. In addition, proper water and heat management within the fuel cell structures are required for obtaining optimal power density from the fuel cell. Hence, enormous efforts are being devoted by various researchers to develop novel flow structures for PEM fuel that will enhance the interaction between the GDL and the flow field to improve the cell performance. A discussion on these research efforts follows.

Um *et al.* [71] developed a transient, multidimensional model to investigate the electrochemical and transport processes inside a PEMFC. They reported that, in the presence of hydrogen dilution in the PEM fuel stream, there is a large decrease in hydrogen presence at the reaction surface which results in lower current density as a consequence of decreased hydrogen transport to the reaction site of the fuel cell system. He *et al.* [72] presented a two-phase model of the cathode of the PEMFC by using interdigitated flow fields. The model was used to investigate the effect of

various electrode and flow field design parameters at the cathode of PEM fuel cell performance. Their result shows that liquid water transport and evaporation form the mechanism for water removal at the cathode section of the PEM fuel cell. Also, higher differential pressure between inlet and outlet channels increase oxygen transport and liquid water removal from the electrode section, thereby increasing the fuel cell performance. They further suggested the need to optimise the electrode thickness for better PEM fuel cell performance.

Chang *et al*. [73] studied flow distribution in the PEM fuel cell stack system, incorporating flow diffusion effects into their model. They reported that higher channel friction factors leads to more uniform flow distribution in the fuel system and the U-type manifold design performs better than the Z-type design. In addition, they observed that, at higher current densities, fuel cell performance is more sensitive to operating conditions such as cathode stoichiometry and inlet pressure. Mazumder and Cole [74] studied liquid water transport in PEM fuel cells using a three-dimensional model. They concluded that, at critical current density, saturation levels could exceed 50% and are more prominently so at the cathode section of the fuel cell. In addition, they also reported that the effect of electro-osmotic drag contributes majorly to the determination of the local saturation level in the MEA of the fuel cell, but was found negligible at impacting on the fuel cell performance.

Dohle *et al.* [75] proposed a model to evaluate the interaction between the GDL and the flow field of PEMFC. Their model was also utilised to develop a suitable match between serpentine flow field and the diffusion layer of the fuel cell system. They reported that, to avoid reactant depletion in the specific region of the fuel cell, the geometry of the serpentine channel should be chosen with regard to permeability of the GDL. In addition, to obtain higher permeability, the serpentine structure should have low pressure loss to ensure good flow homogeneity. In the studies of Gurau *et al.* [76], a multifluid, multiphase model was proposed to evaluate the two-phase transport in PEMFC. The model developed accounts for gas- and liquid-phase

momentum and species transport in the whole structure of the PEM fuel cell system. They documented that the level of water accumulation in the GDL is predominantly determined by the saturation equilibrium at the GDL-channel interface and the GDL permeability. Meanwhile, the level of water accumulation in the catalyst layer is determined by the saturation level in the GDL and the saturation equilibrium at the GDL/catalyst layer interface.

Yan *et al.* [77] presented a model to investigate the effect of flow distributor geometry and diffusion layer porosity on reactant gas transport and PEM fuel cell performance. They reported that increase in channel width fraction, number of channels and porosity of the GDL positively enhance the performance of the studied fuel cell system. In addition, the results shows that better uniformity in current density along the width of the cell can be obtained at relatively low overpotential of the fuel cell. Wang *et al.* [78] proposed a novel serpentine-baffle flow field design, different from conventional serpentine flow field, to improve the PEM fuel cell performance. The model developed was also used to analyse the reactant and product transport and the electrochemical reactions in the fuel cell. They concluded that, at high operating fuel cell voltages, conventional and baffled novel serpentine design shows the same performance. However, at lower operating cell voltages, the baffle design shows better performance than the conventional design. Their result further shows that larger pressure differences are induced on the electrode surface with baffled channels. Consequently, the mass transport is improved, thereby leading to enhanced fuel cell performance.

Jang *et al.* [79] developed a two-dimensional model to investigate the performance of a PEM fuel cell system based on variability in porosity and GDL thickness. Their result shows that the mass transfer increment resulting in high reaction rates can be achieved by increasing the GDL porosity. This improves the fuel cell performance. In addition, they documented that the performance of the fuel cell also increases with the decrease in the thickness of the GDL. However, performance is enhanced in the fuel

cell system by using a co-flow of fuel and air rather than counterflow configuration. Wang *et al.* [80] presented a three-dimensional model of PEM fuel cells with parallel and interdigitated flow fields to investigate the effects of the cathode flow rate and flow channel area ratio on the cell performance. The model also incorporated the effects of liquid water formation on the reactant gas transport in the fuel cell system. It was documented that the performance of the fuel cell system is not impacted at high operating voltages by flow channel designs and operating parameters, but these parameters have a significant effect on the fuel cell performance at low operating voltages. Their result further shows higher performance of the fuel cell system when using interdigitated flow fields, owing to the forced convection created by its baffles to improve transport rates and liquid water removal.

Kim [81] investigated the effect of relative humidity and stoichiometry of reactants on water saturation and local transport process PEMFCs. The result shows that the reactant relative humidity (*RH*) and stoichiometry significantly affect the fuel cell performance. Also, at a constant relative humidity of the anode, *RH* = 100%, a lower cathode relative humidity maintains membrane hydration, resulting in improved fuel cell performance. Conversely, at a constant cathode *RH* of 100%, a lower anode *RH* increases the difference in water concentration between the anode and cathode, resulting in better fuel cell performance. In addition, higher anodic stoichiometry results in the reduction of cathode water saturation due to increase in back-diffusion, thereby increasing the fuel cell performance. Jang *et al.* [82] investigated the effect of humidity of reactant fuel on the cell performance of PEMFC with baffle-blocked flow field designs. They reported that fuel cell performance is enhanced with an increase in inlet *RH* of the hydrogen gas species due to an increase in the chemical reaction and mass transfer of oxygen. There is an adverse effect in performance by increasing the inlet *RH* in the cathode at lower cell voltage due to oxygen depletion in the fuel cell. Their result further shows that cell performance is enhanced with an increase in the number of baffles as a result of an increase in areas of forced convection and oxygen gas diffusion to the catalyst layer. Furthermore, Nguyen and White [83] developed a

model to investigate the effectiveness of varying humidification designs in PEM fuel cells. The model accounts for electro-osmotic and diffusion of water transport in the membrane, a solid phase to gas phase heat transfer and latent heat formation, resulting from evaporation and condensation in the flow channels. Their results show that, at high current densities, large fraction of voltage losses in the cell is due to ohmic loss in the membrane. They proposed that the anode gas stream must be humidified in order to maintain adequate hydration in the cell, especially when the fuel cell is operated at high power densities.

Ko *et al.* [84] investigated the effect of the channel flow pattern on internal properties distribution of a PEM fuel cell for cathode starvation conditions, numerically and experimentally. The fuel cell system performance was investigated by using single, double and mixed serpentine fuel channel configurations. They documented that mixed serpentine channels enhance flow velocity better than other configurations (single and double) and subsequently prevent the channel from flooding. Their result further shows that local temperature and sensitivity to cathode starvation is higher in single serpentine systems than in other configurations and that it is more liable to thermal degradation. Liu *et al.* [85] investigated the application of baffle-blocked flow channel for enhancement of reactant transport and performance of fuel cells. Their result shows that local transport of the reactant gases, current density output and cell performance can be enhanced by the incorporated baffles in the fuel cell flow channel. They further documented that baffle effects enhance gas fuel transport at high operating cell voltages and raise the local current density in the upstream, but lower them at the downstream of the channel.

Soong *et al.* [86] proposed a novel configuration of partially blocked fuel channels with baffle plates transversely inserted in the channel. They evaluated the effects of the blockage with various gap ratios, number of baffle plates, fuel flow Reynolds number and GDL porosity on reactant gas transport and pressure drop across the channel length. They documented that, reducing the gap size between the baffle and

the GDL and/or increasing the baffle number enhances the reactant gas transport but with adverse penalty of high pressure drop. They further proposed that, to ensure high performance and minimal pressure drop, a baffle gap ratio no smaller than 0.1, baffle plates number between 3 to 5 and GDL porosity of about 0.7 will be preferable as design values. Liu *et al.* [87] proposed a model to investigate the reactant gas transport and the PEM fuel cell performance with a tapered flow channel design. Their result shows that fuel cell performance is enhanced by using the tapered flow field design but more prominently so at lower cell voltages. They further documented that the liquid water effect has significant impact on transport phenomena and the performance of PEM fuel cell.

1.2.4 HEAT TRANSPORT AND COOLING IN PEM FUEL CELLS

Thermal management in PEM fuel cells has drawn increasing attention in recent times because technological limitations encountered in PEM fuel cells today depend largely on these aspects [88]. Operating temperature affects the maximum theoretical voltage at which a fuel cell can operate. Higher temperatures correspond to lower theoretical maximum voltages and lower theoretical efficiency [89]. However, increase in temperature at the electrodes increases the electrochemical activity, thereby increasing the fuel cell efficiency. Higher temperature operation of the fuel cell also improves the quality of waste heat derivable from the system. Practically, there is an optimal temperature range within which a specific fuel cell system can perform well and reliably. The main purpose of thermal management in fuel cell systems is to ensure effective stack operation within the specific temperature range. In recent years, efforts have been made to investigate and predict heat/mass transfer phenomenon in PEM fuel cell systems. Some of these research efforts are highlighted below.

Coppo *et al.* [90] presented a 3-D model to study the influence of temperature on the PEM fuel cell operation, including two-phase flow in the gas distribution channel.

The result obtained indicate that both liquid water transport within the GDL and liquid water removal from the surface of the GDL play an important role in determining variations in cell performance where temperature is involved. Yan *et al.* [91] presented a 1-D non-isothermal model to analyse the effect of anode and cathode side temperatures on the membrane water distribution. The results obtained shows that increasing the temperature on the anode side can lead to membrane dehydration, and operating the fuel cell at high current density leads to membrane dehydration on the anode side, due to strong electro-osmotic water drag at high current density.

Ramousse *et al.* [92] developed a 1-D non-isothermal model accounting for heat and mass transfer in a complete cell, and charge and mass transfer in the electrodes. Their study provides for temperature, concentration and potential fields in a single cell. In addition, their work shows that the thermal gradient in MEA could lead to thermal stresses at high current densities. Shimpalee and Dutta [93] conducted a 3-D non-isothermal numerical analysis with a two-phase flow. The effect of heat produced by the electrochemical reaction and phase change of water on the cell performance was critically studied. Their study shows that inclusion of heat transfer in the fuel cell model shows degradation in the fuel cell performance. This research work enumerated the importance of incorporating the heat transfer aspect in fuel cell modelling.

Shan and Choe [94] presented a 1-D model, taking into account the dynamics in temperature gradient across the fuel cell; dynamics in water concentration redistribution in the membrane; dynamics in proton concentration in the cathode catalyst layer; and dynamics in reactant concentration redistribution in the cathode GDL. Their result generally shows that temperature profiles in each of the cell layers tend to follow the current waveform, due to energy losses in these layers. Higher temperature losses are prominent in the membrane and the catalyst layer, due to ohmic losses as a result of membrane resistance and heat released by the chemical reaction. Yuan and Sunden [95] performed a 3-D non-isothermal numerical analysis of heat transfer and gas flow in PEM fuel cell ducts by using a generalised extended

Darcy model. Effects of the effective thermal conductivity, permeability, inertia coefficient and porous layer thickness on gas flow and heat transfer were studied. Their result shows that higher permeability, higher effective thermal conductivity of porous GDL and smaller thickness of the porous layer improved heat transfer in the modelled fuel cell system.

Ju *et al.* [96] presented a 3-D non-isothermal, single-phase model for all seven layers of the PEM fuel cell that accounts for various location-specific heat-generation mechanisms, including irreversible heating due to electrochemical reactions, heating due to entropy, and Joule (ohmic) heating due to membrane ionic resistance. They observed that the thermal effect on PEM fuel cells becomes more critical at higher cell current density and/or lower GDL thermal conductivity. Their result further shows that temperature increase in the membrane is highly dependent on the GDL thermal conductivity and inlet humidity conditions. Perng and Wu [97] proposed a semi-implicit finite element model to investigate the blockage effect generated by a baffle plate or a rectangular cylinder and its effect on the heat transfer enhancement in a PEM fuel cell with the catalyst layer kept at a constant heat flux. Their results show that the installation of transversely placed baffle plates and a rectangular cylinder in the flow channel effectively enhance the local heat transfer performance of the fuel cell system. Meanwhile, the rectangular cylinder has better effective heat transfer performance than a baffle plate, and the larger the cylinder width, the better the heat transfer performance becomes.

Yu *et al.* [98] presented a two-phase model with phase change to investigate the liquid water effect, especially how the inlet water (liquid or vapour) effects on the Ballard PEM fuel cell performance. The results of their study shows that, for the studied Ballard PEM fuel cell stack, the more the water supplied to the anode from its inlet, the higher the voltage and usually the lower the anode exit temperature. Berning and Djilali [99] developed a 3-D model to account for heat and mass transfer in a multicomponent two-phase flow, considering all seven layers of a PEM fuel cell and

the cooling channels. The results of their study show that phase change occurs at both sides of the fuel cell and these phase changes are due to an intricate balance of three competing processes: temperature change, reactant gas depletion and pressure drop inside the GDL. In addition, their study shows that the amount of liquid water formed depends largely on the GDL permeability. Also, condensation as well as evaporation takes place at the cathode GDL, whereas only condensation occurs at the anode GDL except near the inlet.

Kang *et al.* [100] investigated the effect of the inlet temperature and flow configuration on the species, hydration and temperature distribution in a PEM fuel cell system using the quasi-three-dimensional model. The results show that, of all the configurations studied, the configuration that has a fuel-air counter flow and an air-coolant co-flow, has the highest performance in all the ranges of current density because the membrane remains the most hydrated. In addition, they observed that, when the operating current density increases, the effect of temperature on membrane hydration slightly decreases. They concluded that it is possible to lower the fuel cell operating temperature to improve the fuel cell hydration which, in turn, improves fuel cell performance. Also, different flow configurations were observed to have effect on the pressure losses and local current density, membrane hydration and species mole fraction in the studied fuel cell system.

1.3 JUSTIFICATION FOR THIS STUDY

The need for commercialisation and economically viable PEMFCs necessitates further in-depth research into fuel cell designs. Although, there is extensive literature on methods and techniques that are aimed at optimising PEM fuel cell performance, critical issues remain in understanding how different parameters and modifications of the internal structures relates to affect the performance of the fuel cell under real operating conditions. Fuel cell structures such as the gas channels, reactant species

distribution and thermal conditioning greatly impact on the performance of the fuel cell system. Consequently, they are the subject of extensive theoretical and experimental investigations. In the research studies reported in this thesis, the focus is on the numerical approach to fuel cell engineering design, with specific exploration of a unique combination of computational fluid dynamics (CFD) and a robust mathematical optimisation tool to gain deeper understanding of how different fuel cell design parameters interact to determine the overall fuel cell performance. Furthermore, this study identifies novel optimisation techniques that, if integrated into development procedure, will enhance PEM fuel cell performance. The numerical approach implemented in this work provides an exceptional optimisation approach that can be used in determining a combination of optimum operating parameters for fuel cells under real-life operating conditions. In addition, our approach ensures minimum errors in optimised fuel cell design parameters.

Numerical modelling in recent times has made the development of CFD codes more robust. The availability of CFD codes has made it possible to perform an analysis on a series of parametric design variants until a satisfactory design criterion is obtained, whereafter a prototype development can take place. This will greatly reduce the lead time and cost in actual development procedures. Further improvement in the system design process is the use of mathematical optimisation tools. These optimisation tools can be used to overcome the problems of obtaining optimum design which was previously largely constrained by the skill and experience of the modeler. The combination of the computational fluid dynamics and mathematical optimisation can produce great improvement in the design process. This will ultimately reduce the lead time, cost and ease of obtaining generic information needed for better and efficient design of the fuel cell system. This work seeks to develop innovative approach, through modeling and optimisation, aimed at further enhancing PEM fuel cell performance within the identified limiting factors such as: ***operating conditions, channel geometry, reactant gas transport and thermal cooling approach,*** which are very crucial to fuel cell operation.

1.4 RESEARCH OBJECTIVES

The main aim of this research is to investigate on new approaches towards performance enhancement in PEM fuel cell system through numerical modelling and optimisation. It is anticipated that this would provide new insights into new approaches for PEM fuel cell system design technology. It is hoped that this information will be useful in maximising the efficiency and attainment of the commercialisation drive on this new energy technology. In order to realise the aim mentioned above, this study will focus on the following specific research activities:

- to numerically predict the performance of PEMFCs under different operating conditions by using a CFD code;

- to optimise the performance of PEMFCs through gas channel modification, taking into consideration the mass flow rate and porosity nature of the GDL;

- to develop a novel design approach that can improve the reactant species distribution on the GDL, hence improving the performance and reducing parasitic pump power losses;

- to investigate numerically cooling channel geometry scheme in conjunction with operating parameters (that are temperature-related) of PEM fuel cell systems that will allow operation of low temperature PEM fuel cell beyond the critical temperature (≤ 80ºC) to intermediate high temperatures (100-150ºC), without the need for special compatible high temperature resistant materials which are relatively costly.

- to carry out the numerical model validations on the investigated fuel cell models.

The study emphasises that the attainment of these objectives will provide comprehensive understanding of how different fuel cell design parameters interact to improve the performance of PEM fuel cell systems. Some manufacturing parameters and novel approaches are established to optimise the performance of fuel cell systems. In summary, results from this study will lead to improved performance and design information needed for fuel cell manufacturers, which can be applied for better designs of fuel cell stacks.

1.5 ORGANISATION OF THE THESIS

The thesis is presented in a multiple manuscript format for better organisation and ease of reading. Chapters 4, 5, 6 are written as individual research papers. The thesis consists of the following chapters:

- **Chapter 2** gives an in-depth view into relevant literature related to the fundamental structures of a PEMFC and discusses the function of these features in relation to system performance. This chapter also presents the basic transport and electrochemical processes in PEMFC systems.

- **Chapter 3** exhibits an appropriate framework pertaining to the numerical modelling of PEMFC used in this study. Furthermore, the Dynamic-Q algorithm, used for the mathematical optimisation part of this study, is discussed in detail.

- **Chapter 4** deals with the numerical study on the effect of key operating parameters that impact on the performance of PEM fuel cells. The parameters investigated are both design and physical parameters. In addition, numerical optimisation of the fuel cell gas channel is carried out with interest on mutual interdependence of the GDL porous medium, reactant gas flow rate and gas channel geometry on the fuel cell system performance. The GDL morphology

influences greatly on the species distribution from the channel to the catalyst surface in the cell. This is expected to affect the electrochemical reaction rate that subsequently determines the fuel cell performance.

- **Chapter 5** numerically investigates the reactant gas transport in PEM fuel cells with transverse pin fins inserts in the channel flow. This is aimed at improving the system performance via effective distribution of the reactant gases at a reduced pumping power requirement penalty during fuel cell operation. A numerical optimisation tool (Dynamic-Q) was coupled with the CFD code to obtain optimum parameters required for improving PEM system performance. In this chapter, the steps involved in linking the optimisation method to a commercial CFD code are also indicated.

- **Chapter 6** numerically investigates the impact of cooling channel geometry on PEM fuel cell performance, specifically when the system is operated at higher temperatures (HT), beyond the critical temperature typical of conventional low-temperature PEM fuel cells. Optimal cooling channel geometry was obtained using a numerical optimisation algorithm. This will ensure thermal stability of the PEMFC, especially at high temperature conditions.

- **Chapter 7** provides conclusions drawn from this study, makes recommendations and discusses possible future research directions.

2

CHAPTER 2: FUNDAMENTALS OF PEM FUEL CELL SYSTEM

2.1 INTRODUCTION

In this chapter, the basic components of a PEMFC and its functions are briefly discussed. The main physical processes occurring in the fuel cell structure are discussed and the corresponding governing equations used in PEMFC modelling are also presented. Relevant equations include a basic continuity equation or conservation of mass, a momentum equation and an energy equation as applicable to fuel cells. Equations governing kinetics of electrochemical reactions in the fuel cell, charge (i.e. electrons and protons) transport in the MEA, as well as gas flux based on Darcy's diffusion formulation are also discussed. The various assumptions in the mathematical models in each fuel cell component are emphasised.

2.2 THE BASIC STRUCTURE OF A PROTON EXCHANGE MEMBRANE FUEL CELL

Figure 2.1 illustrates a simplified schematic showing basic components of a single PEMFC. The single cell (or unit cell) consists of nine different regions: the cathode current collector, the cathode channel, the cathode diffusion layer, the cathode catalyst layer, the PEM, the anode catalyst layer, the anode diffusion layer, the anode channel and the anode current collector.

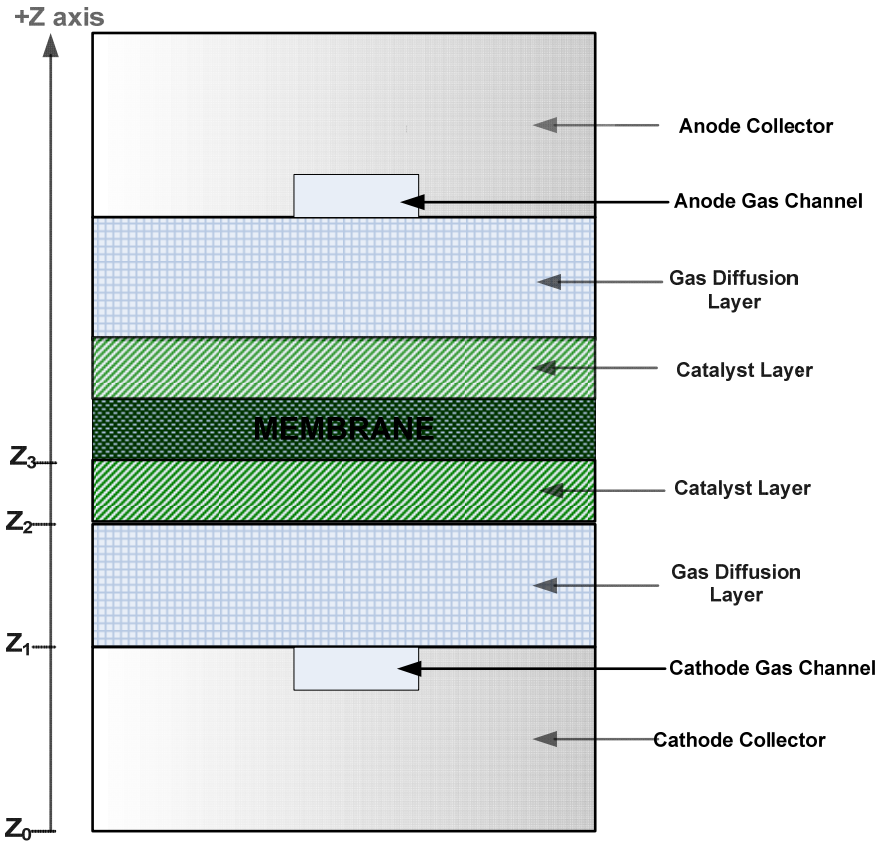

Figure 2.1 Schematic diagram of a single PEM fuel cell

A fuel cell works by catalysis mechanism, wherein electrons and protons are produced by the reactant fuels, such that the electrons are forced to travel through a circuit, thereby producing electrical power. The catalyst usually comprises platinum group metal or alloy. A similar catalytic process takes the electrons back in, combining them with the protons and the oxidant to form simple waste compound like water and heat. In a typical hydrogen-oxygen PEMFC design (Fig. 2.2), a proton-conducting polymer membrane, the electrolyte, separates the anode and cathode sides. On the anode side, hydrogen diffuses to the anode catalyst where it later dissociates into protons and electrons. These protons often react with oxidants causing them to become what is commonly referred to as multi-facilitated proton membrane (MFPM). The protons are conducted through the membrane to the cathode, but the electrons are forced to travel in an external circuit (supplying power) because the membrane is

electrically insulated. On the cathode catalyst, oxygen molecules react with the electrons (which have travelled through the external circuit) and protons to form water, the only waste product in this type of fuel cell.

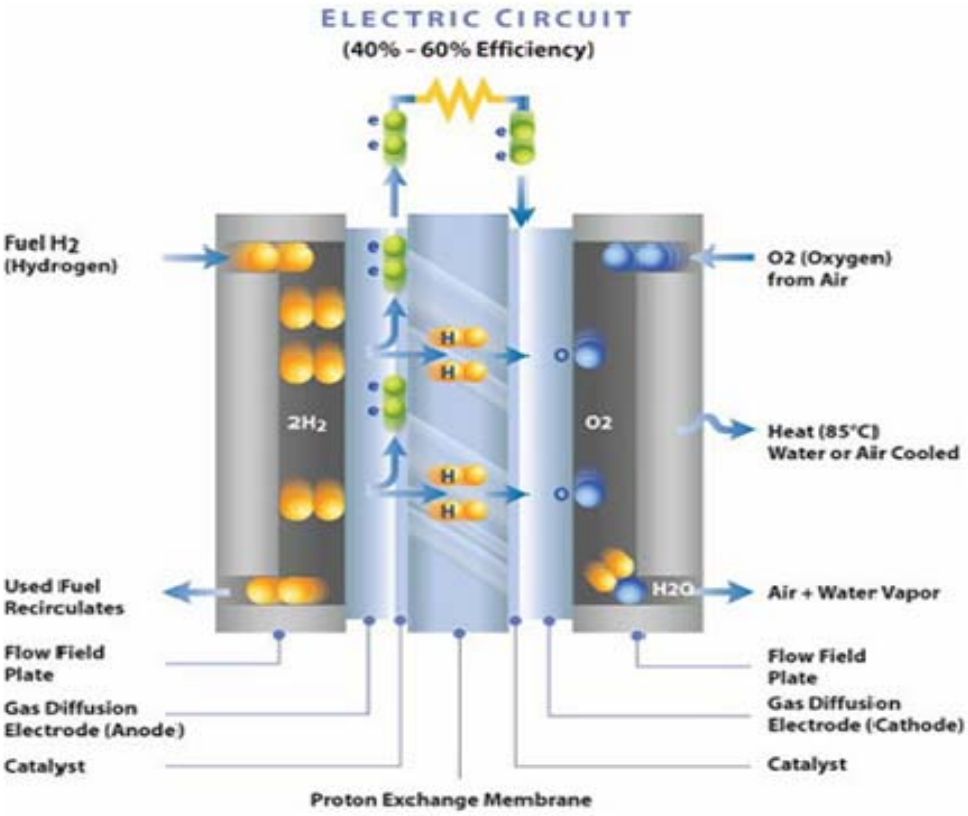

Figure 2.2 The basic structure of a PEM fuel cell showing the path of the electrochemical reaction [15]

Fuel cells are made of four major structural units. These are the following:

1. Proton Exchange Membrane (PEM),
2. Catalyst layers (anode and cathode),
3. Gas diffusion layers (anode and cathode) (GDL),
4. Bipolar plates with flow channels for reactants and coolant in larger cell stacks.

Each of these is discussed further in the following sections.

2.2.1 PROTON EXCHANGE MEMBRANE

The proton exchange membrane (PEM) functions primarily as conductor of ions, but it also serves as a separator between the reactant fuel gases, and acts as an electronic insulator. A functional PEM must also have sufficient mechanical and thermal stability during fuel cell operation. The liquid water in the PEM is transported because of convection, diffusion, dispersion, pressure gradients and electro-osmotic forces being dragged by the moving protons [101]. For effective performance of the PEM, some level of membrane hydration is necessary. However, excess water accumulation in the fuel cell electrodes can result in electrode flooding, so adequate moisture balance must be achieved within the cell.

The most common solid polymer electrolytes consist of a hydrophobic and inert polymer backbone sulfonated with hydrophilic acid clusters to provide adequate conductivity. For example, the most widely used electrolyte membranes in PEMFCs are known by their trade names and are called Nafion®. Nafion® has similar backbone structure as Teflon® but has added sulfonic acid groups [102]. In cases where the amount of water in the membrane becomes low, Nafion® conductance diminishes significantly. The membrane humidification in the fuel cell is mainly achieved through cathode reaction. Many systems utilise reactant gas humidification to maintain hydration. Modern perflourosulfonated ionomer electrolytes for hydrogen gas (H_2) PEMFCs are 18-25 μm thick with a practical operating temperature limit of 120ºC, although PEMFC operation is rarely greater than 90ºC due to adequate humidity requirements and operational lifetimes [103]. There are ongoing efforts [104, 105] to develop a high temperature membrane in order to improve the performance and efficiency of the PEMFC system.

2.2.2 CATALYST LAYERS

High activation energy is required in PEMFCs to induce electrochemical reactions. This is usually achieved by using a catalyst. The catalyst layers (CLs) are essentially

sandwiched between the ionomer membrane and a porous, electrically-conductive substrate. They are the layers where the electrochemical reactions take place (reaction zone). The most common catalyst used in PEMFCs for both oxygen reduction and hydrogen oxidation reactions is platinum. CLs in PEMFCs are made up of a porous, three-dimensional structure, with a thickness of 5-30 μm. In supported CLs, the 2-10 nm catalyst is physically supported on considerable larger, 45-90 nm carbon particles [103]. In preparation of the CLs, the most important is the surface area and not the weight, so it is important to have small platinum particles (4 nm or smaller) with a large surface area finely dispersed on the surface of the catalyst support [106].

There are two distinct ways of preparing a catalyst layer and its attachment to the ionomer membrane. Such a combination of membrane and catalyst layer is referred to as the MEA (membrane electrode assembly). The first way of MEA preparation is to deposit the catalyst layer on the porous substrate, called the GDL, typically carbon fibre paper or carbon cloth, and thereafter hot-press it to the membrane. The second method of MEA preparation is the application of the catalyst layer directly or indirectly (via a decal process) to the membrane, forming the so-called 3-layer MEA or catalysed membrane. The porous substrate may be added later, either as an additional step in the MEA preparation or in a process of stack assembly [106].

Minimising the cell potential losses due to the rate of proton transport and reactant gas permeation in the depth of the electrocatalyst layer requires making the layer relatively thin. Also, the metal-active surface area should be maximised by making the platinum (Pt) particles as small as possible. The first design requirement entails higher Pt/C ratios (>40% by wt), however smaller Pt particles and consequently larger metal areas are achieved with lower loading. In general, higher Pt loading results in an increased voltage gain [107], assuming equal utilisation and reasonable thickness of the catalyst layer. An efficient catalyst layer must have facile transport of ions, electrons, reactants and products with a high electrochemical active surface area where the reactants, catalyst, proton and electron conduction are all available.

2.2.3 GAS DIFFUSION LAYERS

The gas diffusion layer (GDL) consists of a carbon fibre or woven cloth macroporous layer and possibly a highly hydrophobic microporous layer developed to enable better electrical contact between the catalyst layer and fuel system lands. For a GDL to function efficiently in a fuel cell system, it must have the following properties [108]:

- It should be sufficiently porous to allow the flow of both reactant gases (hydrogen and oxygen) and product water. Depending on the design of the flow field, through-plane and in-plane diffusion is important.
- It must be both electrically and thermally conductive, again both through-plane and in-plane conduction are important. Interfacial or contact resistance is typically more important than bulk conductivity.
- The catalyst layer should be made of discreet small particles; hence the pores of the GDL facing the catalyst layer must be minimum.
- It must be sufficiently rigid to support the "flimsy" MEA. However, it must have some flexibility to maintain good electrical contacts.

In addition, the GDL should be able to conduct heat generated at the catalyst layers mainly by conduction to the bipolar plates and by convection in gas phases to the gas flow channels [109]. Carbon fibre based materials such as carbon-fibre papers and woven carbon fabrics or cloths are usually used, considering the conflicting array of GDL requirements. The GDL (both anode and cathode) material is typically treated with a hydrophobic material, such as Teflon, to facilitate water removal and subsequently prevent flooding in their bulk. In addition, the interface with the adjacent catalyst layer may be fitted with a coating or a microporous layer to ensure better electrical contacts, as well as efficient water transport into and out of the diffusion layer. The pores in this layer are usually between 0.1 and 0.5 μm, thus much smaller than the pore size of the carbon fibre papers (20-50 μm) [108].

2.2.4 BIPOLAR PLATES

PEM fuel cells are usually designed by connecting multiple cells in series with bipolar plates (BPPs). These BPPs structurally support the thin MEAs in PEM fuel cells and actually comprise almost all of the volume of the fuel cell stack, and typically over 60% of the weight and 30% of the total cost in a fuel cell stack [70]. The BPPs collect and conduct the current from the anode of one cell to the cathode of the next, while evenly distributing the fuel gas over the surface of the anode, and the oxygen/air over the surface of the cathode through the flow channel. In some designs, it performs the task of facilitating water and heat management. These functions are possible through the plate topologies and material composition of the BPPs. The essential requirements for BPPs, in respect of physiochemical characteristics, are efficient and uniform distribution of the reactant gases over the electrodes to minimise the concentration over potential; high values of electronic conductivity for current collection; adequate mechanical strength for stack integrity; impermeability to reactant gases for safe operation; resistance to corrosion in severe cell environment for long lifetime; cheap materials; and easy and automated fabrication for low cost [110].

In general, two families of materials have been used for PEM fuel cell BPPs, namely polymer-sealed graphite-composite and metallic. The polymer sealing is used to ensure that the normally porous graphite is impermeable to water. For high power density, low weight and robust stack design, however, metallic plates are required [103]. Technical difficulties with metal BPPs include difficulty in scaling and corrosion, which results in rapid electrolyte degradation and poor electrical contact resistance. In fuel cells, a balance exists between gas supply and current conduction. Hence, there is need for large-scale porosity in the flow fields, which requires seeking an optimal flow field design that will efficiently supply the required reactant gases at lower pumping power requirement. The effective design and optimisation of the gas flow fields and BPPs remains a pertinent explored area for reasonable cost reduction and optimum performance attainment for PEM fuel cells [111, 112].

2.3 PEM FUEL CELL STACK DESIGN

Since fuel cells operate at less than 100% efficiency, the voltage output of one cell is less than 1.16 volt. Most applications require much higher voltages than this, (for example, effective commercial electric motors typically operate at 200-300 volts), the required voltage is obtained by connecting individual single fuel cells in series to form a fuel cell stack [113]. In stack design, weight and volume is crucial. Hence, to decrease the overall volume and weight of the stack, instead of two current collectors, only one plate is used with a flow field cut into each side of the plate. This type of arrangement is referred to as bipolar plates (BPPs). The bipolar plate (BPP) separates one cell from the next, with the single plate doing dual work of carrying the hydrogen gas on one side and air on the other side. A typical stack configuration is illustrated in Figure 2.3.

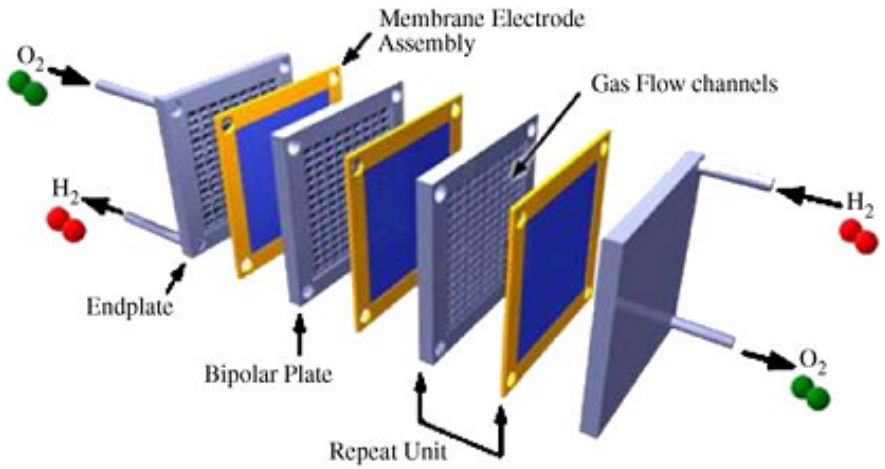

Figure 2.3 Fuel cell stack component [71]

The bipolar configuration is best suited for large fuel cells since the current is conducted through relatively thin conductive plates, thus it travels short distance through a large area. This causes minimum electroresistive losses even with the use of a relatively poor electrical conductor such as graphite (or graphite mixtures). However, for small cells it is possible to connect the edge of one electrode to the

opposing electrode of the adjacent cell by some kind of connector [113]. A good fuel cell stack design should have the following properties [103]:

1. Uniform distribution of reactants to each cell
2. Uniform distribution of reactants inside each cell
3. Minimum resistive losses (choice of materials, configuration, uniform contact pressure)
4. No leak of reactant gases (internal between the cells, or external)
5. Mechanical sturdiness (internal pressure including thermal expansion, and external forces during handling and operation, including shocks and vibrations).

Fuel cell performance is sensitive to the flow rate of the reactant gases, hence it is highly necessary that each stack receives approximately the same amount of reactant gases. Uniformity in flow distribution would result in even performance of the cell. Therefore, to achieve uniform distribution, feeding of the cell in the stack is done in parallel through a manifold that can be either external or internal. In fuel cell design, internal manifolds are commonly employed because of better sealing and versatility in gas flow configuration [113]. The reactant gases entering the fuel cell stack cell must be distributed over the entire active area. This is practically achieved through a flow field, which is basically a form of channels covering the entire area in some pattern or porous structure. The pattern of the flow field in the plate, as well as the width and depth of the channels, have a large impact on the effectiveness and the even distribution of the reactant gases across the active area of the membrane/electrode assembly. The flow field design also affects the water supply to the membrane and water removal from the cathode [113]. The following are the key flow field design variables [106]:

- flow field shape
- flow field orientation
- configuration of channels

- channels shape, dimensions and spacing
- pressure drop through the flow field

Flow field design is a critical aspect in fuel cell manufacturing and is a well-kept secret by stack manufacturers [106]. CFD modelling is a great tool for the design of fuel cell flow fields [114, 71].

2.3.1 HYDROGEN FUEL CELL SYSTEM COMPONENTS

Fuel cell stacks need to be integrated into a complete fuel cell system for it to operate. The fuel cell system must be of appropriate weight and volume to fit into the space provided for operation. The operation of the entire engine must maintain the near-zero emissions and high efficiency of the fuel cells. In addition, all these requirements must be met with components that are both inexpensive and designed for low cost, high volume manufacturing. Figure 2.4 is a schematic of typical hydrogen PEMFC system.

The hydrogen fuel cell system includes the following subsystems and control components [103]:

2.3.1.1 *Reactant storage, delivery and recycling*

This comprises of the pumps and blowers required to supply the fuel cell stack with prescribed flow rates of fuel and oxidiser and to recycle unused fuel back into the anode inlet stream. Typically, only fuel storage and recycling are needed as air is used as the oxidant.

2.3.1.2 *Humidification*

This system is required for humidification of the flow of reactant gases. Portable system designs are passively humidified, thereby eliminating this subsystem completely at the expense of reduced performance.

2.3.1.3 *Cooling*

Systems larger than 1 kW power typically require active cooling of the stack to remain within membrane material tolerances and achieve uniform system performance. Smaller, low-portable systems can be passively cooled. The choice of coolant is an active area of research. Distilled water can be used but will freeze at subzero temperatures. Ethylene glycol is the coolant of choice for contemporary automotive applications and can operate at subzero temperatures, but contact with electrolytes can result in irreversible damage.

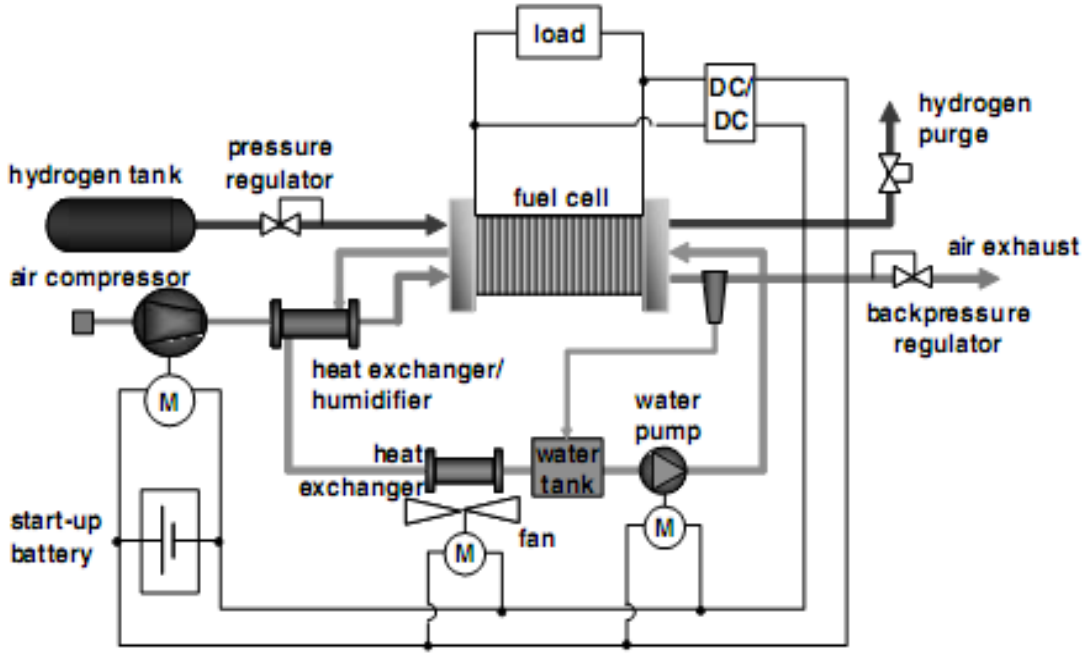

Figure 2.4 A schematic of a complete hydrogen-air fuel cell system [115]

2.3.1.4 *Hydrogen reformation*

In some fuel cell systems, hydrogen fuel is obtained from liquid hydrocarbon or alcohol fuel. This fuel cell type requires a hydrogen generation system. For stationary applications, a fuel reformer is often incorporated. Meanwhile, in automobile or

portable applications, on-board reformation is typically avoided due to the required excessive complexity, cost and transient control limitations.

2.3.1.5 *Power conditioning and control*

Power output from a fuel cell stack is normally in the form of direct current (DC) which must be inverted to alternating current (AC) and conditioned into a suitable voltage range to power equipment. The fuel cell control system is responsible for all system monitoring and maintenance of stable and safe operation through feedback from a variety of flow, pressure, voltage, current and temperature sensors [103].

2.3.1.6 *Startup Power System*

External power inputs are usually incorporated to assist in the system startup. An auxiliary high-power battery to run pumps and heaters during startup, or to provide power to overcome voltage transients and reversals in the fuel cell stack is often required.

2.3.1.7 *System Humidification*

Fuel cells have a precarious balance between a moist electrolyte needed for high ionic conductivity and a flooded cell that degrades fuel cell performance. It is possible that some sections of the same fuel cell or individual plates in a stack will be critically dry and other sections in the cell or different plates in a stack will be flooded. Hence, some humidification is typically required at the inlet of the fuel cell to ensure adequate performance. In addition, strong humidity gradients in the electrolyte can result in internal stresses that limit system durability. Humidification in fuel cell is basically achieved by two main procedures, *passive approach* and *direct approach*. In the former, the water generated by the reaction in the cell is used to maintain a proper

moisture balance and humidity of the incoming reactant flow without external power. However, in active humidification, a separate humidifier is directly employed to provide the humidification of the incoming flow with stored or recycled water.

2.4 THEORIES OF TRANSPORT AND ELECTROCHEMICAL PROCESSES IN PEMFCs

Understanding the transport, electrochemical and coupled spontaneous oscillations of hydrodynamic processes in the fuel cell system requires the understanding the physics of the various processes within the fuel cell structures. The transport and electrochemical processes of a typical PEMFC (Figure 2.1) are discussed below:

- The hydrogen fuel is supplied through the anode gas flow channel and is distributed to the thin catalyst layer section of the fuel cell via the anode GDL.
- The oxidation of the hydrogen molecules occur in the anode catalyst layer to produce protons and electrons which, in turn, are transported to the cathode through the fuel cell membrane and an external circuit, respectively.
- In the cathode catalyst layer, the oxidant molecules (transported from the cathode gas flow channel and GDL) combine with the protons and the electrons from the anode section to produce water.

The basic half-cell reaction occurring in the fuel cell is given as:

anodic: $$H_2 \rightarrow 2H^+ + 2e^-, \tag{2.1}$$

cathodic: $$\frac{1}{2}O_2 + 2H^+ + 2e^- \rightarrow H_2O \text{ , and} \tag{2.2}$$

net-reaction: $H_2 + \frac{1}{2}O_2 \rightarrow H_2O$. (2.3)

From equation 2.3, one of the key advantages of the fuel cells is seen. That is that the only by-product of the reaction is water, which is non-pollutant to the environment compared to the harmful products of combustion using fossil fuels.

Modelling transport and electrochemical processes taking place in the various layers in the fuel requires solving five types of constitutive relations simultaneously: (i) the conservation equations, (ii) constitutive relations for various fluxes, (iii) kinetic equations for reactions, (iv) equilibrium relationships and (v) auxiliary relations such as variable definitions and Faraday's Law [25]. The conservation equations are applicable to all the layers in the fuel cell, while the other four equations are related specifically to sections within the fuel cell: membrane, GDL and the catalyst layers.

2.4.1 CONSERVATION EQUATIONS

The fundamental description of fuel cell operation involves the five conservation principles, namely, mass, momentum, species, electrical charge and thermal energy. Generally, unified and individual modelling approaches are used in fuel cell modelling. These two approaches are used in the present work and have been elaborately discussed by Yang and Pitchumani [116]. A brief discussion on these approaches is presented in this section. A unified-domain approach allows a valid set of governing equations for all the fuel cell layers written in vector form as [117, 118]:

mass: $$\frac{\partial(\varepsilon\rho)}{\partial t} + \nabla\cdot(\rho\mathbf{u}) = S_m\,, \tag{2.4}$$

momentum: $$\frac{1}{\varepsilon}\left[\frac{\partial(\rho\mathbf{u})}{\partial t} + \frac{1}{\varepsilon}\nabla\cdot(\rho\mathbf{u}u)\right] = -\nabla p + \nabla\cdot\tau + S_u\,, \tag{2.5}$$

species: $$\frac{\partial(\varepsilon C_k)}{\partial t} + \nabla \cdot (\mathbf{u} C_k) = \nabla \cdot \left(\mathbf{D}_k^{\,eff} \nabla \mathbf{C}_k\right) + S_k \,, \tag{2.6}$$

charge: $$\nabla \cdot \left(\boldsymbol{\kappa}^{eff} \nabla \boldsymbol{\Phi}_e\right) + j = 0 \,, \tag{2.7}$$

$$\nabla \cdot \left(\boldsymbol{\sigma}^{eff} \nabla \boldsymbol{\Phi}_s\right) - j = 0 \,, \tag{2.8}$$

and finally,

energy: $$\frac{\partial\left[\left(\rho c_p\right)_m T\right]}{\partial t} + \nabla \cdot \left(\rho c_p \mathbf{u} T\right) = \nabla \cdot \left(k^{\,eff} \nabla T\right) + S_T \,. \tag{2.9}$$

The unified-domain approach eliminates the requirement of prescribing assumed or approximate boundary conditions at the interfaces between the various layers of the fuel cell system. The main assumptions made in the conservation equations are: (i) the reactant gases are an ideal gas mixture and (ii) flow is incompressible and laminar due to small flow velocities occurring in the fuel cell system. The dependent variables $\mathbf{u}$, p, $\boldsymbol{C}_k$, Φ_e, Φ_s, and T in the equations denotes the superficial fluid velocity vector, pressure, molar concentration of species k, electrolyte (membrane) phase potential, solid phase potential, and temperature, respectively. The solid phase relates to the electron conducting materials in the fuel cell system, *i.e.,* the flow channel BPPs, the GDL, or the electrocatalyst and its carbon support in the catalyst layer section. In the succeeding section below, other individual equations and the description of their parameters are presented:

2.4.1.1 ***The mass equation (equation 2.4):***

In this equation, t and ε are the time and porosity, respectively, and the density of the gas mixture ρ is given by:

$$\rho = \sum_k MW_k C_k \ , \tag{2.10}$$

where MW_k is the molecular weight of species *k,* and the summation is performed over all the gas species involved. The source term S_m assumes non-zero value at the catalyst layers, resulting from the consumption/production of electrochemical reactions as well as diffusion and osmotic drag of water through the membrane [117]:

$$S_m = -MW_{H_2} \frac{j_a}{2F} + MW_w \left[\nabla \cdot \left(D_{w,m} \nabla C_w - n_d \frac{i_e}{F} \right) \right], \text{ for anode} \tag{2.11}$$

and

$$S_m = -MW_{o_2} \frac{j_c}{4F} + MW_{H_2} \frac{j_c}{2F} - MW_w \left[\nabla \cdot \left(D_{w,m} \nabla C_w - n_d \frac{i_e}{F} \right) \right], \text{ for cathode,} \tag{2.12}$$

where $D_{w,m}$ is the liquid water diffusion coefficient in the membrane, and n_d is the electro-osmotic drag coefficient. The current density in the membrane (resulting from proton flux), i_e, is related to the membrane phase potential, Φ_e, through Ohm's law [71]:

$$\mathbf{i}_e = -\boldsymbol{\kappa}^{eff} \nabla \boldsymbol{\Phi}_e \ , \tag{2.13}$$

where $\boldsymbol{\kappa}^{eff}$ is the effective proton conductivity in the catalyst layer. The current density in the solid phase, $\mathbf{i}_s$, could also be obtained by using Ohm's law as [116]:

$$\mathbf{i}_s = -\sigma \nabla \boldsymbol{\Phi}_s \ , \tag{2.13b}$$

where σ is the electrical conductivity.

2.4.1.2 ***The momentum equation (equation 2.5):***

The effect of porous media is represented by the source term, $S_u = -\mu \mathbf{u}/K$ wherein μ and K denote viscosity and hydraulic permeability, respectively. In the porous layers (*i.e,* the GDLs, hydraulic layers and membrane), the viscous term from the divergence of the viscous stress, $\nabla \cdot \boldsymbol{\tau}$, and the inertial terms may be small and the momentum equation is reduced to Darcy's law [116].

2.4.1.3 ***The species equation (equation 2.6):***

The equation denotes the reactant species diffusion in the fuel cell system. The first term on the right-hand side of the equation indicates that the species diffusion is modeled by Fick's law for a binary mixture, which is an acceptable approximation for multicomponent diffusion in PEM fuel cells [117]. The effective diffusivity for species k is adopted to account for the effects of porous media, and the expression D_k^{eff} represents the effective diffusion coefficient for the species. The source term S_k for hydrogen and oxygen species is due to the electrochemical reactions, which may be written in general form as [117]:

$$\sum_k v_k M_k^z = ne^- \quad , \tag{2.14}$$

where v, M_k and exponent z are the stoichiometric coefficient, the chemical symbol, and charge number for species k, respectively, and n depicts the number of electrons transferred across the charge double layer. The consumption rate of the reactant species, S_k, is related to the volumetric transfer current, j, through Faraday's law [116]:

$$S_k = -\frac{v_k j}{nF} \ , \tag{2.15}$$

with j given by the Butler-Volmer equation [118]:

$$j = A_{av} i_o \left[\exp\left(\frac{2\alpha_a F}{RT} \eta \right) - \exp\left(-\frac{2\alpha_c F}{RT} \eta \right) \right], \tag{2.16}$$

where A_{av} is the electrochemically active area per unit volume, i_o is the exchange current density, and F is the Faraday's constant. The anodic and cathodic charge transfer coefficients, α_a and α_c, represent the portion of the electrical energy harnessed in driving the electrochemical reactions, and the values are between 0 and 1, depending on the reactions and material properties involved. The activation overpotential, η, is defined as:

$$\eta = \Phi_s - \Phi_e - U_0 \ , \tag{2.17}$$

where U_0 is the thermodynamic equilibrium potential, which is determined by using the Nernst equation for the cathode reaction [119]:

$$E = E^0 + \frac{RT}{2F} \ln\left(\frac{a_{H_2} \cdot a_{O_2}}{a_w} \right), \tag{2.18}$$

where E^0 is the electromotive force (emf) at the standard pressure (*i.e.,* 1 bar), R is the universal gas constant, T is the temperature, F is the Faraday constant, and a_{H_2} a_{O_2}, and a_w are the activities of the hydrogen, oxygen, and water species, respectively. The effect of osmotic drag is also added to the source S_k for the water species in the catalyst and membrane layers [117].

2.4.1.4. ***The charge transport equations (Equations 2.7 and 2.8):***

These equations involve the volumetric transfer current, *j,* as a source term. The general Butler-Volmer equation, Eq. (2.16), may be simplified for the anode and cathode catalyst layer depending on the characteristic of the half-cell reactions [117, 120]:

anode: $$j_a = A_{av} i_{0,a}^{ref} \left(\frac{C_{H_2}}{C_{H_{2,ref}}} \right)^{1/2} \left(\frac{\alpha_a + \alpha_c}{RT} F \eta_a \right) \text{ and} \tag{2.19}$$

cathode: $$j_c = A_{av} i_{0,c}^{ref} \left(\frac{C_{O_2}}{C_{O_{2,ref}}} \right) \exp\left(-\frac{\alpha_c}{RT} F \eta_c \right), \tag{2.20}$$

where the sub/superscripts *a, c,* and *ref ,* denote the anode, cathode and reference state, respectively. The hydrogen oxidation reaction (HOR) in the anode catalyst layer is fast and the overpotential η_a is typically small, and j_a in Eq. (2.19) is approximately proportional to η_a. In cases where the PEM fuel cell operates on a reformate feed at the anode section, the electrochemical reactions in the anode catalyst layer involve the adsorption process of CO*,* leading to a decreased active area, A_{av}, at the anode section of the fuel cell [121, 122]. The oxygen reduction reaction (ORR) is typically slow with high η_c, and the expression for j_c, Eq. (2.20), may be obtained by neglecting the anodic reaction term of Eq. (2.16).

2.4.1.5 ***The energy equation (Equation 2.9):***

In the energy equation, K^{eff} is the thermal conductivity, and the heat capacitance in a porous material, $\left(\rho c_p\right)_m$, is a volume-averaged volumetric specific heat over the solid matrix and the fluid in the micropores:

$$\left(\rho c_p\right)_m = \varepsilon\left(\rho c_p\right) + \left(1-\varepsilon\right)\left(\rho c_p\right)_s , \tag{2.21}$$

where the subscript *s* refers to the solid material and $\left(\rho c_p\right)$ pertains to the fluid.

The source term S_T in Eq. (2.9) consists of contributions from three mechanisms, *i.e.,* irreversible heat from the electrochemical reaction, reversible or entropic heat, and Joule heating. In solving the conservation equations discussed in this section, the material property characterisation (*i.e.,* transport properties of the membrane, kinetic data for electrochemical reactions, effective parameters for porous materials, and properties of the reactants and products) must be considered.

2.4.2 MODELS OF INDIVIDUAL PEM FUEL CELL COMPONENTS

The previous discussion focuses on the simulation of entire fuel cell systems. The subsequent discussion will focus on numerical models specific to individual cell components such as cell membrane, GDLs, etc.

2.4.2.1 *Membrane models*

The membrane model discussed here will focus primarily on the two major types of macroscopic models of the membrane, namely, the single phase and the two-phase models. The membrane is one of the most important components of a PEM fuel cell, which serves to effectively separate the anode fuel from the cathode oxidant and to conduct protons at high rates during cell operation. The discussions here focus on the Nafion membrane, owing to the fact that the governing equations for Nafion are generally valid for other types of membranes (only with different property values) [116]. Most macroscopic models consider a membrane consisting of three species: the membrane polymer, proton and water. Other types of ions are neglected in the three-species system [123].

(i) Single-phase models

The single-phase model (or diffusive) considers the vapor-equilibrated membrane. The system is treated as a single, homogeneous phase where the water and proton dissolve in the polymer matrix and is transported by diffusion. The membrane matrix is considered to be stationary in the space, and the fluxes of the dissolved species may be obtained by the dilute solution theory [124] or concentrated solution theory [125, 126]. The dilute solution theory considers only the interactions between each dissolved species and the solvent (i.e., the polymer matrix), and the general motion of charged carriers is governed by the Nernst-Planck equation [116]:

$$\mathbf{N}_i = -z_i u_i F c_i \nabla \Phi_e - D_i \nabla c_i + c_i v_e \ . \tag{2.22}$$

In Eq. (2.22), the first term represents the migration of the charged particles *i* in an electrolyte potential gradient $\nabla \Phi_e$, where z_i is the charge number, and u_i and c_i are the mobility and concentration, respectively. The diffusive and convective fluxes are governed by the second and the third term, respectively, and the diffusion coefficient D_i is related to the mobility u_i by the Nernst-Einstein equation [124]:

$$D_i = RTu_i \ . \tag{2.23}$$

Since the one-phase analysis considers the polymer matrix as stationary solvent, the convective velocity $\boldsymbol{v}_e = 0$, Eq. (2.22) reduces to Ohm's law (*i.e*, Eq. (2.13)) for the case of zero proton concentration gradient, and to Fick's law when $z_i = 0$ in the case of water transport.

The flux of the proton across the membrane induces a flow of water in the same direction via the electro-osmotic drag effect. The electro-osmotic flow is a result of

the proton-water interaction which cannot be modelled by the dilute solution theory. The three-species membrane system is better modelled using the concentrated solution theory, which accounts for the interaction among all the species. Considering the thermodynamic driving force to be a sum of frictional interactions among different species, the following expressions for the ionic and water fluxes are obtained [125, 126]:

$$i_e = -\frac{-\kappa n_d}{F}\nabla\mu_w - \kappa\nabla\Phi_e \quad \text{and} \tag{2.24}$$

$$N_w = n_d\,\frac{\boldsymbol{i}_e}{F} - \alpha_w\nabla\boldsymbol{\mu}_w \ . \tag{2.25}$$

where μ_w and α_w , respectively, denotes the chemical potential and transport coefficient of water. The proton-water interaction is taken into account by the two terms containing the electro-osmotic drag coefficients, n_d , in each of Eqs. (2.24) and (2.25).

(ii) Two-phase models

The two-phase model, also known as the hydraulic model, considers the liquid membrane to consist of two-phases, namely, the polymer matrix and the liquid water. A major assumption concerning two-phase models is the fully hydrated state of the membrane, corresponding to the complete filling of the membrane micro-pores with liquid water. This implies that concentration gradient and the diffusion transport of the liquid water species should be zero. The proton species is assumed to be dissolved in water and moves along with the water molecules. Bernadi and Verbrugge [23, 127] presented one of the first two-phase models and adopted the Nernst-Planck equation, Eq. [2.22], to describe the proton flux. The convective velocity, $\mathbf{V}_w$, is non-zero and is given by Schlogl's equation for the water species [25, 128], that is,

$$\mathbf{V}_w = -\left(\frac{K}{\mu}\right)\nabla p_L - \left(\frac{K_\Phi}{\mu}\right) z_f c_f F \nabla \Phi_e \,, \tag{2.26}$$

where K and K_Φ represent the effective hydraulic and electrokinetic permeability, respectively, p_L is the liquid pressure, μ is the liquid viscosity, and z_f and c_f denote the charge and concentration of fixed ionic sites, respectively. In two-phase models, the water flux is attributed to the combined effects of a potential and a pressure gradient. The portion of water flux driven by the pressure gradient is primarily due to the permeation of water through the micro-pore network of a fully hydrated membrane. When the membrane is partially hydrated, water concentration gradients exist across the membrane thickness and a modification of the hydraulic models becomes necessary.

2.4.2.2 *Gas diffusion layer models*

The GDL is the porous diffusion media between the catalyst layer and the gas channel. It provides structural support, uniform distribution of the reactant gases, and a pathway for electrons and liquid water to or from the catalyst layer. Due to the high conductivity of carbon in the gas diffusion layer, the conduction of electrons is usually ignored in most GDL models. However, the electronic conduction may become an important factor for the current distribution due to small contact areas with the gas channels [129] or the composition of the diffusion media [36]. Ohm's law accounting for porous media effect is adopted for the electrical current, $\boldsymbol{i}_s$, in the GDLs:

$$\boldsymbol{i}_s = -\sigma^{eff}\nabla\boldsymbol{\Phi}_s = -\frac{\varepsilon_s}{\tau_s}\sigma_0\nabla\boldsymbol{\Phi}_s = -\varepsilon_s^{1.5}\sigma_0\nabla\boldsymbol{\Phi}_s \,, \tag{2.27}$$

where σ^{eff} depicts the effective conductivity of the porous GDL, σ_0 is the intrinsic conductivity of the GDL material, and ε_s and τ_s are the volume fraction and tutorsity of the solid conducting phase, respectively. With the assumption of one-dimensional steady-state flow, the fluxes of the various reactants in the GDLs are constant and are related to the current density by the stoichiometric coefficients [130, 131]. However, the water flux may not be constant due to evaporation or condensation in the porous media. A rate term for the phase change, r_w, may be written as [130]:

$$r_w = h_m\left(\rho_w^{sat} - \rho_w\right) = Sh\frac{D_{vg}^{eff}}{L} f_e\left(\rho_w^{sat} - \rho_w\right), \tag{2.28}$$

where h_m is the mass transfer coefficient, ρ_w is the partial density of water vapor and ρ_w^{sat} is the saturation partial density of water, which may be correlated for the pore effects via the Kelvin equation [132]. The mass transfer coefficient, h_m, is related to the Sherwood number, Sh, via the correlation:

$$h_m = Sh\frac{D_{vg}^{eff}}{L} f_e, \tag{2.29}$$

where L is the characteristic length scale, D_{vg}^{eff} is the effective diffusion coefficient of water vapor, and f_e is the specific area of the liquid/vapor interface. In the GDL, it is evident that two-phase flow existed. These are gas and liquid water phase flow, which are further discussed hereafter.

(i) Gas-phase transport in gas diffusion layers

The transport of a multicomponent gas mixture through a porous media is usually described by the Stefan-Maxwell equations [133]:

$$\nabla x_i = \sum_j \frac{x_i \mathbf{N}_j - x_j \mathbf{N}_i}{c_T \mathbf{D}_{ij}^{eff}} \quad , \tag{2.30}$$

where x_i and N_i are the mole fraction and the molar flux of species i, respectively, c_T is the total concentration or molar density of all the gas species, and D_{ij}^{eff} is the effective binary diffusion coefficient for species i and j, which may be related to the binary diffusion coefficient D_{ij} via the Bruggeman relation:

$$\boldsymbol{D}_{ij}^{eff} = \varepsilon_G^{1.5} \boldsymbol{D}_{ij} \quad , \tag{2.31}$$

where ε_G denotes the volume fraction of the gas phase, and equals to the bulk porosity of the media when the liquid water is ignored. In the case of two-phase flow, ε_G must be determined from the liquid saturation condition in the GDL. With a decrease in pore size in the GDL, the gas molecules collide more often with the pore wall than with each other, resulting in Knudsen diffusion from the intensified gas-wall interaction [134]. From an order-of-magnitude analysis, it is noted that the bulk diffusion dominates when the mean-free path of a molecule is less than 1% of the pore radius, while Knudsen diffusion dominates when the mean-free path is more than 10 times the pore radius [134]. In accounting for the gas-wall interaction, a Knudsen diffusion term is added to the Stefan-Maxwell equation based on a dusty-gas analysis [135]:

$$\nabla x_i = -\frac{\mathbf{N}_i}{c_T \mathbf{D}_{k_i}^{eff}} + \sum_j \frac{x_i \mathbf{N}_j - x_j \mathbf{N}_i}{c_T \mathbf{D}_{ij}^{eff}}, \tag{2.32}$$

where the effective Knudsen diffusion coefficient $D_{k_i}^{eff}$ is proportional to the mean pore radius, r_p, and the mean thermal velocity of the gas molecules [136]:

$$D_{k_i}^{eff} = \frac{2}{3} r_p \sqrt{\frac{8RT}{\pi MW_i}}, \tag{2.33}$$

where *R, T, and* MW_i are the gas constant, temperature, and molecular weight of species *i,* respectively.

Most models treat the gas transport in the GDL as a pure diffusion problem where total gas pressure remains constant through the thickness of the porous media whereas, in computational fluid dynamics (CFD) models the average convective velocity, $\boldsymbol{v}_G$, is computed by adopting Darcy's law for the gas phase [133]:

$$\boldsymbol{v}_G = -\frac{K_G}{\mu_G} \nabla p_G, \tag{2.34}$$

where K_G and μ_G are the permeability and viscosity for the gas mixture, respectively, and most computational fluid models incorporate Eq. (2.34) as a source term into the momentum equation.

Generally, the pressure difference through the GDLs from most simulation results is small and the assumption of uniform pressure may be valid for typical operating conditions [127, 137]. This observation is not totally unexpected, since the gas mixture has convective flow in the channel direction and transportation is only feasible through the porous by diffusion due to a no-slip condition at the pore walls.

(ii) Liquid Water Transport in Gas Diffusion Layers

Liquid water transport is critical to cell performance. Sufficient liquid water is desirable for high membrane conductivity, while excessive liquid may block the pores in the GDL, preventing the reactants from reaching the reaction sites. In some simplified models, liquid water is treated as a stationary species that occupies a

certain volume fraction in the GDL pores [31, 138]. The effective binary diffusivities are thus decreased (see Eq. 2.31) and the flooding effect of liquid is accounted for to some extent. Most of the simplified models use the liquid volume fraction as a fitting parameter [31]. More elaborate models treat the liquid water to be fine droplets that flow with the gas mixture [83, 139]. Evaporation and condensation may take place, however, a separate liquid phase is not considered. In these models, the liquid is assumed to be a component of the gas and exerts negligible influence on the gas flow field. The models keep track of the liquid water volume fraction at various locations without resulting in complicated two-phase transport analyses.

The two types of models mentioned above essentially describe single-phase transport, while more accurate treatment of liquid water flow requires two-phase flow models. To account for liquid water flux, some simple two-phase models assume isolated gas and liquid pores in the media [130, 127, 140]. This assumption is based on the fact that the GDL is a mixture of hydrophobic Teflon and hydrophilic carbon solid. The flux of liquid water follows from Darcy's law:

$$\mathbf{N}_{w,L} = -\frac{K}{V_w \mu} \nabla p_L \ , \tag{2.35}$$

where the subscript L denotes the liquid phase and V_w is the molar volume of water. However, some models adopted a phase mixture approach where all the properties pertain to a gas-liquid mixture [141, 142]. These models use Eq. (2.35) to perform liquid flux computation, which is omitted by the single-phase models. An oversimplification in this approach is that the liquid flows with the same velocity as the gas, consequently, the interaction between the gas and the liquid is not adequately accounted for.

Gas-liquid two-phase flow in porous media is a well-known problem in a wide range of engineering applications, and rigorous modeling of the phenomenon has been

reported in the literature [143, 144]. Here, we restrict our discussion to gas-liquid diffusion in fuel cells. Thus, the interaction between the gas and the liquid is characterised by a capillary pressure, p_C, defined as [145]:

$$p_C = p_L - p_G = -\frac{2\gamma\cos\theta}{r} \quad , \tag{2.36}$$

where γ is the surface tension of water, θ is the contact angle of a water droplet with a pore wall, and r is the pore radius. Depending on the wetting characteristic of the GDL material, the contact angle has a range of $\theta^o \le \theta \le 90^0$ for a hydrophobic material, and $90^o \le \theta \le 180^o$ for a hydrophilic one. An important goal of the two-phase models is to predict the distribution of liquid saturation, s, which is defined as the portion of pore volume filled with liquid. Thus, the volume fraction of the gas phase, ε_G, is related to the porosity of the GDL, ε_0 as:

$$\varepsilon_G = \varepsilon_0(1-s). \tag{2.37}$$

The equation implies that the increase in saturation results in a decrease in gas phase volume fraction and effective diffusion coefficients (Eq. 2.37). In determining the liquid saturation, s, empirical constitutive equations are adopted to relate the capillary pressure, p_C, to the saturation, s [146, 147]. Wang and Cheng [147] gave a correlation for p_C as a function of s. Thus,

$$p_C = \gamma\cos\theta\left(\frac{\varepsilon_0}{K}\right)^{0.5}\left[1.417(1-s) - 2.120(1-s)^2 + 1.263(1-s)^3\right], \tag{2.38}$$

where the surface tension is taken to be 0.0625 Nm^{-1} for the liquid water-air system at 80°C and K is the effective permeability of the GDL. The functional form for the

$p_C - s$ relationship is also determined using a bundle-of-capillary model [145]. The capillary pressure in Eq. (2.38) at various locations in the porous media must be known to determine the liquid saturation. In typical two-phase flow models, Darcy's law [Eqs. (2.34) and (2.35)] is employed to calculate the pressure fields for both liquid and gas phases, and subsequently utilised in Eqs. (2.36) and (2.38) to obtain the liquid saturation distribution. In some models, capillary pressure is used as the driving force for the liquid-water flow [148]:

$$\mathbf{N}_{w,L} = -\frac{K}{V_w \mu}\nabla p_L = -\frac{K}{V_w \mu}(\nabla p_G + \nabla p_C) = -\frac{K}{V_w \mu}\nabla p_C \,. \tag{2.39}$$

The rightmost expression in Eq. (2.39) assumes that the gas pressure is constant within the GDL. The effective permeability K in Eqs. (2.38) and (2.39) is commonly related to a relative permeability, K_r, as:

$$K = K_r K_{sat} \,, \tag{2.40}$$

where the permeability at complete saturation, K_{sat}, depends only on the structure of the porous medium. Many empirical relations existed in the literature for K_r as a function of the saturation. Some adopts a linear dependence of K_r on saturation [149, 150]. Most other models represent the relative permeabilities for liquid and gas phases, namely, K_{rl} and K_{rg}, with the following expressions [146]:

$$K_{rl} = s^3, \text{ and} \tag{2.41}$$

$$K_{rg} = (1-s)^3 \,. \tag{2.42}$$

The constitutive relations in Eqs. [2.36-2.42] is commonly incorporated in the multiphase model to simulate two-phase flow in the PEM fuel cells [146, 147].

2.4.2.3 *Catalyst layer models*

The catalyst layer is a critical component of a fuel cell. The physical processes in a catalyst layer include the electron conduction in the solid phase; the proton transport in the membrane phase; the gas diffusion in the gas, liquid and membrane phases; and the electrochemical reactions on the active catalyst sites. The HOR occurs in the anode catalyst layer and the ORR takes place in the cathode catalyst layer.

Models that are often used for the catalyst layer are either microscopic or macroscopic. The macroscopic model is classified into four different types, namely, (i) the interface model that treat the catalyst layer with zero thickness, (ii) the macrohomogeneous approach, (iii) the film models, and (iv) the agglomerate models. The catalyst models are usually for the cathode, due to the fact that the cathode reaction is slower and contributes to the principal losses in the fuel cell. However, the modelling approaches for the cathode are generally applicable to the anode catalyst layer, with only different kinetic expressions and values of properties.

(i) Microscopic models

The microscopic model is further divided into gas pore models [151, 152] and the flooded-agglomerate models [153, 154]. Since the two modelling approaches are very similar, only one, that is, the flooded-agglomerate model will be presented here. In this model, the catalyst layer is made up of a number of porous cylinders flooded with the electrolyte. The species diffusion and reaction occur within the cylinders [155]. During fuel cell operation, reactant gas diffuses through the gas pore, dissolves and diffuses in the electrolyte contained in the agglomerates, and reacts on the active sites

of the catalyst particles. The diffusion of the reactant gas is governed by Fick's law with a source term accounting for the simultaneous bulk reaction [155]:

$$D_m^{eff}\frac{\partial^2 C(r)}{\partial r^2}+D_m^{eff}\frac{1}{r}\frac{\partial C(r)}{\partial r}-S_k=0, \tag{2.43}$$

where D_m^{eff} is the effective diffusion coefficient of the dissolved species and $S_k=\frac{\nu_k j}{nF}$ is the consumption rate given by Eq. (2.15). The activation overpotential, η, in the source term S_k, is a function of *x*, and may be obtained from Ohm's law expressed as:

$$\frac{d^2\eta}{dx^2}=\frac{2nFD_m^{eff}}{K^{eff}r_0}\left(\frac{\partial C}{\partial r}\right)_{r=r_0}, \tag{2.44}$$

where K^{eff} is the effective ionic conductivity. Equation (2.44) could be solved numerically to obtain the radial distribution of current density at various locations. Subsequently it can be used to evaluate the performance of the electrode as a function of physical properties such as the intrinsic activity of the catalyst, agglomerate size, internal porosity and active surface area.

(ii) Macroscopic models

The macroscopic model is classified into different types and each is discussed below:

- *Interface models:* This model treats the catalyst layer as an infinitely thin interface between the GDL and the membrane. It is used in fuel cell simulations when the emphasis is not on the catalyst-layer but rather on the membrane, the water balance, or the nonisothermal effects. The catalyst is treated as a location where

the reactants are consumed and the water is produced especially in models focusing on water management [156, 157].

Faraday's law, Eq. (2.15), is used in the boundary conditions for the mass balance of each species between the membrane and the GDL. The overall polarisation behaviour, as a function of the catalyst interface, is also studied by using this model [138, 158]. Generally, the interface model assumes that the values of the relevant variables are constant across the thickness of the catalyst layers, based on the fact that the layers are extremely thin. However, detailed treatment of the catalyst layer is required when the structure parameters of the layer, such as the catalyst loading, need to be optimised.

- *Macrohomogeneous and thin film models:* In this model framework, the catalyst layer is assumed to consist of a uniformly-dispersed carbon-supported catalyst and the ionomer electrolyte without the gas pores. The gas species dissolve and diffuse in the membrane phase and, consequently, the diffusion rate is low. In the thin film model, gas pores are assumed to exist and the catalyst particles are covered by a thin film of electrolyte polymer. The macrohomogeneous models [159] and the thin film models ignore the microstructural details and share similar governing equations. The major distinction between the two models is the values of the diffusion coefficients, since the reactant gas diffuses in different phases, namely, in the gas phase for the thin film models and in the membrane phase for the macrohomogeneous models. A one-dimensional macrohomogeneous model for a cathode catalyst with thickness δ_{cat} is summarized in Ref. 159 and is presented here for completion. In the model, the oxygen flux, No_2 through the catalyst thickness is determined by Fick's law of diffusion:

$$\frac{dCo_2}{dx} = -\frac{No_2}{D_{o_2}^{eff}} = \frac{i(x) - I_o}{4FD_{o_2}^{eff}}, \tag{2.45}$$

where $D_{o_2}^{eff}$ is the effective oxygen diffusion coefficient, $i(x)$ is the local proton current density, and I_0 is the total current density through the cell. The solid phase is considered to be equipotential (i.e., $\Phi_s = 0$), since the ohmic losses are negligible in the highly conductive materials. Consequently, the local electrode potential, $\eta(x)$, defined as the potential difference between the membrane and solid phase, is only determined by the local electrolyte potential. Thus,

$$\eta(x) = \Phi_e - \Phi_s = \Phi_e(x). \tag{2.46}$$

Ohm's law for the conduction of protons in the ionomer phase yields:

$$\frac{d^2\eta(x)}{dx^2} = \frac{d^2\Phi_e(x)}{dx^2} = \frac{j_c(x)}{\kappa^{eff}}, \tag{2.47}$$

where $j_c(x)$ is the volumetric transfer current and κ^{eff} is the effective proton conductivity. The effect of the effective oxygen diffusion coefficient $D_{0_2}^{eff}$ and effective proton conductivity κ^{eff} on the cathode performance could be obtained through Eqs. (2.46) and (2.47). Also both $D_{0_2}^{eff}$ and κ^{eff} are functions of the membrane in the catalyst layer, hence the model could be used to determine an optimal membrane gradient that significantly improves the cathode performance via optimising both the oxygen diffusion and proton transport [159].

- *Agglomerate models:* The macrohomogeneous and thin film models deal with the transport processes on macroscale across the layer thickness, while neglecting the variation of physical variables in the local agglomerate-scale. To investigate the effect in changes in the agglomerate or pore-scale on the accuracy of the modeling of the phenomenon, the characteristic length of the pore-agglomerate must be compared with the diffusion lengths, *i.e.*, the distances over which the physical

variables related significantly to the transport process change. The characteristic pore scale lengths of a PEMFC are in the range 10^{-7} to 10^{-8} m, while the diffusion lengths for the reactants in the electrolyte phase specifically changes from 10^{-7} to 10^{-8} m [160].

A one-dimensional, steady-state, isothermal agglomerate model was developed by Wang *et al.* [161]. In this model, the cathode catalyst layer is assumed to consist of uniformly distributed spherical agglomerates with radius R_a and void space. The ohmic losses within the solid are ignored, hence the potential within the agglomerate is constant. The diffusion and oxygen reaction within the agglomerate is given as [161]:

$$D_a^{eff}\frac{1}{r^2}\frac{d}{dr}\left(r^2\frac{dC_{O_2}}{dr}\right)=-\frac{j_c}{nF}\ , \tag{2.48}$$

where D_a^{eff} is the effective diffusivity of oxygen in the porous agglomerate and j_c is the volumetric transfer current. When oxygen concentration in the agglomerate is $C_{O_2}^{s}$, an analytical solution to Eq. (2.48) is given as [161]:

$$C_{O_2}=C_{O_2}^{s}\frac{R_a}{r}\frac{\sinh(\phi r)}{\sinh(\phi R_a)}\ , \tag{2.49}$$

where the product ϕR_a is commonly called the Thiele modulus and is defined as:

$$\phi R_a=\sqrt{\frac{A_{av}i_{0,c}^{ref}}{nFD_a^{eff}C_{O_2}^{ref}}}R_a\exp\left(\frac{\alpha_c F}{2RT}\eta\right). \tag{2.50}$$

The current produced in the agglomerate, I_a, is obtained by using Faraday's law and Eq. (2.49):

$$I_a = nF(4\pi R_a^2)N_{O_2}(r = R_a) = -4\pi nFR_a D_a^{eff} C_{O_2}^s [\phi R_a \coth(\phi R_a) - 1], \tag{2.51}$$

where $N_{O_2}(r = R_a)$ is the oxygen flux at the agglomerate surface, and concentration $C_{O_2}^s$ is related to the gas concentration in the void space, $C_{O_2'g}$, by Henry's law:

$$C_{O_2}^s = H_{O_2} C_{O_2'g} \ , \tag{2.52}$$

where H_{O_2} is Henry's constant for the oxygen gas.

The current density variation in the macroscopic catalyst scale, $i(x)$, may be obtained from the proton mass balance in the layer, based on the solution of the current in the agglomerate, Eq. (2.51). Thus,

$$\frac{di}{dx} = -\rho_a I_a \ , \tag{2.53}$$

where ρ_a is the density of the agglomerates in the catalyst layer and is defined by:

$$\rho_a = \frac{1 - \varepsilon_c}{(4/3)\pi R_a^3} , \tag{2.54}$$

where ε_c is the porosity of the catalyst layer. Also, the overpotential is governed by Ohm's law:

$$\frac{d\eta}{dx} = \frac{i}{\kappa^{eff}} \quad . \tag{2.55}$$

The oxygen concentration in the gas pores may be obtained from Eq. (2.53) and Fick's law:

$$nFD^{eff}_{O_2'c} \frac{d^2 C_{O_2'g}}{dx^2} = -\rho_a I_a \quad , \tag{2.56}$$

where $D^{eff}_{O_2'c}$ is the effective oxygen diffusivity in the gas phase. The agglomerate-type models agree better with the physical picture and they are easily implemented in fuel-cell simulation.

CONCLUSION

This part of the thesis provided a background to the basic components of a PEM fuel cell system and their respective functions. General overviews of numerical models of dynamics within PEMFC structures, highlighting governing equations, were also discussed, as well as the applicable theoretical framework employed in the PEM fuel cell modelling carried out in this thesis. The numerical models were implemented in the CFD code employed in this study and the results are reported in Chapters 4 to 6 of this thesis.

3

CHAPTER 3: NUMERICAL MODELLING FRAMEWORK

3.1 INTRODUCTION

In this chapter, we present the numerical and optimisation procedures employed in this research. Numerical modelling provides key benefits to fuel cell designers. It enables the design and building of system components in parallel without other stack hardware being in place. Therefore, as a result of numerical approaches to the design, the production cost of a fuel cell is relatively lower when compared to cost resulting from trial and error design approach, which is often exacerbated by expensive fuel cell hardware components. Hence, the role of numerical modelling in fuel cell production cannot be overemphasised. In this chapter, a general overview is presented of domain discretisation and optimisation techniques employed in fuel cell models used in this study. However, further details regarding grid independence and boundary conditions, as applied for each fuel cell modelling design problem in this thesis, are presented in subsequent sections, i.e., in Chapters 4-6.

3.2 NUMERICAL METHOD

The numerical method involves the flow modelling, discretisation of the flow domain, solving the flow governing equations and data processing. The numerical study was conducted by using the finite volume method [162]. A commercial computational fluid dynamics (CFD) code, ANSYS Fluent® [163] with Gambit® [164] as a pre-processor, is used. The CFD code has an add-on package for fuel cells. The detailed analysis of the numerical modelling techniques will be discussed later, in subsequent sections.

3.2.1 NUMERICAL MODELLING PROCEDURES

The governing sets of mathematical equations that describe the flow field in the modelled fuel cells are based on fundamental fluid dynamics principles, mass conservation, conservation of momentum and conservation of energy. CFD involves the numerical solving of Navier-Stokes and energy equations on a discritised domain. This numerical process commences by first defining the domain and thereafter creating the grid. The grid generation is basically the division of the domain into smaller control volumes. Generally, the numerical algorithm integrates the governing equations over the control volumes and, with the aid of the discretisation, the integral equations are converted into algebraic equations which are then solved iteratively [162]. Navier-Stokes and energy equations are then solved in these smaller volumes. The CFD code employed in this research solves these equations on a discretised domain when relevant flow boundary conditions are specified. The general form of the equation in vector form has been previously presented in section 2.4.1 of this thesis (Eqs. 2.4-2.9).

In modelling the fuel cell, some basic assumptions were made:

- the cell operates under steady-state conditions;
- isothermal boundary conditions were used for external walls;
- the flow in the cell is considered to be laminar;
- reactant and products are assumed to be ideal gas mixtures; and
- the electrode is assumed to be an isotropic and homogeneous porous medium.

These assumptions could be varied when required and additional assumptions may also be specified for a specific fuel cell model as will be shown in Chapters 4-6. The numerical analysis is divided into three stages: pre-processing, the solver (solution technique) and post-processing. The geometry development and grid generation within the flow domain is the pre-processing stage, while solving the flow governing equation at various nodal points within the flow domain is regarded as the solver or

solution technique. The results analysis which involves graphical presentation of simulation data outputs, contour, velocity fields and floods of various parameters are classified as post-processing. A commercial automated grid generator, Gambit® (Geometry and Mesh Building Intelligent Toolkit) that works with a graphical user interface in grid creation, has been used to generate the grid for the pre-processing stage. Gambit® has an added advantage of being able to parameterise the source file of the model domain. This advantage enables a quasi-automation of the grid generation by using journal files which are text files that contain commands that indicate the steps to be followed in the design of the model of interest. The use of the journal files eliminates the need for the graphical user interface or the repetition involved in its usage. ANSYS Fluent® commercial software was used as the solver and part of the post processing. However, the major part of the post-processing was carried out using KaleidaGraph 4.0 software.

Several works have been done towards development of metrics for validation and verification of the computational code used in fluid flow modelling. American Institute of Aeronautics and Astronautics (AIAA) and American Society of Mechanical Engineers (ASME) have also declared policy statements and guidelines for the verification and validation of computational fluid dynamics simulations [43, 44]. These metrics include assessment for iterative convergence, spatial grid convergence and comparison of the CFD results to experimental data. These criteria are used in this thesis for the validation of the solved models. Numerical models used in solving each proposed fuel cell problem in this thesis are first constructed, after which the model is verified by conducting grid independence tests and comparing specific cases against other reported studies in the literature. Modelling validation was done largely by comparison with reported modelling and experimental studies in the literature and this is presented in subsequent sections, i.e., Chapters 4-6. The detail grid adaptation technique for each fuel cell model and the time ranges for each simulation will be presented in subsequent chapters in relation to each model examined. The simulations were carried out on an Intel® Core(TM) 2Duo 3.00 GHz PC with 3.24 GB of DDRam.

3.3 NUMERICAL OPTIMISATION

Recent advancement in digital computer technology has spurred outstanding progress in the area of numerical methods for optimisation. Several methods have been developed for unconstrained and constrained optimisation [165, 166]. Engineering applications for optimisation usually involve solving a nonlinear constrained optimisation problem. Nonlinear constrained problems basically involve the search for a minimum of a nonlinear objective function subject to a set of nonlinear constraints. Numerical optimisation deals with determining the best solution to problems which can be expressed mathematically or numerically. In other words, it implies choosing the best element from a range of available alternatives.

3.3.1 CONSTRAINED OPTIMISATION

Consider the constrained optimisation problem of the general mathematical form:

$$\min f(\mathbf{x}); \mathbf{x} = [x_1, x_2, ..., x_i, ..., x_n]^T, \mathbf{x} \in R^n$$

subject to constraints below:

$$\begin{aligned} g_j(\mathbf{x}) &\le 0;\ j = 1,2,.....,\ m \\ h_k(\mathbf{x}) &= 0; k = 1,2,.....,\ p < n \end{aligned} \tag{3.1}$$

The function $f(\mathbf{x})$ is the objective function to be minimised (or maximised). The $g_j(\mathbf{x})$ and $h_k(\mathbf{x})$ represents the inequality and equality constraint functions, respectively. The components $x_i, i = 2,....., n$ of $\boldsymbol{x}$ are referred to as the design variables. The optimum vector $\boldsymbol{x}$ that solves the problem denoted by Eq. (3.1) is denoted by the vector:

$$x^* = [x_1^*, x_2^*, ..., x_n^*]^T, \tag{3.2}$$

with the corresponding lowest function value $f(\mathbf{x}^*)$ subject to the given inequality and equality constraints.

There are different approaches to solving the optimisation problem described in Eq. 3.1. An approach is to use the gradient-based algorithms [166] (i.e., successive approximation sequential quadratic programming (SQP) method), or stochastic methods (genetic algorithm). The use of genetic algorithm methods is usually too expensive in terms of number of function evaluations (numerical simulations) when compared with SQP [167, 168]. In this thesis, a relatively new gradient-based and successive approximation Dynamic-Q method of Snyman and Hay [169] is employed. This method has been found to be of equal competitiveness to the conventional SQP method [169], with an advantage of being able to handle problems with severe noise and mixed integer problems [170, 171]. The Dynamic-Q method consists of applying the dynamic trajectory, LFOPC (Leapfrog Optimisation Program for Constrained Problems) optimisation algorithm, to successive quadratic approximations of the actual optimisation problem [169]. The Dynamic-Q method is capable of handling general constrained optimisation problems, and it is discussed in detail in the subsequent section.

3.3.2 THE DYNAMIC-Q METHOD

The Dynamic-Q algorithm method [172] employed in this study uses the LFOP algorithm [173, 174] to handle constrained problems and which includes the use of penalty function approach that is implemented in three distinct phases to increase the capability of obtaining optimal design in a short span of time. Considering a general optimisation problem depicted in Eq. (3.1), the associated penalty function that

transforms the constrained problem to an unconstrained problem form, is thus formulated as [173]:

$$p(\boldsymbol{x}) = f(\boldsymbol{x}) + \sum_{j=1}^{m} \rho_j g_j^2(\boldsymbol{x}) + \sum_{j=1}^{p} \beta_k h_k^2(\boldsymbol{x}), \tag{3.3}$$

where $\rho_j = \begin{cases} 0 \; if g_j(\boldsymbol{x}) \leq 0 \\ \alpha_j \; if g_j(\boldsymbol{x}) > 0 \end{cases}$.

To increase the simplicity of the algorithm, the penalty parameters α_j and β_k takes the same large positive value of μ and the higher the value of μ, the more accurate the obtained solution. Meanwhile, at extreme values of μ, the optimisation problem becomes ill-conditioned. This is resolved by increasing the penalty function piece-wise until a favourable limit value of μ is obtained and then keeping it constant at this limit value until convergence is achieved [175]. The LFOP dynamic trajectory method phases applied to the penalty function are highlighted below.

Phase 0:

Given an initial starting guess of the design variables $\mathbf{x}^0$, the LFOP is applied with some overall penalty parameter μ_0 to $P(\mathbf{x}, \mu_0)$. This gives an optimum design variable vector $\mathbf{x}^*(\mu_0)$ at convergence. The constraints are checked at this optimum value to ensure that no active constraints are neglected (violated). If none of the active constraints are violated, the optimal point is taken as the actual optimal minimum of the optimisation problem being solved and the algorithm is subsequently terminated.

Phase 1:

In a case where there is an active constraint being violated after checks in Phase 0, this phase is initialised. The initialisation process involves applying LFOP with an increasing value of μ and using the obtained optimum ($\mathbf{x}^*(\mu_0)$) in phase 0 as the initial guess. Thereafter, the penalty parameter is then minimised and active constraints are identified. If no active constraints are violated, the optimisation algorithm is terminated and the obtained solution $\mathbf{x}^*(\mu_1)$ is accepted as the optimal solution of the optimisation problem.

Phase 2:

This phase uses the optimal solution from the preceding Phase 1 as the starting guess to apply the LFOP. The algorithm will search for the optimal solution which corresponds to the intersection of the active constraints. During the search, if the active constraints do not intersect, the algorithm will find the best probable solution, which is usually close enough to the actual solution with the lowest possible constraint violation.

3.3.3 DYNAMIC-Q APPROACH: CONSTRUCTING SPHERICAL QUADRATIC SUBPROBLEMS

Dynamic-Q offers a robust optimisation algorithm due to its capability to deal with numerical analyses from CFD and finite element method (FEM) simulations. It does this by handling associated noises generated due to errors created by environmental influences, grid changes, incomplete convergence and numerical accuracy of the computer. The numerical computational time (for an objective function not analytically given or expensive to compute numerically) is reduced in the Dynamic-Q approach by substituting computationally expensive functions by simpler spherically quadratic approximate functions obtained from a few expensive function evaluations (simulations). These approximate functions are utilised to construct successive sub-

problems $P[i], i = 0,1,2,....$ at successive design iteration points i^k. The approximated function can be an objective function and/or the constraint function depending on the optimisation problem being handled. In this Dynamic-Q algorithm, the classical steepest descent (SD) algorithm method used to solve the general function of the form $f(x)$ is modified for better overall performance by applying the SD method successfully to a sequence of very simple quadratic approximations of $f(x)$. The identical curvature entries along the diagonal of the Hessian, means that the level surfaces of the quadratic approximation $\tilde{f}_k(x)$, are concentric hyper-spheres. Hence, the modified classical steepest descent algorithm is aptly referred to as spherical quadratic approximations. The constructions of these spherical quadratic approximations are described below [175, 176]:

$$\begin{aligned}
\tilde{f}(\mathbf{x}) &= f(\mathbf{x}^i) + \nabla^T f(\mathbf{x}^i)(\mathbf{x}-\mathbf{x}^i) + \frac{1}{2}(\mathbf{x}-\mathbf{x}^i)^T\,\mathbf{A}(\mathbf{x}-\mathbf{x}^i) \\
\tilde{g}_j(\mathbf{x}) &= g_j(\mathbf{x}^i) + \nabla^T g_j(\mathbf{x}^i)(\mathbf{x}-\mathbf{x}^i) + \frac{1}{2}(\mathbf{x}-\mathbf{x}^i)^T\,\mathbf{B}_j(\mathbf{x}-\mathbf{x}^i) \\
\tilde{h}_k(\mathbf{x}) &= h_k(\mathbf{x}^i) + \nabla^T h_k(\mathbf{x}^i)(\mathbf{x}-\mathbf{x}^i) + \frac{1}{2}(\mathbf{x}-\mathbf{x}^i)^T\,\mathbf{C}_k(\mathbf{x}-\mathbf{x}^i)
\end{aligned} \tag{3.4}$$

$\mathbf{A}$, $\mathbf{B}_j$ and $\mathbf{C}_k$ are Hessian matrices of the objective, inequality and equality functions, respectively, and often take on the simple forms:

$$\begin{aligned}
\mathbf{A} &= \text{diag}(a, a, ..., a) = a\,\mathbf{I} \\
\mathbf{B}_j &= b_j\,\mathbf{I} \\
\mathbf{C}_k &= c_k\,\mathbf{I} \quad ,
\end{aligned} \tag{3.5}$$

where **I** represents the identity matrix.

∇^T, $\nabla^T g_j$ and $\nabla^T h_k$ are gradient vectors. If these vectors are not known analytically, they are approximated from functional data by means of first-order forward finite differences [176].

Intermediate move limits are employed in the Dynamic-Q algorithm to achieve convergence in a controlled and stable form. The move limit δ_j takes on the form of a constraint by limiting the movement of each design variable, $\mathbf{x}_j^{(i-1)}$, by preventing the new design point from moving too far away from the current design point. An additional constraint of the form is:

$$\begin{aligned} &\mathbf{x}_j - \mathbf{x}_j^{(i-1)} - \delta_j \le 0 \\ &-\mathbf{x}_j^{(i-1)} + \mathbf{x}_j - \delta_j \le 0 \end{aligned} \quad ; j = 1, 2, \ldots, n \quad . \tag{3.6}$$

The Dynamic-Q algorithm terminates when the following step size and function value criteria are satisfied:

- Step size:

$$\Delta x_{norm} = \frac{\| x^k - x^{k-1} \|}{1 + \| x^k \|} < \varepsilon_x \ ; \tag{3.7}$$

- Function value:

$$\Delta f_{norm} = \frac{| f^k - f_{best} |}{1 + | f_{best} |} < \varepsilon_f \ ; \tag{3.8}$$

where ε_x and ε_f are the step sizes and function value tolerances, respectively.

3.3.4 THE OBJECTIVE AND CONSTRAINT FUNCTIONS GRADIENT APPROXIMATION

The Snyman Dynamic-Q method requires the gradients of the objective and constraint functions. When these gradient functions are not analytically available, the components of the gradients are calculated as follows:

$$\frac{\partial f(\mathbf{x})}{\partial x_i} = \frac{f(\mathbf{x}+\Delta \mathbf{x}_i) - f(\mathbf{x})}{\Delta x_i}, \quad i = 1,2,...,n \quad , \tag{3.9}$$

where the differencing step size is given as:

$$\Delta \mathbf{x}_i = [0,0,...,\Delta x_i,...,0]^T \quad . \tag{3.10}$$

The gradients of the inequality and equality constraint function components used in the spherical approximation are similarly approximated and depicted in the Eq. (3.10). Thus,

$$\frac{\partial g_i(\mathbf{x})}{\partial x_i} = \frac{g_i(\mathbf{x}+\Delta \mathbf{x}_i) - g_i(\mathbf{x})}{\Delta x_i}, \quad i = 1,2,...,n \quad ,$$
$$\frac{\partial h_i(\mathbf{x})}{\partial x_i} = \frac{h_i(\mathbf{x}+\Delta \mathbf{x}_i) - h_i(\mathbf{x})}{\Delta x_i}, \quad i = 1,2,...,p \quad , \tag{3.11}$$

also with the differencing step size being:

$$\Delta \mathbf{x}_i = [0,0,...,\Delta x_i,...,0]^T \quad . \tag{3.12}$$

In practice, new CFD simulation is required to approximate each of the components (i.e., at each optimisation iteration, n+1). This tends to increase the computational

cost but could be reduced by assuming a constant differencing step size for each design variable.

Simulation processes are always accompanied by noises that are introduced by the step size $\Delta \mathbf{x}$, used in the differencing scheme. Therefore, choosing an appropriate step size that gives good results and at the same time eliminates noise generation during simulation, remains very pertinent. This is done by using the Dynamic-Q algorithm. The experience of the modeller to solve this associated problem then comes in handy. To ensure an appropriate step size, different starting guesses should be used a couple of times and, if the converged solution values are the same, then the chosen step size is accepted as sufficient. In cases where the converged solution value differs, the step size should be modified until the variations in the results are eliminated.

In summary, the Dynamic-Q algorithm can be stated as follows [169]:

i. Choose a starting point $\mathbf{x}^1$ and move limits δ_j, $j = 1,2,...,n$ and set $i := 1$.

ii. Evaluate $f(\mathbf{x}^i)$, $g_j(\mathbf{x}^i)$, and $h_k(\mathbf{x}^i)$, as well as $\nabla f(\mathbf{x}^i)$, $\nabla g_j(\mathbf{x}^i)$, and $\nabla h_k(\mathbf{x}^i)$. If termination criteria are satisfied then set $\mathbf{x}^* = \mathbf{x}^i$ and stop.

iii. Construct a local approximation, $P[i]$, to the optimisation problem at $\mathbf{x}^i$, using approximations for the objective and constraint functions.

iv. Solve the approximated sub-problem, $P[i]$, to give $\mathbf{x}^{*i}$, by using LFOPC [173].

v. Set $i := i+1$, $\mathbf{x}^i := \mathbf{x}^{*(i-1)}$ and return to step ii.

3.3.5 ADVANTAGE OF DYNAMIC-Q ALGORITHM

The use of spherically quadratic approximation in the Dynamic-Q algorithm offers a competitive advantage when compared with other methods in terms of the computational and storage requirements. The $O(n^2)$ calculations and storage locations required for the second order derivatives are not required since the second derivatives

of the objective function and constraints are approximated by using function and gradient data. The Dynamic-Q computational and storage resources are thus practically reduced to O(n). At the most, $4 + p + q + r + s \;\; n -$ vectors need be stored (where p, q, r and s are the number of inequality and equality constraints and the number of lower and upper limits of the variables, respectively). The storage savings becomes highly significant when the number of variables becomes large [169]. Therefore, the particular strength of the Dynamic-Q method makes it well suited for optimisation of engineering problems with large number of variables.

CONCLUSION

This chapter focused on the description of numerical methods and mathematical optimisation algorithm used in this study. The DYNAMIC-Q, which builds on the LFOPC algorithm, is discussed in detail. The strength of this mathematical optimisation choice was also highlighted in terms of storage savings where large numbers of variables and noise handling during simulation were being considered.

4

CHAPTER 4: NUMERICAL OPTIMISATION OF OPERATING AND DESIGN PARAMETERS FOR A PEM FUEL CELL

4.1 INTRODUCTION

Fuel cell technology is rapidly advancing due to the need for high energy efficiency and low environmental impact. Fuel cells are regarded as a potential reliable future source of energy supply due to the fact that they are one of the cleanest and most efficient alternatives for generating power. However, the large initial capital costs of fuel cell technology have offset the advantages it offers and slowed down its adoption for widespread applications [177]. The PEMFC using hydrogen is one of the emerging fuel cells with many advantages ranging from emission of water as waste, operation at low temperatures for quick start-up, and the use of solid polymers as electrolytes, reducing both construction and safety complications [71]. This fuel cell type is seriously being considered as an alternative power source for stationary and mobile applications, but there are several technical challenges which have to be overcome before it can be adopted for use in these devices.

One of the means of reducing the cost of a PEMFC is by improving its performance through system optimisation. This facilitates the understanding of how different parameters affect the performance of the fuel cell in real operating conditions and subsequently reduce the cost involved in prototype development. Fuel cell modelling has received tremendous attention in the last two decades with the ultimate aim of better understanding the underlying phenomenon of operating fuel cells. Much research has been carried out on PEMFCs ranging from one-dimensional models, showing phenomena where mass transport limitation is taken into account, and two- or three-dimensional models encompassing thermal and water management. This two-

or three-dimensional model also combines electrochemical, thermodynamic and fluid dynamic equations. Heat transfer equations and mass and energy balances were also incorporated into some studies to provide detailed understanding of emerging processes in fuel cell systems.

In the landmark works on PEMFC by Bernardi [157], Bernardi and Verbrugge [23] and Springer *et al.* [24], which are based on one-dimensional models, the focus is on humidification requirements of inlet gases and issues related to variable membrane humidification. The work by this group [23, 24, 157] provided the required framework for the multidimensional models that followed in subsequent years. A vast number of previous works are also CFD-based. More recent works that are CFD-based can be found in [30, 53, 66, 80, 141, 178, 179]. Available experimental work to date has been conducted mostly to validate highly sophisticated CFD simulations against the cell global polarisation curves. Some of the experimental studies can be found in [68, 180-182].

Another issue of significant importance in PEM fuel cells is the pressure drop, especially at the cathode side of the cell. The product water generated at the cathode channel must be removed from the cell and this requires a high pressure drop. Too high pressure drops create excessive parasitic power requirement for the pumping of air through cells, hence, the effective design of the fuel channel is required to ensure a balance in pressure drop requirements at the fuel cell cathode section.

Inoue *et al.* [58] studied gas flow through the GDL and the internal phenomena of a single PEMFC. The result shows an increase in flow when the differential pressure between adjoining channels is increased, and an increase in the output density as the depth of the separator channel become smaller. Liu *et al.* [183] studied the two-phase flow and water flooding of reactants in the cathode flow channels of an operating transparent PEMFC experimentally. The effect of the flow field type, cell temperature, cathode flow rate and operation time on the water build-up and cell performance formed part of this study. The results indicate the adverse effect of liquid

water accumulation on mass transport and the subsequent reduction of the performance of the fuel cell.

Rodatz *et al.* [184] conducted studies on the operational aspects of a PEMFC stack under practical conditions. Their study focused particularly on the pressure drop, two-phase flow and effect of bends. They observed a decrease in the pressure drop at a reduced stack current. Maharudrayya *et al.* [185] studied the pressure drop and flow distribution in the multiple parallel channel configurations that are used in PEMFC stacks. Through their study, they developed an algorithm to calculate the flow distribution and pressure drop in multiple U- and Z-type flow configurations of a fuel cell. Ahmed *et al.* [59] used a numerical model to investigate the performance of a PEMFC at high operating current densities for various channel cross-sectional configurations, while maintaining the same reactant flow rates and inlet boundary conditions. The obtained results reveal that rectangular channel cross-sections give higher cell voltages, while the trapezoidal channel cross-section gives more uniform distributions at the membrane-cathode GDL interface. The results further reveal the presence of an optimum channel-shoulder ratio for optimal fuel cell performance.

Most of the existing models in the literature address the effect of fuel channel geometric parameters on the performance of the PEM fuel cell without investigating the mutual interdependence of the GDL porous medium, reactant gas flow rate and gas channel geometry on the fuel cell system performance. Studies on PEM fuel cell performances which incorporate the determination of optimal operating values for fuel cell design parameters, taking into consideration the combined mutual effect of channel geometry, flow rate and GDL characteristics are still very limited in the literature. A good understanding of the interactive interdependence of these fuel cell parameters is therefore essential for optimum fuel cell design. One crucial design consideration in fuel cell design is the reactant flow in the flow field because of the dominant effect of the parasitic losses caused by frictional losses, reactant consumption, species production and blockages resulting from the two-phase flow.

Therefore, the purpose of this chapter in the thesis is to investigate the effect of a range of operating conditions such as reactant flow rates, GDL porosity, channel geometry and flow orientation on the performance of a single PEM fuel cell, and also to determine the optimal operating conditions for this class of fuel cell. In addition, this chapter sought to determine the optimal fuel cell performance at different geometric configurations for a given GDL porosity and reactant species flow rate, which has not been given much attention in the literature. In this chapter, a three-dimensional steady-state computational model for a single PEM fuel cell was developed to predict the fuel cell performance under different operating conditions, and subsequently add to the knowledge base needed to produce generic design information for fuel cell systems, which can be applied to better designs of fuel cell stacks.

4.2 MODEL DESCRIPTION

Figure 4.1 shows a schematic diagram of a typical PEM fuel cell cross-section indicating the different zones and species transport across the zones. This consists of seven different regions: the cathode flow channel, cathode diffusion layer, cathode catalyst layer, PEM, anode catalyst layer, anode diffusion layer and the anode flow channel. It was assumed that the fuel used is hydrogen at the anode side which diffuses through the porous GDL and comes into contact with the catalyst layer. At this layer, it forms hydrogen ions and electrons. The hydrogen ion diffuses through the polymer electrolyte membrane at the centre, while the electrons flow through the GDL to the current collectors and into the attached electric load.

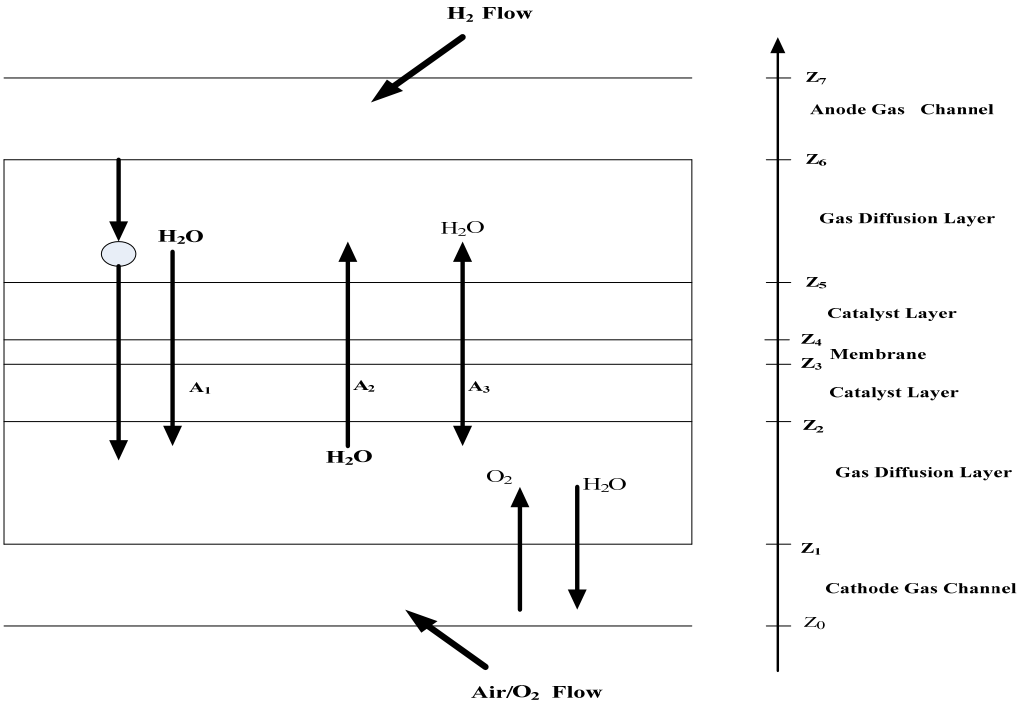

Figure 4.1 Schematic diagram of a PEM fuel cell showing different zones and species transport across the zones. The net water flux is the sum of: (A_1) electro-osmotic effect, (A_2) diffusion effect and (A_3) the permeability effect

The electrochemical reactions are:

anodic: $H_2 \rightarrow 2H^+ + 2e^-$, (4.1)

cathodic: $\frac{1}{2}O_2 + 2H^+ + 2e^- \rightarrow H_2O$, (4.2)

net reaction: $H_2 + \frac{1}{2}O_2 \rightarrow H_2O$. (4.3)

Figure 4.2 depicts the computational domain consisting of the anode flow channel, anode diffusion layer, MEA, cathode diffusion layer, and cathode flow channel. In this model, the numerical domain is a full single-cell geometry domain. Pure hydrogen and air were used as reactant gases in the model. The inlet flow velocity was controlled by the stoichiometry numbers of 1.2 at the anode and 2.0 at the

cathode. The operating pressure was 101 kPa absolute at the exit of the cell. The details of the flow field and other physicochemical parameters used for the base case are summarised in Table 4.1 and Table 4.2.

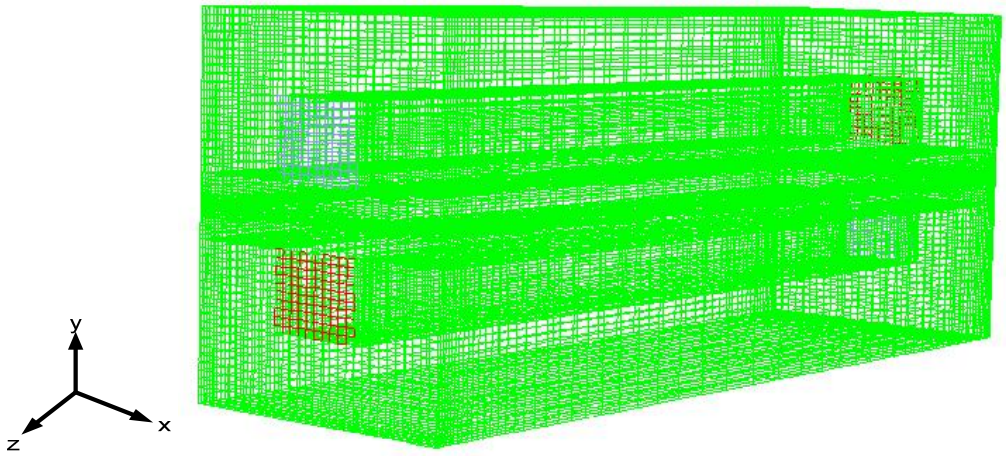

Figure 4.2 The discretised three-dimensional computational domain of a single PEM fuel cell

Table 4.1 Base case geometric parameters of the modelled fuel cell

Channel length (mm)	120
Channel width (mm)	1.0
Channel depth (mm)	1.2
Membrane thickness (mm)	0.036
Catalyst layer thickness (mm)	0.012
Electrode thickness (mm)	0.21

Table 4.2 Physicochemical properties of the modelled fuel cell

Description	Value
Cell operating temperature (^{o}C)	70
Air-side/fuel-side inlet pressure (atm)	3/3

Open-circuit voltage (V)	0.95
Porosity of GDL	0.4
Permeability of GDL (m^2)	1.76×10^{-11}
Tortuosity of GDL	1.5
Porosity of catalyst layer	0.4
Permeability of catalyst layer (m^2)	1.76×10^{-11}
Tortuosity of catalyst layer	1.5
Porosity of membrane	0.28
Permeability of membrane (m^2)	1.8×10^{-18}
Reference diffusivity of H_2	11×10^{-5} m^2 s^{-1}
Reference diffusivity of O_2	3.2×10^{-5} m^2 s^{-1}
Electric conductivity of catalyst layer $(\Omega^{-1} m^{-1})$	190
Electric conductivity of GDL $(\Omega^{-1} m^{-1})$	300
Electric conductivity in carbon plate $(\Omega^{-1} m^{-1})$	4000
O_2 stoichiometry ratio	1.2
H_2 stoichiometry ratio	2.0
Oxygen mole fraction	0.406
Relative humidity of inlet fuel/air	100%
Reference current density of anode (A/m^2)	7500
Reference current density of cathode (A/m^2)	20
Anode transfer coefficient	2.0
Cathode transfer coefficient	2.0

4.2.1 MODEL ASSUMPTIONS

Regarding the modelling of the fuel cell, the following assumptions were made:

- the cell operates under steady-state conditions;
- isothermal boundary conditions were used for external walls;
- the flow in the cell is considered to be laminar;
- reactant and products are assumed to be ideal gas mixtures; and
- the electrode is assumed to be an isotropic and homogeneous porous medium.

4.2.2 GOVERNING TRANSPORT EQUATIONS

The basic transport equation (conservation of mass and momentum) applies to the transport of gas mixtures in the gas channels in the fuel cell. The corresponding governing equations are written as follows:

Continuity equation: $$\frac{\partial(\rho v_x)}{\partial x}+\frac{\partial(\rho v_y)}{\partial y}+\frac{\partial(\rho v_z)}{\partial z}=S_m \quad (4.4)$$

where S_m is the source term, owing to electrochemical reactions corresponding to the hydrogen depletion during reactions, which is applicable at both the anode and cathode GDL/MEA interface and calculated by [178]:

$$S_m = 0, \quad z_0 \le z \le z_2 \quad \text{and} \quad (4.5)$$

$$S_m = -\frac{\lambda[H_2]}{\kappa+[H_2]}, \quad z_2 \le z \le z_3 \ , \quad (4.6)$$

where $[H_2]$ is the concentration of hydrogen in the domain of interest, and λ and κ are terms of which the values are dependent upon the rate constants for the atomic oxidation of H_2 and the platinum loading in the catalyst layer. The value of κ was set

equal to 1 and λ assumed different values, which were subject to different values of the concentration of Pt initially in the catalyst layer, as discussed by Hontanon *et al*. [178]. The momentum conservation, also referred to as the Navier-Stokes equation, is:

Momentum (*x*-direction):

$$v_x \frac{\partial(\rho v_x)}{\partial x} + v_y \frac{\partial(\rho v_x)}{\partial y} + v_z \frac{\partial(\rho v_x)}{\partial z}$$

$$= -\frac{\partial P}{\partial x} + \frac{\partial}{\partial x}\left(\mu \frac{\partial v_x}{\partial x}\right) + \frac{\partial}{\partial y}\left(\mu \frac{\partial v_x}{\partial y}\right) + \frac{\partial}{\partial z}\left(\mu \frac{\partial v_x}{\partial z}\right) + S_{px} \quad , \tag{4.7}$$

Momentum (*y*-direction):

$$v_x \frac{\partial(\rho v_y)}{\partial x} + v_y \frac{\partial(\rho v_y)}{\partial y} + v_z \frac{\partial(\rho v_y)}{\partial z}$$

$$= -\frac{\partial P}{\partial y} + \frac{\partial}{\partial x}\left(\mu \frac{\partial v_y}{\partial x}\right) + \frac{\partial}{\partial y}\left(\mu \frac{\partial v_y}{\partial y}\right) + \frac{\partial}{\partial z}\left(\mu \frac{\partial v_y}{\partial z}\right) + S_{py} \quad \text{and} \tag{4.8}$$

Momentum (*z*-direction):

$$v_x \frac{\partial(\rho v_z)}{\partial x} + v_y \frac{\partial(\rho v_z)}{\partial y} + v_z \frac{\partial(\rho v_z)}{\partial z}$$

$$= -\frac{\partial P}{\partial z} + \frac{\partial}{\partial x}\left(\mu \frac{\partial v_z}{\partial x}\right) + \frac{\partial}{\partial y}\left(\mu \frac{\partial v_z}{\partial y}\right) + \frac{\partial}{\partial z}\left(\mu \frac{\partial v_z}{\partial z}\right) + S_{pz} \quad . \tag{4.9}$$

The source terms account for situations where a fluid passes through a porous medium. The term is applicable to the electrode and catalyst zones. For low velocities encountered in fuel cells, these source terms are applicable at the GDLs and are given by Darcy's law:

$$S_{px} = -\frac{\mu v_x}{\beta_x}, \tag{4.10}$$

$$S_{py} = -\frac{\mu v_y}{\beta_y} \quad \text{and} \tag{4.11}$$

$$S_{pz} = -\frac{\mu v_z}{\beta_z} \quad \text{at} \quad z_1 \le z \le z_6 \ , \tag{4.12}$$

where μ is the fluid viscosity in the medium and β is the permeability of the electrode material. The permeability of the medium was assumed to be isotropic as stated in the assumptions in this model, hence β_x, β_y and β_z all have the same value stated in Table 4.2 (1.76 x 10^{-11} m^2). Other source terms for the equations above used in the model were taken from Dutta *et al.* [141]. The local current density, i_o, is a measure of the electrochemical reaction rate and generally given by the Butler-Volmer equation [60]:

$$i_o = i_{o,ref}\left\{\exp\left[\frac{\alpha_{an} nF}{RT}\eta\right] - \exp\left[\frac{-\alpha_{cat} nF}{RT}\eta\right]\right\} \quad , \tag{4.13}$$

where η is the overpotential and defined as

$$\eta = \left(\Phi_s - \Phi_e\right) - E_{ocv} \quad . \tag{4.14}$$

The energy conservation equation is:

$$\frac{\partial(\rho v_x h)}{\partial x} + \frac{\partial(\rho v_y h)}{\partial y} + \frac{\partial(\rho v_z h)}{\partial z} = \frac{\partial}{\partial x}\left(k\frac{\partial T}{\partial x}\right) + \frac{\partial}{\partial y}\left(k\frac{\partial T}{\partial y}\right) + \frac{\partial}{\partial z}\left(k\frac{\partial T}{\partial z}\right) + S_T \cdot \tag{4.15}$$

For the energy equation, additional volumetric sources are present, because not all chemical energy released in the electrochemical reaction can be converted to

electrical work due to irreversibilities of the process. The total source that goes to the thermal energy equation (i.e., enthalpy) is [163]:

$$S_h = h_{react} - R_{an,cat}\eta_{an,cat} + I^2 R_{ohm} + h_L \ . \tag{4.16}$$

PEMFCs operate under relatively low temperature (< 100°C) and thus water vapour may condense to liquid water, especially at high current densities. The existence of the liquid water keeps the membrane hydrated, but it also blocks the GDL passage, reduces the diffusion rate and the effective reacting surface area. The water formation and transport of liquid water is modelled by using a saturation model based on [186, 187]. In this approach, the liquid water formation and transport is governed by the conservation equation for the volume fraction of liquid water, *s*, or the water saturation [163]:

$$\frac{\partial(\varepsilon\rho_l s)}{\partial t} + \nabla\cdot\left(\rho_l \vec{V}_l s\right) = r_w \ , \tag{4.17}$$

where the subscript l represents liquid water, and r_w is the condensation rate modelled as:

$$r_w = c_r \max\left(\left[(1-s)\frac{\rho_{wv}-\rho_{sat}}{RT}M_{w,H_2O}\right],[-s\rho_l]\right), \tag{4.18}$$

where r_w is added to the water vapor equation as well as the pressure correction (mass source). The condensation rate constant is hardwired to $c_r = 100s^{-1}$. It was assumed that the liquid velocity, V_l, is equivalent to the gas velocity inside the gas channel. Inside the highly-resistant porous zones, the use of the capillary diffusion term allows the replacement of the convective term in Eq. (4.17):

$$\frac{\partial(\varepsilon\rho_l s)}{\partial t} + \nabla\cdot\left[\rho_l \frac{Ks^3}{\mu_l}\frac{dp_c}{ds}\nabla s\right] = r_w \ . \tag{4.19}$$

Depending on the wetting phase, the capillary pressure is computed as a function of s (the Leverett function) [163, 81]:

$$p_c = \begin{cases} \frac{\sigma \cos \theta_c}{(\frac{K}{\varepsilon})^{0.5}}(1.417\ (1-s) - 2.12\ (1-s)^2 + 1.263\ (1-s)^3, \theta_c < 90\ ^oC \\ \frac{\sigma \cos \theta_c}{(\frac{K}{\varepsilon})^{0.5}}(1.417\ s - 2.12\ s^2 + 1.263\ s^3), \theta > 90\ ^oC \end{cases} \quad (4.20)$$

Eq. (4.17) models various physical processes such as condensation, vaporisation, capillary diffusion and surface tension. The clogging of the porous media and the flooding of the reaction surface are modelled by multiplying the porosity and the active surface area by (1- s), respectively.

4.2.3 CHANNEL CROSS-SECTION

Flow channels in fuel cells are typically rectangular in cross-section, though other configurations such as triangular, trapezoidal, and semi-circular shapes have been explored for fuel cell designs [178]. The manufacturing processes of the flow channels in fuel cells are quite time-consuming and expensive since graphite, which is hard and brittle, is typically used as the material of choice. Hence, the making of the flow channel is a major cost in the development of a complete PEM fuel cell. In the design of small fuel cells, where the pressure drop is in the order of 0.5-1 bar [188], serpentine or interdigitated channels could be applicable, but in larger fuel cells this is not possible, as the pressure drop would be in the order of a few bars. From cost considerations and manufacturing and performance requirements, the geometrical shape of the channel cross-section has traditionally been either rectangular or square. The rectangular cross-section was used in the design of the PEM fuel cell in this study and is schematically shown in Figure 4.3.

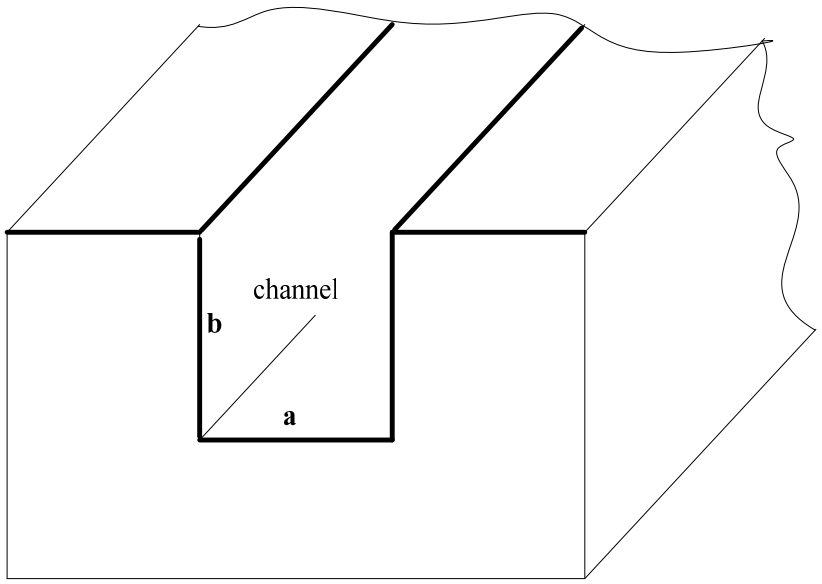

Figure 4.3 Channel cross-sectional view

For internal flows such as the ones in fuel cell channels, the Reynolds number is conventionally defined as [189]:

$$Re_{D_h} = \frac{\rho V_{avg} D_h}{\mu} \quad \text{where} \tag{4.21}$$

$$V_{avg} = \frac{\dot{m}}{\rho A_c} \; . \tag{4.22}$$

For a rectangular channel in this study, D_h is defined as [189]:

$$D_h = \frac{4A_c}{P} \; . \tag{4.23}$$

For the channel under consideration in Figure 4.3, the cross-sectional area is equal to the product of the channel width and the channel depth:

$$A_c = ab \tag{4.24}$$

and the wetted perimeter is:

$$P^* = 2(a + b) \ . \tag{4.25}$$

The pressure drop for a flow in a channel of length, *L,* is usually expressed by using the following relation [189]:

$$\Delta p = f \frac{L}{D_h} \frac{\rho V_{avg}^2}{2} \ , \tag{4.26}$$

where the friction factor, f, for steady fully-developed laminar flows in a channel with a square cross-section is given as:

$$f = \frac{56.91}{Re_{D_h}} \ . \tag{4.27}$$

Substituting the above relation Eq. (4.27) for Eq. (4.26), and taking into consideration Eqs. (4.21) to (4.25), the pressure drop can be obtained for flow channels with square cross-section (a = b), as:

$$\Delta P = 28.455\left(\frac{\mu \dot{m}}{\rho}\right)\left(\frac{L}{a^4}\right) \quad . \tag{4.28}$$

Thus, the flow channel length for flow channels with a square cross-section can be determined as:

$$L = \frac{\Delta p \rho a^4}{28.455 \mu \dot{m}} \quad . \tag{4.29}$$

Similarly, the flow channel length for a rectangular cross-section can be obtained by:

$$L = \frac{8\Delta p \rho (ab)^3}{C\mu \dot{m}(a+b)^2} \quad , \tag{4.30}$$

where $C = fRe D_h$ is a function of the b/a for rectangular flow channels [189].

The pressure drop in the channel can be obtained using the flow rate (q) – pressure drop ΔP relationship for a rectangular cross-section relation [190]:

$$q = \frac{4ba^3}{3\mu} \times \frac{-\Delta P}{\Delta L}\left[1 - \frac{192}{\pi^5 b}\sum_{i=1,3,5,}^{\infty} \frac{\tanh\left(i\pi b/2a\right)}{i^5}\right] . \tag{4.31}$$

4.2.4 FLUID FLOW THROUGH GAS DIFFUSION LAYER

In fuel cells, the fluid flow diffuses through the GDL for the reaction to take place on the MEA. The effective diffusivity for the gas-phase flow in porous media can be written as:

$$D_{eff} = D\frac{\varepsilon}{\tau} \quad . \tag{4.32}$$

The tortuosity (τ) is a difficult parameter to estimate except through experimentation. Hence, it is usually correlated in fuel cell studies using a Bruggeman correlation. This correlation assumes that τ is proportional to $\varepsilon^{-0.5}$, resulting in the simpler expression [191]:

$$D_{eff} = D\varepsilon^{1.5} \, . \tag{4.33}$$

The porosity correlation is used to adjust for the longer effective path length through the porous media.

4.2.5 BOUNDARY CONDITIONS

Pressure boundary conditions were specified at the outlets since the reactant gas flow is usually separate and at different pressures. The inlets were all assigned as mass flow inlets. The GDL and the catalyst layer were surrounded by sealed plates at the inlet and outlet planes, so the boundary conditions at the inlet and outlet planes take the no-slip condition for the velocity and non-permeable condition for the species mass fraction. The membrane-electrode interface was defined as a wall, primarily to inhibit species and electron crossover through the membrane. This also prevents pressure problems at the interface. In the areas at which the gas diffusion electrodes were in contact with the bipolar plates, a constant reference voltage equal to zero was assigned as a boundary condition both at the anode and at the cathode terminals. The electron flux was set to zero at all other walls. The anode was grounded (V = 0) and the cathode terminal was set at a fixed potential (0.75 V), less than the open-circuit potential (0.95 V). Both anode and cathode terminals were assigned wall boundaries.

4.2.6 SOLUTION TECHNIQUE

The model equations were solved using the CFD software ANSYS Fluent® 12.0 with Gambit® (2.4.6) as a pre-processor. The CFD code has an add-on package for fuel cells, which has the requirements of the source terms for species transport equations, heat sources and liquid water formations [163]. Control volume technique was used for solving the problem. The meshes were more refined at the membrane-catalyst assembly regions. The conservation of mass, momentum and energy equations in the three-dimensions were solved in turn, until the iterative process met the convergence criteria. In this study, the definition of convergence criteria indicates that the largest relative error between two consecutive iterative residuals within the overall computational domains is less that 10^{-6}.

The domain was divided into hexahedral volume elements. A computational mesh of about 257 346 volume elements was obtained with the grid. The grid independence was verified at the preliminary test runs. Four structured grid configurations were evaluated for the PEMFC. The number of elements in the *x-, y-* and *z*-directions was: (a) 70 × 70 × 25, (b) 87 × 87 × 34, (c) 104 × 87 × 34 and (d) 104 × 104 × 43. The influence of the number of elements on the local current density at an operating voltage of 0.4 V was investigated. The local current density for grid (a) differs from that of (b-d) with a deviation of about 4.2%. However, the local current density distributions for grids (b), (c) and (d) do not show any significant differences. The difference between the local current densities for (b) and (c) is about 0.36% and the difference between (c) and (d) is 0.48%. Grid (c) was chosen for the simulations as a trade-off between accuracy and cost of time.

The solution strategy was based on the SIMPLE algorithm [192]. Momentum equations were solved for the velocity followed by solving the continuity equation, which updates the pressure and the flow rate. Results were then verified for convergence. The simulation for each operating potential converged in 45-60 minutes

depending on the current density on an Intel® Core(TM) 2Duo 3.00 GHz PC with 3.24 GB of DDRam.

4.2.7 MODEL VALIDATION

The validation of physical and numerical models is very important, hence comparison with available experimental data is highly desirable. To describe the performance of fuel cells, polarisation curve or voltage-current curve is often used. Also, by comparing the polirisation curve from modelling with experiments, the accuracy or otherwise of a model could be validated [193]. The polarisation curve obtained for the base case operating conditions have been compared with experimental measurements of Wang *et al.* [33] and Cheng *et al.* [60] and are shown in Figure 4.4. There is a good agreement between the experimental curves in the low load region. However, the model current density in the high mass transport limited region (> 2.75 A/cm^2) is higher than the experimental values.

This observation is common in models where the effect of reduced oxygen transport, due to water flooding at the cathode at higher current density, cannot be properly accounted for [99]. Nonetheless, the prediction from the model could still be used successfully for better understanding of the complex processes in fuel cell systems.

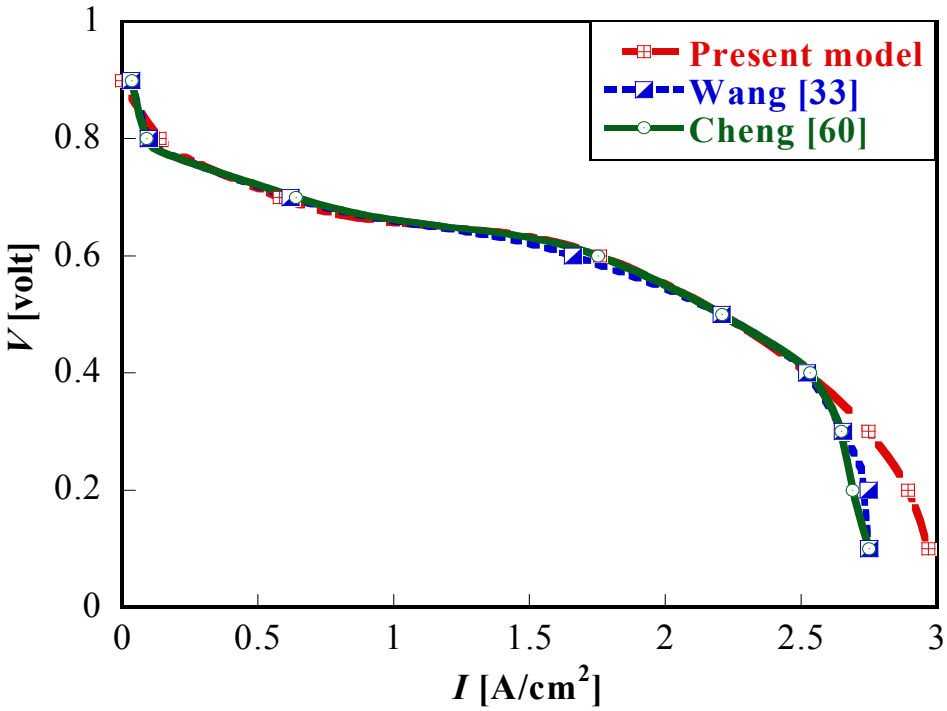

Figure 4.4 Comparison of numerical model prediction and experimental polarisation curves at base condition

4.3 MODEL RESULTS AND DISCUSSION

4.3.1 PRESSURE DROP IN FLOW CHANNEL

Figure 4.5 shows the calculated pressure drops for the rectangular flow channel over a range of air mass flow rates at a channel depth and width of 1.2 mm and 1.0 mm, respectively. The results indicate that the pressure drop increases as the mass flow rate at the cathode is increased. This is expected since an increase in the mass flow rate increases the reaction of the reactant species and also reduces the resident water in the cathode channel of the fuel cell. Generally, fuel cells with high pressure drops in the flow field exhibit a more even distribution of the reactant species flow than those with low pressure drops in their flow fields. These even distributions of reactant species greatly enhance the fuel cell performance [194].

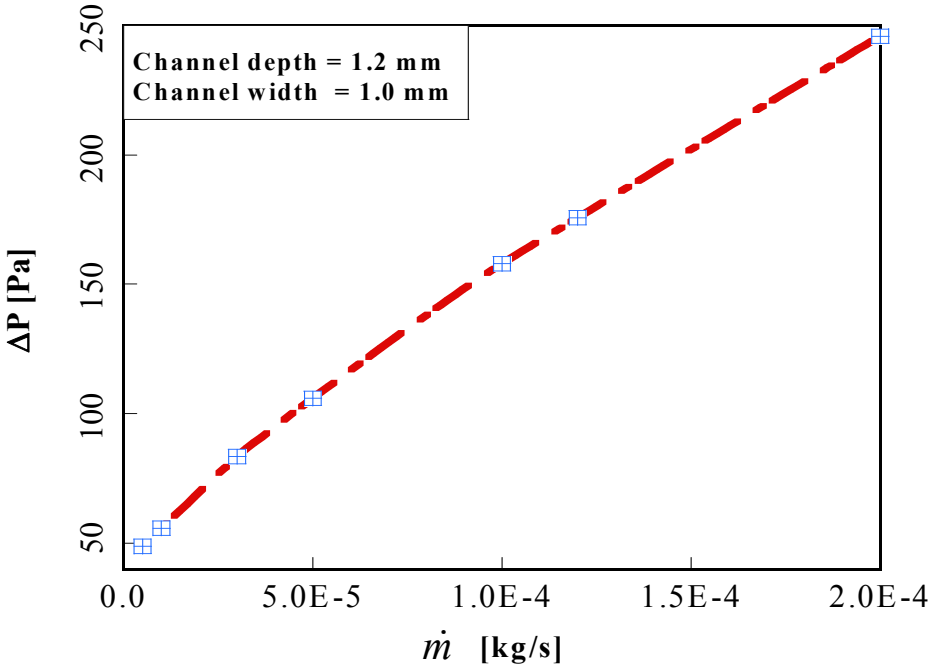

Figure 4.5 Pressure drop along the model flow channel at base operating conditions for a channel depth of 2.0 mm and width of 1.2 mm

4.3.2 EFFECT OF PHYSICAL PARAMETERS ON PROTON EXCHANGE MEMBRANE FUEL CELL PERFORMANCE

Figure 4.6 illustrates the polarisation curves obtained from the model (cell voltage 0.3 V) at several operating temperatures from 60-90^{o}C at stoichiometry ratios of 1.2 and 2.0, respectively, for the anode and the cathode. The curve indicates that the fuel cell performance increases with an increase in temperature and is at the optimum at temperatures of approximately 60-80^{o}C. This is consistent with literature [179, 195]. The increase in fuel cell performance with the increase in temperature can be attributed to an increase in gas diffusivity and membrane conductivity at higher operating temperatures.

The polarisation curves are also lower at 75-80 ^{o}C compared with 60-70 ^{o}C in the lower current density region, primarily due to the lower reaction rates resulting in low water content in the membrane. The condensation of water easily occurs at lower

temperatures resulting in the flooding and deterioration of the gas diffusivity in the catalyst layer and the GDLs. At temperatures beyond 80°C, the cell performance declines, since membrane conductivity decreases at high temperatures due to the onset of reduction in relative humidity of reactant gases and water content in the membrane.

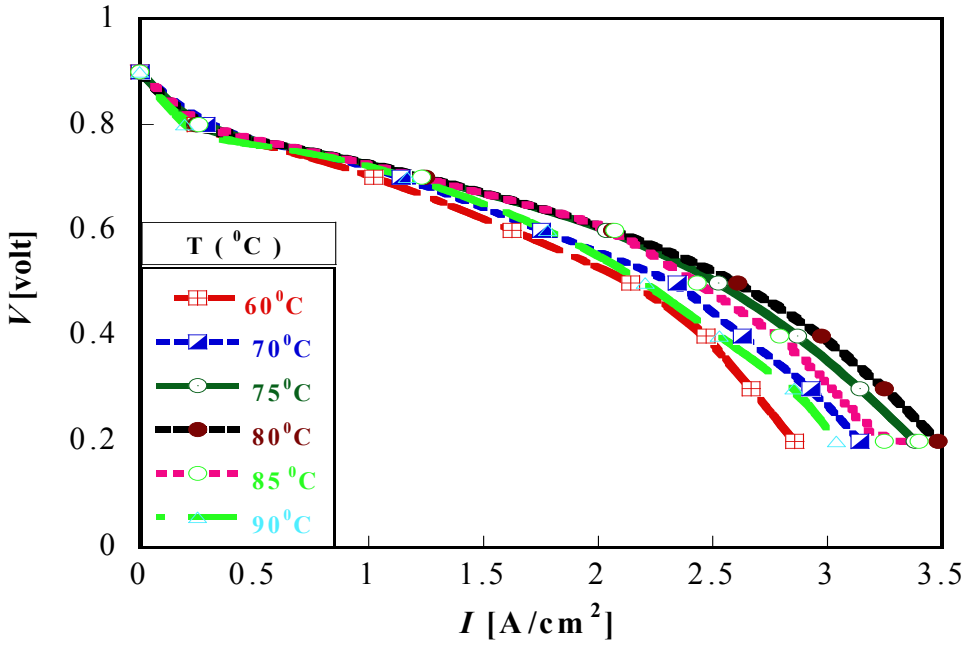

Figure 4.6 Effect of temperature on cell performance at base conditions

Hence, the fuel cell performance is adversely affected at temperatures between 80 and 90°C. Increasing the cell temperature beyond 80°C, results in higher levels of water loss in the cell until a critical temperature is attained where the evaporated water is greater than the amount of water being generated in the cell, thereby resulting in a total dry-out of the membrane. This could eventually lead to fuel cell failure. This model ascertains the fact that these fuel cells need to be operated at temperatures below 80°C. A humidifier may be required if operation at higher temperatures is required but this adds to the capital and running costs of fuel cells.

Figure 4.7 shows the effect of changing the oxygen mass flow rate from 5.0E-06 to 1.6E-04 kg/s on the fuel cell performance. When the cathode gas mass flow rate is increased, the fuel cell performance is enhanced, especially at lower operating fuel

cell voltages. The reason is the increase in oxygen gas through the GDL to the reaction sites, which increases the rate of reaction. At low operating voltages, more liquid water is produced, due to stronger electrochemical reaction rates, which is expected to reduce fuel cell performance.

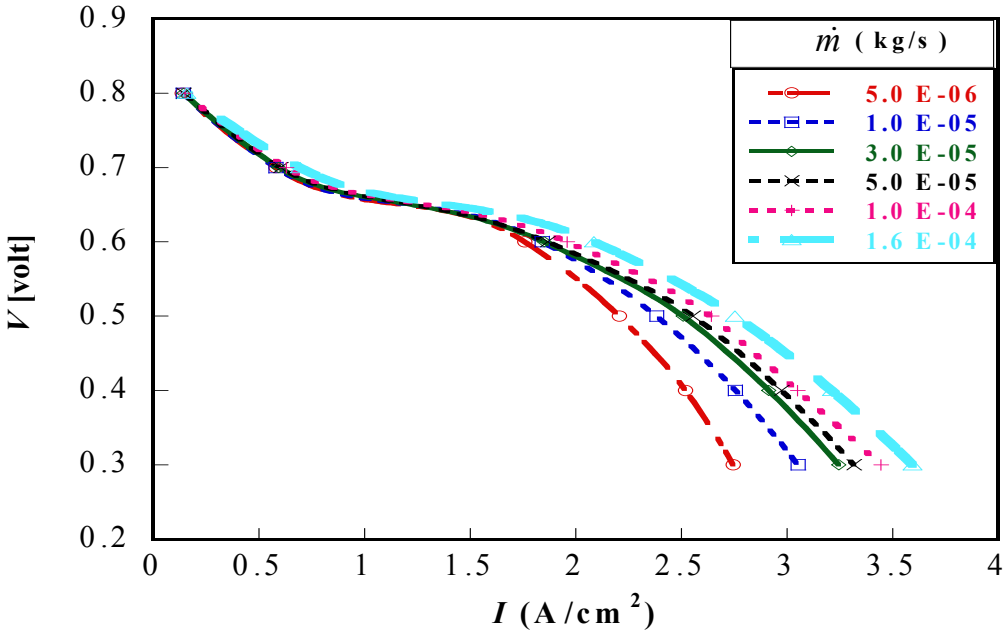

Figure 4.7 Effect of cathode gas flow rate on cell performance at base conditions

However, the high oxygen mass flow rates in the porous layer generate high shear forces, which aid the transport of liquid water downstream in the flow channel along the flow direction. The effect is minimal at high operating voltages as observed on the curves, primarily due to low membrane humidification. Wang and Liu [196] obtained similar results in their experimental work on PEM fuel cell performance. This is because a low amount of water presence occurs at these voltage levels, due to slow reaction rates coupled with an increase in the oxygen gas supply which results in reduced cell performance.

The effect of the GDL porosity on the performance of the PEM fuel cell is shown in Figure 4.8. The results show the fact that the effect of the GDL porosity on fuel cell performance is significant when the GDL is in the low value region (0.1-0.4).

Increasing the diffusion layer porosity size has an increasingly weaker effect on the performance. A GDL porosity beyond 0.6 does not have a significant effect on the fuel cell polarisation curve. This observation is in agreement with the optimisation work of Lin *et al.* [195]. They reported an optimum GDL porosity of 0.5913 for the PEM fuel cell modelled in their study. Therefore, maintaining a porosity level between 0.4 and 0.6 is a reasonable value for the fuel cell if durability issues in the fuel cell structure are taken into consideration.

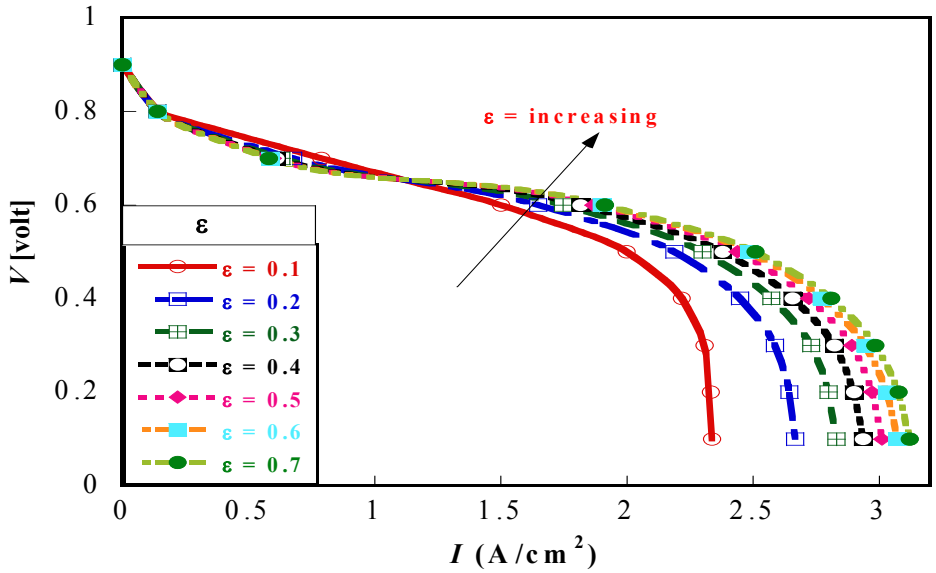

Figure 4.8 Effect of gas diffusion layer porosity on cell performance at base conditions

Fuel cell performance is also largely influenced by the operating pressure. In this study, the fuel cell operating pressure varied from 1-5 atm at a constant operating temperature of 70^{o}C. The polarisation curves for different operating pressures are shown in Figure 4.9. As the operating pressure increased from 1-5 atm, the fuel cell performance also improved. There was a significant increase in the fuel cell performance from 1-3 atm, however, after 3 atm the increase was minimal. Increasing pressure improves the reactant's interaction with the electrolyte, hence increasing fuel cell performance. The pressure impact on the fuel cell performance is prominent at a higher current density of operation. Generally, the polarisation curve shifts position positively as the pressure increases.

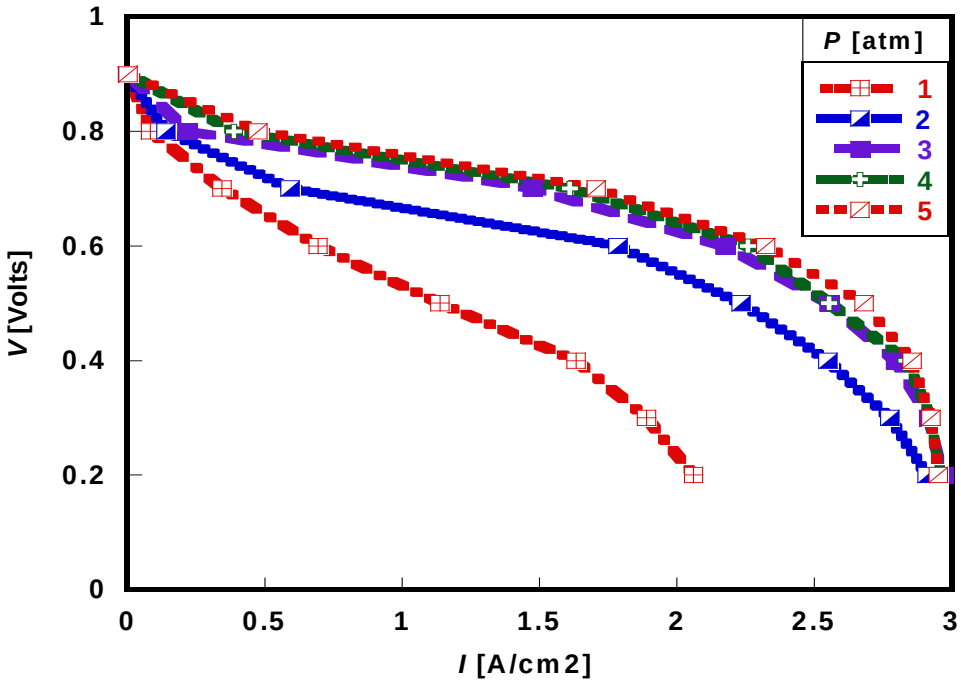

Figure 4.9 Effect of operating pressure on cell performance at base conditions

Figure 4.10 shows the effect of changing the cathode gas stoichiometry ratio on the fuel cell performance. The temperature, pressure and porosity were maintained at constant values of 70^{o}C, 2 atm and 0.4, respectively. Very small changes in the overall cell performance are observed at an increased cathode gas stoichiometry, especially at higher operating current densities. Performance at low stoichiometries

(<3.0) shows a reduced fuel cell performance and at higher levels (>3.5) the increment becomes insignificant. This increase in performance is due to the increment in oxygen availability and the humidity of the membrane. At low cathode gas stoichiometry, there are limitations of oxygen availability towards the end of the flow channel and, furthermore, the water removal rate is reduced leading to a reduction in performance. Operating a fuel cell at lower voltages increases electrical resistance within the cell that also hinders an increase in performance. However, performance could be augmented by increasing the stoichiometry rate at these operating voltages.

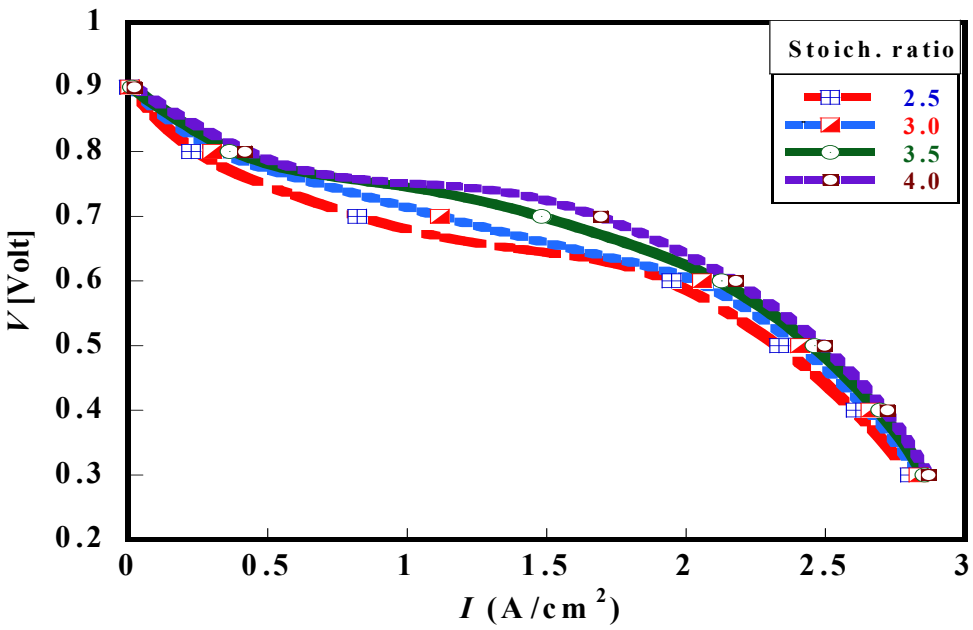

Figure 4.10 Effect of cathode gas stoichiometry on cell performance at base conditions

4.3.3 EFFECT OF DESIGN PARAMETERS ON PROTON EXCHANGE MEMBRANE FUEL CELL PERFORMANCE

Simulations were performed for different sets of channel dimensions. Two different parameters, i.e., channel width and channel depth, were chosen for the study. Figure 4.11 illustrates the effect of channel depth on the fuel cell performance at a constant channel length. The optimal current density for the fuel cell was obtained at a channel depth of 2.0 mm (current density: 2.62 A/cm^2). A further increase in depth showed a decline in fuel cell performance.

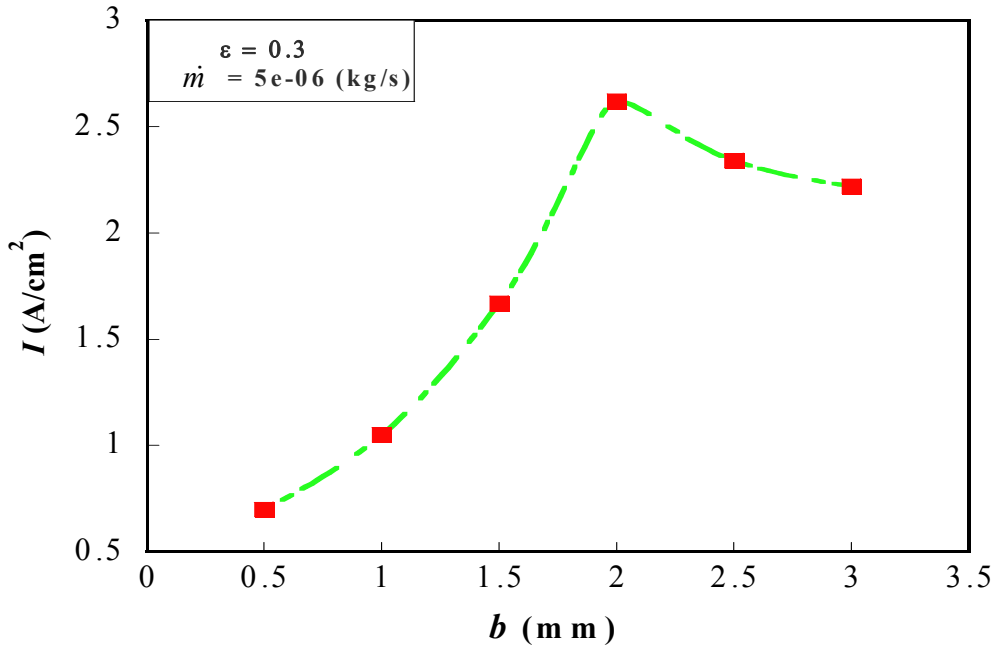

Figure 4.11 The cell current density at different channel depths at a cell potential of 0.3 V, a temperature of 70 °C and a mass flow rate of 5e-06 kg/s

Figure 4.12 shows the fuel cell performance for the six cases of channel widths considered. Performance increased gradually from case 1 (0.6 mm – current density: 1.30 A/cm^2) until an optimum was obtained at case 4 (1.2 mm – current density: 2.45 A/cm^2).

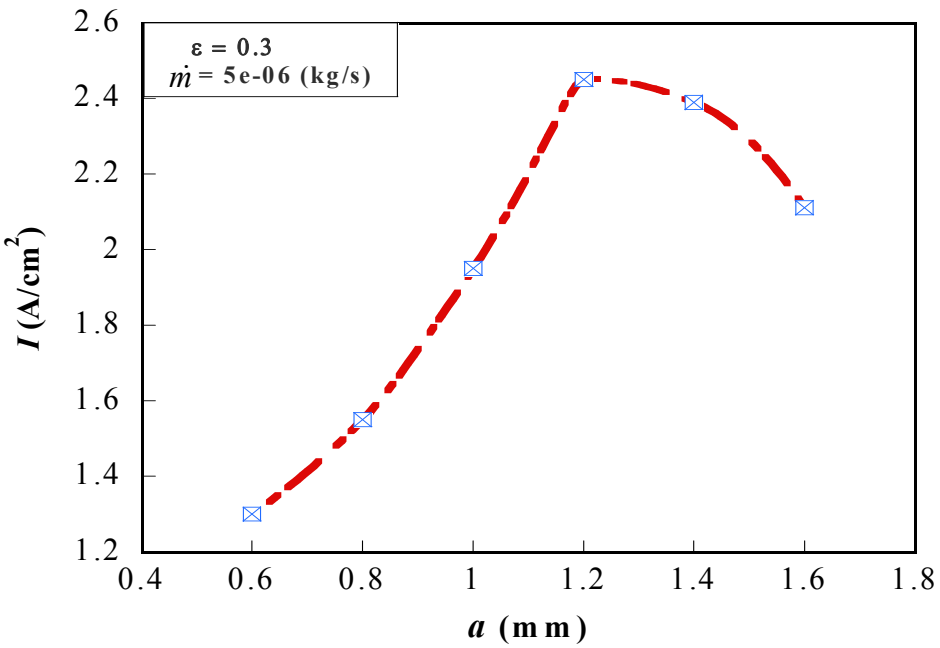

Figure 4.12 The cell current density at different channel widths at a cell potential of 0.3 V and a temperature of 70 ºC

Increasing the channel width beyond 1.2 mm showed a reduction in fuel cell performance. These results were consistent with those observed by other researchers. Watkins *et al.* [197] studied optimal dimension for cathode-side channels. They claimed that the most preferred ranges are 1.02-2.04 mm for channel depths and 1.14-1.4 mm for channel widths. Figures 4.11 and 4.12 suggest the existence of an optimal channel depth and width for the PEM fuel cell that will offer the best system performance.

The effect of species flow orientation on the performance of the fuel cell was investigated for the base case. It was found that the direction of flow affects the performance of the fuel cell. Co-flow and counterflow affect the fuel cell performance at different operating cell voltages. Figure 4.13 depicts the fuel cell performance at the base case conditions and, for a channel depth and width of 2.0 mm and 1.2 mm, respectively, the counterflow and the co-flow orientations. Current densities of 2.61 A/cm^2 and 2.54 A/cm^2 were obtained for the counterflow and co-flow cases,

respectively. Counterflow creates better performance for the fuel cell, especially at higher current voltages.

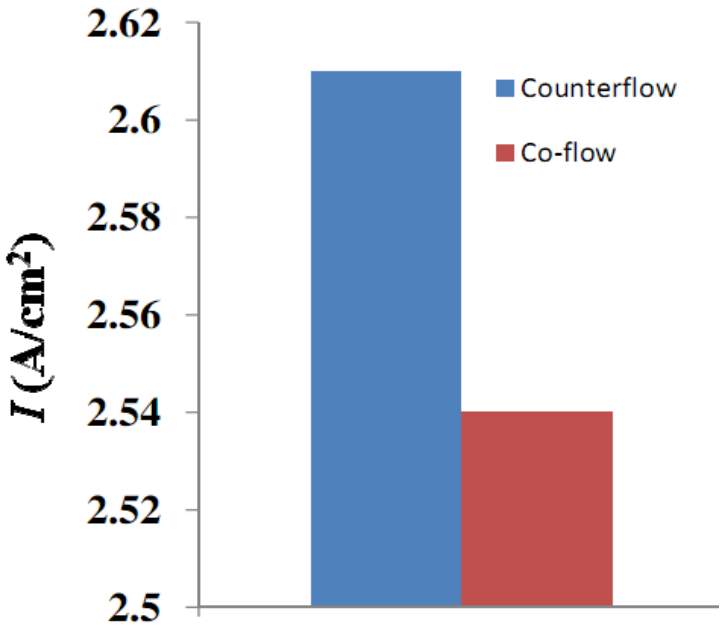

Figure 4.13 The cell current density for counterflow orientation (2.61 A/cm^2) and co-flow orientation (2.54 A/cm^2) at base case conditions, for a channel depth of 2.0 mm and a channel width of 1.2 mm

Figure 4.14 shows the contours of mass fraction for hydrogen at the anode flow channel for counterflow (Figure 4.14a) and co-flow cases (Figure 4.14b), respectively. The contour shows that counterflow configuration allows more uniform distribution of the hydrogen species at the anode flow channel, which subsequently improves the performance of the fuel cell. The effective species distribution generally aids reaction on the membrane sites and this leads to increased current density.

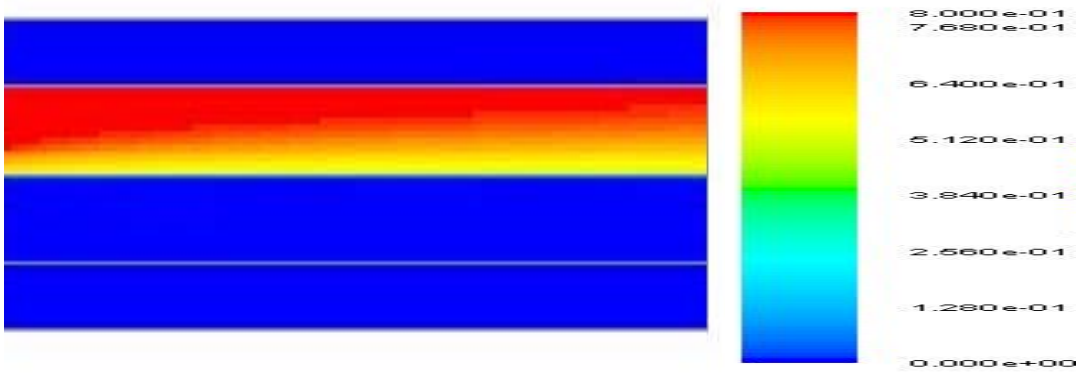

(a.) Counter flow

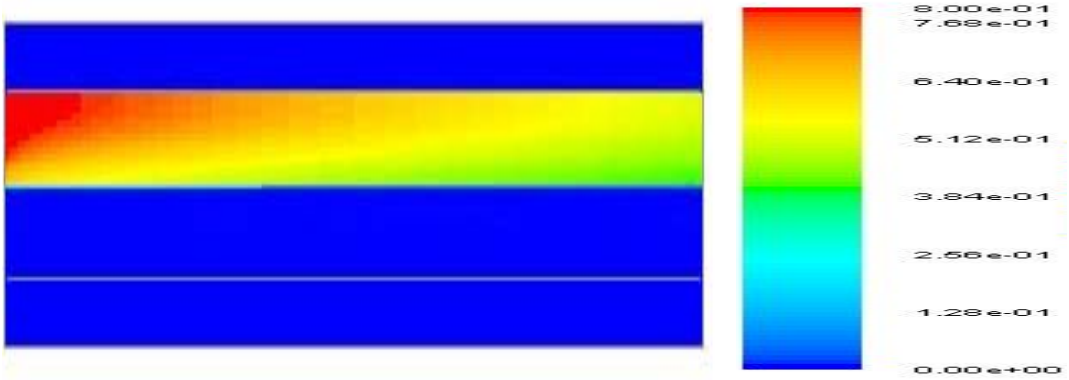

(b.) Co-flow

Figure 4.14 Contours of mass fraction of hydrogen at the anode for (a.) counterflow and (b.) co-flow cases at the base case operating conditions

4.3.4 OPTIMAL CHANNEL GEOMETRY

The results in Section 4.3.3 (Figures 4.11 and 4.12) depict the existence of an optimal channel depth and width for a PEM fuel cell system. The search for an optimal channel depth and width was carried out for the PEM fuel channel at varying GDL porosities. The first run of the simulation was carried out by fixing the cathode gas flow rate at 5e-06 kg/s, width of channel at 1.2 mm, cell operating voltage at 0.3 V and GDL porosity at 0.2. The channel depth was then varied between

0.5 and 3.0 mm. An optimal channel depth, b_{opt} , was found for this configuration. The procedure was repeated for other values of GDL porosities in the range of $0.2 \leq \varepsilon \leq 0.6$ as shown in Figure 4.15, until an optimal channel depth, which corresponds with the maximum current density, was obtained at each value of the GDL porosity.

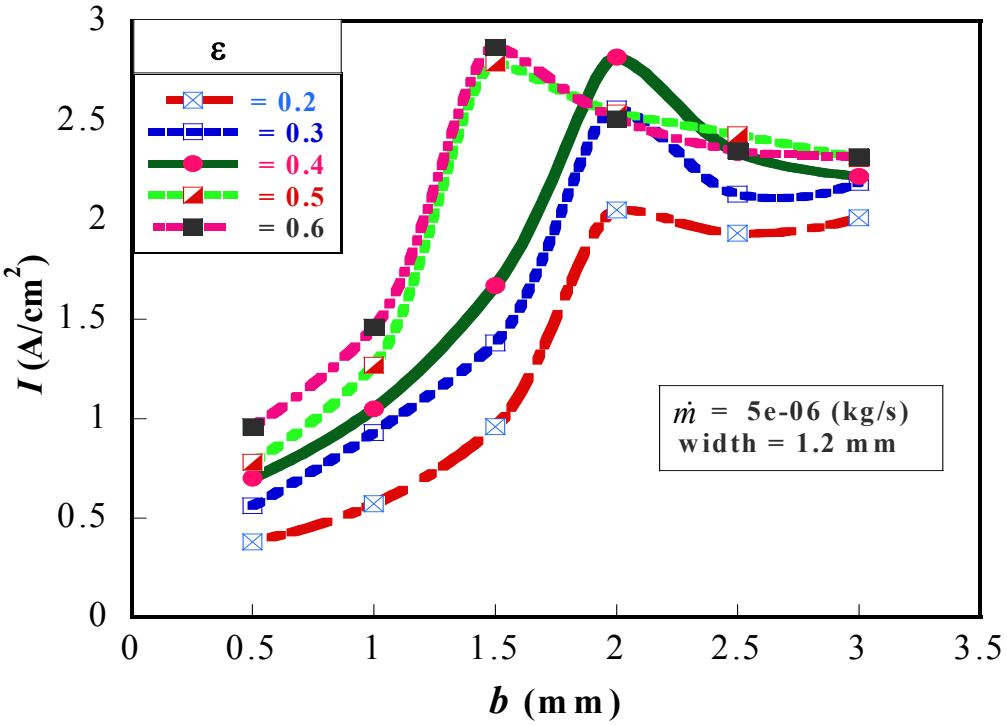

Figure 4.15 Effect of porosity and channel depth on the cell current density

Figure 4.16 gives the optimum channel depth, b_{opt}, for different cathode gas mass flow rates for different gas diffusion layer porosities. The optimal channel depth decreases as the mass flow rate increases.

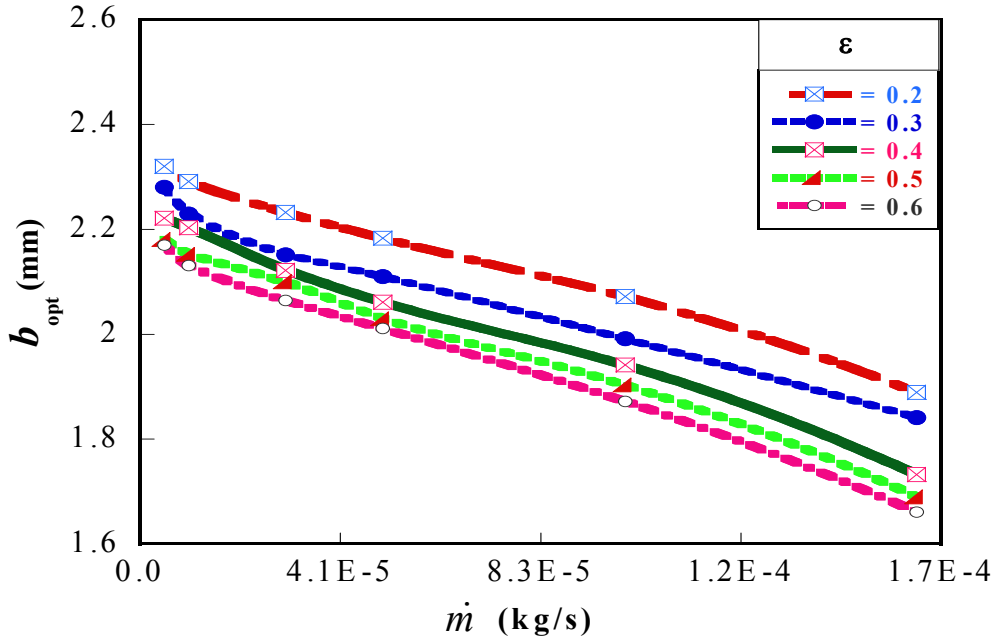

Figure 4.16 Optimum depths as a function of flow rate and gas diffusion layer porosity

Figure 4.17 shows the behaviour of the maximum current density, I_{max}, with varying cathode gas mass flow rates. Each point of the figure depicts the result of a full optimisation with respect to channel depth. The graph shows that maximised current density increases as the mass flow rate of the reactant gas increases. In each case, there is an optimal channel depth that maximises the current density of the fuel cell. Similarly, the search for optimal channel widths, a_{opt}, corresponding to the maximum current density, I_{max}, was carried out as conducted for the channel depths. Figure 4.18 shows the current density value as a function of the channel widths for different values of GDL porosities. The cathode gas mass flow rate and channel depth were initially fixed at 5e-06 kg/s and 2.0 mm, respectively.

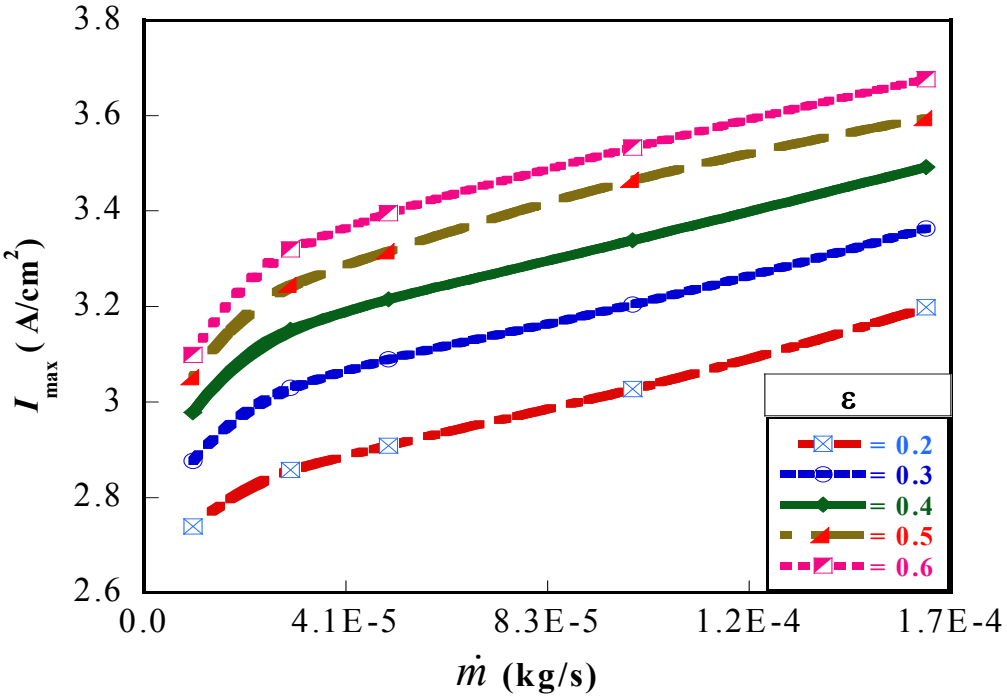

Figure 4.17 Effect of flow rate and gas diffusion layer porosity on the cell current density

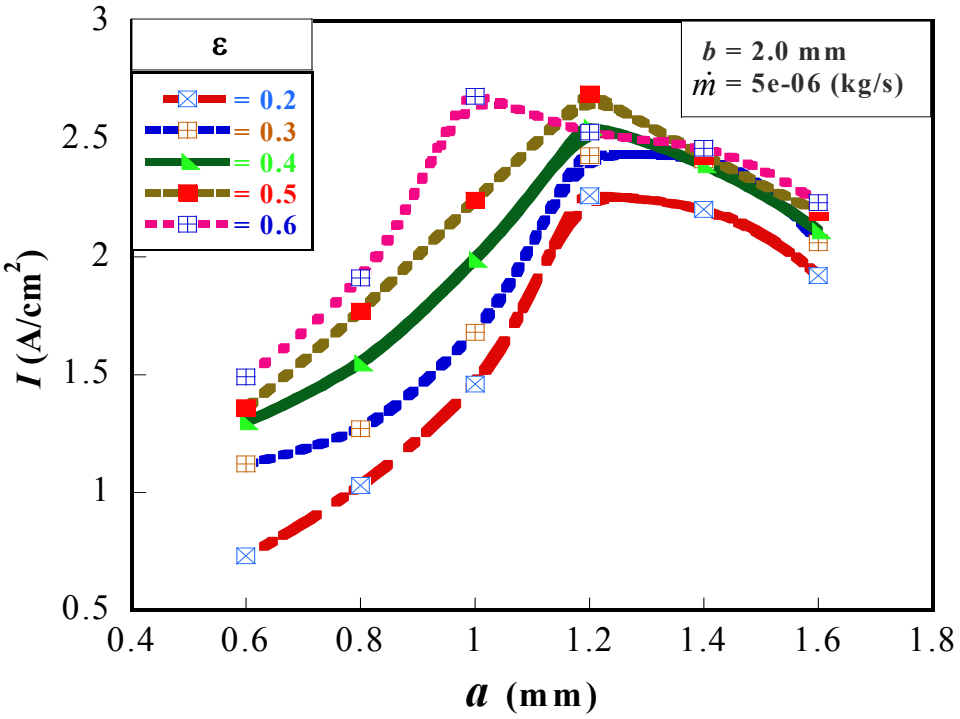

Figure 4.18 Effect of porosity and channel width on the cell current density

Figure 4.19 depicts the optimal value of the channel width as a function of the cathode gas mass flow rate for each of the values of GDL porosities ($0.2 \leq \varepsilon \leq 0.6$). The optimal channel widths, a_{opt}, from the figure decreases as the mass flow rate increases. The results obtained from Figures 4.16 and 4.19 both suggest that optimal channel depth and width decrease at increasing cathode gas mass flow rates. In designing PEM fuel cells, it can be concluded that the matching of fuel cell operating conditions and gas fuel channel configuration is very important for optimum operation issues.

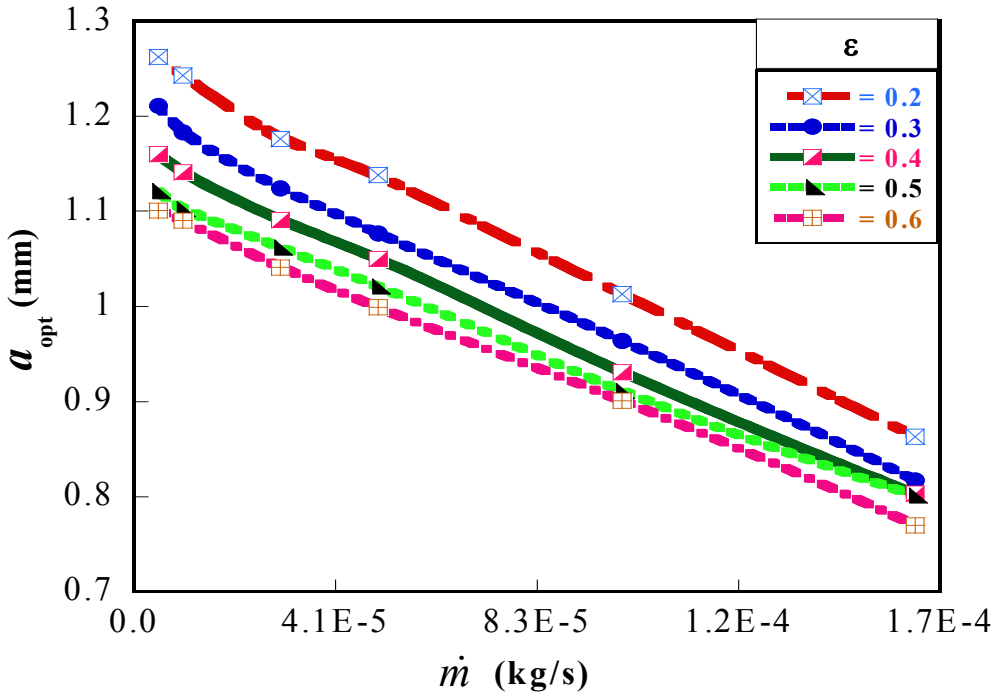

Figure 4.19 Optimum widths as a function of flow rate and gas diffusion layer porosity

CONCLUSION

In this chapter, a steady-state three-dimensional computational model was established to study the performance of a single-channel PEMFC under varying operating conditions. The model prediction was validated by its good agreement with available

experimental results. The numerical results provided detailed information on the effect of varying operating parameters of a single-channel fuel cell performance. It was proved that temperature, GDL porosity, cathode gas mass flow rate and species flow orientation affect the performance of the fuel cell. Specifically, we show that fuel cell performance increases with an increase in temperature from 60-80^{o}C. Further increases in temperature, beyond 80°C, shows a decline in fuel cell performance. The porosity of the GDL also affects the fuel cell performance. The porosity effects on fuel cell performance are more significant at porosity levels of 0.1-0.4 than at porosity levels of 0.5-0.7. The effect of the operating and design parameters on PEM fuel cell performance is also more dominant at low operating cell voltages than at higher operating fuel cell voltages. In addition, this study establishes the need to match the PEM fuel cell parameters such as porosity, species reactant mass flow rates and fuel gas channels geometry in the system design for maximum power output.

5

CHAPTER 5: OPTIMISING REACTANT GAS TRANSPORT IN A PROTON EXCHANGE MEMBRANE FUEL CELL WITH A PIN FIN INSERT IN CHANNEL FLOW

5.1 INTRODUCTION

The flow distribution in a fuel cell bipolar plate is one of the most important enhancing factors of PEM fuel cell systems. One of the critical issues in PEM fuel cell design is the efficient design of the flow channels to ensure uniform distribution of the reactant gases in the fuel cell stack. The flow field geometry and pattern have great influence on the reactant gas transport, water management and the efficient utilisation of the fuel. The flow field design of fuel cells is one of the critical technical challenges for PEM fuel cell designs and operation and impacts on the performance and the life-span of the system [65, 198].

Several studies have been carried out in recent years to improve fuel cell performance through flow-field design such as parallel, serpentine, interdigitated and many other novel combinations of these conventional types [30, 94, 69, 185, 199]. The serpentine channel type is the most widely used among the studied flow channels due to its outstanding performance when compared with others under the same operating and design conditions [197]. However, a serpentine flow field has its associated problems and is not an ideal flow field configuration. Some of the associated problems are:

- high reactant pressure loss resulting in significant parasitic power requirement to pressurise air, especially at the cathode section [62];

- loss of reactant gas concentration along the channel from the inlet towards the outlet, and membrane dehydration near the channel inlet region;
- resultant liquid water flooding near the exit region of the channel, as a result of excessive liquid water carried downstream by the reactant gas stream and collected along the flow channel [117];

These serpentine flow channel characteristics proved their effectiveness in small cells ($\leq 560 \times 250 \times 330$ mm and power rating ≤ 1000 W) where the pressure drop is in the order of 0.5-1 bar. However, serpentine flow channels perform poor for larger cells ($> 560 \times 250 \times 330$ mm and power rating ≥ 1500 W) where the pressure drop is in the order of a few bars [56]. Hence, parallel flow channels have several applications, especially for larger cell applications, but the problems of cathode gas flow distribution and cell water management need to be solved.

In these channels, apart from issues related to maldistribution of reactant gases, water coalescence forms droplets of varying numbers and sizes in the channels. This subsequently forces the reactant gas to flow preferentially through the path of least obstruction [70]. Performance improvement for this type of channel and others have been documented in the literature, but there is little information in the open literature regarding the design procedure and cross-sectional dimensions that includes pressure drops for flow in the channels [62]. Performance improvement of PEM fuel cells can be achieved in many ways and researchers have developed varieties of flow-field layouts for this purpose.

An interdigitated flow-field design was first proposed by Nguyen [200] with the addition of baffles at the end of the channels. The design forces the reactants through the GDL and the generated shear forces help blow the trapped water into the inner layer of the electrodes resulting in better fuel cell performance. Kumar and Reddy [201] presented a three-dimensional steady-state numerical mass-transfer single-cell model for a PEM fuel cell, by using metal foam in the flow field of the bipolar/end

plates rather than using conventional rectangular channels. Their result showed a significant effect of the metal foam on the permeability of the reactant species, which improved the performance of the fuel cell. They proposed the use of metal foam instead of conventional rectangular channels, especially in thinner channels where there are manufacturing constraints.

Liu *et al.* [85] investigated the effect of baffle-blocked channels on the reactant transport and cell performance using a conventional parallel flow field. Their results showed improved cell performance due to an increasing reactant spread over the GDL which enhances chemical reactions. Soong *et al.* [86] developed a novel flow channel configuration by inserting baffles in the channel of conventional flow fields to form a partially blocked fuel channel. They discovered that enhanced fuel cell performance could be achieved by reducing the gap size and/or increasing the baffle number along the channel, though with the penalty of higher pressure loss.

Liu *et al.* [87] studied the reactant gas transport and cell performance of a PEM fuel cell with a tapered flow channel design. The results obtained from the study revealed that fuel cell performance can be enhanced with a tapered fuel channel and enhancement is more prominent at lower cell voltage. The reactant gas in the tapered channel is accelerated and forced into the GDL, thereby enhancing the electrochemical reaction that improves cell performance. Xu and Zhao [61] presented a new flow-field design, termed the convection-enhanced serpentine flow field (CESFF) for polymer electrolyte-based fuel cells. They observed that the CESFF design induces larger pressure differences between adjacent flow channels over the electrode surface when compared with the conventional flow field. This design characteristic increases the mass transport rates of reactants and products to and from the catalyst layer and reduces liquid water entrapped in the porous electrode which subsequently, enhances fuel cell performance.

Wang *et al.* [78] similarly studied the use of baffles in a serpentine flow field to improve cell performance. The results showed that the novel baffle serpentine flow field, even though it induces larger pressure differences between adjacent flow channels over the entire electrode surface than the conventional serpentine design does; helps gas diffusion which leads to enhanced current density and improved cell performance.

These investigations have shown that the addition of bluff bodies (baffles) in the flow channels can increase the convection of reactants through the GDL thereby enhancing fuel cell performance. This enhanced performance and operating stability in fuel cells are achieved through improved reactant mass transport. Meanwhile, a proper understanding of the phenomenon of mass transfer through the GDL, under the influence of disturbances along the flow channels and associated pressure drop, will facilitate a proper design of PEM fuel cells.

From the literature survey above, it is clear that issues of high penalty in terms of pressure loss due to high flow resistance occur in most of the baffle-enhanced PEM flow-field designs and therefore need to be addressed. In addition, to the best knowledge of the authors, the application of pin fins for performance enhancement in PEM fuel cells has not been examined before, especially for determining the optimal geometry of the employed pin fins in PEM flow channels. Therefore, one of the major objectives of this study is to investigate the effect of a pin fin insert in the flow field of a fuel cell with the aim of improving performance as well as pressure drop along the fuel cell flow channel. The cell overpotential at the anode side of the PEM fuel cell is negligible in comparison with the cathode-side overpotential [32], hence the choice of considering oxygen mass transport at the cathode side of the fuel cell system.

Extended surfaces (fins) are frequently used in heat exchanging devices for the purpose of increasing the heat transfer between the primary surface and the

surrounding fluid. Extended surfaces of various shapes have been employed for this purpose in heat and mass transfer studies, ranging from relatively simple shapes, such as rectangular, square, cylindrical, annular, tapered or pin fins, to a combination of different geometries. Literature shows that pin fins are some of the most widely employed extended surfaces considering its hydrodynamics along flow channels [202-204]. A pin fin is a cylinder or other shaped element attached perpendicularly to a wall, with the transfer fluid passing in cross-flow over the element. Pin fins with a height to diameter ratio between 0.5 and 4 are accepted as short fins, whereas long fins have a pin height to diameter ratio exceeding 4 [203]. The effective selection of the pin fin geometric parameters will result in the improvement of the reactant gas distribution in the flow channel due to the mixing of the main flow and/or the flow in the near-wall region and, subsequently, will permit effective reactant spread over the GDL.

In the present work, the main motive is to investigate the effect of pin fins transversely arranged along the flow channel on the reactant gas distribution, and pressure drop characteristics of the fuel cell reactant gas channel. Pin fins of small hydraulic diameter, which can reduce the additional pressure drop, are employed and the effect on PEM performance is investigated. In addition, a mathematical optimisation tool is used to select the best pin fin geometric configuration that improves the fuel cell performance at a reduced pumping power requirement penalty in the PEM fuel cell flow channel. This chapter presents a novel approach at enhancing the oxygen mass transfer through the PEM fuel cell GDL at a reduced pressure drop.

5.2 MODEL DESCRIPTION

In this chapter, a two-dimensional half-cell model of a PEM fuel cell system for the cathode-side fuel gas channel and the GDL is considered. Figure 5.1 shows a

schematic diagram of the two-dimensional half-cell model with two pin fins along the transverse section of the flow channel.

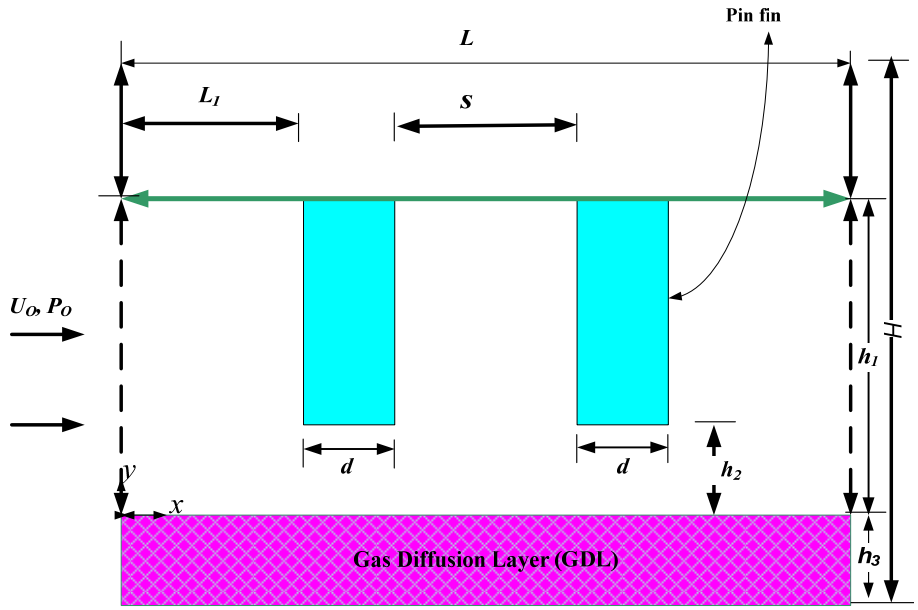

Figure 5.1 PEMFC half-cell model with two transverse pin fins along the flow channel

The fluid considered here is air at an inlet pressure, P_0, and velocity, U_0. The fin disturbance employed in this study protrudes from a rectangular base towards the GDL at a height to diameter ratio between 0.5 and 4. The parameters h_1, h_2 and h_3 (Figure 5.1) depict the flow channel height, tip clearance size and GDL thickness, respectively. The tip clearance size is characterised by defining a dimensionless parameter named, clearance ratio, $\lambda \equiv h_2/h_1$, for the study. The values of $\lambda = 0$ and 1 indicate fully blocked and block-free conditions, respectively, and the values in between are a measure of various levels of blockage [86]. Also defined, is another dimensionless parameter: the ratio of the distance between pin distances in the transverse direction to the fin thickness (pitch), $\zeta = s/d$. The effects of the tip clearance size, the pitch, the fuel flow Reynolds number (Re) and the porosity (ε) of

the GDL on the reactant gas transport, and the pressure drop across the channel are critically explored. The porosity, ε, of the porous medium is defined as the fraction of the total volume of the medium that is occupied by void space. In this study, parameters were varied in the following range: $0.2 \le \lambda \le 0.6$, $5.0 \le \zeta \le 10$, $50 \le Re \le 350$ and $0.2 \le \varepsilon \le 0.6$. Other parameters used for the modelled PEM fuel cell are shown in Table 5.1. The idea proposed in this chapter is aimed at improving the reactant species distribution over the catalyst layer in the fuel cells in order to increase the fuel cell performance at reduced pumping power requirement.

Table 5.1 Parameters of the modelled fuel cell

Channel length (mm)	120
Channel width (mm)	1.0
Channel depth (mm)	1.2
Membrane thickness (mm)	0.036
GDL thickness (mm)	0.21
Membrane porosity	0.5
Cell operating temperature (^{o}C)	70
Cell operating pressure (atm)	3
GDL permeability (m^2)	1.76×10^{-11}
Electric conductivity of GDL $(\Omega^{-1}m^{-1})$	300
Relative humidity	100%

5.2.1 GOVERNING EQUATIONS

The present chapter provides a two-dimensional solution for the half-cell model of a PEM fuel cell. The following assumptions are used in this study:

- the reactant gas (air) is an ideal gas, and the flow is incompressible steady and laminar;
- the GDL is from an isotropic porous material and uniform;

- the catalyst layer is treated as an ultra-thin layer (regarded as a boundary condition), hence the reactant gas is totally consumed in the reaction;
- the reaction is assumed to be fast, ensuring that the transport time scale is dominant when compared with the reaction time scale- this assumption allows treating the chemical reaction simply as a boundary condition at the catalyst layer; and
- the fuel cell operates at a constant temperature.

Based on these assumptions, the following governing equations for the gas channel and the GDL can be written as [147]:

In the gas channel section, the governing equations are:

$$\frac{\partial u}{\partial x}+\frac{\partial v}{\partial y}=0, \tag{5.1}$$

$$u\frac{\partial u}{\partial x}+v\frac{\partial u}{\partial y}=-\frac{1}{\rho}\frac{\partial P}{\partial x}+\nu\left(\frac{\partial^2 u}{\partial x^2}+\frac{\partial^2 u}{\partial y^2}\right), \tag{5.2}$$

$$u\frac{\partial v}{\partial x}+v\frac{\partial v}{\partial y}=-\frac{1}{\rho}\frac{\partial P}{\partial y}+\nu\left(\frac{\partial^2 v}{\partial x^2}+\frac{\partial^2 v}{\partial y^2}\right), \quad \text{and} \tag{5.3}$$

$$u\frac{\partial W_i}{\partial x}+v\frac{\partial W_i}{\partial y}=D_i\left(\frac{\partial^2 W_i}{\partial x^2}+\frac{\partial^2 W_i}{\partial y^2}\right), \tag{5.4}$$

where D_i and W_i depict the diffusivity and mass fraction of the species, respectively.

In the GDL section, the governing equations are:

$$\frac{\partial u}{\partial x}+\frac{\partial v}{\partial y}=0, \tag{5.5}$$

$$\varepsilon\left(u\frac{\partial u}{\partial x}+v\frac{\partial u}{\partial y}\right)=-\frac{\varepsilon}{\rho}\frac{\partial P}{\partial x}+\upsilon\varepsilon\left(\frac{\partial^2 u}{\partial x^2}+\frac{\partial^2 u}{\partial y^2}\right)-\frac{\upsilon\varepsilon^2}{k}u-\frac{\varepsilon^3 C_F\rho u}{\sqrt{k}}\sqrt{u^2+v^2}\ , \tag{5.6}$$

$$\varepsilon\left(u\frac{\partial v}{\partial x}+v\frac{\partial v}{\partial y}\right)=-\frac{\varepsilon}{\rho}\frac{\partial P}{\partial y}+\upsilon\varepsilon\left(\frac{\partial^2 v}{\partial x^2}+\frac{\partial^2 v}{\partial y^2}\right)-\frac{\upsilon\varepsilon^2}{k}v-\frac{\varepsilon^3 C_F\rho v}{\sqrt{k}}\sqrt{u^2+v^2} \tag{5.7}$$

and,

$$\varepsilon\left(u\frac{\partial W_i}{\partial x}+v\frac{\partial W_i}{\partial y}\right)=D_{i,eff}\left(\frac{\partial^2 W_i}{\partial x^2}+\frac{\partial^2 W_i}{\partial y^2}\right). \tag{5.8}$$

C_F in Eqs. (5.6) and (5.7) depicts the quadratic drag factor. The Blake-Kozeny correlation [86] is used for the relationship between the porosity and permeability, *k, of* the GDL:

$$k=\left(\frac{D_d^2}{150}\right)\left[\frac{\varepsilon^3}{(1-\varepsilon)^2}\right]\ , \tag{5.9}$$

where

$$D_d\equiv\frac{6V_d'}{S_d'}\ . \tag{5.10}$$

The last two terms in Eqs. (5.6) and (5.7) are drag force terms, added due to the presence of the porous wall, which might increase the pressure drop. The porous diffusion layer quantity is represented by the subscript *d* and V_d'/V_s' is a geometrical parameter which depicts the volume-to-surface ratio of the GDL [86]. In fuel cells, the fluid flow diffuses through the GDL for the reaction to take place on the MEA. The effective diffusivity $(D_{i,eff})$ for gas-phase flow in porous media can be written as:

$$D_{i,eff} = D\frac{\varepsilon}{\tau} \tag{5.11}$$

The porosity, ε, is the void volume fraction in the porous media. The tortuosity, τ, is a measure of the average path length of the species flow through the porous media compared to the linear path length in the direction of the species transport. The quantity (tortuosity) is usually estimated through experiment. Therefore, it is conventionally correlated in fuel cell studies using the Bruggeman correlation. This correlation assumes τ is proportional to $\varepsilon^{-0.5}$, resulting in the simpler expression [191]:

$$D_{i,eff} = D\varepsilon^{1.5}. \tag{5.12}$$

The porosity correlation is used to account for geometric constraints of the porous media.

The Reynolds number was defined as [205]:

$$\mathrm{Re} = \dot{m}D_{ch}/(\mu A_{ch}). \tag{5.13}$$

For hydraulic performance in the channel, an apparent friction factor, f, was evaluated by using the following equation [205]:

$$f = (\Delta P / L)D_{ch}/(\rho w^2/2), \tag{5.14}$$

where

$$w = \dot{m}/(\rho A_{ch}). \tag{5.15}$$

The channel flow resistance, $(\Delta P/\dot{m})$, is defined as [206]:

$$R_f = 2Po\nu L/D_{ch}^2 A_{ch}, \tag{5.16}$$

where Po is the Poiseuille constant.

The pumping power is evaluated by using the relation:

$$P_{pump} = \int_0^L \left[\frac{dp(x)}{dx} Q(x) \right] dx . \tag{5.17}$$

The water formation and transport of liquid water are modelled using a saturation model based on [72, 187]. In this approach, the liquid water formation and transport are governed by the conservation equation for the volume fraction of liquid water, s_w, or the water saturation [163]:

$$\frac{\partial(\varepsilon \rho_l s_w)}{\partial t} + \nabla \cdot (\rho_l \vec{V}_l s) = r_w, \tag{5.18}$$

where subscript l represents liquid water, and r_w is the condensation rate modelled as:

$$r_w = c_r \max\left(\left[(1 - s_w) \frac{P_{wv} - P_{sat}}{RT} M_{w,H_2O} \right], [-s_w \rho_l] \right) , \tag{5.19}$$

where r_w is added to the water vapour equation. The condensation rate is constant at $c_r = 100 s^{-1}$.

The clogging of the porous media and the flooding of the reaction surface are modelled by multiplying the porosity and the active surface area by $(1 - s_w)$, respectively.

5.2.2 NUMERICAL PROCEDURE

The model equations were solved using a finite-volume computational fluid dynamics code Fluent [163] with Gambit® (2.4.6) as a pre-processor. The CFD code has an add-on package for fuel cells, which has the requirements for the source terms for species transport equations, heat sources and liquid water formations. The domain was discretised using a second-order discretisation scheme. The pressure-velocity coupling was performed with the SIMPLE algorithm [192] for convection-diffusion analysis. Numerical convergence was obtained at each test condition when the ratio of the residual source (mass, momentum and species) to the maximum flux across a control surface was less than 10^{-6}.

Uniform isothermal free stream and fully developed fluid (air) with constant properties were assumed at the inlet and flows were fully developed at the outlet of the channel. At the interface between the gas channel and the GDL layer interface, the same velocity, the same concentration and the same gradients were imposed. No-slip no-penetration boundary conditions were enforced on the pin fins and wall surfaces.

The domain was divided into hexahedral volume elements. A grid independence test was carried out to ensure that solutions were independent of the dimensions of the chosen grid, with consideration of both accuracy and economics. For this purpose, four grid systems at 37 × 27, 82 × 27, 120 × 60 and 150 × 80 were tested. For the case of Re = 350, $\lambda = 0.6$, $\zeta = 7.0$ and $\varepsilon = 0.5$, the maximum relative deviation for the skin friction between the 120 × 60 grid and the 150 × 80 grid was less than 3%. It was considered that the system of 120 × 60 was sufficient for the study as a trade-off between accuracy and cost of time. A typical grid network for the computational domain is shown in Figure 5.2. The model and solution were implemented using an Intel® Core(TM) 2Duo 3.00 GHz PC with 3.24 GB of DDRam.

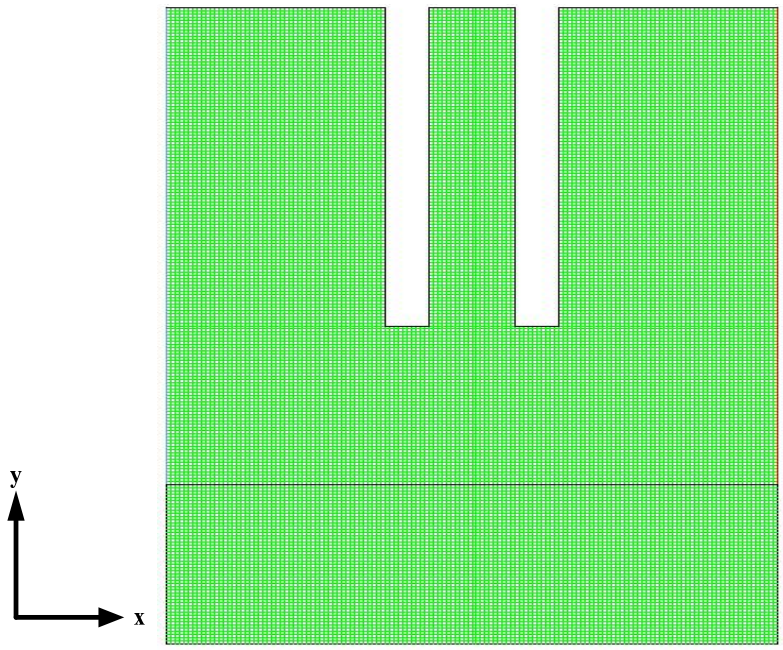

Figure 5.2 The representative grid system and computational domain

5.3 MATHEMATICAL OPTIMISATION ALGORITHM

The Dynamic-Q optimisation algorithm [166] previously discussed in Chapter 3 was used in this study. The algorithm is a robust multidimensional gradient-based optimisation algorithm which does not require an explicit line search and it is ideally robust for cases where the function evaluations are computationally expensive. The algorithm applies the dynamic trajectory LFOPC which is adapted to handle constrained problems through approximate penalty function formulation [166]. This dynamic approach is applied to successive quadratic approximations of the actual optimisation problem. The successive sub-problems are formed at successive design points by constructing spherically quadratic approximations, which are used to approximate the objective functions or constraints (or both) if they are not analytically given or very expensive to compute numerically [169, 207]. The use of spherically quadratic approximation in the Dynamic-Q algorithm offers a competitive advantage when compared with other algorithms in terms of computational and storage

requirements [169]. The storage savings become highly significant when the numbers of variables becomes large. Therefore, this particular strength of the Dynamic-Q method makes it well suited for optimisation of engineering problems with large numbers of variables and it has been used to successfully solve a large variety of engineering problems [207-213].

5.4 OPTIMISATION PROBLEM FORMULATION

The optimisation problem was tailored towards finding the best pin fin geometric parameters, which would give the maximum reactant species diffusion to the GDL of the fuel cell for a fixed Reynolds number, GDL thickness and GDL porosity at a reduced channel flow resistance, contributing to the increase in pressure drop along the channel. The apparent pressure drops increase the pumping power requirement for operating a fuel cell system. The design variables which greatly affect the hydrodynamic performance of pin fins are the geometric parameters s, d, h_2 and h_1 as depicted in the half-cell model shown in Figure 5.1.

The objective function for the optimisation can be written mathematically as,

$$I_{\max} = f(\lambda_{opt}, \varsigma_{opt}, \varepsilon_{opt}, Re_{opt}) \tag{5.20}$$

where $I_{\max}$ is the maximized current density output for the optimised design variables.

5.4.1 OPTIMISATION CONSTRAINTS

The optimisation problem was carried out subject to the following constraints:

5.4.1.1 *Total pin fin area constraint*

In pin fin application, the weight and material cost of pin fins are limiting factors. Hence, the total area of pin fins is fixed to a constant value:

$\therefore \sum A^c{}_j =$ Constant

$$\sum \pi D_j H_j = C \tag{5.21}$$

and

$$\sum D_j H_j = \frac{C}{\pi} \tag{5.22}$$

where $j = 1, 2$ and A^c is the pin fin area.

5.4.1.2 *The tip clearance size*

The tip clearance size, λ, is the ratio of the gap size between the pin fin tip and the GDL to the channel height. This was varied between 0.2 and 0.6:

$$0.2 \leq \left[\lambda = \frac{h_2}{h_1} \right] \leq 0.6. \tag{5.23}$$

5.4.1.3 *The pitch*

The pitch is the ratio of the distance between successive pin fins to the pin fin diameter. This was allowed to vary between 5 and 10:

$$5 \leq [\zeta = s/d] \leq 10\,. \tag{5.24}$$

5.4.1.4 *Manufacturing constraint*

The solid area fraction, φ, which is defined as the ratio of the pin fin material to the total area of the fuel cell channel was allowed to vary between 0.5 and 4. This is based on manufacturing and size constraints [214, 215]:

$$0.5 \le \left[\varphi = \frac{h_1 - h_2}{d} \right] \le 4. \tag{5.25}$$

Also, the interfin spacing is limited to 50 microns based on pin fin fabrication techniques [216, 217]:

$$s \ge 50\ \mu m. \tag{5.26}$$

5.4.2 OPTIMISATON PROCEDURE

The optimisation problem defined in Section 4.1 was solved by coupling the Dynamic-Q optimisation algorithm with CFD code FLUENT [163] and grid generation (GAMBIT [164]) code in a MATLAB [218] environment. Figure 5.3 depicts a flow diagram of how the automation was carried out until convergence (either by step size or function value criteria) was attained. To ensure that the converged solution obtained was indeed the global minimum, a multi-starting guess approach was employed.

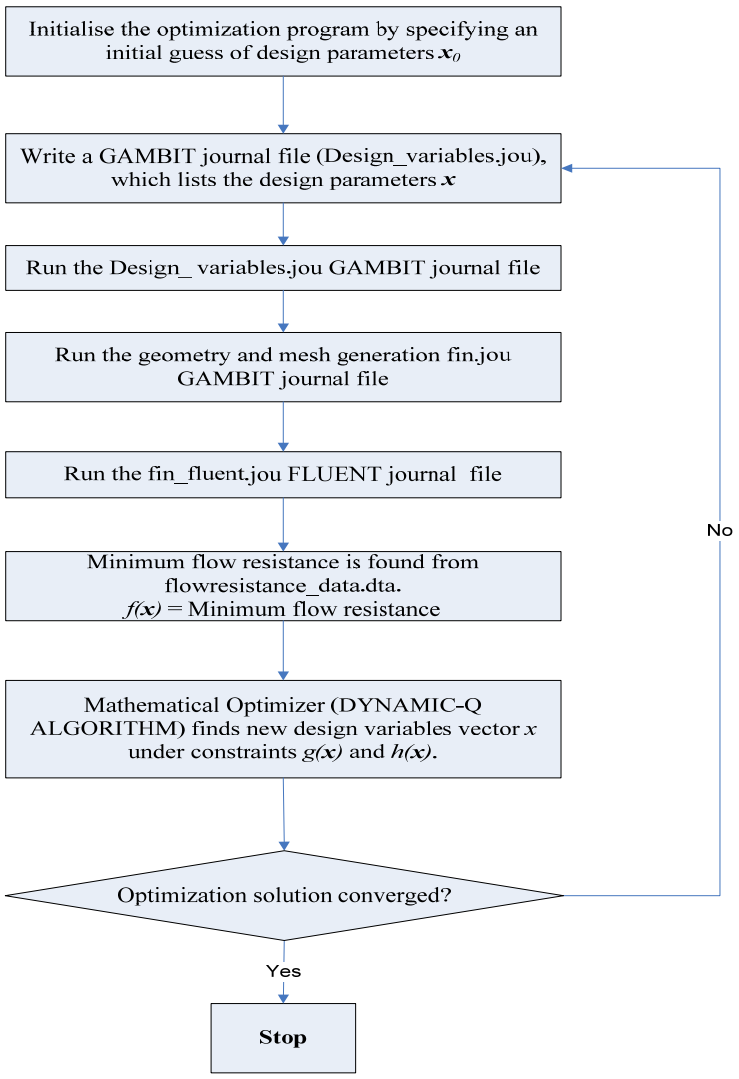

Figure 5.3 Optimisation automation flow diagram

5.5 RESULTS AND DISCUSSION

5.5.1 RESULTS OF FLOW FIELD

The pin fins employed in this work are expected to induce high levels of mixing of the main flow and/or the flow in the near-wall region and, subsequently, to improve the convection of reactant gas through the GDL. The power output in the fuel cell system is the consequence of the electrochemical reaction. Subsequently, the consumption of oxygen through diffusion into the catalyst membrane region is an index of the cell performance [78]. Higher oxygen mass flow rates through the GDL to the catalyst layer result in better fuel cell performance, since this reaction gas is more available to participate in the electrochemical reaction per unit of time. A qualitative description of the flow velocity pattern around the pin fin and within the GDL is presented in Figures 5.4-5.6 to illustrate the hydrodynamic phenomenon in the computational domain.

Figure 5.4 shows the Reynolds number influence on the flow pattern for the case of *s/d* = 5, and $\lambda = 0.2$ at a fixed GDL porosity of 0.5. The Reynolds number has a significant effect on the flow field and the diffusion of the reactant gas through the GDL medium. The rate of diffusion increases as the Reynolds number increases, thereby improving the reaction rate in the fuel cell system. The wake-shedding generated by the front pin fin interacts with the pin fin immediately behind it along the channel, which affects the flow-field characteristics. At a low Reynolds number of 50 (Figure 5.4a), there is flow attachment between the front pin and the back pin tips. This flow attachment also occurs at a Reynolds number of 150 (Figure 5.4b), but for a Reynolds number of 250 (Figure 5.4c), a flow separation occurs at the tip between the front pin and the back pin.

This increased Reynolds number creates the phenomenon of increasing the wake generation and the diffusion pattern into the GDL of the cell. The angle of separation of flow depends on the Reynolds number and the level of clearance ratio. As the clearance ratio increases, the location of the boundary layer separation moves forward. This movement is practically due to the change in the velocity distribution inside the boundary layer formed on the pin fins.

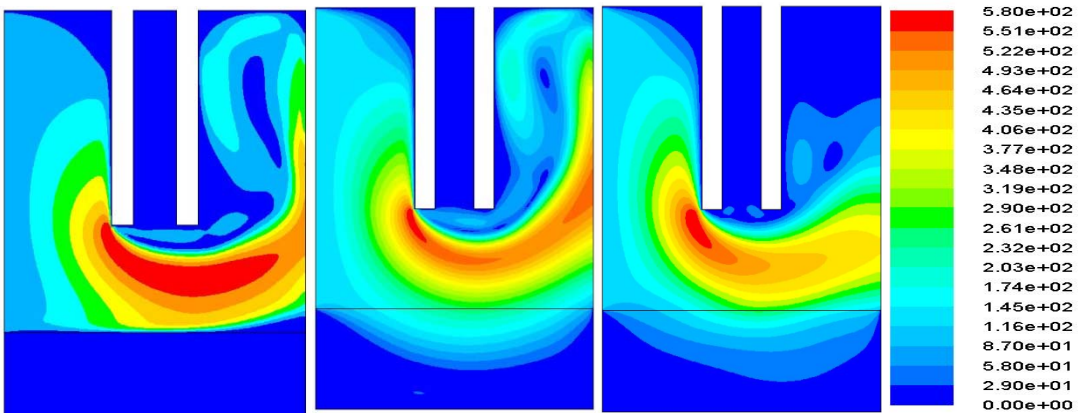

(a.) **(b.)** **(c.)**

Figure 5.4 Effect of Reynolds number on the flow field for different flow field configurations ($s/d = 5, \lambda = 0.2$): (a) Re = 50, (b) Re = 150, (c) Re = 250

The flow pattern for a higher tip clearance ($\lambda = 0.6$) is shown in Figure 5.5, where the effect of the Reynolds number (at fixed GDL porosity of 0.5) can also be clearly observed. The flow pattern in Figure 5.5 depicts the significant influence of the increase in the tip clearance between the pin fin and the GDL at the rate of reactant diffusion through the GDL into the catalyst reaction site.

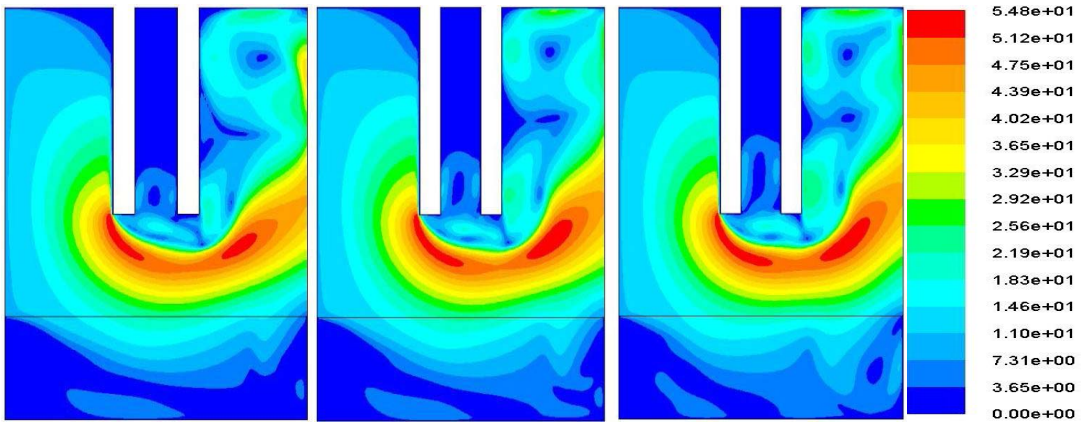

(a) **(b)** **(c)**

Figure 5.5 Effect of Reynolds number on the flow field for different flow field configurations ($s/d = 5, \lambda = 0.6$): (a) Re = 50, (b) Re = 150, (c) Re = 250

The reactant gases are forced down the GDL, hence improving the rate of electrochemical reaction for improved performance. In Figure 5.6, the contours of the tangential velocity profiles for the same case described in Figure 5.5 are shown. High pressure points are shown at the tips of the front pin. The rate of reactant gas diffusion into the GDL improves from Contours (a) to (c).

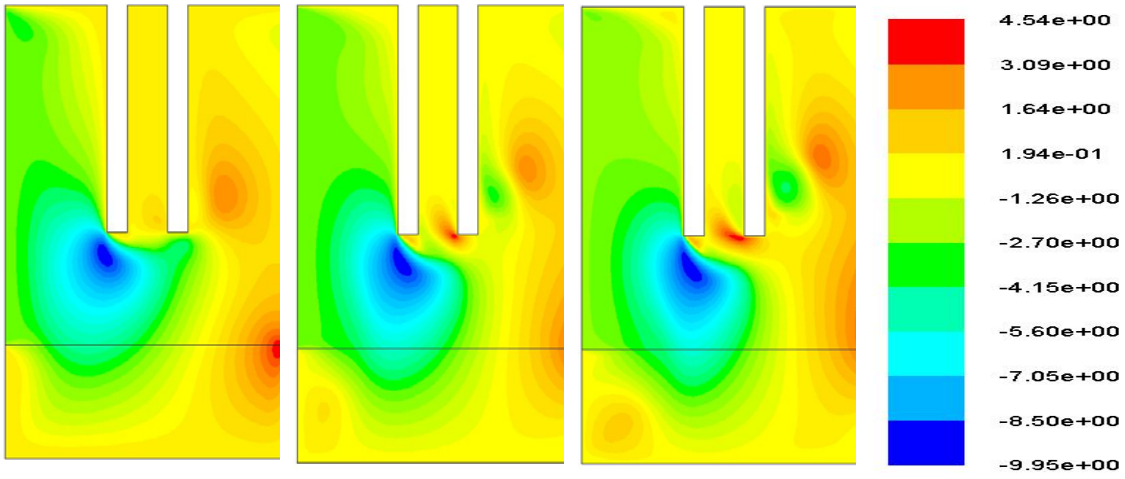

(a) (b) (c)

Figure 5.6 Contours of tangential velocity for different flow field configurations ($s/d = 5, \lambda = 0.6$): (a) Re = 50, (b) Re = 150, (c) Re = 250

5.5.2 RESULTS OF PIN FIN GEOMETRY

In Figure 5.7, we present the friction factor, *f,* as a function of the channels Reynolds number and the pitch (ratio of distance between the pin fin and the pin fin diameter). The friction factor decreased with the increasing Reynolds number. The data obtained in Figure 5.7 further shows that, as the pitch increases, the friction factor decreases. This implies lower diffusion of reactant gas, consequently reducing the performance of the fuel cell. Hence, lower pitch value, which generates more flow disturbance between the pin fin tip and GDL surface, will be more appropriate as this improves the fuel transport rate and subsequently, the reaction rate at the catalyst layer is improved. However, this should also be optimised for minimum power requirement.

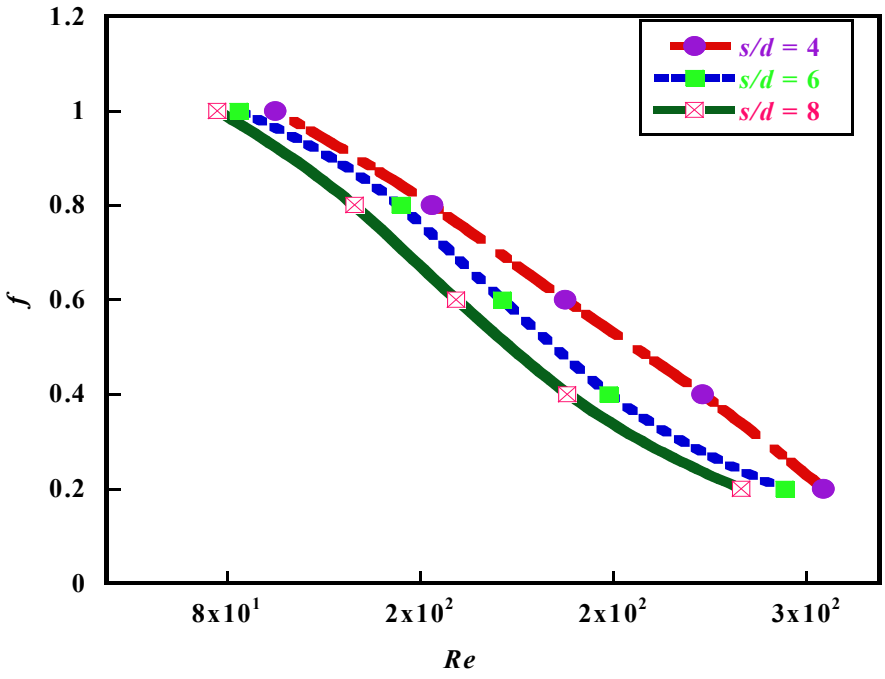

Figure 5.7 Fuel channel friction factor as a function of the Reynolds number and pitch at a clearance ratio, $\lambda = 0.3$

Figure 5.8 shows the variation of the friction factor as a function of the channel Reynolds number and the clearance ratio (λ) between the pin fin and the GDL surface. Decreasing λ, means that the height of the fin towards the GDL increases.

Similarly, decreasing the height of the pin fin reduces the pressure drop in the gas channel flow and subsequently reduces the convectional flow through the fuel cell GDL, thereby reducing cell performance. Increasing the height of the pin fin increases the fluid flow into the reaction site of the fuel cell. This is due to the tangential flow velocity created by the pin fin and flow-mixing effects, however, with a penalty of increasing the pumping power requirement due to increased pressure drop along the fuel channel. This is also supported by the flow description experienced at a higher λ in Figure 5.5. An optimised clearance ratio will reduce the associated pressure drop due to the increase in pin length towards the GDL and pumping cost will therefore decrease.

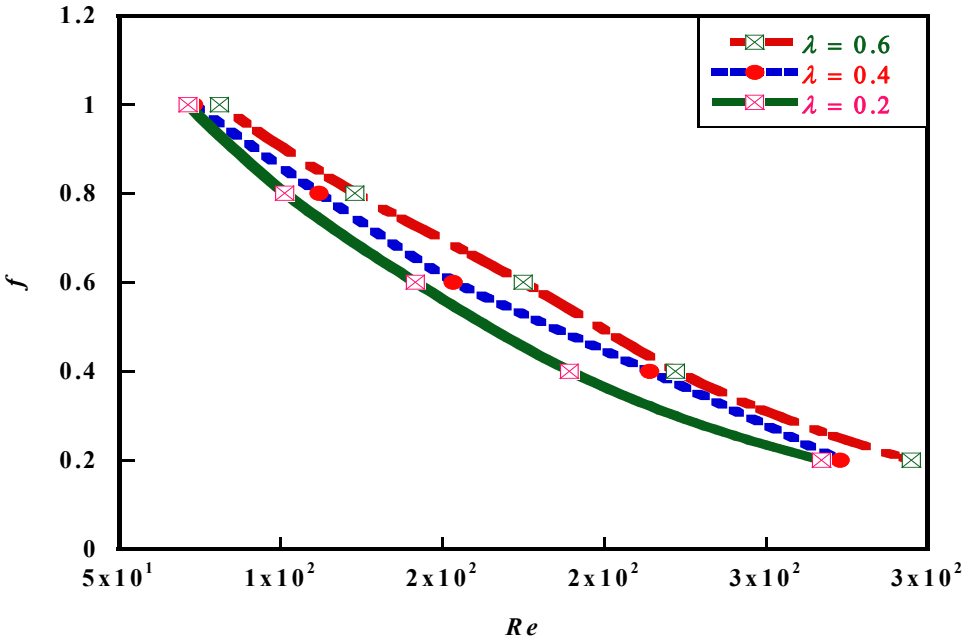

Figure 5.8 Fuel channel friction factor as a function of the Reynolds number and clearance ratio at a pitch, $s/d = 5$

Figure 5.9 depicts the friction factor as a function of channel Reynolds number and the GDL porosity. The results show a decrease in the friction factor with an increase in the GDL porosity of the fuel cell. The increased GDL porosity improves the convection flow through the GDL and subsequently improves fuel cell performance. The flow resistance in the channel at the larger GDL porosity (e.g. 0.7) is much less

than with the smaller porosity (e.g. 0.3). The pressure drop along the flow channel enhanced with pin fins can be reduced considerably with an appropriate higher GDL porosity.

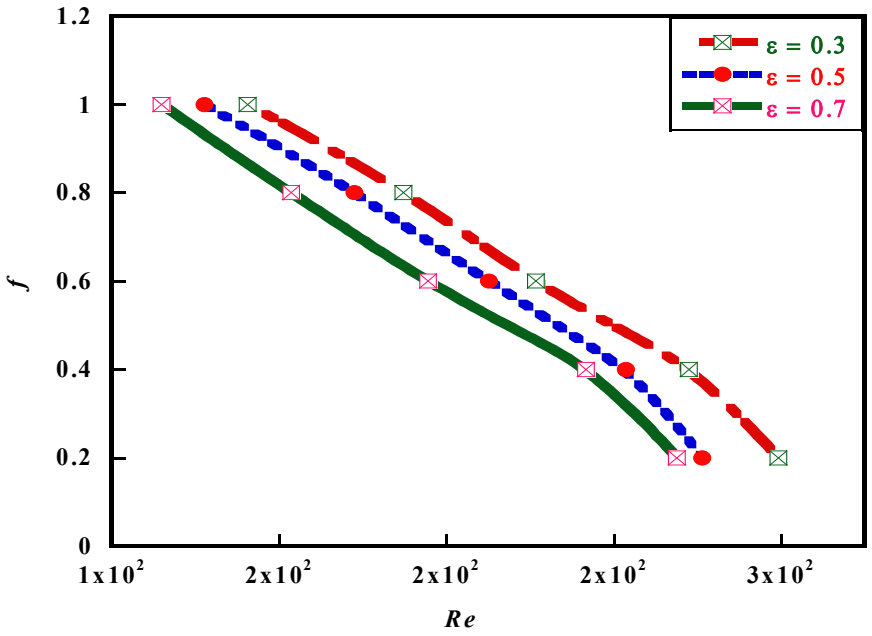

Figure 5.9 Fuel channel friction factor as a function of the Reynolds number and GDL porosity at a pitch, $s/d = 5$, and a clearance ratio, $\lambda = 0.3$

Figure 5.10 shows the peak channel flow resistance as a function of the clearance ratio and the GDL porosity. There is an optimum clearance ratio at $\lambda \approx 0.39$ in which the peak flow resistance in the fuel gas channel is minimised.

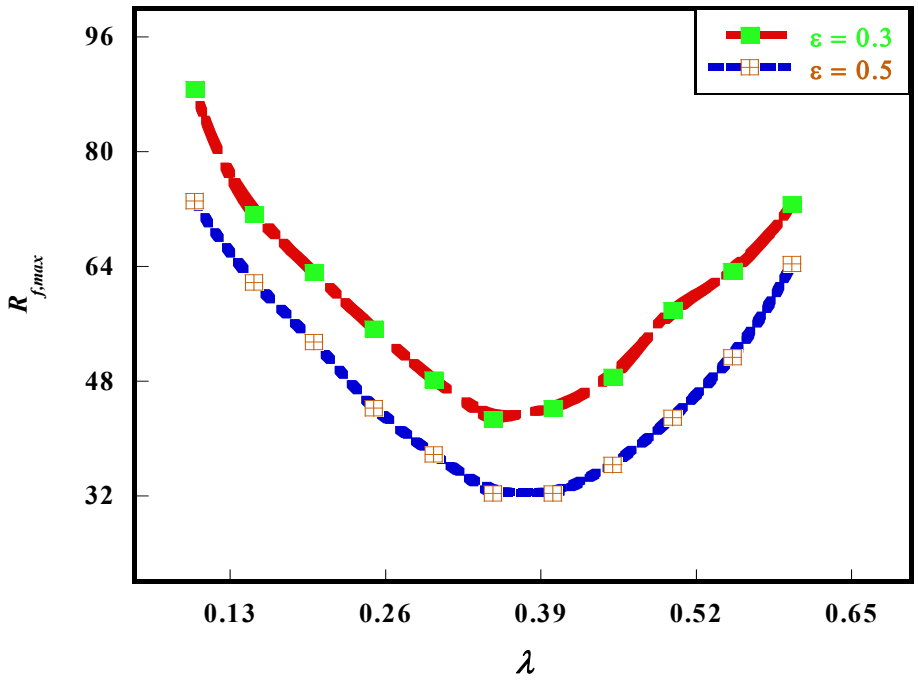

Figure 5.10 Effect of optimised clearance ratio on the peak channel flow resistance

Also, Figure 5.11 shows the peak channel flow resistance as a function of the pitch and the GDL porosity. There is also an optimal pitch at $s/d \approx 7.8$, which minimises the fuel channel friction. These results support the fact that an optimal arrangement of the pin fin parameters could effectively minimise the fuel channel friction and reduce the pressure drop along the fuel channel with a corresponding increase in reaction rate on the catalyst layer, thereby improving the fuel cell performance. Figures 5.10 and 5.11 also show that the GDL porosity has a significant effect on the peak flow resistance along the fuel gas channel. An increase in the GDL porosity reduces the peak flow resistance in the fuel channel. This observation is in agreement with previous work of Soong *et al.* [86].

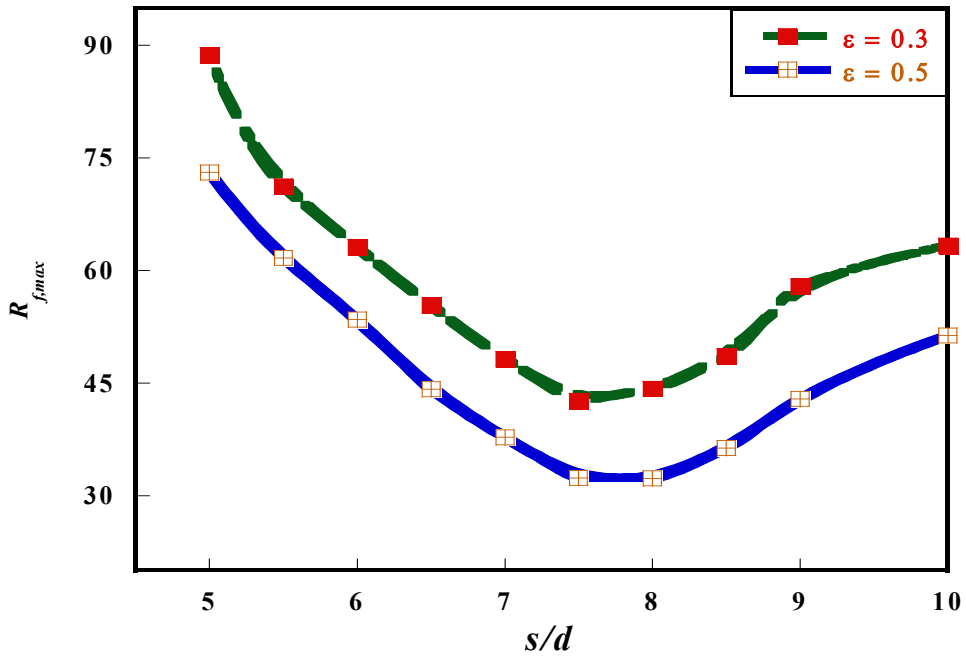

Figure 5.11 Effect of optimised pitch on the channel peak fuel channel flow resistance

5.5.3 OPTIMISATION RESULTS

In this section, the optimisation algorithm was applied to obtain the best geometric configuration of the pin fin that would offer optimal flow resistance along the fuel cell channel, thus ensuring optimum performance of the fuel cell system. From the results in Section 5.2, it is clear that the pin fin geometric parameters (clearance ratio and pitch) optimally exist, which minimises the channel flow resistance. This optimal geometric parameters and the porosity of the GDL have a significant influence on fuel cell performance through reactant gas distribution and the reaction rate on the catalyst layer. Reducing the inherent flow resistance along the flow channel will reduce the additional pressure drop, therefore reducing the pumping power requirement. A series of numerical optimisations and calculations were conducted within the design constraint ranges given in Section 4.1 and the results are presented in the succeeding section to highlight the optimal behaviour of the fuel cell system. Figure 5.12 shows

the effect of the minimised flow resistance as a function of the Reynolds number for a fixed clearance ratio of 0.3 and a GDL porosity of 0.5. Minimised flow resistance decreases with an increase in the Reynolds number.

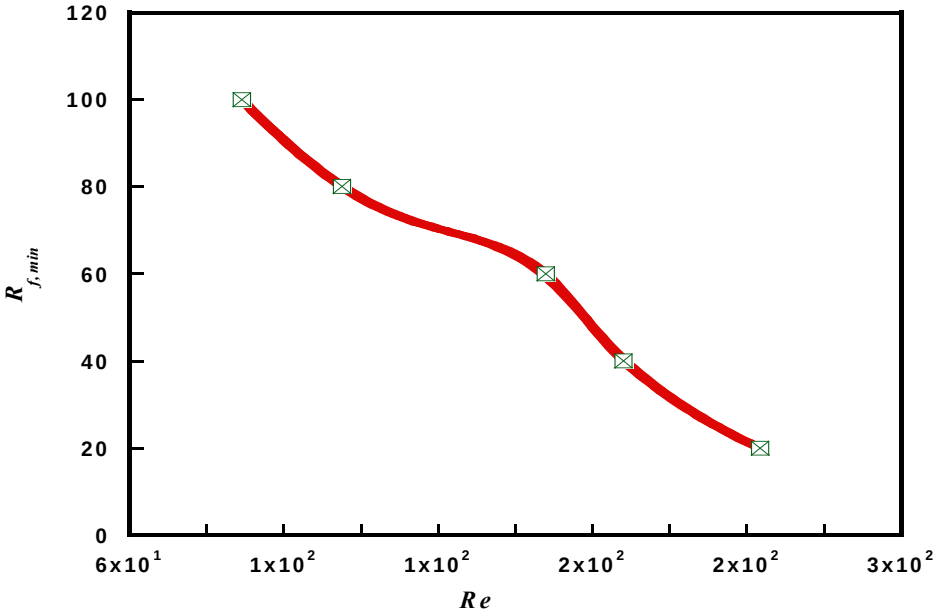

Figure 5.12 The minimised fuel channel flow resistance as a function of Reynolds number for a fixed GDL porosity, $\varepsilon = 0.5$, and a tip clearance ratio, $\lambda = 0.3$

Figure 5.13 shows that the optimal pin fin clearance ratio decreases as the Reynolds number increases. This result affirms the fact that a unique optimal pin fin clearance ratio exists for the fuel gas Reynolds numbers. Similarly, Figure 5.14 shows the optimal pitch as a function of the fuel gas Reynolds number at a fixed clearance ratio of 0.3 and a GDL porosity of 0.5. The result also shows the existence of a unique optimal pitch for the fuel gas Reynolds number.

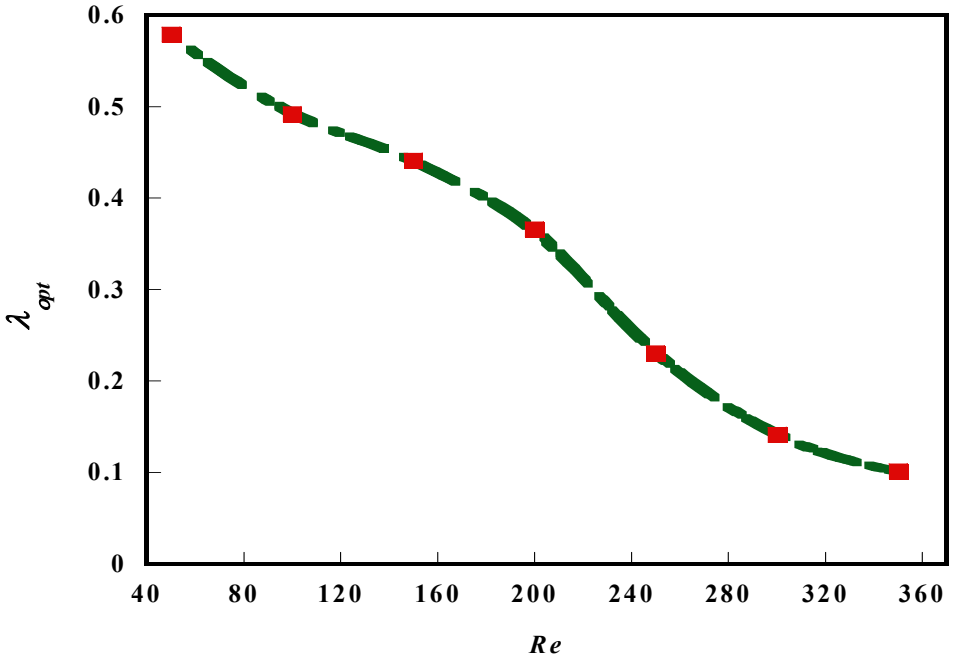

Figure 5.13 Optimal clearance ratio as a function of Reynolds number at a fixed pitch, $s/d = 5$, and a GDL porosity, $\varepsilon = 0.5$

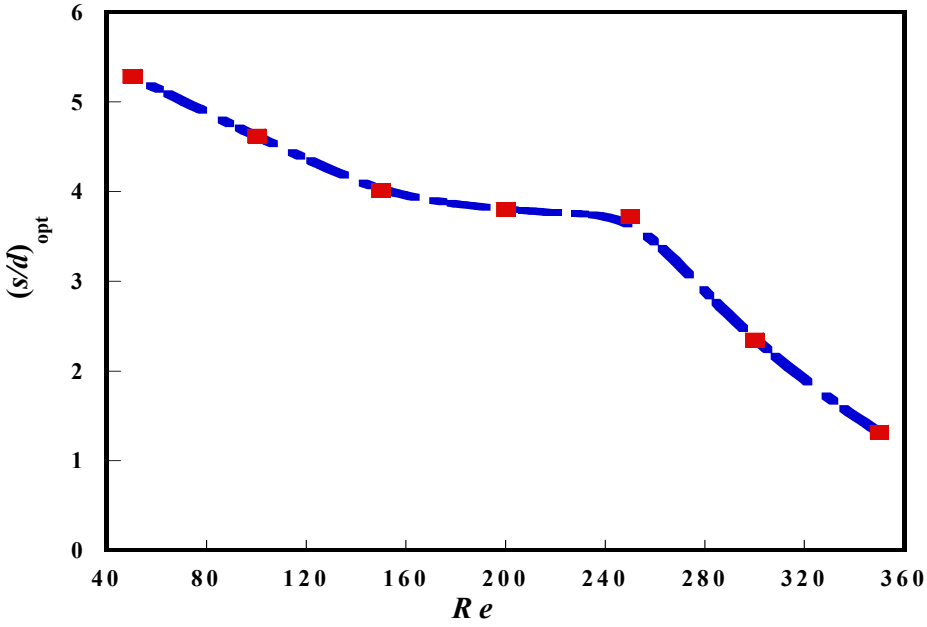

Figure 5.14 Optimal pitch as a function of Reynolds number at a fixed clearance ratio, $\lambda = 0.3$, and a GDL porosity, $\varepsilon = 0.5$

The effect of channel flow resistance on the optimised channel clearance ratio at a porosity of 0.5, pitch of 5 and Reynolds number of 250 was investigated in Figure 5.15. The result shows that channel flow resistance has a significant effect on the optimised clearance ratio. As the flow resistance increases, the optimal clearance ratio decreases.

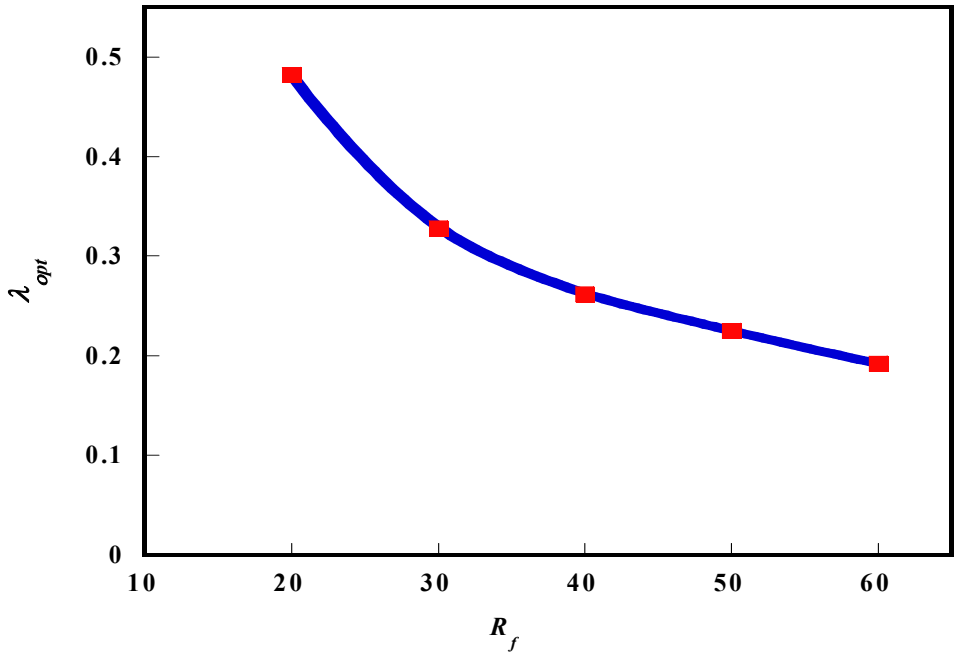

Figure 5.15 Effect of channel flow resistance on the optimised clearance ratio at a fixed pitch, $s/d = 5$, and a GDL porosity, $\varepsilon = 0.5$, at Reynolds number of 250

Also in Figure 5.16, the effect of channel flow resistance on the optimised pin fin pitch was investigated at a clearance ratio of 0.3, GDL porosity of 0.5 and Reynolds number of 250. The result shows that the optimised pitch decreases with an increase in channel flow resistance. Generally, in this model, the flow resistance decreases when the Reynolds number increases. The optimal clearance ratio and pitch also decrease with increasing channel flow resistance, but an optimal level of these factors (clearance ratio and pitch) exists which minimises the flow resistance of reactant gases in the fuel cell gas channel.

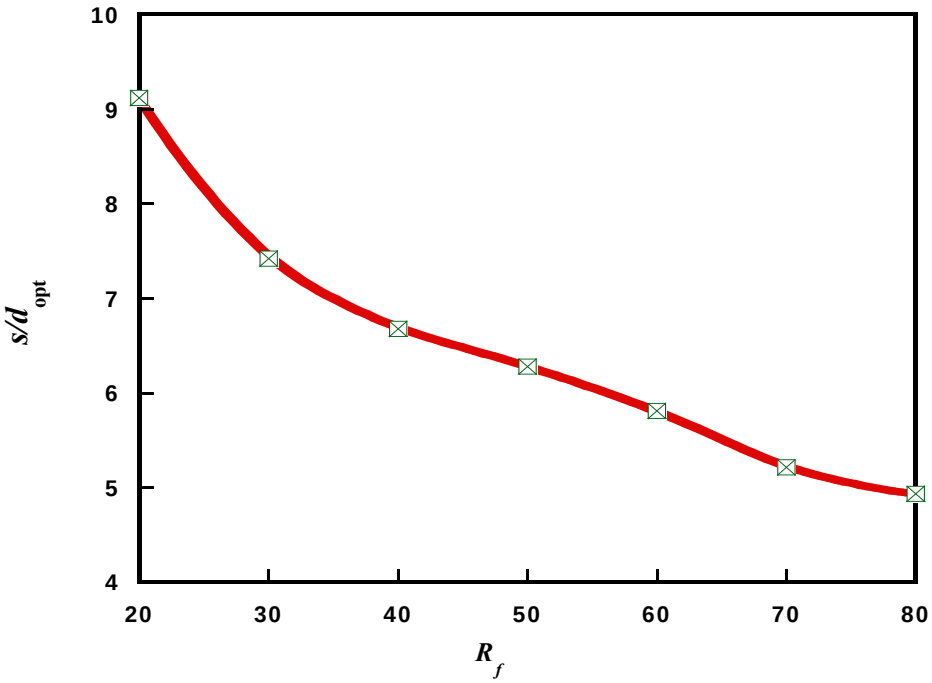

Figure 5.16 Effect of channel flow resistance on the optimised pitch at a fixed clearance ratio, $\lambda = 0.3$, and a GDL porosity, $\varepsilon = 0.5$, at a Reynolds number of 250

5.5.4 PERFORMANCE EVALUATION

Generally, in heat transfer studies using pin fins for enhancement, performance analysis is done by using performance evaluation criteria [203, 219]. Therefore, it is necessary to perform a similar analysis for this study and state the performance in terms of pressure drop for a fuel cell channel equipped with pin fins and one without pin fins. Figure 5.17 shows the pressure drop characteristic for a fuel cell channel with and without pin fins. As can be expected, the figure shows that higher pressure drops occur in the fuel channel with pin fins than in the fuel channel without pin fins. However, the difference obtained along the flow channel for all the pin fin geometry cases considered in this study was less than 6%.

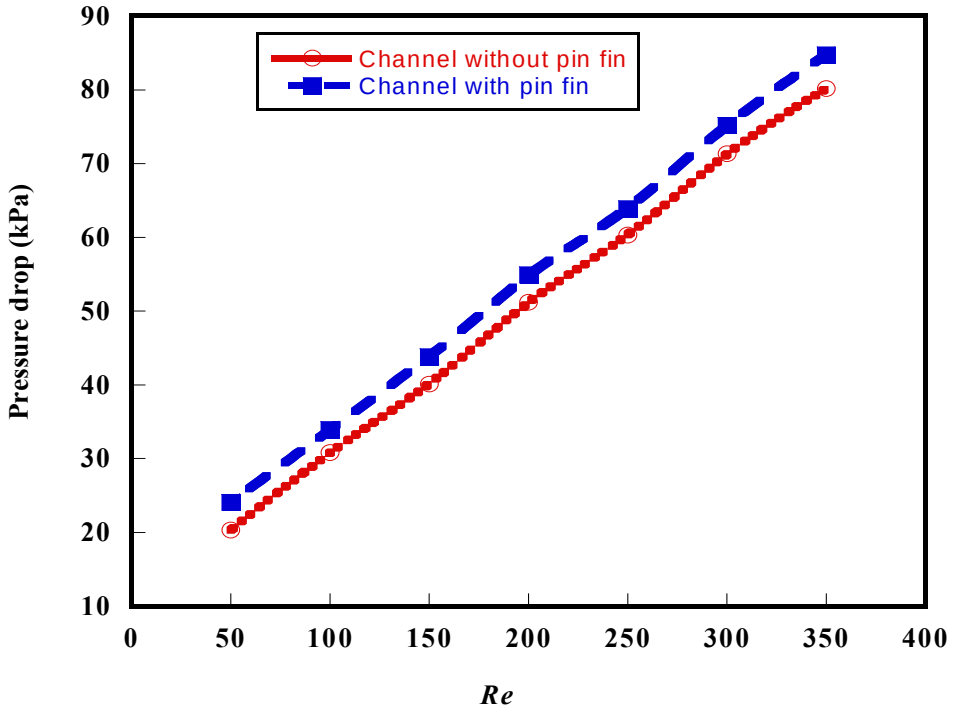

Figure 5.17 Fuel channel pressure drop as a function of the applied pressure drop for a channel with pin fin ($s/d = 5, \lambda = 0.3$) and one without pin fin

Thus, it is evident from this study that, in terms of both high performance enhancement and reasonable pressure drop in a fuel cell system, the pin-fin-enhanced fuel channel is a promising approach for the optimal design of a fuel cell system. Figure 5.18 shows the pumping power as a function of the clearance ratio at a Reynolds number of 250 for a pitch of 5 and GDL porosity of 0.6. The pumping power is the product of the volumetric flow rate and pressure drop. The result shows a minimum pumping power for the friction factor of the fuel channel at a fixed Reynolds number and a specified pitch and GDL porosity of the fuel cell system. In general, the clearance ratio, λ, which has a significant effect on the fuel gas flow, can be optimised to improve fuel cell performance at a reduced pumping power requirement.

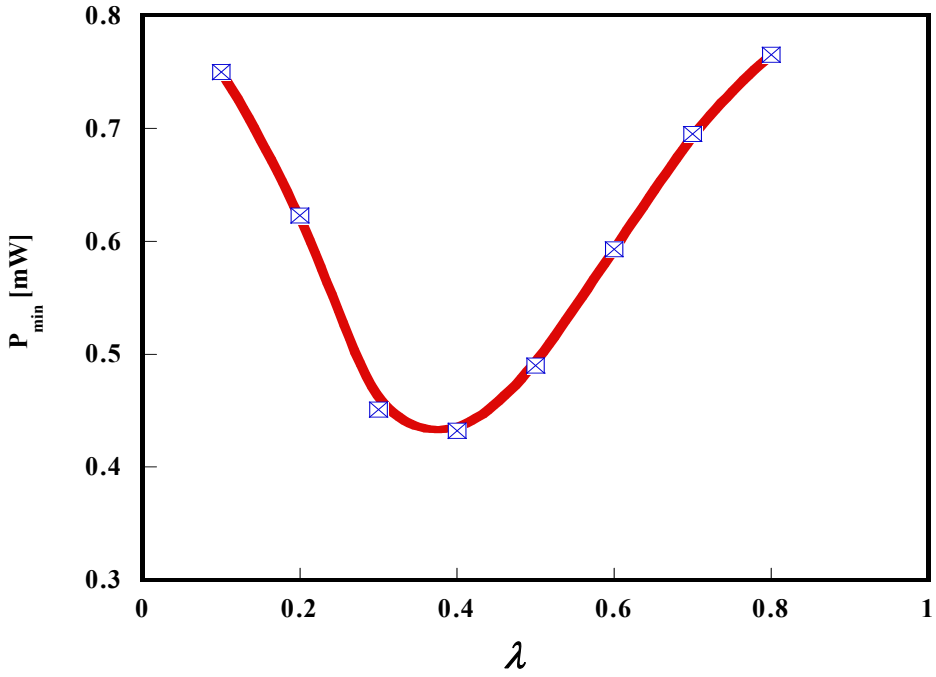

Figure 5.18 Pumping power as a function of tip clearance ratio at a pitch, *s/d* = 5, and GDL porosity, ε = 0.6, at a Reynolds number of 250

CONCLUSION

Using the numerical approach, the reactant gas transport phenomenon in the gas flow channel of a half-cell model of a PEM fuel cell with pin fin insert was investigated. The effect of the flow and geometrical parameters of the pin fin on the flow distribution in the GDL, as well as friction characteristics in the channel were critically studied. Pumping power requirements at varying pin fin clearance ratios to evaluate performance was also explored. The conclusions are summarised as:

- The flow Reynolds number had a significant effect on the reactant flow field, and the diffusion of the reactant gas through the GDL medium increased as the Reynolds number increased.

- The friction factor increased with an increasing clearance ratio of the pin fin in the channel.
- The optimal clearance ratio and pitch for the considered fuel cell channel decreased with an increase in the fuel channel friction.
- The friction factor decreased with an increase in the GDL porosity. Hence, the channel friction and pressure drop can be reduced significantly with increased GDL porosity.
- An optimal pin fin clearance ratio existed which offered minimum pumping power requirement.
- An enhanced fuel cell performance was achieved by using pin fins in a fuel cell gas channel, which ensured high performance and low fuel channel pressure drop of the fuel cell system.

6

CHAPTER 6: MODELLING AND OPTIMISATION OF COOLING CHANNEL GEOMETRIC CONFIGURATION FOR OPTIMAL THERMAL PERFORMANCE OF A PROTON EXCHANGE MEMBRANE FUEL CELL

6.1 INTRODUCTION

A fuel cell is an electrochemical energy device that directly converts the chemical energy in the fuel into electrical energy. Applications include: portable power, stationary applications, vehicle propulsion and large electrical plants. PEM fuel cell researchers are moving ahead at a rapid pace because of the many attractive features, like rapid start-up, high power density, high efficiency and the belief of being the most promising among fuel cell types for transportation application, due to its fast start-up and dynamic response to changes in the demand for power during vehicular operations [71, 220, 221]. These features have made it one of the most promising clean and highly efficient power generation technologies in the 21st century. Operating temperatures of fuel cell systems affect the maximum theoretical voltage at which a fuel cell can operate [89]. Higher operating temperatures correspond to lower theoretical maximum voltages and lower theoretical efficiency. However, higher temperature at fuel cell electrodes increases electrochemical activity which, in turn, increases efficiency [89]. Most current PEM fuel cells operate at low temperatures (< 80^{o}C) encountering several performance difficulties, especially vehicular applications such as reduced electrochemical kinetics at electrode sites; flooding due to two-phase flows emergence; intolerance to impurities such as CO; insufficient heat rejection capability and relatively high cost. A recent approach is to operate this class of fuel cell at higher temperature (> 100^{o}C) which eliminates some of these obstacles [88,

222-224]. Operating at higher temperatures increases the reaction rates at both electrodes and consequently increases system efficiency. The quality of waste heat from the fuel cell stack, which could be used in other system components requiring heat or used to run an additional thermodynamic heat for additional power, is also enhanced at higher operating temperature. Also, there is a substantial reduction in the incidence of water "flooding" that restricts oxygen transport by blocking the channel path and pores of the gas diffusion electrodes when fuel cells are operated at a higher temperature. Several approaches are also on-going, especially on developing PEM materials (polymers, catalyst layers and MEA compositions) that will be relatively stable for compatibility with operation at high temperatures [104, 225, 226]. The development of these materials comes with an additional cost of operating a PEM fuel cell.

Moderate temperature ranges exist within which a specific fuel cell type will operate efficiently and reliably. Subsequently, the goal in fuel cell thermal management is to ensure effective stack operation at a specified temperature range. A PEMFC operated at 80^{o}C with an efficiency of 40-50% produces an enormous amount of heat (~ 50% waste heat) due to the exothermic nature of the cell reaction that must be removed if the integrity of the cell structure is to be maintained [222]. In a typical modern vehicle based on the internal combustion engine (ICE), the cooling system rejects < 40% of the generated waste heat and the exhaust manifold removes the bulk of the waste heat in the system [227]. In contrast, a typical PEM fuel cell stack operating at 80^{o}C must reject all the heat produced via the cooling system.

The heat rejection capability of a PEM fuel cell system operating below 100^{o}C is very inefficient and requires elaborate cooling systems for adequate system performance [88]. Basically, cooling methods are predominantly determined by the size of the fuel cell system [119]. The size of the fuel cell system also has a direct link with the required power output from the fuel cell system. Fuel cell units below 2 kW are better cooled using air, while systems between 2 kW and 10 kW require judicious decision-making to use water or air cooling [89]. Water cooling requires more complex system

design when considering the need to monitor the temperature and pressure of the cooling water and the need for an oil-free water pump to supply cooling water. Air cooling could be achieved through increasing the reactant air flow to the fuel cell system but with the risk of too much air drying out the PEM [119]. This associated problem usually necessitates the use of a separate reactant air supply and a cooling system for the fuel cell system.

Temperature distribution in fuel cells is usually non-uniform, even when there is a constant mass flow rate in the flow channels [228]. This occurs primarily as a result of the heat transfer and phase changes in PEM fuel cells. It usually causes temperature fluctuations within the fuel cell system structure and affects the fuel cell performance. Heat transfer in PEM fuel cells occurs in the following ways [228]:

- Between the cell component layers and the flowing air and fuel streams. This way of heat transfer is usually described in terms of heat transfer coefficients h_a (for air channel) and h_f (for fuel channel) due to forced convective heat transfer with or without natural convection.
- Between the fuel and air streams across the interconnect layer, described as overall heat transfer coefficient, *U;*
- In solid structures, described as heat conduction with different thermal conductivities, k_i ($i =$ electrolyte, electrodes and current interconnect layers).

In order to alleviate the excessive temperature build-up in a PEM fuel cell, the heat generated by the various processes in the fuel cell structure should be removed properly. Thermal management has a very strong impact on fuel cell performance, since it affects the transport of water and gaseous species as well as electrochemical reactions in the cells. Thermal management still remains a critical issue that needs to be resolved in order for PEM fuel cell technology to be feasible for various commercial applications [229, 230]. A number of numerical modelling works has been carried out in the literature to investigate heat/mass transfer in PEM fuel cells.

Yu *et al.* [98] investigated the performance of the Ballard PEM fuel cell in terms of electrochemical characteristics and water management. The study shows that the more the water supplied to the anode from its inlet, the higher the voltage and usually the lower the anode exit temperature. Coppo *et al.* [90] presented a 3-D model to study the influence of temperature on PEM fuel cell operation which includes a two-phase flow in the gas distribution channel. The obtained result indicates that both liquid water transport within the GDL and liquid water removal from the surface of the GDL play an important role in determining variations in cell performance as far as temperature is concerned.

Yan *et al.* [91] presented a 1-D non-isothermal model to analyse the effect of anode and cathode side temperatures on the membrane water distribution. The obtained results shows that a temperature increase on the anode side can lead to membrane dehydration and fuel cell operation at high current density leads to membrane dehydration on the anode side, due to the strong electro-osmotic water drag at high current density. Ramousse *et al.* [92] developed a 1-D non-isothermal model accounting for heat and mass transfer in a complete cell with charge and mass transfer in the electrodes. Their study provides temperature, concentration and potential fields in a single cell. In addition, their work shows that the thermal gradient in MEA could lead to thermal stresses at high current densities.

Shimpalee and Dutta [93] conducted a 3-D non-isothermal numerical analysis with a two-phase flow phenomenon incorporated in their model. The effect of the heat produced by the electrochemical reaction and phase change of water on the cell performance was studied critically. Their study shows that the inclusion of heat transfer in fuel cell model shows degradation in fuel cell performance. This research work enumerated the importance of incorporating the heat transfer aspect in fuel cell modelling. Shan and Choe [94] presented a 1-D model taking into account the dynamics in temperature gradient across the fuel cell; the dynamics in water concentration redistribution in the membrane; the dynamics in proton concentration in the cathode catalyst layer; and the dynamics in reactant concentration redistribution in

the cathode GDL. This study's general result shows that temperature profiles in each of the cell layers tend to follow the current waveform due to energy losses in these layers. Higher temperature losses are prominent in the membrane and catalyst layer due to ohmic losses as a result of the membrane resistance and heat released by the chemical reaction.

Yuan and Sunden [95] performed a 3-D non-isothermal numerical analysis of heat transfer and gas flow in PEM fuel cell ducts using a generalised extended Darcy model. The effects of effective thermal conductivity, permeability, inertia coefficient and porous layer thickness on gas flow and heat transfer were studied. Their result shows that higher permeability, higher effective thermal conductivity of porous GDL and smaller thickness of the porous layer improved heat transfer in the modelled fuel cell system. Ju *et al.* [96] presented a 3-D non-isothermal single-phase model for all seven layers of the PEM fuel cell that accounts for various location-specific heat-generation mechanisms. These mechanisms include irreversible heating due to electrochemical reactions and entropy, and Joule (ohmic) heating due to membrane ionic resistance. They observed that the thermal effect on PEM fuel cells becomes more critical at higher cell current density and/or lower GDL thermal conductivity. Their result further shows that temperature increase in the membrane is highly dependent on the GDL thermal conductivity and inlet humidity conditions.

A number of modelling approaches has been developed in the literature to predict the thermal effect in PEM fuel cells as described above [90, 98, 91-96] but, although they represent a significant contribution in fuel cell thermal modelling, there are few reports on thermal cooling approaches to enhance thermal management in a PEM fuel cell structure. Furthermore, most models on thermal management in PEM fuel cells emphasise approaches to understand and improve the kinetic process for thermal prediction aimed at improving individual fuel cell model performance, rather than a practical approach to reduce the incident temperature generated in the fuel cell structure. One of the enhancement techniques to reduce excessive temperature build-

up in a PEM fuel cell is by using air/water (depending on fuel cell size) cooling, conveyed through cooling channels, as an integral part of the fuel cell flow structure.

To the author's knowledge, studies on the impact of the geometric configuration of cooling channels on effective thermal heat transfer and performance in the fuel cell system is still limited in the literature and this phenomenon is explored in this study. A numerical modelling study that investigates the geometrical effect of cooling channels on the thermal performance of a PEM fuel cell is described in this chapter. A parametric study on the effect of temperature, stoichiometry ratio, relative humidity and the cooling channel aspect ratio on cell performance were initially conducted, since these factors contribute to the extent of membrane hydration in a fuel cell system. Optimal results of these parameters were subsequently combined with the different aspect ratio of the cooling channels and the system performance was evaluated for elevated fuel cell system temperatures (100-150°C). In addition, a mathematical optimisation tool was used to select the best geometric configuration that would improve cooling and enhance fuel cell performance for a given cooling gas flow Reynolds number. The results of this study will be of interest to fuel cell engineers who are striving to improve thermal management in fuel cell systems and enhance system performance.

6.2 MODEL DESCRIPTION

In this chapter, a numerical study and optimisation of geometric parameters of the cooling channel of a PEM fuel cell is attempted, based on a three-dimensional full cell model, and the impact on cell performance is explored. The single-cell PEMFC consists of the anode flow channel, anode diffusion layer, MEA assembly, cathode diffusion layer, cathode flow channel, as well as an array of cooling channels on the carbon plates. Figure 6.1 shows the 3-D schematic of the model of the PEM fuel cell system. The influential factors considered in this study that could affect the fuel cell thermal behaviour and subsequently performances are the stoichiometry ratio, the

relative humidity, the cooling channel aspect ratio and the coolant air Reynolds number. The construct of three (3) cooling channels transversely placed at equal distances at each side (anode and cathode) of the bipolar plates of the PEM fuel cell are shown in Figure 6.1. These parameters are selected as the design parameters to be optimised in this study. The other geometric and physicochemical properties for the fuel cell system are kept constant in this study and given in Table 6.1.

The Dynamic-Q optimisation algorithm [166] is employed herein as the optimisation search scheme. This study is aimed at optimising these identified factors, so that the best performance in terms of the optimal current density (the objective function) of the PEM fuel cell system at prescribed operating conditions can be achieved. The optimisation algorithm is expected to ensure robust optimal values for the factors investigated in this study.

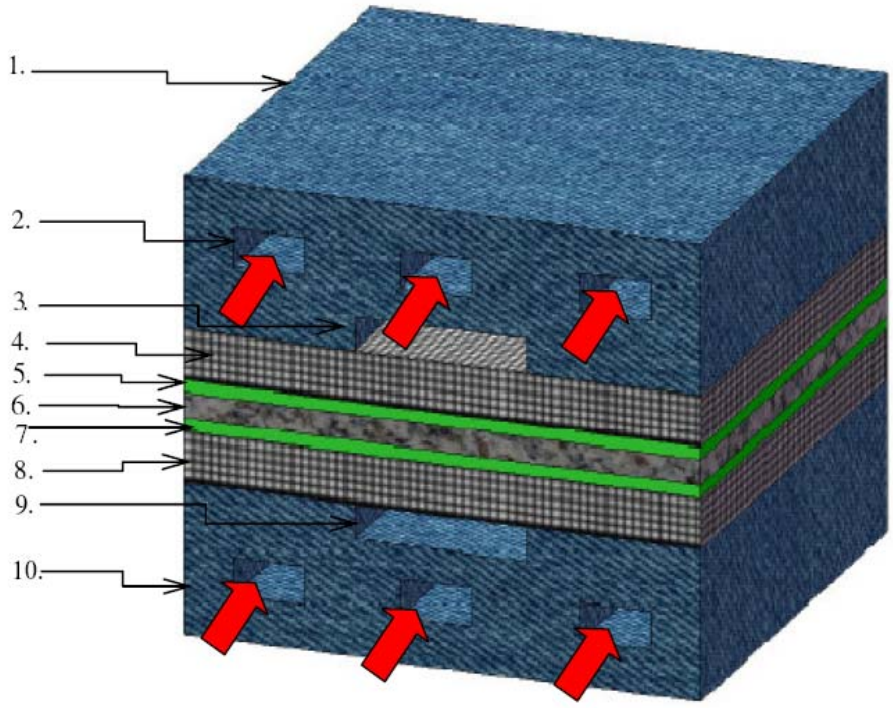

Figure 6.1 A schematic diagram of a 3-D model of PEM fuel cell system with cooling channels embedded in the bipolar plates

1. Anode-side bipolar plate
2. Cooling channel
3. Hydrogen fuel channel
4. Anode GDL
5. Anode catalyst layer
6. Membrane
7. Cathode catalyst layer
8. Cathode GDL
9. Air gas channel
10. Cathode-side bipolar plate

Table 6.1 Parameters and properties used in the present model

Description	Value
Cell operating temperature (^{o}C)	70
Air-side/fuel-side inlet pressure (atm)	3/3
Open-circuit voltage (V)	0.95
Porosity of GDL	0.4
Permeability of GDL (m^2)	1.76×10^{-11}
Tortuosity of GDL	1.5
Porosity of catalyst layer	0.4
Permeability of catalyst layer (m^2)	1.76×10^{-11}
Tortuosity of catalyst layer	1.5
Porosity of membrane	0.28
Permeability of membrane (m^2)	1.8×10^{-18}
Reference diffusivity of H_2	0.915×10^{-4} m^2 s^{-1}
Reference diffusivity of O_2	0.22×10^{-4} m^2 s^{-1}
Electric conductivity of catalyst layer $(\Omega^{-1}m^{-1})$	190
Electric conductivity of GDL $(\Omega^{-1}m^{-1})$	300
Electric conductivity in carbon plate $(\Omega^{-1}m^{-1})$	4000

O_2 stochiometry ratio	1.2
H_2 stochiometry ratio	2.0
Oxygen mole fraction	0.406
Relative humidity of inlet fuel/air	100%
Reference current density of anode	7 500
Reference current density of cathode (A/m^2)	20
Anode transfer coefficient	0.5
Cathode transfer coefficient	0.5
Evaporation and condensation rate	100 s^{-1}

6.2.1 BASIC ASSUMPTIONS

The electrochemical reactions in the fuel cell are complicated, hence the following simplifying assumptions are made:

1. Ideal gas mixture in the flow channels and the porous electrode;
2. Incompressible and laminar flow;
3. Isotropic and homogeneous porous medium;
4. Ionic conductivity of both the membrane and catalyst layer are constant;
5. No pressure gradient between the anode and the cathode side (only gas diffusion is considered);
6. "ultra thin" electrode layer, hence gas transport resistance through the electrode porous layer could be neglected;
7. Identical inlet conditions for both the anode and cathode as well as the coolant channel;
8. No gas pressure drop along the gas channels;
9. Liner temperature gradient across the layers in the fuel cell;
10. Constant thermal conductivity of the materials in the fuel cell.

6.2.2 GOVERNING EQUATIONS

The employed governing equations are a single set applicable to all domains (flow channels, GDL and catalyst layer). This approach is based on the previous work of Um *et al.* [71]. The conservation equations of mass, momentum, species, proton, electron and energy are presented below:

Continuity equation:

$$\nabla \cdot (\rho \mathbf{u}) = 0 \tag{6.1}$$

Momentum:

$$\frac{1}{\varepsilon^2}\nabla \cdot (\rho \mathbf{u}\mathbf{u}) = -\nabla p + \nabla \cdot \tau + S_u \tag{6.2}$$

Species:

$$\nabla \cdot (\mathbf{u} C_k) = \nabla \cdot (D_k^{eff} \nabla C_k) + S_k \tag{6.3}$$

Proton:

$$\nabla \cdot (\kappa^{eff} \nabla \Phi_e) + S_\Phi = 0 \tag{6.4}$$

Electron:

$$\nabla \cdot (\sigma_s^{eff} \nabla \Phi_s) + S_\Phi = 0 \tag{6.5}$$

Energy:

$$\nabla \cdot \left(\rho c_p \mathbf{u} T\right) = \nabla \cdot \left(k^{eff} \nabla T\right) + S_T \tag{6.6}$$

The energy source term, S_T, depicts the sum of the reversible heat release and the irreversible heat generation. In the catalyst layer, the reversible and irreversible reaction heats, as well as latent heat of water phase change, are considered. For the membrane, the ohm heating of the current due to the large resistance of the membrane is also considered. The detailed source terms used for the model in the equations above are presented in Table 6.2.

Table 6.2 The governing equation source terms in various regions of the fuel cell

	Gas channel	Diffusion layer	Catalyst layer	Membrane
Mass	$S_m = 0$	$S_m = 0$	Anode: $S_m = S_h + S_w$, Cathode: $S_m = S_o + S_w$,	$S_m = 0$
Momentum	$S_u = 0$	$S_u = -\frac{\mu_g}{k k_{rg}} \mathbf{u}_g$	$S_u = -\frac{\mu_g}{k k_{rg}} \mathbf{u}_g$	$S_u = 0$
Species:				
O_2	$S_o = 0$	$S_o = 0$	$S_o = -(i_c/4F)M_o$	$S_o = 0$
H_2	$S_h = 0$	$S_h = 0$	$S_h = -(i_a/2F)M_h$	$S_h = 0$
Charge:				
Solid phase -	$S_{\Phi,s} = 0$	$S_{\Phi,s} = 0$	$S_{\Phi,s} = -I$	$S_{\Phi,s} = 0$
Membrane phase-	$S_{\Phi,m} = 0$	$S_{\Phi,m} = 0$	$S_{\Phi,m} = I$	$S_{\Phi,m} = 0$

Energy	$S_T = 0$	$S_T = 0$	$S_T = i\left(\eta + T\frac{dV_{oc}}{dT}\right) + \frac{I^2}{\kappa_m}$ $S_T = \frac{I^2}{\kappa_m}$

The transfer current densities at the anode and the cathode are calculated using the Butler-Volmer equation [60]:

$$i_o = i_{o,ref}\left\{\exp\left[\frac{\alpha_{an} nF}{RT}\eta\right] - \exp\left[\frac{-\alpha_{cat} nF}{RT}\eta\right]\right\} \quad , \tag{6.7}$$

where η is the overpotential and defined as,

$$\eta = \left(\Phi_s - \Phi_e\right) - E_{ocv} \quad , \tag{6.8}$$

where F is the Faraday constant, α_{an} and α_{cat} represents the experimental anodic and cathodic transfer coefficients, respectively, and R is the universal gas constant. The effective diffusivity ($D_{i,eff}$) for the gas-phase flow in porous media can be written as:

$$D_{i,eff} = D\frac{\varepsilon}{\tau}. \tag{6.9}$$

The quantity (τ = tortuosity) is usually estimated through experiment. Therefore, it is conventionally correlated in fuel cell studies using the Bruggeman correlation [103]. This correlation assumes τ is proportional to $\varepsilon^{-0.5}$, resulting in the simpler expression [103]:

$$D_{i,eff} = D\varepsilon^{1.5}. \tag{6.10}$$

The porosity correlation is used to account for geometric constraints of the porous media.

The Reynolds number was defined as [205]:

$$\mathrm{Re} = \dot{m}D/(\mu A). \tag{6.11}$$

6.2.3 NUMERICAL PROCEDURE

The model equations were solved by using a finite-volume computational fluid dynamics code Fluent [163] with Gambit® (2.4.6) [164] as a pre-processor. The CFD code has an add-on package for fuel cells, which has the requirements for the source terms for species transport equations, heat sources and liquid water formations. The domain was discretised using a second-order discretisation scheme. The SIMPLE algorithm [192] for convection-diffusion analysis was utilised to deal with the pressure-velocity coupling. Numerical convergence was obtained at each test condition when the relative error of each dependent variable between two consecutive iterations was less than 1.0×10^{-7}. The domain was divided into hexahedral volume elements. A grid independence test was carried out to ensure that solutions were independent of the dimensions of the chosen grid with consideration for both accuracy and economics. For this purpose, five grid systems at 24 × 12 × 60, 34 × 12 × 60, 34 × 22 × 60, 44 × 22 × 60 and 34 × 34 × 60 were tested. The obtained results of the average current density under different grid systems, when the PEM fuel cell system operating voltage was 0.7 V, are summarised in Table 6.3. It was considered that the system of 34 × 22 × 60 (I = 1.7054 A/cm^2) was sufficient for the present study as a trade-off between accuracy and cost of time. A typical grid network for the computational domain is shown in Figure 6.2. The model and solution were implemented using an Intel® Core(TM) 2Duo 3.00 GHz PC with 3.24 GB of DDRam.

Table 6.3 Grid independence test

Grid size	I_{av} [A/cm^2]
24 × 12 × 60	1.7012
34 × 12 × 60	1.7048
34 × 22 × 60	1.7054

44 × 22 × 60	1.7055
34 × 34 × 60	1.7057

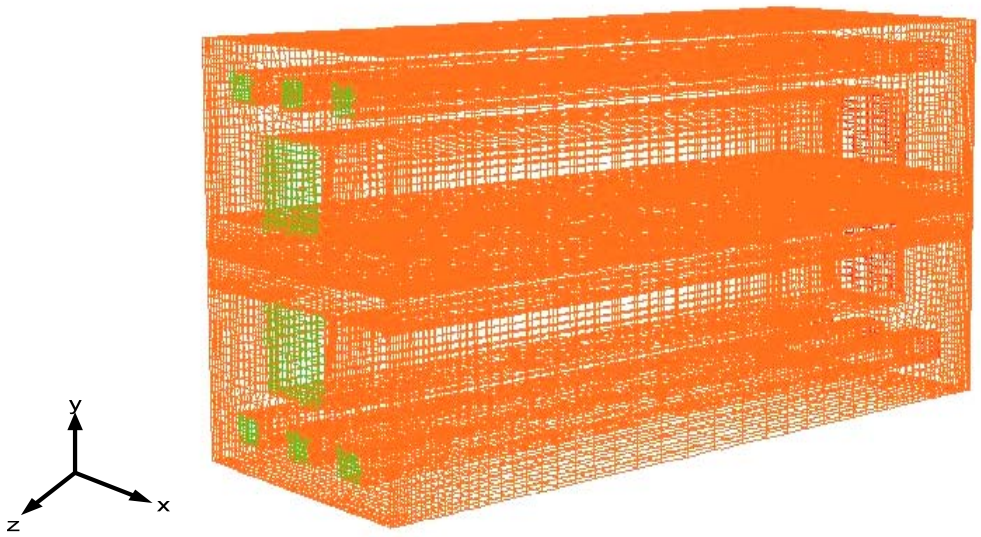

Figure 6.2 The discretised three-dimensional computational domain of a single PEM fuel cell with cooling channels

6.3 MATHEMATICAL OPTIMISATION ALGORITHM

The Dynamic-Q optimisation algorithm [166], previously discussed in detail in Chapter 3 of this thesis, was used in this study. The algorithm is a robust multidimensional gradient-based optimisation algorithm which does not require an explicit line search and is ideally robust for cases where function evaluations are computationally expensive. The algorithm applies the dynamic trajectory LFOPC which is adapted to handle constrained problems through approximate penalty function formulation [166]. This dynamic approach is applied to successive quadratic approximations of the actual optimisation problems. The successive sub-problems are formed at successive design points by constructing spherically quadratic approximations, which are used to approximate the objective functions or constraints (or both), if they are not analytically given or very expensive to compute numerically

[169, 207]. The use of spherical quadratic approximation in the Dynamic-Q algorithm offers a competitive advantage when compared with other algorithms in terms of the computational and storage requirements [169]. Storage savings become highly significant when the number of variables becomes large. Therefore, this particular strength of the Dynamic-Q method makes it well suited for optimisation of engineering problems with a large number of variables and it has been used to successfully solve a large variety of engineering problems [208, 210-213].

6.4 OPTIMISATION PROBLEM FORMULATION

The optimisation problem was tailored towards finding the best operating design parameters which would give the best performance in PEM fuel cells. The design variables which greatly affect the performance of PEM fuel cells, especially at high operating temperatures are the air stoichiometry ratio, relative humidity (*RH*), the aspect ratio of cooling channels and the coolant Reynolds number. The objective function here is the maximised current density of the fuel cell system at optimised operating factors (stoichiometry ratio, relative humidity, cooling channel aspect ratio and coolant Reynolds number) at a pressure drop of less than 3 atm. Table 6.4 shows the dimensions of the cooling channels used at base case condition for this study.

Table 6.4 Dimension of the cooling channels investigated for initial simulations

Test Case	W(mm)	H(mm)	L(mm)	$\alpha(=H/W)$
1	0.8	1.5	120	1.875
2	1.2	3.0	120	2.500
3	1.6	4.5	120	2.813

The objective function for the optimisation can be written mathematically as

$$I_{max} = f(\lambda_{opt}, RH_{opt}, H/W_{opt}, Re) \quad , \tag{6.12}$$

where I_{max} is the maximised current density output for the optimised design variables. The maximised current density approach in PEM fuel cell design has shown to be robust and allows the determination of maximum parameteric values that are sharp and robust enough for practical design applications [231]. In addition, when identified accurately they pave way for increasing the cell stack net power efficiency, approaching the actual PEMFC first-law efficiency level [231, 232]. The maximised current densities in this study were examined at the fuel cell voltage of 0.7V.

6.4.1 DESIGN VARIABLE CONSTRAINTS

Total fixed volume. For each of the optimisation problems, the cooling channel volume is kept constant.

The following constraints are imposed for the optimisation:

$$1 \leq \lambda \leq 5 \tag{6.13}$$

$$0.2 \leq RH \leq 1.0 \tag{6.14}$$

$$1.5 \leq H/W \leq 3.5 \tag{6.15}$$

$$100 \leq Re \leq 500 \tag{6.16}$$

6.4.2 OPTIMISATION PROCEDURE

The optimisation problem defined in Section 6.4.1 was automatically carried out in a MATLAB [218] environment by simultaneously using GAMBIT [164] for mesh generation and FLUENT [163] for modelling. This was made feasible by using both GAMBIT [164] and FLUENT [163] journal files, which were executed in MATLAB [218] by Windows executable files. Figure 6.3 depicts a flow diagram of how

automation is carried out until convergence (either by step size or function value criteria) is attained. To ensure that the converged solution obtained is indeed the global minimum, a multi-starting guess approach was employed.

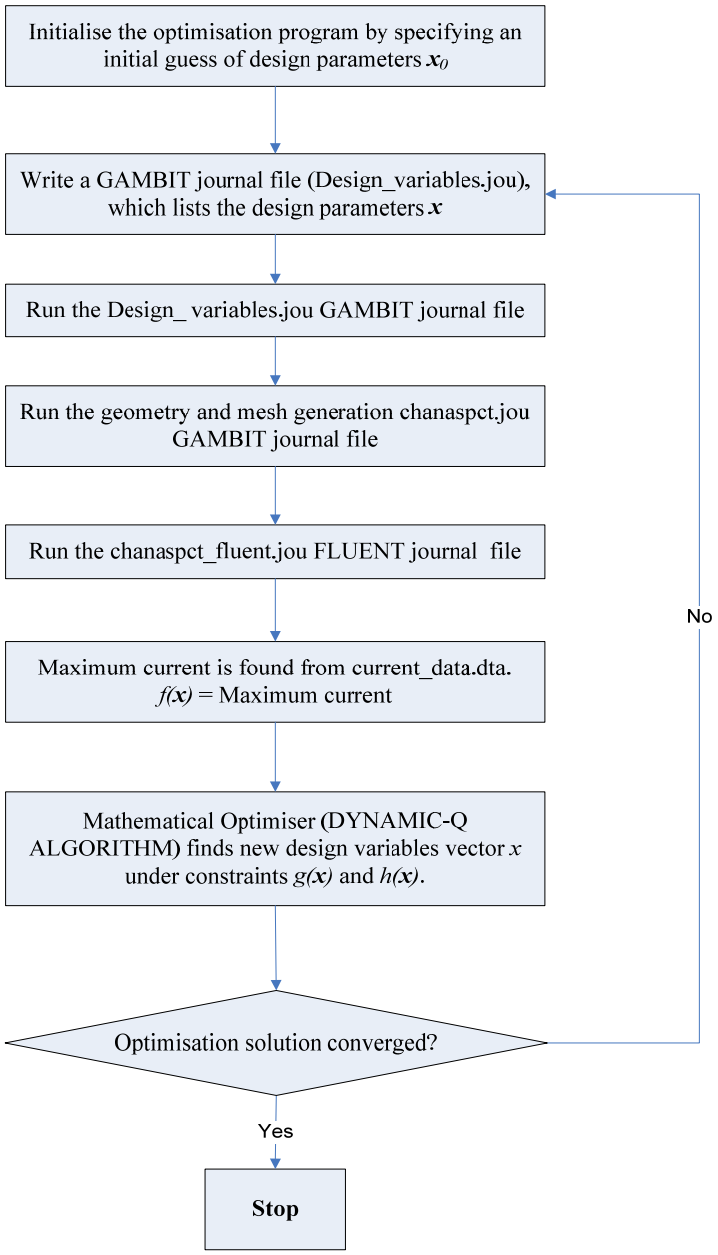

Figure 6.3 Optimisation automation flow diagram

6.5 RESULTS AND DISCUSSION

6.5.1 MODEL VALIDATION

In computational modelling, grid independence study and comparison of the CFD results with experimental data are the prescribed metrics for validation and verification of the CFD modelling studies. For fuel cell performance description, the polarisation or voltage-current (*IV*) curve is one of the most important final outcomes of numerical simulation and is widely used for validation purposes [193]. The simulation results for the base case operating conditions were verified against experimental measurements of Wang *et al.* [33]. The computed polarisation curve shown in Figure 6.4 is in good agreement with the experimental curves in the low load region. However, the model current density in the high mass transport limited region (> 1.5 A/cm^2) is higher than the experimental values. This might be due to possible experimental uncertainty or inadequate account of the effect of reduced oxygen transport, as a result of water flooding at the cathode side of the fuel cell at higher current density [150]. However, the predicted dependent variable distribution patterns could still be used successfully for better understanding of the complicated processes in fuel cell systems.

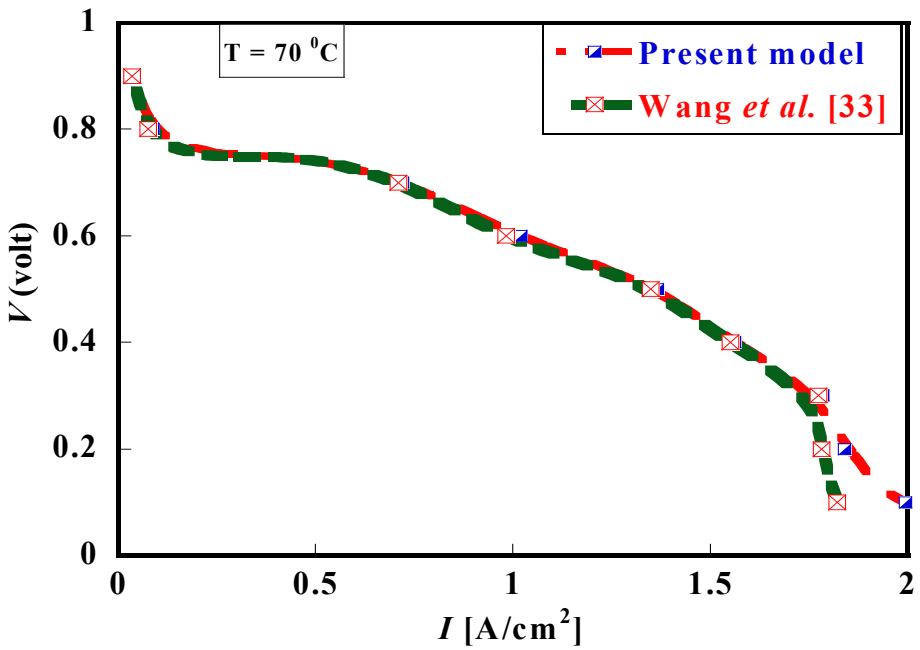

Figure 6.4 Comparison of numerical model prediction and experimental polarisation curves at base condition

6.5.2 PARAMETRIC STUDY RESULTS

In this section, a series of simulations was performed on a range of PEM fuel cell operating parameters to investigate their effect on the performance of the system. These parameters were investigated at operating cell voltage of 0.7 V and results are presented below.

First, the effect of temperature on the performance of a PEM fuel cell and the investigation of an optimal temperature range for the modelled PEM fuel cell system in this study is shown. Figure 6.5 shows the effect of an operating temperature from 50ºC to 90ºC on the performance of the PEM fuel cell system at steps of 10°C. The PEM fuel performance increase with the increase in cell temperature between 50ºC and 75ºC, since the water removal is easier and prevents incidence of flooding. The cell improvement at this temperature range is more noticeable at higher cell current

density. Meanwhile, an onset of decline in performance is observed as the operating temperature is increased beyond 75ºC. Profound performance deterioration occurred at temperatures between ≈75ºC and 90ºC, practically as a result of high membrane dehydration at these elevated temperatures.

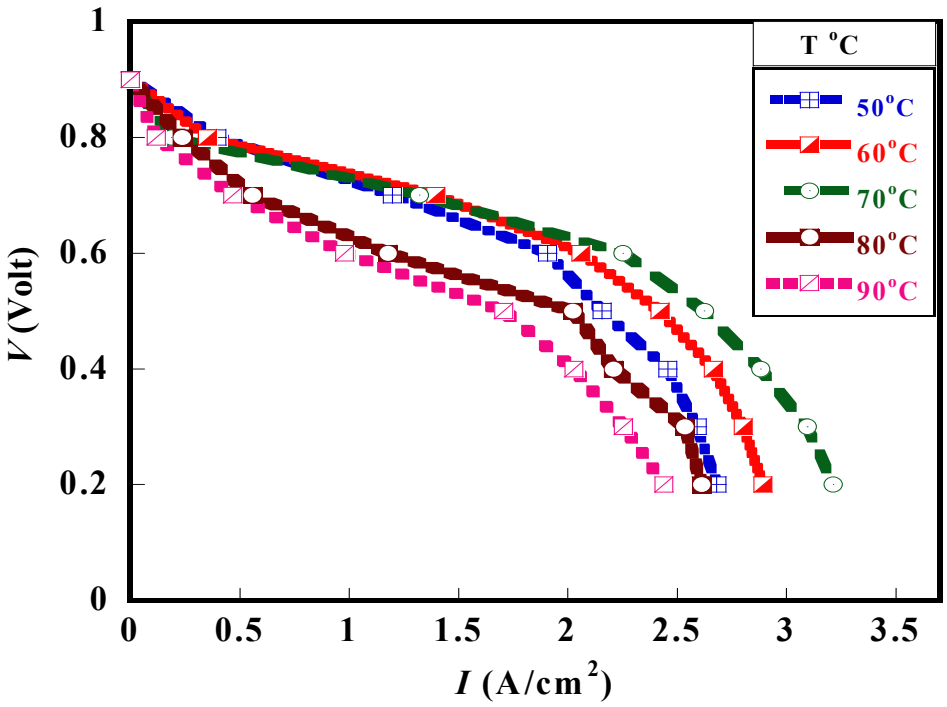

Figure 6.5 Effect of temperature on the PEM fuel cell performance at base conditions

Figure 6.6 clearly shows the optimal performance behaviour for the PEM fuel cell model and the point of decline of performance as the cell temperature increases beyond the optimal range level. This observed performance reduction phenomenon is a critical factor hindering the operation of PEM fuel cells beyond a certain temperature range to avoid fuel cell failure.

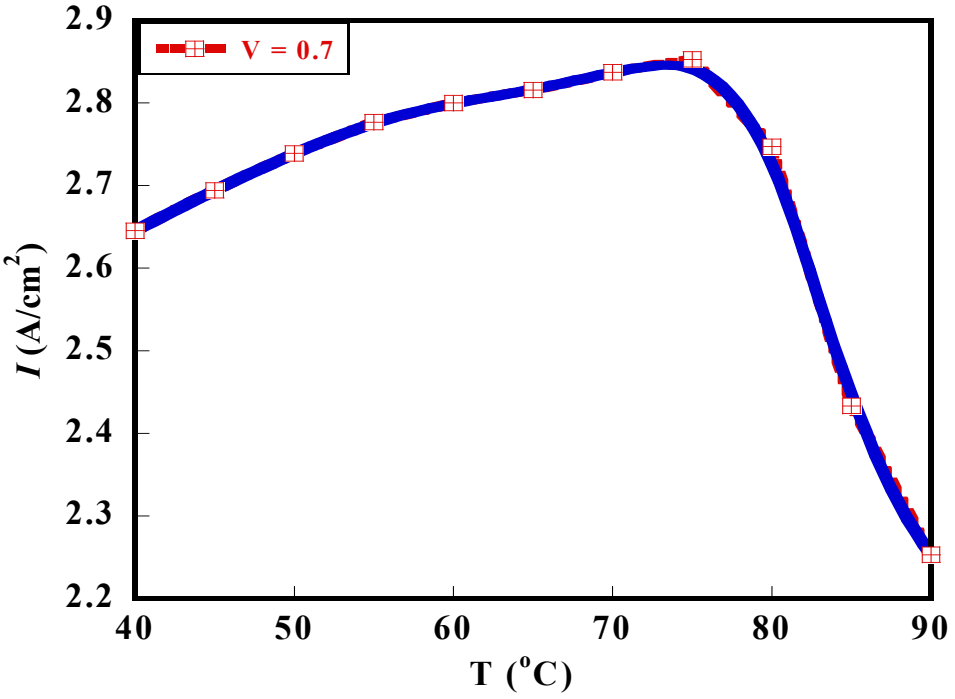

Figure 6.6 The cell current density as a function of temperature and the operating cell voltage

Figure 6.7 shows the polarisation curve at a varying stoichiometry number for a constant temperature (70°C) and pressure (P = 3 bar). For a low stoichiometry number, the removal of the cathode outlet flow decreases, thereby keeping the water concentration in the membrane layer increasing. This results in lower membrane resistance and subsequent lower ohmic over-potential, hence the improvement in cell performance. Meanwhile, at higher current density of the fuel cell, the low stoichiometry number adversely affects the cathode over-potential due to excessive resident water in the catalyst layer of the fuel cell system. Figure 6.8 depicts the PEM fuel cell behaviour at varying stoichiometry ratios of the cathode for three different current density loads. The figure shows that, at relatively low current density of the fuel cell system (0.42 A/cm^2), the air stoichiometry has little impact on the temperature.

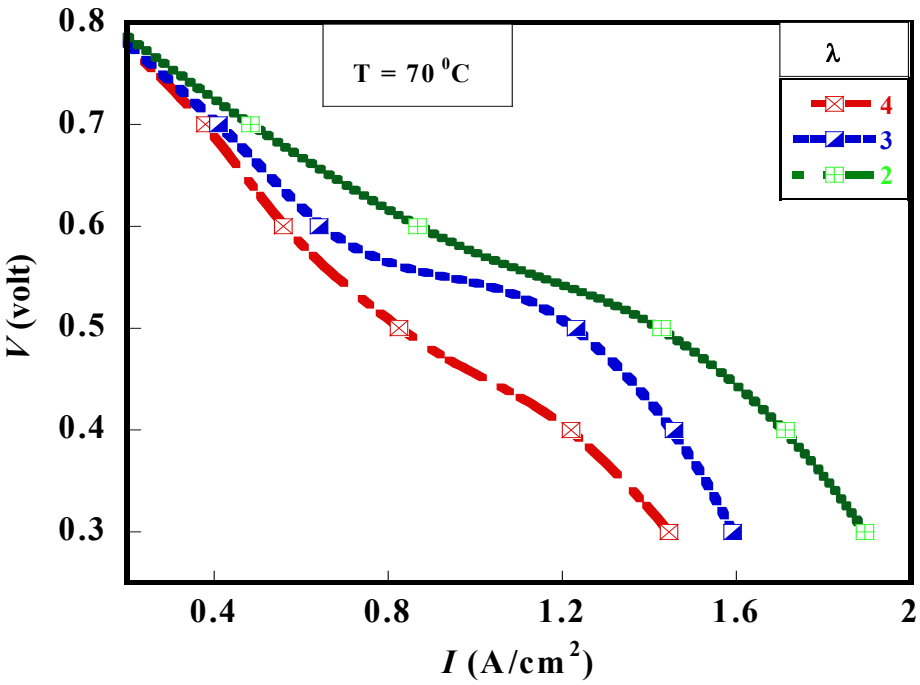

Figure 6.7 *I-V* curve at varying stoichiometry number. P = 3.0 bar and Re = 500

At this low current density, the rate of fuel consumption is small and the heat generation in the fuel cell system is minimal. For an increased current density (i.e. 0.72 A/cm^2) of the fuel cell system, which corresponds to higher reaction rates in the fuel cell system and subsequently increases in heat generation, the effect of the stoichiometry ratio becomes glaring on the cell temperature. The increased air stream improves heat transfer in the fuel cell system. This shows the possibility of an optimal match of temperature and stoichiometry ratio for improved fuel cell system performance.

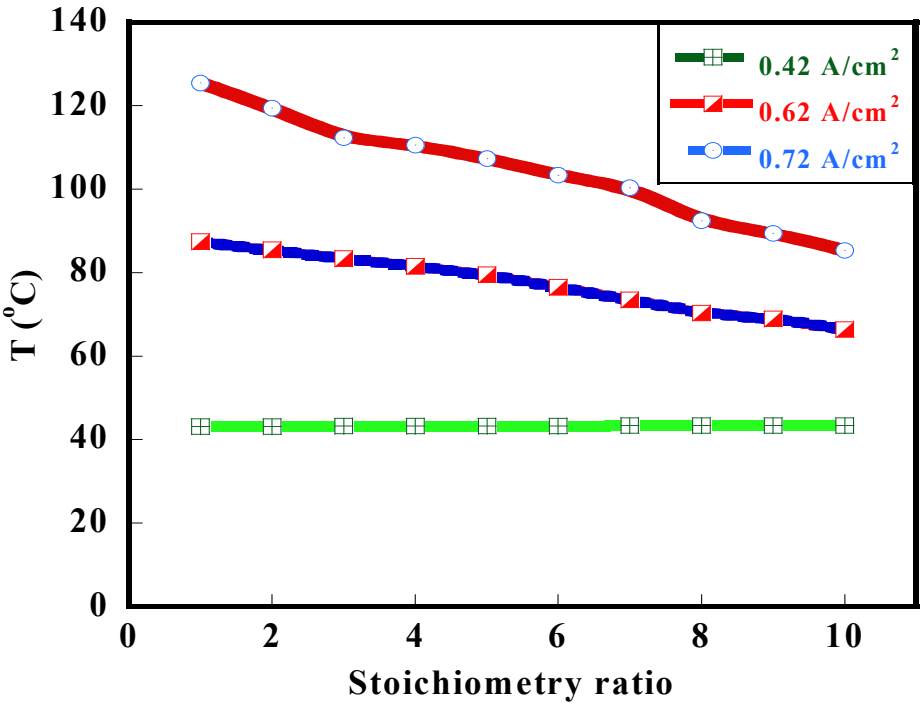

Figure 6.8 Effect of stoichiometry ratio on the PEM cell temperature at cell voltage of 0.7 V

Figure 6.9 shows the influence of relative humidity at the cathode inlet on the fuel cell output voltage. At an increased relative humidity at the cathode inlet, air transport to the catalyst is hindered. This results in an increase in the cathode over-potential, especially at a high operating current density of the fuel cell system. There is an increase in the generation of liquid water formation which results in reduced PEM fuel cell performance. This result shows that the relative humidity of the cathode inlet has a significant effect on liquid water formation and the extent of heat removal within the fuel cell system. For optimal system performance, this effect could be optimised in relation to other operating parameters.

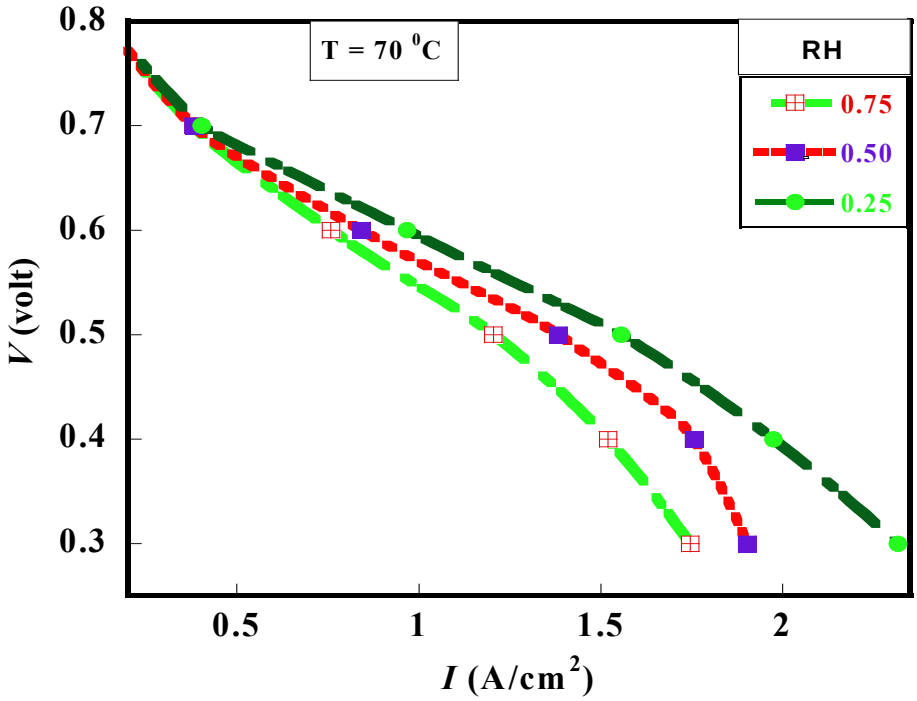

Figure 6.9 *I-V* curve at varying relative humidity (*RH*). *P* = 3.0 bar and Re = 500

Figure 6.10 shows the fuel cell performance at different aspect ratios of the cooling channels for a Reynolds number of 500. The result shows that fuel cell performance increases as the aspect ratio of the cooling channels increases to an operating temperature of 70ºC, until it reaches an optimal aspect ratio of ≈ 3.0 mm. Beyond the aspect ratio of about 3.0, cell performance starts to deplete. This result shows the existence of an optimal channel aspect ratio that optimises fuel cell performance in terms of current density. Figure 6.11 shows the *IV* curve for the cooling channel aspect ratios (Table 6.4) investigated at the base operating condition of the fuel cell. It is observed that fuel cell performance increases with the increase of the cooling channel aspect ratio at a cell operating temperature of 70°C. This increase in performance is likely due to an improvement in the cooling within the PEM fuel cell system, thereby increasing the cell membrane hydration and subsequently positively aiding cell performance.

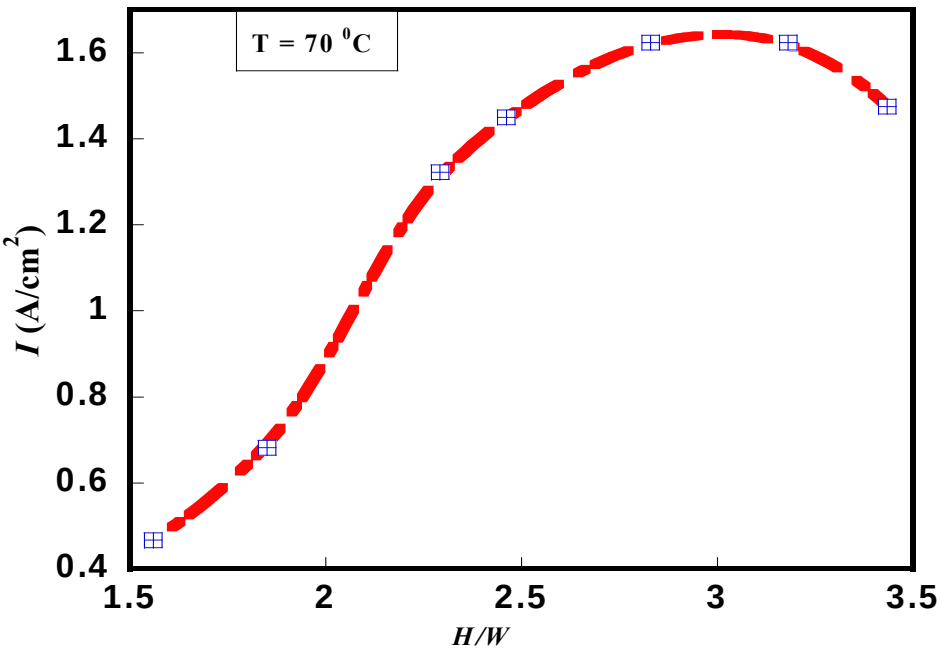

Figure 6.10 The cell current density at different aspect ratio at a cell potential of 0.7 V and a fixed Reynolds number of 500

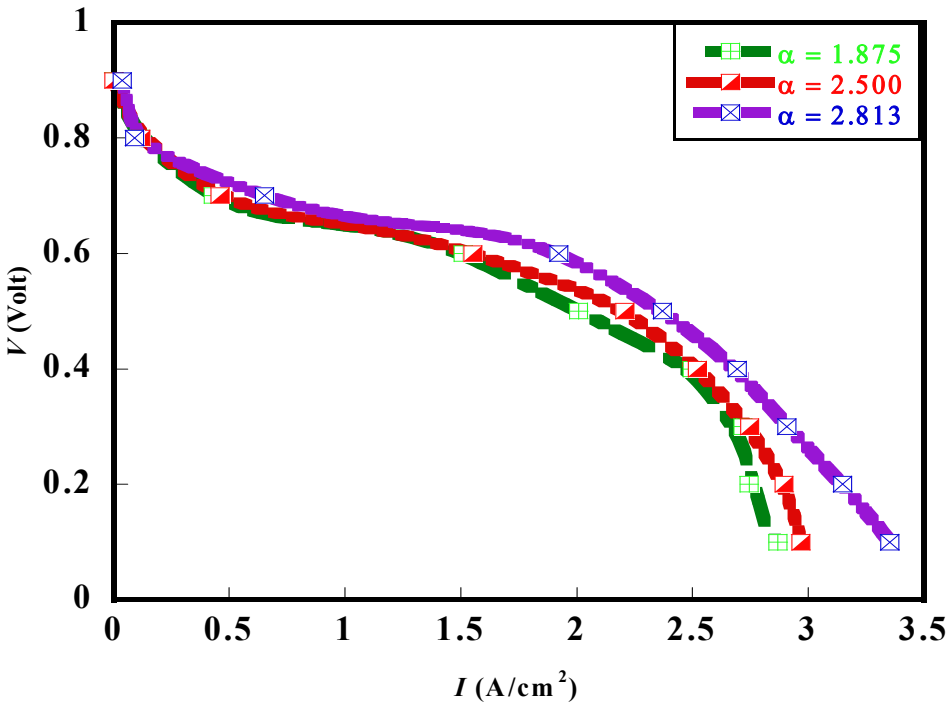

Figure 6.11 Current density at three cases of channel aspect ratio and Re = 500

6.5.3 OPTIMISATION RESULTS

The results obtained previously on the effect of the stoichiometry ratio, relative humidity and cooling channel aspect ratio on performance of the PEM fuel cells suggest the possibility of an optimal combination of these parameters for improved performance of PEM fuel cells when temperature is increased beyond the critical operating temperature which is typical of low temperature PEM fuel cells. Moreover, these factors are mutually dependent, especially in determining the rate of membrane hydration which, in turn, determines the reaction and transport characteristics in the fuel cell system. These factors are combined with varying cell operating temperatures to predict cell performance, especially when operation at higher temperatures (HT) is desired. It is well know that operating PEM fuel cells at higher operating temperatures eliminates some of the complications hindering improved performance. An intermediate HT-PEM (100-150°C) operating situation was investigated in this study. A series of numerical optimisations and calculations within the specified design constraint ranges in Section 6.4.1 were conducted to highlight the optimal

performance of the PEM fuel cell model studied in this work. Table 6.5 presents the obtained optimal values for the optimised parameters when using the Dynamic-Q algorithm.

Table 6.5 Values of optimised parameters

Model parameters	Optimised values (0.7V)
λ	4.161
RH	0.782
H/W	3.182

The maximised fuel cell performance was investigated at varying cell operating voltage for the combination of the optimal parameters in Table 6.5 at higher cell operating temperatures of the fuel cell. Table 6.6 shows the polarisation data based on the optimal design parameters for the different operating fuel cell voltages and temperatures.

Table 6.6 Polarisation data at optimised conditions and varying cell operating temperatures at Re = 500

Cell voltage (V)	I (A/cm^2) (T = 120 °C)	I (A/cm^2) (T = 130 °C)	I (A/cm^2) (T = 150 °C)
0.7	3.1421	3.6213	3.8228
0.6	4.0627	4.7341	5.1431
0.5	4.6814	5.4326	5.6314
0.4	5.3343	5.9531	6.3281

The results presented in Table 6.6 above shows that there is improvement in cell performance at different cell voltages with increasing cell operating temperatures. Higher performance was obtained al low cell operating voltages compared to higher cell voltages at different temperature ranges. The increase in cell current density difference was more prominent between the temperatures of 120°C and 130°C, but as

temperature increased towards 150°C, cell performance started to deplete negatively. When the operation was conducted beyond the 150°C level, the cell performance reduction became highly noticeable. This is most likely due to high level membrane dehydration beyond this temperature (150°C) level. The cooling to sustain the thermal build-up in the cell structure was no longer effective at this higher temperature level. Moreover, thermal stresses in PEM fuel cells are shown to rise as cell current density increases.

Figure 6.12 shows the peak current density as a function of cooling channel aspect ratio and cell temperature. An optimum cooling channel aspect ratio exists for the examined temperature ranges in which the peak fuel cell current density is maximised. This obtained result suggests that optimal arrangements of the channel geometry (aspect ratio), that could effectively maximise the cell current density of the fuel cell system, are feasible. In Figure 6.13, the optimal aspect ratio is shown as a function of the coolant Reynolds number and temperatures. The figure depicts an increase in the aspect ratio of the cooling channels as the Reynolds number increases from 100 to ≈ 300, but the rate of increment starts declining as the Reynolds number increases from 300.

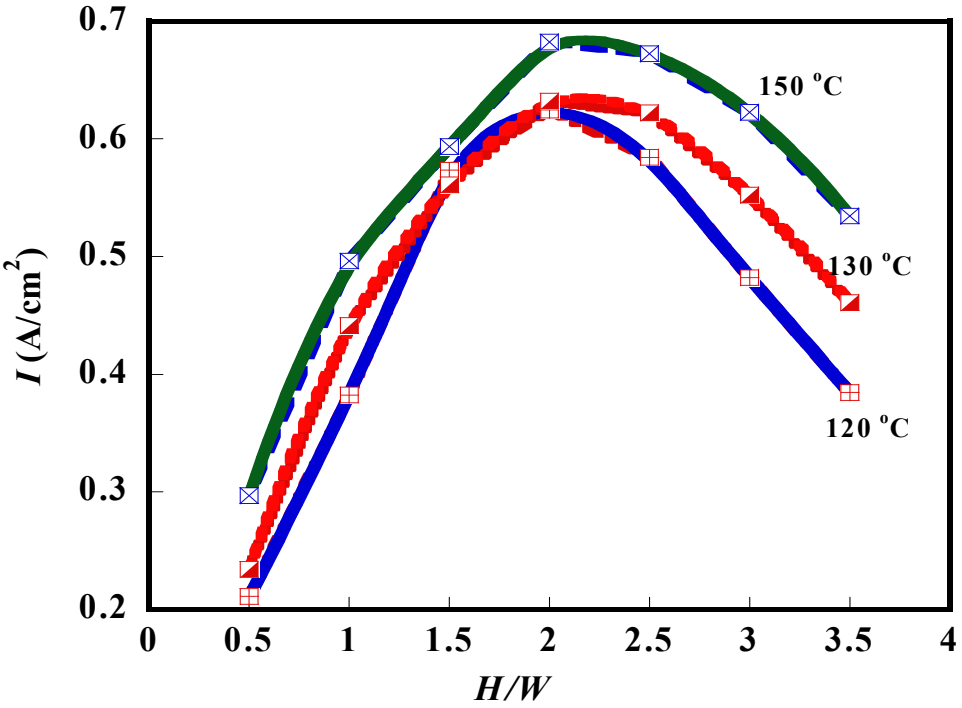

Figure 6.12 Effect of optimised cooling channel aspect ratio on the peak fuel cell current density at different temperatures and cell potential of 0.7V

The result further shows that, for an increased temperature to operate the fuel cell system, the required optimal aspect ratio increases, but at a relatively lower rate due to reduced system temperature as the coolant Reynolds number is increased. The result presented in Figure 6.13 can be correlated at temperature T = 110ºC by

$$\left(H/W\right)_{opt} = 2.22\,Re^{0.058} \quad . \tag{6.17}$$

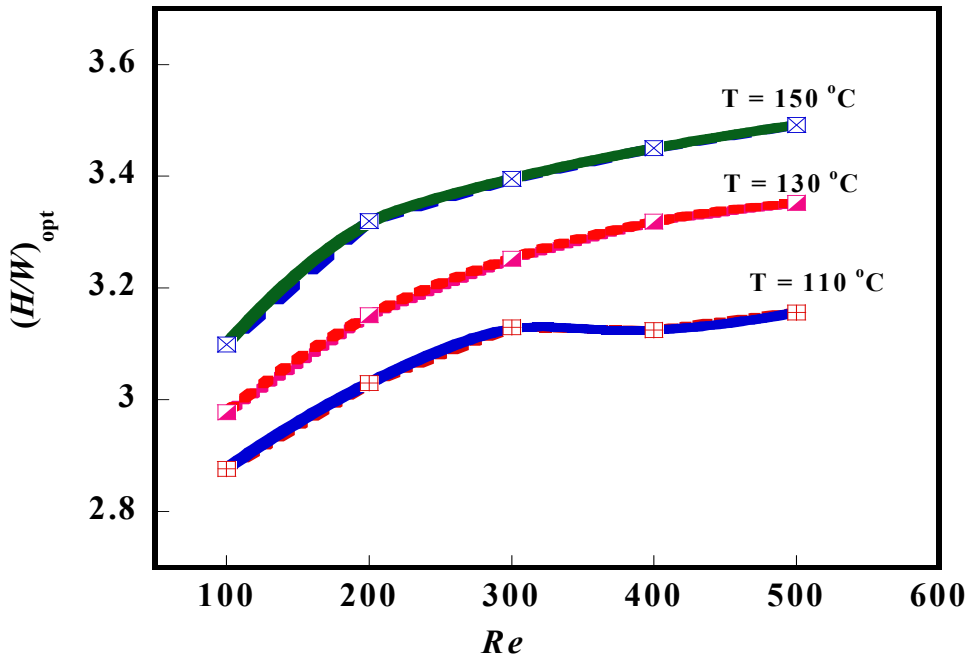

Figure 6.13 Effect of Reynolds number and temperature on the optimised aspect ratio of the cooling channel and cell potential of 0.7V

Figure 6.14 shows the effect of the maximised fuel cell current density as a function of the cooling gas Reynolds number for fixed cell temperatures and a fixed cooling channel aspect ratio of 2.50 mm. The maximised current density increases with an increase in the cooling channel Reynolds number. The result presented in Figure 6.14 can be correlated at temperature T = 130ºC by

$$I_{max} = 1.93\, Re^{0.092} \quad . \tag{6.18}$$

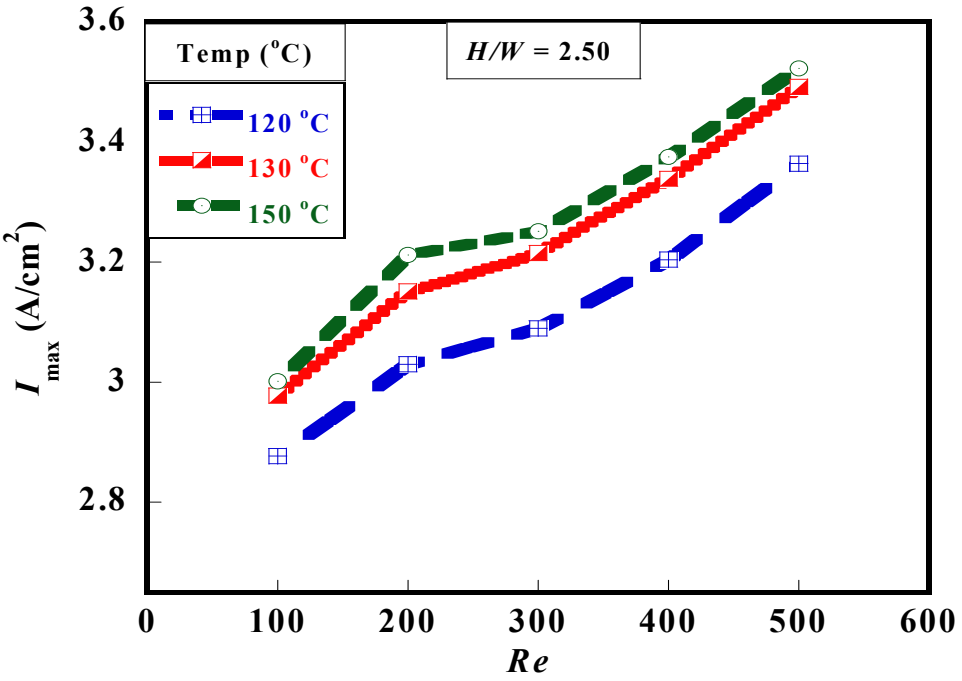

Figure 6.14 Effect of Reynolds number on the maximum current density at different cell temperatures and cell potential of 0.7V

In Figure 6.15, temperature contours on the membrane section of the fuel cell system are presented for varying cooling channel aspect ratios for a fuel cell voltage of 0.7 and a Reynolds number of 500. The result shows an improved temperature profile on the membrane section as the aspect ratio of the cooling channel increases for the examined cooling air Reynolds number.

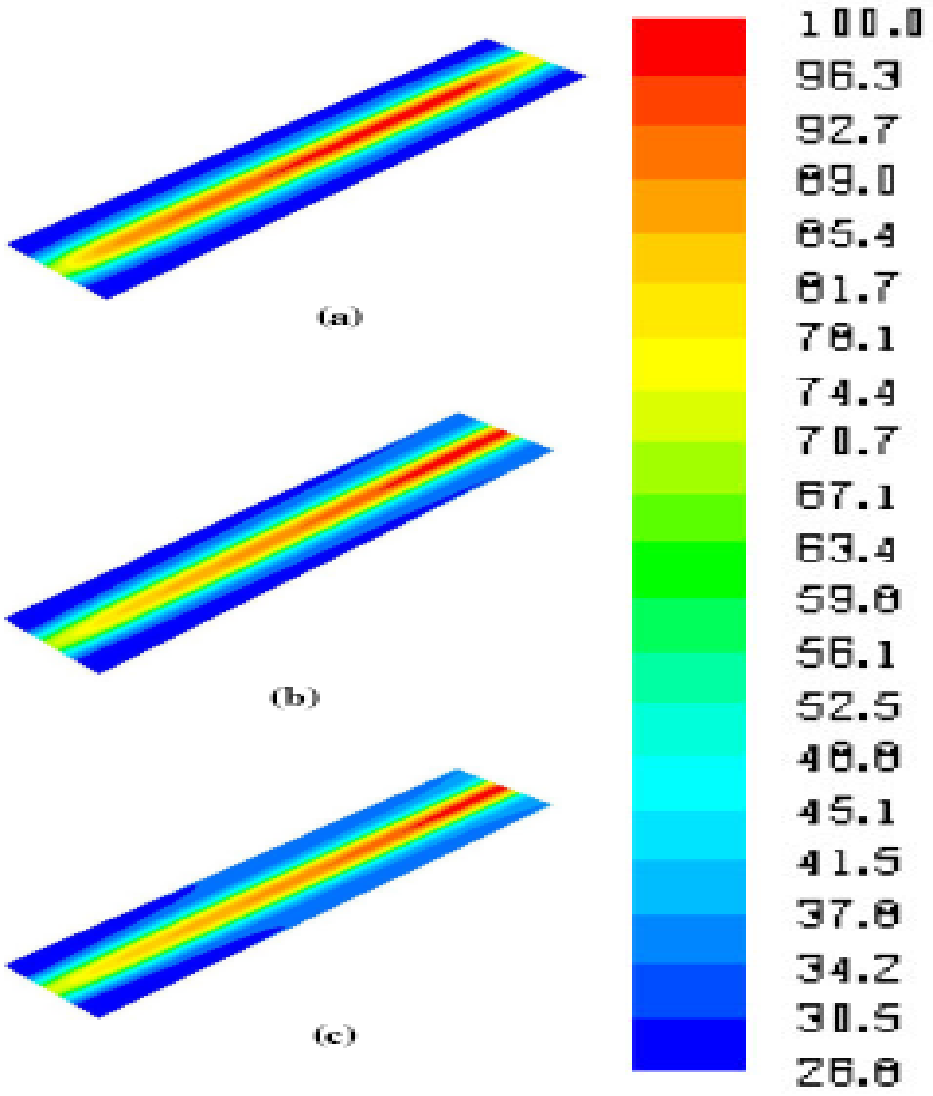

Figure 6.15 The local distribution of temperature along the membrane at different cooling channel aspect ratios and cell operating voltage of 0.7 V and Re = 500: (a) H/W = 1.875, (b) H/W = 2.500 and (c) H/W = 2.813

CONCLUSION

This chapter of the thesis is aimed at developing a numerical approach to improving PEM fuel cell performance at elevated operating temperatures through the combination of operating parameters with cooling channel aspect ratios. Numerical results indicate that operating parameters such as the stoichiometry ratio, relative

humidity and the cooling channel aspect ratio have a significant effect on fuel cell performance, primarily in determining the level of membrane dehydration of PEM fuel cells. Optimal values of the stoichiometry ratio, relative humidity and cooling channel aspect ratios were obtained by integrating a direct problem solver with an optimiser (Dynamic-Q). For the particular PEM fuel cell model operating conditions considered in this work, fuel cell performance is considerably enhanced when combining the studied parameters. Performance is more outstanding at temperatures between 120°C and 130°C. The performance increment then declines gradually from 130°C to 150°C. It should be noted that beyond 150°C, there is no significant increase in cell performance. The result of this work further shows that maximised current density also exist for varying cooling channel aspect ratios of the fuel cell system. The result also shows the possibility of operating low temperature PEM fuel cells beyond the typical critical temperatures ($\approx$ 75-80ºC), by using the combined optimal of the stoichiometry ratio, relative humidity and cooling channel geometry without the need for special temperature resistant materials for the PEM fuel cell. This study can easily be extended to varying cooling channel geometries and scaled for application in PEM stack systems for enhanced PEM fuel cell performance.

7

CHAPTER 7: CONCLUSIONS AND RECOMMENDATIONS

Although fossil fuel energy systems are affordable and widely available, they are finite and often accompanied by environmental pollution which has a negative impact on agriculture, health, social and the economic condition of the populace. Thus, the search for an alternative pollution-free affordable and widely-available energy source to replace the conventional fossil fuel has been receiving increased attention in the last decade. In this regard, the proton exchange membrane (PEM) fuel cell system has been touted to be one of the most promising clean and highly efficient power generation technologies of the future. In this thesis, factors that can enhance the performance of PEM fuel cell systems have been explored by using a combined numerical modelling and optimisation approach. The methodology developed in this work ensures an effective and accurate prediction of PEM fuel cell performance under different operating conditions. Novel approaches to performance enhancement were also introduced, especially in areas of reactant gas and thermal cooling optimisation for PEM fuel cells. The enhancement methodologies form the basis for new component geometry development that can be utilised to improve the advancement in system performance and manufacturing.

7.1 CONCLUSIONS

The major achievements and conclusions drawn from this study are summarised in the following.

(1) *Development of a finite-volume model to predict the performance of a PEM fuel cell system under different operating and design parameters:*

- This model highlights that temperature, GDL porosity, cathode gas mass flow rate and species flow orientation has significant impact on the performance of a PEM fuel cell.

- The model further shows that the impact of operating parameters on the performance of a PEM fuel cell is more significant at low operating cell voltages than at higher operating fuel cell voltages

- The results from the model underscore the interactive mutual interdependence of these fuel cell parameters during fuel cell operation and the need for an optimal match for these parameters for optimum fuel cell design.

(2) *Development of a finite-volume approach, combined with an optimisation algorithm to model reactant gas transport in a PEM fuel cell with a pin fin insert in the channel flow:*

- This model shows that performance in PEM fuel cells could be improved significantly by incorporating a pin fin in the channel flow. The Reynolds number had a significant effect on the diffusion of the reactant gas through the GDL medium.

- The fuel channel friction factor also increased with an increase in the clearance ratio of the pin fin while it decreased with an increasing GDL porosity. Hence, the channel friction and pressure drop can be reduced significantly with the increasing GDL porosity, though at an optimal value.

- The optimal clearance ratio and pitch for the considered fuel cell channel

decreased with an increase in the fuel channel friction factor. Optimal pin fin clearance ratio exists which offered a minimum pumping power requirement.

(3) *Development of a finite-volume approach, combined with an optimisation algorithm to model the impact of cooling channel geometry on the thermal management and performance of a PEM fuel cell system:*

- The results from this model show that fuel cell performance is considerably enhanced when PEM fuel cells operate at combined optimised design parameters. Performance is more outstanding at temperatures between 120°C and 130°C. However, the performance increment rate declines gradually from 130°C to 150°C.

- The result of this study shows the possibility of operating a PEM fuel cell beyond the critical temperature range (≤ 80°C) by using the combined optimised stoichiometry ratio, relative humidity and cooling channel geometry, without the need for special temperature resistant materials for the PEM fuel cell which constitute additional cost for PEM fuel cell development.

- It should also be noted that this study can easily be extended to different cooling channels (apart from the rectangular channels used in this study) in order to enhance the performance of PEM fuel.

In summary, this research work has shown the feasibility of designing fuel cells with enhanced performance by using only the CFD approach or this approach in combination with an optimiser. The use of the CFD approach alone provides improvement in the lead time reduction for PEM fuel cell system development when compared with development based solely on an experimental method (design and test approach). However, the obtained results are not usually a distinct optimum for system design. An optimiser such as the Dynamic-Q combined with the CFD codes

show a more robust and distinct optimal result that is more accurate and suitable for implementation during system design. Furthermore, it should be stressed that there is a need for proper understanding of the problem formulation and implementation of the modelling approach for a successful outcome, especially when combining the CFD codes with the optimisation algorithm. This hinges more on the modelling skill, expertise and experience of the modeller. The modelling methodology implemented in this thesis can be applied to other fuel cell system designs (such as Solid oxide fuel cell structure), provided a proper problem formulation is implemented. Also, scaling of the obtained results in this research work is practicable for large scale PEM fuel cell stack system design.

7.2 RECOMMENDATIONS

The numerical methodologies and models presented in this research work could be further improved and/or extended in the following directions:

- In the models presented in this thesis, assumptions of isotropic and homogeneous properties of the porous medium were applied. There is a need to evaluate PEM fuel cell system performance under different material properties of the porous medium, including the catalyst.

- In real PEM fuel cell system operation, the incidences of two-phase flow of liquid in the channel structure are inevitable and have significant impact on fuel cell performance. The physics governing the model could be improved in order to increase the applicability of this model by extension to two-phase capability.

- In modelling the phase change of liquid water, the assumptions of evaporation and condensation rate constants are commonly used. More detailed models on system performance should incorporate a functional dependence of evaporation and condensation rates rather than a constant value.

- In terms of computational complexity, large scale simulation using parallel computing will reduce the computational time, especially in such models as presented in this thesis, where multi-parameter evaluation, which combines CFD with an optimisation algorithm, is involved.

- In computational fuel cell models, such as the ones presented in this research, there is a need to validate the results against adequate experimental data. Future work should involve the design of modelled systems studied on standard fuel cell test stations. This will ensure adequate validity and implementation of model results in the PEM development process.

REFERENCES

1. Dincer, I., and Rosen, M. A., A worldwide perspective on energy environment and sustainable development, *International Journal of Energy Research*, vol. 22, pp. 1305-1321, 1998.

2. Asif, M., and Muneer, T., Energy supply, its demand and security issues for developed and emerging economies, *Renewable Sustainable Energy Review*, vol. 11, pp. 1388-1413, 2007.

3. Dorian, J. P., Franssen, H. T., and Simbeck, D.R., Global challenges in energy, *Energy policy*, vol. 34, pp. 1984-1991, 2006.

4. Dincer, I., Environmental and sustainability aspects of hydrogen and fuel cell systems, *International Journal of Energy Research*, vol. 31, pp. 29-55, 2007.

5. Energy Information Administration. World energy outlooks 2007. Preprint 99-43 (SBF), Energy Information Administration, February 2007.

6. Frey, G. W., and Linke, D. M., Hydropower as a renewable and sustainable resource meeting global energy challenges in a reasonable way, *Energy policy*, vol. 30, pp. 1261-1265, 2002.

7. Painuly, J. P., Barriers to renewable energy penetration; a framework for analysis, *Renewable energy*, vol. 24 no. 1, pp. 73-89, 2001.

8. DeLuchi, M. A., Hydrogen vehicles: an evaluation of fuel storage, performance, safety, environmental impacts, and cost, *International Journal of Hydrogen Energy*, vol. 14 no. 2, pp. 81-130, 1989.

9. Rigas, F., and Sklavounos, S., Evaluation of hazards associated with hydrogen storage facilities, *International Journal of Hydrogen Energy*, vol. 30 no. 13, pp. 1501-1510, 2005.

10. Songprakorp, R., Investigation of transient phenomena of proton exchange membrane fuel cells. PhD Thesis, Department of Mechanical Engineering, University of Victoria, 2008.

11. Karim, G. A., Hydrogen as a spark ignition engine fuel, *International Journal of Hydrogen Energy*, vol. 28, pp. 569-577, 2003.

12. Barreto, L., Makihira, A., and Riahi, K., The hydrogen economy in the 21st century: a sustainable development scenario, *International Journal of Hydrogen Energy*, vol. 28, pp. 267-284, 2003.

13. O'M Bockries, J., On hydrogen futures: towards a sustainable energy system, *International Journal of Hydrogen*, vol. 28, pp. 131-133, 2003.

14. Cropper, M. A. J., Geiger, S., and Jollie, D. M., Fuel cells: a survey of current development, *Journal of Power Sources*, vol. 131, pp. 57-61, 2004.

15. How fuel cells work: http://auto.howstuffworks.com/fuel-efficiency/alternative-fuels/fuel-cell5.htm. Accessed on 2 June, 2011.

16. Brown, J. E., Hendry, C. N., and Harborne, P., An emerging market in fuel cells? Residential combined heat and power in four countries, *Energy Policy*, vol. 35, pp. 2173-2186, 2007.

17. Giner, J., and Hunter, C.J., The mechanism of operation of the Teflon-bonded gas diffusion electrode: A mathematical model, *Journal of Electrochemical Society*, vol. 116 no. 8, pp. 1124-1130, 1969.

18. Yang, S. C., and Cutlip, M. B., Further development of an approximate model for mass transfer with reaction in porous gas-diffusion electrodes to include substrate, *Journal of Electrochimica Acta.* vol. 34, pp. 703-705, 1989.

19. Cutlip, M. B., Yang, S. C., and Stonehart, P., Simulation and optimisation of porous gas-diffusion electrodes used in hydrogen oxygen phosphoric acid fuel cells- II development of a detailed anode model, *Electrochimica Acta*, vol. 36 no. 3-4, 547-553, 1991.

20. Paganin, V. A., Ticianelli, E. A., and Gonzalez, E. R., Development and electrochemical studies of gas diffusion electrodes for polymenr electrolyte fuel cells, *Journal of Applied Electrochemistry*, vol. 26 no. 3, pp. 297-304, 1996.

21. Parthasarathy, A., Srinivasan, S., Appleby, A. J., and Martin, C. R., Pressure dependence of the oxygen reduction reaction at the platinum microelectrode/Nafion interface: Electrode kinetics and mass transport, *Journal of Electrochemical Society*, vol. 139, pp. 2856-2861, 1992.

22. Kim, J., Lee, S. M., Srinivasan, S., and Chamberlin, C. E., Model of proton exchange fuel cell performance using an empirical equation, *Journal of Electrochemical Society*, vol. 142, pp. 2670-2674, 1995.

23. Bernardi, D. M., and Verbrugge M. W., Mathematical model of a gas diffusion electrode bonded to a polymer electrolyte, *AIChE Journal*, vol. 37 no. 8, pp. 1151-1163, 1991.

24. Springer, T. E., Zawodzinski, T. A., and Gottesfeld, S., Polymer electrolyte fuel cell model, *Journal Electrochemical Society*, vol. 138 no. 8, pp. 2334-2342, 1991.

25. Weber, A. Z., and Newman, J., Modeling transport in polymer-electrolyte fuel cells, *Journal of Chemical Reviews*, vol. 104, pp. 4679-4726, 2004.

26. Yi, J. S., and Nguyen, T. V., Multicomponent transport in porous electrodes of proton exchange membrane fuel cells using the interdigitated gas distributors, *Journal of Electrochemical Society*, vol. 146 no. 1, pp. 38-45, 1999.

27. Chan, S. H., and Tun, W. A., Catalyst layer models for proton exchange membrane fuel cells, *Chemical Engineering & Technology*, vol. 24 no. 1, pp. 51-57, 2001.

28. Jaouen, F., Lindberg, G., and Sundholm, G. Investigation of mass-transport limitations in the solid polymer fuel cell cathode, *Journal Electrochemical Society*, vol. 149 no. 4, pp. A437-A447, 2002.

29. Berning, T., Lu, D. M., and Djilali, N., Three-dimensional computational analysis of transport phenomena in a PEM fuel cell, *Journal of Power Sources*, vol. 106, pp. 284-294, 2002.

30. Kazim, A., Forges, P., and Liu, H. T., Effects of cathode operating conditions on performance of a PEM fuel cell with interdigitated flow fields, *International Journal of Energy Research*, vol. 27, pp. 401-414, 2003.

31. Chu, H. S., Yeh, C., and Chen, F., Effects of porosity change of gas diffuser on performance of proton exchange membrane fuel cell, *Journal of Power Sources*, vol. 123, pp. 1-9, 2003.

32. Jeng, K. T., Lee, S. F., Tsai, G. F., and Wang, C. H., Oxygen mass transfer in PEM fuel cell gas diffusion layer, *Journal of Power Sources*, vol. 138, pp. 41-50, 2004.

33. Wang, L., Husar, A., Zhou, T. H., and Liu, H. T., A parametric study of PEM fuel cell performances, *International Journal of Hydrogen Energy*, vol. 28 no. 11, pp. 1263-1272, 2003.

34. Lee, H. K., Park, J. H., Kim, D. Y., and Lee, T. H., A study on the characteristics of the diffusion layer thickness and porosity of the PEMFC, *Journal of Power Sources*, vol. 131, pp. 200-206, 2004.

35. Hwang, J. J., Chen, C. K., Savinell, R. F., Liu, C. C., and Wainright, J., A three-dimensional numerical simulation of transport phenomena in the cathode side of a PEMFC, *Journal of Applied Electrochemistry*, vol. 34, pp. 217-224, 2004.

36. Meng, H., Wang, C. Y., Electron transport in PEFCs, *Journal of Electrochemical Society*, vol. 151 no. 3, pp. A358-A367, 2004.

37. Du, C. Y., Shi, P. F., Cheng, X. Q., and Yin, G. P., Effective protonic and electronic conductivity of the catalyst layers in proton exchange membrane fuel cells, *Electrochemistry Commununications*, vol. 6, pp. 435-440, 2004.

38. Pasaogullari, U., and Wang, C.Y., Two-phase modeling and flooding prediction of polymer electrolyte fuel cells, *Journal of Electrochemistry Society*, vol. 152 no. 2, pp. A380-A390, 2005.

39. Lu, K. W., and McGurick, J. J., 2D and 3D modeling of a PEMFC cathode with interdigitated gas distributors, *Journal of Electrochemical Society*, vol. 152 no. 4, pp. A811-A817, 2005.

40. Sun, W., Pepply, B. A., and Karan, K., Modeling the influence of GDL and flow-field plate parameters on the reaction distribution in the PEMFC cathode catalyst layer, *Journal of Power Sources*, vol. 144, pp. 42-53, 2005.

41. Zhou, T. H., and Liu, H. T., A 3D model for PEM fuel cells operated on reformate, *Journal of Power Sources*, vol. 138, pp. 101-110, 2004.

42. Chan, S. H., Goh, S. K., and Jiang, S. P., A mathematical model of polymer electrolyte fuel cell with anode CO kinetics, *Electrochimica Acta*, vol. 48, pp. 1905-1919, 2003.

43. Baschuk, J. J., Rowe, A. M., and Li, X., Modeling and simulation of PEM fuel cells with CO poisoning, *Transactions of the ASME*, vol. 125, pp. 94-100, 2003.

44. Mawardi, A., and Pitchumani, R., Effects of parameter uncertainty on the performance variability of proton exchange membrane (PEM) fuel cells, *Journal of Power Sources*, vol. 160 no. 1, pp. 232-245, 2006.

45. Hsieh, S. S., Yang, S. H., Kuo, J. K., Huang, C. F., and Tsai, H. H., Study of operational parameters on the performance of micro PEMFCs with different flow fields, *Energy Conversion Management*, vol. 47 no.13-14, pp. 1868-1878, 2006.

46. Yan, Q. G., Toghiani, H., and Causey, H., Steady state and dynamic performance of proton exchange membrane fuel cells (PEMFCs) under various operating conditions and load changes, *Journal of Power Sources*, vol. 161 no.1, pp. 492-502, 2006.

47. Amirinejad, M., Rowshanzamir, S., and Eikani, M. H., Effects of operating parameters on performance of a proton exchange membrane fuel cell, *Journal of Power Sources*, vol. 161 no. 2, pp. 872-875, 2006.

48. Zhou, B., Huang, W. B., Zong, Y., and Sobiesiak, A., Water and pressure effects on a single PEM fuel cell, *Journal of Power Sources*, vol. 155 no.2, pp. 190-202, 2006.

49. Yan, X. Q., Hou, M., Sun, L. Y., Liang, D., Shen, Q., and Xu, H. F., AC impedance characteristics of a 2 kW PEM fuel cell stack under different operating conditions and load changes, *International Journal of Hydrogen Energy*, vol. 32 no. 17, pp. 4358-4364, 2007.

50. Zhang, J. L., Tang, Y. H., Song, C. J., Xia, Z. T., Li, H., and Wang, H. J., PEM fuel cell relative humidity (RH) and its effect on performance at high temperatures, *Electrochimical Acta*, vol. 53 no. 16, pp. 5315-5321, 2008.

51. Hung, A. J., Sung, L. Y., Chen, Y. H., and Yu, C. C., Operation-relevant modeling of a experimental proton exchange membrane fuel cell, *Journal of Power Sources*, vol. 171 no. 2, pp. 728-737, 2007.

52. Hwang, J. J., Chao, C. H., Ho, W. Y., Chang, C. L., and Wang, D. Y. Effect of flow orientation on thermal-electrochemical transports in a PEM fuel cell, *Journal of Power Sources*, vol. 157, pp. 85-97, 2006.

53. Yuan, W., Tang, Y., Pan, M., Li, Z., and Tang, B., Model prediction of effects of operating parameters on proton exchange membrane fuel cell performance, *Renewable Energy*, vol. 35, pp. 656-666, 2010.

54. Ludlow, D. J., Calebrese, C. M., Yu, S. H., Dannehy, C. S., Jacobson, D. L., Hussey, D. S., Arif, A., Jensen, M. K., and Eisman, G. A., PEM fuel cell membrane hydration measurement by neutron imaging, *Journal of Power Sources*, vol. 162, pp. 271-278, 2006.

55. Kumar, A., and Reddy, R. G., Effect of channel dimensions and shape in the flow-field distributor on the performance of polymer electrolyte membrane fuel cells, *Journal of Power Sources*, vol. 113, pp. 11-18, 2003.

56. Maharudrayya, S., Jayanti, S., and Deshpande, A. P., Flow distribution and pressure drop in parallel-channel configurations of planar fuel cells, *Journal of Power Sources*, vol. 144, pp. 94-106, 2005.

57. Shimpalee, S., Greenway, S., and Van Zee, J. W., The impact of channel path length on PEMFC flow-field design, *Journal of Power Sources*, vol. 160, pp. 398-406, 2006.

58. Inoue, G., Matsukuma, Y., and Minemoto, M., Effect of gas channel depth on current density distribution of polymer electrolyte fuel cell by numerical analysis including gas flow through gas diffusion layer, *Journal of Power Sources*, vol. 157, pp. 136-152, 2006.

59. Ahmed, D. H. and Sung, H. J., Effects of channel geometric configuration and shoulder width on PEMFC performance at high current density, *Journal of Power Sources*, vol. 162, pp. 327-339, 2006.

60. Cheng, C., Lin, H., and Lai, G., Design for geometric parameters of PEM fuel cell by integrating computational fluid mechanics with optimization method, *Journal of Power Sources*, vol. 165, pp. 803-813, 2007.

61. Xu, C., and Zhao, T. S., A new flow field design for polymer electrolyte-based fuel cells, *Journal of Electrochemistry Communications*, vol. 9, pp. 497-503, 2007.

62. Li, X., Sabir, I., and Park, J., A flow channel design procedure for PEM fuel cells with effective water removal, *Journal of Power Sources*, vol. 163, pp. 933-942, 2007.

63. Shimpalee, S., and Van Zee, J. W., Numerical studies on rib and channel dimension of flow-field on PEMFC performance, *International Journal of Hydrogen Energy*, vol. 32, pp. 842-856, 2007.

64. Owejan, J. P., Trabold, T. A., Jacobson, D. L., Arif, M., and Kandlikar, S. G., Effects of flow field and diffusion layer properties on water accumulation in a PEM fuel cell, *International Journal of Hydrogen Energy*, vol. 32, pp. 4489-4502, 2007.

65. Peng, L., Lai, X., Liu, D., Hu, P., and Ni, J., Flow channel shape optimum design for hydroformed metal bipolar plate in PEM fuel cell, *Journal of Power Sources*, vol. 178, pp. 223-230, 2008.

66. Sinha, P. K., Wang, C., and Beuscher, U., Effects of flow field design in the performance of elevated-temperature polymer electrolyte fuel cells, *International Journal of Energy Research*, vol. 31, pp. 390-411, 2007.

67. Hsieh, S., and Chu, K., Channel and rib geometric scale effects of flowfield plates on the performance and transient thermal behavior of a micro-PEM fuel cell, *Journal of Power Sources*, vol. 173, pp. 222-232, 2007.

68. Ferng, Y., Su, A., and Lu, S., Experiment and simulation investigation for effects of flow channel patterns on the PEMFC performance, *International Journal of Energy Research*, vol. 32, pp. 12-23, 2008.

69. Wang, X., Duan, Y., Yan, W., and Peng, X., Local transport phenomena and cell performance of PEM fuel cells with various serpentine flow field designs, *Journal of Power Sources*, vol. 175, pp. 397-407, 2008.

70. Li, X., and Sabir, I., Review of bipolar plates in PEM fuel cells: Flow-field designs, *International Journal of Hydrogen Energy*, vol. 30, pp. 359-371, 2005.

71. Um, S., Wang, C. Y., and Chen, K. S., Computational fluid dynamics modeling of proton exchange membrane fuel cells, *Journal of Electrochemical Society*, vol. 147 no. 12, pp. 4485-4493, 2000.

72. He, W., Yi, J. S., and Nguyen, T. V., Two-phase flow model of the cathode of PEM fuel cells using interdigitated flow fields, *AIChE Journal*, vol. 46 no. 10, pp. 2053-2064, 2000.

73. Chang, M. H., Chen F., Teng H. -H., Two-phase flow analysis of cathode gas diffusion layer of proton exhange membrane fuel cells, *Journal of Power Sources*, vol. 160, pp. 268-276, 2006.

74. Mazumder, S., and Cole, J. V., Rigorous 3-D mathematical modeling of PEM fuel cells II. Model predictions with liquid water transport, *Journal of Electrochemical Society*, vol. 150 no. 11, pp. A1510-A1517, 2003.

75. Dohle, H., Jung, R., Kimiaie, N., Mergel, J., and Muller, M., Interaction between the diffusion layer and the flow field of polymer electrolyte fuel cells-experiment and simulation studies, *Journal of Power Sources*, vol. 124, pp. 371-384, 2003.

76. Gurau, V., Zawodzinski, T. A., Mann, J. A., Two-phase transport in PEM fuel cell cathodes, *Journal of Fuel Cell Technology*, DOI: 10.1115/1.2821597, 2008.

77. Yan, W. M., Soong, C. Y., Chen, F., and Chu, H. S., Effects of flow distributor geometry and diffusion layer porosity on reactant gas transport and performance of proton exchange membrane fuel cells, *Journal of Power Sources*, vol. 125, pp. 27-39, 2004.

78. Wang, X. D., Duan, Y. Y., Yan, W. M., Novel serpentine flow field design for proton exchange membrane fuel cell, *Journal of Power Sources*, vol. 173, pp. 210-221, 2007.

79. Jang, J. H., Yan, W. M., Shih, C. C., Numerical study of reactant gas transport phenomena and cell performance of proton exchange membrane fuel cells, *Journal of Power Sources*, vol. 156, pp. 244-252, 2006.

80. Wang, X. D., Duan, Y. Y., and Yan, W. M., Numerical study of cell performance and local transport phenomena in PEM fuel cells with various flow channel area ratios, *Journal of Power Sources*, vol. 172, pp. 265-277, 2007.

81. Kim, Y.B., Study on the effect of humidity and stoichiometry on the water saturation of PEM fuel cells, *International Journal of Energy Research*, vol. 36, pp. 509-522, 2012.

82. Jang, J. H., Yan, W. M., Li, H. Y., and Chou, Y. C., Humidity of reactant fuel on the cell performance of PEM fuel cell with baffle-blocked flow field designs, *Journal of Power Sources*, vol. 159, pp. 468-477, 2006.

83. Nguyen, T. V., White, R. E., A water and heat management model for proton-exchange membrane fuel cells, *Journal of Electrochemical Society*, vol. 140 no. 8, pp. 2178-2186, 1993.

84. Ko, D. S., Kang, Y. M., Yang, J. S., Jeong, J. H., Choi, G. M., and Kim, D. J., The effect of channel flow pattern on internal properties distribution of a proton exchange membrane fuel cell for cathode starvation conditions, *Journal of Mechanical Science and Technology*, vol. 24 no. 2, pp. 537-543, 2010.

85. Liu, H. C., Yan, W. M., Soong, C. Y., and Chen, F., Effects of baffled-blocked flow channel on reactant transport and cell performance of a proton exchange membrane fuel cell, *Journal of Power Sources*, vol. 142, pp. 125-133, 2005.

86. Soong, C. Y., Yan, W. M., Tseng, C. Y., Liu, H. C., Chen, F., and Chu, H. S., Analysis of reactant gas transport in a PEM fuel cell with partially blocked fuel flow channel, *Journal of Power Sources*, vol. 143, pp. 36-47, 2005.

87. Liu, H. C., Yan, W. M., Soong, C. Y., Chen, F., and Chu, H. S., Reactant gas transport and cell performance of proton exchange membrane fuel cells with tapered flow field design, *Journal of Power Sources*, vol. 158, pp. 78-87, 2006.

88. Zhang, J., Xie, Z., Zhang, J., Tang, Y., Song, C., Navessin, T., Shi, Z., Song, D., Wang, H., Wilkinson, D. P., Liu, Z. -S., Liu, Z. -S., and Holdcroft S., High temperature PEM fuel cells (Review), *Journal of Power Sources*, vol. 160, pp. 872-891, 2006.

89. Faghri, A., and Guo, Z., Challenges and opportunities of thermal management issues related to fuel cell technology and modeling, *International Journal of Heat Mass Transfer*, Vol. 48, pp. 3891-3920, 2005.

90. Coppo, M., Siegel, N. P., and von Spakovsky, M. R., On the influence of temperature on PEM fuel cell operation, *Journal of Power Sources*, vol. 159, pp. 560-569, 2006.

91. Yan, W. -M., Chen, F., Wu, H. -Y., and Chu, H. -S., Analysis of thermal and water management with temperature-dependent diffusion effects in membrane of proton exchange membrane fuel cells, *Journal of Power Sources*, vol. 129, pp. 127-137, 2004.

92. Ramousse, J., Deseure, J., Lottin, O., Didierjean, S., and Maillet, D., Modeling of heat, mass and charge transfer in a PEMFC single cell, *Journal of Power Sources*, vol. 145, pp. 416-427, 2005.

93. Shimpalee, S., and Dutta, S., Numerical prediction of temperature distribution in PEM fuel cells, *Numerical Heat Transfer (Part A)*, vol. 38, pp. 111-128, 2000.

94. Shan, Y., and Choe, S. -Y., A high dynamic PEM fuel cell model with temperature effects, *Journal of Power Sources*, vol. 145, pp. 30-39, 2005.

95. Yuan, J., and Sunden, B., Numerical analysis of heat transfer and gas flow in PEM fuel cell ducts by a generalized extended Darcy model, *International Journal of Green Energy*, vol. 1 no. 1, pp. 47-63, 2004.

96. Ju, H., Meng, H., Wang, C. Y., A single –phase, non-isothermal model for PEM fuel cells, *International Journal of Heat and Mass Transfer*, vol. 48, pp. 1302-1315, 2005.

97. Perng, S. -W., and Wu H. -W., Heat transfer in channel flow, *Applied Thermal Engineering*, vol. 29 no. 17, pp. 3579-3594, 2009.

98. Yu, X., Zhou, B., and Sobiesiak, A., Water and thermal management for Ballard PEM fuel cell stack, *Journal of Power Sources*, vol. 147, pp. 184-195, 2005.

99. Berning, T., and Djilali, N., A 3D multiphase, multicomponent model of the cathode and anode of a PEM fuel cell, *Journal of Electrochemical Society*, vol. 150 no. 12, pp. A1589-A1598, 2003.

100. Kang, S., Min, K., Mueller, F., and Brouwer, J., Configuration effects of air, fuel, and coolant inlets on the performance of a proton exchange membrane fuel cell for automotive applications, *International Journal of Hydrogen Energy*, vol. 34, pp. 6749-6764, 2009.

101. Biyikoglu, A., Review of proton exchange membrane fuel cell models, *International Journal of Hydrogen Energy*, vol. 30, pp. 1181-1212, 2005.

102. O'Hayre, R., Cha, S., Colella W., and Prinz, F. B., *Fuel Cell Fundamentals*, JohnWiley & Sons, New York, 2006.

103. Mench, M. M., *Fuel Cell Engines,* John Wiley & Sons, New Jersey, 2008.

104. Kerres, J. A., Blended and cross-linked ionomer membranes for application in membrane fuel cells, *Fuel Cells*, vol. 5, pp. 230-247, 2005.

105. Bai, Z., Putthanarat, S., Rodrigues, S. J., and Dang, T. D., Properties and performance of composite electrolytes membranes based on sulfonated poly (arylenethioethersulfone) and sulfonated ploybenzimidazole, *Polymer*, vol. 52, pp. 3381-3388, 2011.

106. Barbir, F., *PEM Fuel Cells: Theory and Practice*, Elsevier Academic Press, New York, 2005.

107. Gasteiger, H. A., Gu, W., Makharia, R., and Mathias, M. F., Catalyst utilization and mass transfer limitations in the polymer electrolyte fuel cells, Electrochemical Society Meeting, Orlando, September, 2003.

108. Mathias, M. F., Roth, J., Fleming, J., and Lehnert, W., Diffusion media materials and characterization. In Vielstich, W., Lamm, A., and Gastegier, H. A. (Eds.) *Handbook of Fuel Cells, Fundamentals, Technology and Applications*, vol. 3, Fuel Cell Technology and Applications, pp. 517-537, John Wiley & Sons Ltd., 2003.

109. Arnost, D., Scheineider, P., Dynamic transport of multicomponent mixtures of gases in porous solids, Chemical Engineering Journal, vol. 57, pp. 91-99, 1995.

110. Barbir, F., Braun, J., and Neutzler, J., Properties of molded graphite bi-polar plates for PEM fuel cells, *International Journal on New Materials for Electrochemical Systems*, vol. 2, pp. 197-200, 1999.

111. Chalk, S. G., Miller, J. F., and Wagner, F. W., Challenges for fuel cells in transport applications, *Journal of Power Sources*, vol. 86, pp. 40-51, 2000.

112. Cacciola, G., Antonucci, V., and Freni, S., Technology update and new strategies on fuel cells, *Journal of Power Sources*, vol. 100, pp. 67-69, 2001.

113. http://www.lanl.gov/orgs/mpa/mpa11/Green%20Power.pdf. Accessed on 4 October 2010.

114. Naseri-Neshat, H., Shimpalee, S., Dutta, S., Lee, W. K., and Van Zee, J. W., Predicting the effect of gas-flow channel spacing on current density in PEM fuel cells, *Advanced Energy Systems*, vol. 39, pp. 337-350, 1999.

115. Barbir, F., Nadal, M., and Fuchs, M., Fuel cell powered utility vehicles, In

Buchi, F. (Ed.), *Proceedings of the Portable Fuel Cell Conference*, Lucerne, Switzerland, June 1999, pp. 113-126.

116. Yang, F., and Pitchumani, R., Transport and electrochemical phenomena. In Fuel cell technology-reaching towards commercialization, Sammes, N., (Ed.), vol. 1; Springer: London, 2006.

117. Wang, C. Y., Fundamental models for fuel cell engineering, *Chemical Review*, vol. 104, pp. 4727-4766, 2004.

118. Yao, K. Z., Karan, K., McAuley, K. B., Oosthuizen, P., Pepply, B., and Xie, T., A Review of mathematical models for hydrogen and direct methanol polymer electrolyte membrane fuel cells, *Fuel Cells*, vol. 4 no. 1-2, pp. 3-29, 2004.

119. Larminie, J., and Dicks, A., *Fuel Cell Systems Explained*. John Wiley & Sons Ltd., West Sussex England, 2000.

120. Gurau, V., Barbir, F., and Liu, H. An analytical solution of a half-Cell model for PEM fuel cells, *Journal of Electrochemical Society*, vol. 147, pp. 2468-2477, 2000.

121. Springer, T. E., Rockward, T., Zawodzinski, T. A., and Gottesfeld, S., Model for Polymer Electrolyte Fuel Cell Operation on Reformate Feed, *Journal of Electrochemical Society*, vol. 148 no. 11, pp. A11-A23, 2001.

122. Mishra, V., Yang, F., and Pitchumani, R., Analysis and design of PEM fuel Cells, *Journal of Power Sources*, vol. 141, pp. 47-64, 2005.

123. Weber, A., Darling, R., Meyers, J., and Newman, J., *In Handbook of Fuel Cells: Fundamentals, Technology, and applications*, Vielstich, W., Lamm,

A., Gasteigher, H. A., (Eds.) vol. 1, John Wiley & Sons, New York, 2003.

124. Newman, J. *Electrochemical Systems*, 2nd ed., Prentice Hall, Englewood Cliffs, NJ, 1991.

125. Bennion, D. N., *Mass transport of binary electrolyte solutions in membranes*. Water Resources Center Desalination Report No. 4, Department of Engineering, University of California Los Angeles, 1966.

126. Pintauro, P. N., and Bennion, D. N., Mass transport of electrolytes in Membranes, Development of Mathematical Transport Model, *Industrial & Engineering Chemistry Fundamentals*, vol. 23, pp. 230-234, 1984.

127. Bernardi, D. M., and Verbrugge, M. W., A Mathematical model of the solid polymer electrolyte fuel cell, *Journal of Electrochemical Society*, vol. 139 no. 9, pp. 4277-2745, 1992.

128. Verbrugge, M. W., Hill, R. F., Analysis of promising perfluorosulfonic acid membranes for fuel-cell electrolytes, *Journal of Electrochemical Society*, vol. 137, 3770-3776, 1990.

129. Weber, A. Z., Newman, J., Transport in polymer-electrolyte membranes, I. physical model, *Journal of Electochemical Society*, vol. 150 no. 7, pp. 1008-1015, 2003.

130. Rowe, A and Li, X., Mathematical modeling of proton membrane fuel cells, *Journal of Power Sources*, vol. 102, pp. 82-96, 2001.

131. Mishra, V., Yang, F., and Pitchumani, R., Analysis and design of PEM fuel cells, *Journal of Power Sources*, vol. 141, pp. 47-64, 2005.

132. Dullien, F. A. L., *Porous Media: Fluid Transport and Pore Structure*, 2nd ed., Academic Press, New York, 1992.

133. Bird, R. B., Stewart, W. E., and Lightfoot, E. N., *Transport Phenomena*, 2nd ed., John Wiley & Sons, New York, 2002.

134. Knudsen, M., *The kinetic Theory of Gases,* Methuen, London, 1934.

135. Mason, E. A., and Malinauskas, A. P., *Gas Transport in Porous Media: The Dusty-Gas Model*, Elsevier, Amsterdam, 1983.

136. Ackmann, T., de Haart, L. G. J., Lehnert, W., and Stolten, D., Modeling of Mass and Heat Transport in Planar Substrate Type SOFCs, *Journal of Electrochemical Society*, vol. 150 no. 6, pp. A783-A789, 2003.

137. Weber, A. Z., and Newman, J., Transport in polymer-electrolyte membranes III. Model validation in a simple fuel-cell model, *Journal of Electrochemical Society*, vol. 151, pp. A326-339, 2004.

138. Springer, T. E., Zawodzinski, T. A., and Gottesfield, S., Polymer electrolyte fuel cell model, *Journal of Electrochemical Society*, vol. 138 no. 8, pp. 2334-2342, 1991.

139. Gurau, V., Liu, H., and Kakac, S., Two-dimensional model for proton exchange membrane fuel cells, *AIChE Journal*, vol. 44 no. 11, pp. 2410-2422, 1998.

140. Berning, T., Lu, D. M., and Djilali, N., Three-dimensional computational analysis of transport phenomena in a PEM fuel cell*, Journal of Power Sources*, vol. 106, pp. 284-294, 2002.

141. Dutta, S., Shimpalee, S., and Van Zee, J.W., Numerical prediction of mass exchange between cathode and anode channels in a PEM fuel cell, *International Journal of Heat Mass Transfer*, vol. 44, pp. 2029-2042, 2001.

142. Shimpalee, S., and Dutta, S., Numerical prediction of temperature distribution in PEM fuel cells, *Numerical Heat Transfer*, Part A, vol. 38, pp. 111-128, 2000.

143. Parker, J. C., Lenhard R. J., and Kuppusamy T., A parametric model for constitutive properties governing multiphase flow in porous media, *Water Resources Research*, vol. 23 no. 4, pp. 618-624, 1987.

144. Drew, D. A., Mathematical modelling of two-phase flow, *Annual Review of Fluid Mechanics*, vol. 15, pp. 261-291, 1983.

145. Dullien, F. A. L., Porous media: Fluid Transport and Pore Structure, 2nd ed., Academic Press, New York, 1992.

146. Wang, Z. H., Wang, C. Y., and Chen, K. S., Two-phase flow and transport in the air cathode of proton exchange membrane fuel cells, *Journal of Power Sources*, vol. 94, pp. 40-50, 2000.

147. Wang, C. Y., and Cheng, P., Multiphase flow and heat transfer in porous media, *Advance Heat Transfer*, vol. 30, pp. 183-196, 1997.

148. Weber, A. Z., Darling, R. M., and Newman, J., Modeling two-phase behaviour in PEFCs, *Journal of Electrochemical Society*, vol. 151 no. 10, pp. A1715-A1727, 2004.

149. Natarajan, D., and Nguyen, T. V., Three-dimensional effects of liquid water flooding in the cathode of a PEM fuel cell, *Journal of Power Sources*, vol.

115, pp. 66-80, 2003.

150. Berning, T., and Djilali, N., A 3D, multiphase, multicomponent model of the cathode and anode of a PEM fuel cell, *Journal of Electrochemical Society*, vol. 150, pp. A1589-A1598, 2003.

151. Grens, E. A., Turner, R. M., and Katan, T., A model for analysis of porous gas electrodes, *Advanced Energy Conversion*, vol. 4, pp. 109-119, 1964.

152. Viitanen, M., and Lampinen, M. J., A mathematical model and optimization of the structure for porous air electrodes, *Journal of Power Sources*, vol. 32, pp. 207-231, 1990.

153. Grens, E. A., Analysis of operation of porous gas electrodes with two superimposed scales of pore structure, *Industrial and Engineering Chemistry Fundamentals*, vol. 5, pp. 542-547, 1966.

154. Yang, S. C., Cutlip, M. B., and Stonehart, P., Simulation and optimization of porous gas-diffusion electrodes used in hydrogen/oxygen phosphoric acid fuel cells-I: application of cathode model simulation and optimization to PAFC cathode development, *Electrochimical Acta*, vol. 35, pp. 869-878, 1990.

155. Giner, J., and Hunter, C., The mechanism of operation of the teflon-bonded gas diffusion electrode: A mathematical model, *Journal of Electrochemical Society*, vol. 116 no. 8, pp. 1124-1130, 1969.

156. Janssen, G. J. M., A phenomenological model of water transport in a proton exchange membrane fuel cell, *Journal of Electrochemical Society*, vol. 148, pp. A1313-A1323, 2001.

157. Bernadi, D. M., Water-balance calculations for solid polymer electrolyte fuel cells, *Journal of Electrochemical Society*, vol. 137 no. 11, pp. 3344-3351, 1990.

158. Mann, R. F., Amphlett, J. C., Hooper, M. A. I., Jensen, H. M., Pepply, B. A., and Roberge, P. R., Development and application of a generalized steady-state electrochemical model for a PEM fuel cell, *Journal of Power Sources*, vol. 86, pp. 173-180, 2000.

159. Wang, Q., Eikerling, M., Song, D., Liu, Z., Navessin, T., Xie, Z., and Holdcroft, S., Functionality graded cathode catalyst layers for polymer electrolyte fuel cells I. Theoretical modelling, *Journal of Electrochemical Society*, vol. 151 no. 7, pp. A950-A957, 2004.

160. Pisani, L., Valentini, M., and Murgia, G., Analytical pore scale modeling of the reactive regions of polymer electrolyte fuel cells, *Journal of Electrochemical Society*, vol. 150 no. 12, pp. A1549-A1559, 2003.

161. Wang, Q., Song, D., Navessin, T., Holdcroft, S., and Liu, Z., A mathematical model and optimization of the cathode catalyst layer structure in PEM fuel cells, *Electrochimica Acta*, vol. 50, pp. 725-730, 2004.

162. Versteeg, H. K., and Malalasekra W., *An introduction to computational fluid dynamics: the finite volume method*, 2nd Ed., Prentice Hall, England, 2007.

163. Ansys *Fluent® 12.0 Users Guide Documentation*, Ansys Inc., Southpointe, SAS, 2009.

164. Fluent Inc., Gambit Version 6 Manuals, Centerra Resource Park, 10 Cavendish Court, Lebanon, New Hampshire, USA 2001 (www.fluent.com).

165. Gallart, M. S., Computational modeling and optimisation of proton exchange membrane fuel cells, PhD Thesis, Department of Mechanical Engineering, University of Victoria, 2007.

166. Snyman, J. A., *Practical mathematical optimisation: an introduction to basic optimisation theory and classical and new gradient-based algorithms,* Springer, New York, 2005.

167. Baumal, A. E., McPhee, J., and Calamai, P. H., Application of genetic algorithm of an active vehicle suspension design, *Computer Methods in Applied Mechanics and Engineering*, vol. 163, pp. 87-94, 1998.

168. Eberhard, P., Schiehlen, W., and Bestle, D., Some advantages of stochastic methods in multi-criteria optimization of multibody systems, *Archive of Applied Mechanics*, vol. 69, pp. 543-554, 1998.

169. Snyman, J. A., and Hay, A. M., The DYNAMIC-Q optimisation method: an Alternative to SQP?, *Computer and Mathematics with Applications*, vol. 44, pp. 1589-1598, 2002.

170. Els, P. S., and Uys, P. E., Investigation of the applicability of the Dynamic-Q optimisation algorithm to vehicle suspension design, *Mathematical and Computer Modeling*, vol 37 no. 9-10, pp. 1029-1046, 2003.

171. Motsamai, O. S., Optimisation techniques for combustor design, PhD Thesis, Department of Mechanical Engineering, University of Pretoria, 2008.

172. Snyman, J. A., A new and dynamic method for unconstrained minimization, *Applied Mathematical Modeling*, vol. 6, pp. 449-462, 1982.

173. Snyman, J. A., The LFOPC leap-frog algorithm for constrained optimisation,

Computer and Mathematics with Applications, vol. 40, pp. 1085-1096, 2000.

174. Hay, A. M., Optimal dimensional synthesis of planar parallel manipulators with respect to workplaces, PhD Thesis, Department of Mechanical and Aeronautical Engineering, University of Pretoria, South Africa, 2003.

175. Snyman, J. A., Stander, N., and Roux, W. J., A dynamic penalty function method for the solution of structural optimisation problems, *Applied Mathematical Modelling*, vol. 18, pp. 453-460, 1994.

176. Snyman, J. A., and Standar, N. A., A new successive approximation method for optimum structural design, *AIAA Journal*, vol. 32, pp. 1310-1315, 1994.

177. Rowe, A., and Li, X., Mathematical modeling of proton exchange membrane fuel cells, *Journal of Power Sources*, vol. 102, pp. 82-96, 2001.

178. Hontanon, E., Escuder, M. J., Bautista, C., Garcia-Ybarra, P. L., and Daza, L., Optimization of flow-field in polymer electrolyte membrane fuel cells using computational fluid dynamics techniques, *Journal of Power Sources*, vol. 86, pp. 363-368, 2000.

179. Yan, Q., Toghiani, H., and Causey, H., Steady state and dynamic performance of proton exchange membrane fuel cells (PEMFCs) under various operating conditions and load changes, *Journal of Power Sources*, vol. 161, pp. 492-502, 2006.

180. Cheddie, D. F., and Munroe, N. D. H., A two-phase model of an intermediate temperature PEM fuel cell, *International Journal of Hydrogen Energy*, vol. 32, pp. 832-841, 2007.

181. Mench, M. M., Wang, C. Y., and Ishikawa, M., In-situ current distribution

measurements in polymer electrolyte fuel cells, *Journal of Electrochemical Society*, vol. 150 no. 8, pp. A1052-A1059, 2003.

182. Weizhong, L., Zhixiang, L., Cheng, W., Zongqiang, M., and Milin, Z., The effects of pinholes on proton exchange membrane fuel cell performance, *International Journal of Energy Research*, vol. 35, pp. 24-30, 2010.

183. Liu, X., Guo, H., and Ma, C., Water flooding and pressure drop characteristics in flow channels of proton exchange membrane fuel cells, *Electrochimica Acta*, vol. 52, pp. 3607-3614, 2007.

184. Rodatz, P., Buechi, F., Onder, C., and Guzzella, L., Operational aspects of a large PEFC stack under practical conditions, *Journal of Power Sources*, vol. 128, pp. 208-217, 2004.

185. Maharudrayya, S., Jayanti S., and Deshpande, A. P., Pressure drop and flow distribution in multiple parallel-channel configurations used in proton-exchange membrane fuel cell stacks, *Journal of Power Sources*, vol. 157, pp. 358-367, 2006.

186. Nguyen, T. V., Modeling two-phase flow in the porous electrodes of proton exchange membrane fuel cells using the interdigitated flow fields, *Tutorials in Electrochemical Engineering Mathematical Modeling*, vol. 99 no. 14, pp. 222-241, 1999.

187. Nam, J. H, and Karviany, M., Effective diffusivity and water-saturation distribution in Single-and two-layer PEMFC diffusion medium, *International Journal of Heat and Mass Transfer*, vol. 46, pp. 4595-4611, 2003.

188. Maharudrayya, S., Jayanti, S., and Deshpande, A.P., Pressure losses in laminar flow through serpentine channels in fuel cell stacks, *Journal of Power Sources*,

vol. 138, pp. 1-13, 2004.

189. White, F. M., *Fluid Mechanics*, McGraw Hill, New York, 1986.

190. White, F. M., *Viscous Fluid Flow*, McGraw Hill, New York, 1991.

191. Mench, M. M., *Fuel Cell Engines*, John Wiley & Sons, New Jersey, 2008.

192. Pantakar, S. V., *Numerical Heat Transfer and Fluid Flow*, Hemisphere Publishing Corp., New York, 1980.

193. Tao, W. Q., Min, C. H., Liu, X. L., He, Y. L., Yin, B. H., and Jiang, W., Parameter sensitivity examination and discussion of PEM fuel cell simulation model validation Part I. Current status of modeling research and model development, *Journal of Power Sources*, vol. 160, pp. 359-373, 2006.

194. Labaek, J., Bang, M., and Kaer, S. K., Flow and pressure distribution in fuel cell Manifolds, *ASME Journal of Fuel Cell Science and Technology*, **7**/061001-1, 2010.

195. Lin, H. H., Cheng, C. H., Soong, C. Y., Chen, F., and Yan, W. M., Optimisation of key parameters in the proton exchange membrane fuel cell, *Journal of Power Sources*, vol. 162, pp. 246-254, 2006.

196. Wang, L., and Liu, H., Performance studies of PEM fuel cells with interdigitated flow fields, *Journal of Power Sources*, vol. 134, pp. 185-196, 2004.

197. Watkins, D. S., Dircks, K. W., and Epp, D. G., Novel fuel cell fluid flow field Plate, *US Patent 4988583*, 1991.

198. Gamburzev, S., Boyer, C., and Appleby, A. J., Proceedings of Fuel Cell Seminar, Portland, USA, 1998, pp. 556-559, 1998.

199. Kasim, A., Liu, H. T., and Forges, P., Modeling of performance of PEM fuel cell with conventional and interdigitated flow fields, *Journal of Applied Electrochemistry*, 29, pp. 1409-1416, 1999.

200. Nguyen, T. V., A gas distributor design for proton-exchange-membrane fuel cells, *Journal of Electrochemistry Society*, vol. 143, pp. L103-L105, 1996.

201. Kumar, A., and Reddy, R. G., Modeling of polymer electrolyte membrane fuel cell with metal foam in the flow-field of the bipolar/end plates, *Journal of Power Sources*, vol. 114, pp. 54-62, 2003.

202. Bello-Ochende, T., Meyer, J. P., and Bejan, A., Constructal multi-scale pin fins, *International Journal of Heat Mass and Transfer*, vol. 53, pp. 2773-2779, 2010.

203. Sara, O. N., Performance analysis of rectangular ducts with staggered square pin fins, *Energy Conversion Management*, vol. 44, pp. 1787-1803, 2003.

204. Uzol, O., and Camci C., Heat transfer, pressure loss and flow field measurements downstream of staggered two-row circular and elliptical pin fin arrays, *ASME Journal of Heat Transfer*, vol. 127, pp. 458-71, 2005.

205. Tanda, G., Heat transfer and pressure drop in a rectangular channel with diamond-shaped elements, *International Journal Heat and Mass Transfer*, vol. 44: pp. 3529-3541, 2001.

206. Bejan, A., and Lorente, S., *Design with Constructal Theory*, John Wiley & Sons Ltd., 2008.

207. Bello-Ochende, T., Meyer, J. P., and Ighalo, F. U., Combined numerical optimization and constructal theory for the design of microchannel heat sinks, *Numerical Heat Transfer (Part A)*, vol. 58 no. 11, pp. 882-899, 2010.

208. Morris, R. M., Snyman, J. A., and Meyer, J. P., Jets in crossflow mixing analysis using computational fluid dynamics and mathematical optimization, *AIAA Journal of Propulsion and Power*, vol. 23 no. 3, pp. 618-28, 2007.

209. Ighalo, F. U., Bello-Ochende, T., and Meyer, J. P., Mathematical optimization: application to the design of optimal micro-channel heat sinks, *Engenharia Termica*, vol. 8 no. 1, pp. 58-64, 2009.

210. Motsamai, O. S., Snyman, J. A., and Meyer, J. P., Optimization of gas turbine combustor mixing for improved exit temperature profile, *Heat Transfer Engineering*, vol. 31 no. 5, pp. 402-418, 2010.

211. Le Roux, W. G., Bello-Ochende, T., and Meyer, J. P., Operating conditions of an open and direct solar thermal Brayton cycle with optimised cavity receiver and recuperator, *Energy*, vol, 36, pp. 6027-6036, 2011.

212. Meyer, J. P., Constructal law in technology, thermofluid and energy systems, and in design education, *Physics of Life Review*, vol. 8 no. 3, pp. 247-248, 2011.

213. Le Roux, W. G., Bello-Ochende, T., and Meyer, J. P., Thermodynamic optimization of an integrated design of a small-scale solar thermal Brayton cycle, *International Journal of Energy Research*, DOI: 10.1002/ER.1859, 2011.

214. Chanta, V. S., An experimental study of end wall heat transfer enhancement for Flow past staggered non-conducting pin fin arrays, PhD Thesis, Department of Mechanical Engineering, Texas A & M University, USA, 2003.

215. Lyall, M. E., Heat transfer from low aspect ratio pin fins, PhD Thesis, Department of Mechanical Engineering, Virginia Polytechnic Institute and State University, USA, 2006.

216. Li, J., and Peterson G. P., Geometrical optimization of a micro heat sink with liquid Flow, *IEEE Transactions on Components, Packaging and Manufacturing Technology*, vol. 29 no. 1, pp. 145-154, 2006.

217. Husain, A., and Kim, K., Shape optimization of micro-channel heat sink for micro-electronic cooling, *IEEE Transactions on Components, Packaging and Manufacturing Technology*, vol. 31 no. 2, pp. 322-330, 2008.

218. The Mathworks Inc., MATLAB & Simulink Release Notes for R2008a, 2008.

219. Tagliafico, L., Tanda, G., A thermodynamic method for the comparison of plate-fin exchanger performance, *ASME Journal of Heat Transfer*, vol. 118, pp. 805-809, 1996.

220. Jung, H. M., Lee, W. Y., Park, J. S., Kim, C. S., Numerical analysis of a polymer electrolyte fuel cell, *International Journal of Hydrogen Energy*, vol. 29, pp. 945-954, 2004.

221. Du, L., and Jana, S. C., Highly conductive/graphite composites for bipolar plates in proton exchange membrane fuel cells, *Journal of Power Sources*, vol. 172, pp. 734-741, 2007.

222. Li, Q. F., He, R. H., Jensen, J. O., and Bjerrum, N. J., Approaches and recent development of polymer electrolyte membranes for fuel cells operating above 100 ^{o}C, *Journal of Chemical Materials*, vol. 15, pp. 4896-4915, 2003.

223. Shao, Y. Y., Yin, G. P., Wang, Z. B., and Gao, Y. Z., Proton exchange

membrane fuel cell from low temperature to high temperature: material challenges, *Journal of Power Sources*, vol. 167, pp. 235-242, 2007.

224. Li, Q. F., Rudbeck, H. C., Chromik, A., Jensen, J. O., Pan, C., Steenberg, T., Calverley M., Jerrum N. J., and Kerres J., Properties, degradation and high temperature fuel cell test of different PBI and PBI blend membranes, *Journal of Membrane Science*, vol. 347, pp. 260-270, 2010.

225. Satterfield, M. B., Majsztrik, P. W., Ota, H., Benziger J. B., and Bocarsly A. B., Mechanical properties of Nafion and Titania/Nafion composite membranes for polymer electrolyte membrane fuel cells, *Journal of Polymer Science Part B: Polymer Physics*, vol. 43, pp. 786-795, 2005.

226. Bai, Z., Putthanarat, S., Rodrigues, S. J., and Dang, T. D., Properties and performance of composite electrolytes membranes based on sulfonated poly (arylenethioethersulfone) and sulfonated polybenzimidazole, *Polymer*, vol. 52, pp. 3381-3388, 2011.

227. Frank, G., Proceeding of the second European PEFC Forum P749, Lucerne, Switzerland, 2003.

228. Yuan, J., Faghiri, M., and Sunden, B., On heat and mass transfer phenomena in PEMFC and SOFC and modelling approaches, In: Sunden, B., Faghiri, M., (Eds.) *Transport phenomena in fuel cells*, WIT Press, pp. 133-174, 2005.

229. Zhang, Y. J., Ouyang, M. G., Luo, J. X., Zhang, Z., and Wang, Y. J., Mathematical modeling of vehicle fuel cell power system thermal management, *SAE Paper*, vol. 1, pp. 11-46, 2003.

230. Andrew, R., and Li, X. G., Mathematical modeling of proton exchange membrane fuel cells, *Journal of Power Sources*, vol. 102, pp. 82-96, 2001.

231. Vargas, J.V.C., Ordonez, J.C., and Bejan, A., Constructal PEM fuel cell stack design, *International Journal Heat and Mass Transfer*, vol. 48: pp. 4410-4427, 2005.

232. Vargas, J.V.C., Ordonez, J.C., and Bejan, A., Constructal flow structure for a PEM fuel cell, *International Journal Heat and Mass Transfer*, vol. 47: pp. 4177-4193, 2004.

APPENDICES

APPENDIX A:

SAMPLE GAMBIT JOURNAL FILE (GRID GENERATION AND MESHING): SINGLE CHANNEL PEM FUEL CELL.

```
/
$htot = 0.8
$wtot = 3
$offr1x = ($wtot/2)
$offr1y = ($htot/2)
$ys = 0.6
$xs = 0.5
$offsy = $htot - $ys
$offsx = ($wtot/2) - ($xs/2)
$offr2x = ($xs/2)
$offr2y = ($ys/2)
face create width $wtot height $htot offset $offr1x $offr1y 0 xyplane rectangle
face create translate "edge.3" vector 0 0.21 0
face create translate "edge.7" vector 0 0.012 0
face create translate "edge.10" vector 0 0.036 0
face create translate "edge.13" vector 0 0.012 0
face create translate "edge.16" vector 0 0.21 0
face create translate "edge.19" vector 0 $htot 0
face create width $xs height $ys offset $offr2x $offr2y 0 xyplane rectangle
face move "face.8" offset $offsx $offsy 0
face cmove "face.8" multiple 1 offset 0 1.08 0
face split "face.1" connected faces "face.8"
face split "face.7" connected faces "face.9"
undo begingroup
```

```
edge modify "edge.4" "edge.20" "edge.21" backward
edge picklink "edge.4" "edge.20" "edge.21" "edge.2"
edge mesh "edge.2" "edge.4" "edge.20" "edge.21" successive ratio1 1 intervals \
  20
undo endgroup
undo begingroup
edge modify "edge.22" backward
edge picklink "edge.22" "edge.1"
edge mesh "edge.1" "edge.22" successive ratio1 1 intervals 30
undo endgroup
undo begingroup
edge modify "edge.33" "edge.40" "edge.38" backward
edge picklink "edge.33" "edge.40" "edge.38" "edge.36" "edge.39" "edge.19" \
  "edge.3" "edge.31" "edge.32" "edge.34" "edge.37" "edge.35"
edge mesh "edge.35" "edge.37" "edge.34" "edge.32" "edge.31" "edge.33" \
  "edge.3" "edge.19" "edge.39" "edge.40" "edge.38" "edge.36" successive \
  ratio1 1 intervals 10
undo endgroup
undo begingroup
edge picklink "edge.7" "edge.10" "edge.13" "edge.16"
edge mesh "edge.16" "edge.13" "edge.10" "edge.7" successive ratio1 1 \
  intervals 30
undo endgroup
undo begingroup
edge modify "edge.14" "edge.15" backward
edge picklink "edge.14" "edge.15" "edge.9" "edge.12" "edge.11"
edge mesh "edge.14" "edge.11" "edge.15" "edge.12" "edge.9" successive ratio1 \
  1 intervals 4
undo endgroup
undo
/Undone to: undo begingroup
```

```
undo begingroup
edge modify "edge.14" "edge.15" backward
edge picklink "edge.14" "edge.15" "edge.9" "edge.12" "edge.8" "edge.11"
edge mesh "edge.14" "edge.11" "edge.8" "edge.15" "edge.12" "edge.9" \
  successive ratio1 1 intervals 4
undo endgroup
undo begingroup
edge modify "edge.6" backward
edge picklink "edge.6" "edge.18" "edge.17" "edge.5"
edge mesh "edge.5" "edge.17" "edge.6" "edge.18" successive ratio1 1.15 \
  intervals 10
undo endgroup
face mesh "face.1" "face.2" "face.3" "face.4" "face.5" "face.6" "face.9" \
  "face.8" "face.7" submap size 1
undo
/Undone to: face mesh "face.1" "face.2" "face.3" "face.4" "face.5" "face.6" "face
undo
/Undone to: undo begingroup
undo begingroup
edge modify "edge.5" "edge.6" backward
edge picklink "edge.5" "edge.6" "edge.18" "edge.17"
edge mesh "edge.17" "edge.18" "edge.5" "edge.6" successive ratio1 1 intervals \
  4
undo endgroup
face mesh "face.1" "face.2" "face.3" "face.4" "face.5" "face.6" "face.9" \
  "face.8" "face.7" submap size 1
edge create translate "vertex.16" vector 0 0 125
undo begingroup
edge picklink "edge.41"
edge mesh "edge.41" successive ratio1 1.1 ratio2 1.1 intervals 60
undo endgroup
```

```
volume create translate "face.1" "face.2" "face.3" "face.4" "face.5" "face.6" \
  "face.9" "face.8" "face.7" onedge "edge.41" withmesh
window modify invisible mesh
window modify visible mesh
window modify invisible mesh
physics create "inlet-a" btype "MASS_FLOW_INLET" face "face.54"
physics create "inlet-c" btype "MASS_FLOW_INLET" face "face.8"
physics create "outlet-a" btype "PRESSURE_OUTLET" face "face.9"
physics create "outlet-c" btype "PRESSURE_OUTLET" face "face.59"
physics create "wall-terminal-a" btype "WALL" face "face.67"
physics create "wall-terminal-c" btype "WALL" face "face.12"
physics create "wall-ch-a" btype "WALL" face "face.51" "face.53" "face.52"
physics create "wall-ch-c" btype "WALL" face "face.16" "face.14" "face.17"
physics create "wall-ends" btype "WALL" face "face.1" "face.2" "face.3" \
  "face.4" "face.5" "face.6" "face.7" "face.20" "face.27" "face.32" "face.37" \
  "face.42" "face.49" "face.68"
physics create "wall-gdl-a" btype "WALL" face "face.48" "face.46"
physics create "wall-gdl-c" btype "WALL" face "face.18" "face.19"
physics create "wall-sides" btype "WALL" face "face.13" "face.15" "face.24" \
  "face.25" "face.29" "face.30" "face.34" "face.35" "face.39" "face.40" \
  "face.44" "face.45" "face.64" "face.66"
physics create "catalyst-a" ctype "FLUID" volume "volume.5"
physics create "catalyst-c" ctype "FLUID" volume "volume.3"
physics create "channel-a" ctype "FLUID" volume "volume.7"
physics create "channel-c" ctype "FLUID" volume "volume.8"
physics create "gdl-a" ctype "FLUID" volume "volume.6"
physics create "gdl-c" ctype "FLUID" volume "volume.2"
physics create "membrane" ctype "FLUID" volume "volume.4"
physics create "current-a" ctype "SOLID" volume "volume.9"
physics create "current-c" ctype "SOLID" volume "volume.1"
window modify visible mesh
```

```
export fluent5 "pem-single-channel1011.msh"
save name "C:\\pem-single101110\\pem-single-channelnew.dbs"
save
export fluent5 "C:\\pem-single101110\\pem-single-channelnew.msh"
```

APPENDIX B:
THE DYNAMIC-Q OPTIMISATION ALGORITHM IN MATLAB

B-1 DYNQ.M

```
function [X,F]=dynq(x0,varargin);
tic
%
%       DYNAMIC-Q ALGORITHM FOR CONSTRAINED OPTIMISATION
%           GENERAL MATHEMATICAL PROGRAMMING CODE
%           ------------------------------------
%
% This code is based on the Dynamic-Q method of Snyman documented
% in the paper "THE DYNAMIC-Q OPTIMISATION METHOD: AN
ALTERNATIVE TO SQP?" by J.A. Snyman and A.M. Hay. Technical Report, Dept
Mech. Eng., UP.
%
%                   MATLAB implementation by A.M. HAY
%               Multidisciplinary Design Optimisation Group (MDOG)
%           Department of Mechanical Engineering, University of Pretoria
%                           August 2002
%
%                       UPDATED : 23 August 2002
%
%                           BRIEF DESCRIPTION
%                           -----------------

%  Dynamic-Q solves inequality and equality constrained optimisation
%  problems of the form:
```

```
%
%                 minimise F(X)  ,  X={X(1),X(2),...,X(N)}
%    such that
%                  Cp(X) <= 0        p=1,2,...,NP
%    and
%                  Hq(X) =  0        q=1,2,...,NQ
%    with lower bounds
%       CLi(X) = V_LOWER(i)-X(NLV(i)) <= 0   i=1,2,...,NL
%    and upper bounds
%       CUj(X) = X(NUV(j))-V_UPPER(j) <= 0   j=1,2,...,NU
%
% This is a completely general code - the objective function and the
% constraints may be linear or non-linear. The code therefore solves
% LP, QP and NLP problems.
%
%                   -----------------
%
% User specified functions:
%
% The objective function F and constraint functions C and H must be
% specified by the user in function FCH. Expressions for the respective
% gradient vectors must be specified in function GRADFCH.
%
% {The user may compute gradients by finite differences if necessary
%  - see example code in GradFCH}
%
% Side constraints should not be included as inequality constraints
% in the above subroutines, but passed to the dynq function as
% input arguments LO and UP. (Described below)
%
```

```
% In addition to FCH and GRADFCH the following functions are called
% by DYNQ and should not be altered:
%
DQLFOPC,DQFUN,DQCONIN,DQCONEQ,DQGRADF,DQGRADC,DQGRADH
%
% In addition the script HISTPLOT.m plots various optimisation
% histories. To suppress automatic plotting set PRNCONST=0 below.
%
%                  -----------------
%
%   synopsis:
%
%         [X,F] = dynq(x0,lo,up,dml,xtol,ftol,clim,np,nq,kloop);
%
%   outputs:
%      X  = optimal solution (1xN)
%      F  = optimal function value
%
%   inputs:
%      x0 = starting point (1xN)
%      lo = NLx2 matrix associated with lower limits on the variables
%           containing variable index NLV(i) in the first column and
%           associated value V_LOWER of that limit in the second column
%           (optional, otherwise assumed no lower side constraints)
%      up = NUx2 matrix associated with lower limits on the variables
%           containing variable index NUV(i) in the first column and
%           associated value V_UPPER of that limit in the second column
%           (optional, otherwise assumed no upper side constraints)
%     dml = the move limit which should be approximately the same order
%           of magnitude as the "radius of the region of interest"
```

```
%             = sqrt(n)*max-variable-range (optional, default =1)
%    xtol = convergence tolerance on the step size (optional, default =1e-5)
%    ftol = convergence tolerance on the function value (optional, default =1e-8)
%    clim = tolerance for determining whether constraints are violated
%             (optional, default =ftol*1e2)
%      np = number of inequality constraints (optional)
%      nq = number of equality constraints (optional)
%             Note: Both np and nq are optional and determined automatically
%             if not specified, but at the cost of an extra function evalution.
%   kloop = maximum number of iterations (optional, default = 100)
%
%    NOTE: use [] to activate default inputs, for example
%
% [X,F]=dynq(x0,[],[],2); uses dml=2 but default values for all other inputs.
%
%      See FCH and GRADFCH for an example problem.
%
%  ---- This program is for educational purposes only ----


%*****PLOT OPTIMISATION HISTORIES AT END OF
PROGRAM?*******************
%          YES: 1       OR          NO: 0
%
PRNCONST=1;
%*************************************************************************
***

clc;
```

```
N=length(x0);   % Determine number of variables
X=x0;

[dum,D]=size(varargin);
vars=cell(1,9);
vars(1:D)=varargin;

LO=vars{1};
UP=vars{2};
DML=vars{3};
XTOL=vars{4};
FTOL=vars{5};
CLIM=vars{6};
NP=vars{7};
NQ=vars{8};
KLOOPMAX=vars{9};

% default values
[NL,dum]=size(LO);
if NL>0
   NLV=LO(:,1)';
   V_LOWER=LO(:,2)';
else
   NLV=[];
   V_LOWER=[];
end
[NU,dum]=size(UP);
if NU>0
   NUV=UP(:,1)';
   V_UPPER=UP(:,2)';
```

```
else
   NUV=[];
   V_UPPER=[];
end
if isempty(DML)
   DML=1; end
if isempty(XTOL)
   XTOL=1e-5; end
if isempty(FTOL)
   FTOL=1e-8; end
if isempty(CLIM)
   CLIM=FTOL*1e2; end
if isempty(NP)|isempty(NQ)
   [F,C,H]=fch(X);
   NP=length(C);
   if isempty(C)
      NP=0;
   end
   NQ=length(H);
   if isempty(H)
      NQ=0;
   end
end
if isempty(KLOOPMAX)
   KLOOPMAX=100; end

%#########################################################################
###C
%*************************************************************************
***C
```

```
%     MAIN PROGRAM FOLLOWS: Do not alter!!!!
%*****************************************************************
***C
%#################################################################
###C

%*****OPEN OUPUT
FILES************************************************C
%
fidA=fopen('Approx.out','wt+');
fidD=fopen('DynamicQ.out','wt+');
fidH=fopen('History.out','wt+');
%
%*****SPECIFY INITIAL APPROXIMATION
CURVATURES************************C
%
ACURV=0.D0;
BCURV=zeros(1,NP);
if NP==0
   BCURV=[];
end
CCURV=zeros(1,NQ);
if NQ==0
   CCURV=[];
end
%
%
%
%*****INITIALIZE
OUTPUT*********************************************C
```

```
FEASIBLE=0;

fprintf(fidA,' DYNAMICQ OUTPUT FILE \n');
fprintf(fidA,' ---------- \n');
fprintf(fidA,' Number of variables [N]= %i \n',N);
fprintf(fidA,' Number of inequality constraints [NP]= %i \n',NP);
fprintf(fidA,' Number of equality constraints [NQ]= %i \n',NQ);
fprintf(fidA,' Move limit= %12.8e \n',DML);

fprintf(1,'\n DYNAMICQ OPTIMISATION ALGORITHM \n');
fprintf(1,' ---------- \n');
% (MAXX=Maximum number of X-values to be displayed on screen)
MAXX=4;
if N<=MAXX
   fprintf(1,' Iter Function value  ? XNORM      RFD        ');
   fprintf(1,'X(%i)       ',1:N);
   fprintf(1,'\n ----------');
   for I=1:N
      fprintf(1,'------------',1:N);
   end
   fprintf(1,'\n');
else
   fprintf(1,' Iter Function value  ? XNORM      RFD ');
   fprintf(1,'\n ----------\n');
end

fprintf(fidD,' DYNAMICQ OPTIMISATION ALGORITHM\n');
fprintf(fidD,' ----------\n');
fprintf(fidD,' Iter Function value       ? XNORM      RFD        ');
fprintf(fidD,'X(%i)          ',1:N);
```

```
fprintf(fidD,'\n');

fprintf(fidD,' ------------------------------------------------');
for i=1:N
   fprintf(fidD,'---------------');
end
fprintf(fidD,'\n');

% Initialize outer loop counter
KLOOP=0;

% Arbitrary large values to prevent premature termination
F_LOW=1.D6;
RFD=1.D6;
RELXNORM=1.D6;

C_A=zeros(1,NP+NL+NU+1);

%*****START OF OUTER OPTIMISATION
LOOP*********************************C

while KLOOP<=KLOOPMAX

%*****APPROXIMATE
FUNCTIONS*****************************************C

% Determine function values
   [F,C,H]=fch(X);

% Calculate relative step size
```

```
   if KLOOP>0
      DELXNORM=sqrt((X_H(KLOOP,:)-X)*(X_H(KLOOP,:)-X)');
      XNORM=sqrt(X*X');
      RELXNORM=DELXNORM/(1+XNORM);
   end

% Determine lowest feasible function value so far
   if KLOOP>0
   FEASIBLE=1;
      check=find(C<CLIM);
      if isempty(check)&NP>0;
         FEASIBLE=0;
      end
      check=find(abs(H)<CLIM);
      if isempty(check)&NQ>0;
         FEASIBLE=0;
      end
      for I=1:NL
         if C_A(I+NP)>CLIM
            FEASIBLE=0;
         end
      end
      for I=1:NU
         if C_A(I+NP+NL)>CLIM
            FEASIBLE=0;
         end
      end
   end

% Calculate relative function difference
```

```
   if F_LOW~=1.D6&FEASIBLE==1
      RFD=abs(F-F_LOW)/(1+abs(F));
   end

   if FEASIBLE==1&F<F_LOW
      F_LOW=F;
   end

% Store function values
   X_H(KLOOP+1,:)=X;   % Need to adjust from Fortran version since
   F_H(KLOOP+1)=F;     % Matlab does not accept 0 as a matrix index
   if NP>0
      C_H(KLOOP+1,1:NP)=C;
   end
   if NL>0
      C_H(KLOOP+1,NP+1:NP+NL)=C_A(NP+1:NP+NL);
   end
   if NU>0
      C_H(KLOOP+1,NP+NL+1:NP+NL+NU)=C_A(NP+NL+1:NP+NL+NU);
   end
   C_H(KLOOP+1,NP+NL+NU+1)=C_A(NP+NL+NU+1);
   if NQ>0
      H_H(KLOOP+1,:)=H;
   end

% Determine gradients
   [GF,GC,GH]=gradfch(X);

% Calculate curvatures
   if KLOOP>0
```

```
      DELX=X_H(KLOOP,:)-X_H(KLOOP+1,:);
      DELXNORM=DELX*DELX';

% Calculate curvature ACURV
      DP=GF*DELX';
      ACURV=2.*(F_H(KLOOP)-F_H(KLOOP+1)-GF*DELX')/DELXNORM;

      for J=1:NP
         DP=GC(J,:)*DELX';
% Calculate corresponding curvature BCURV(J)
         BCURV(J)=2.*(C_H(KLOOP,J)-C_H(KLOOP+1,J)-
GC(J,:)*DELX')/DELXNORM;
      end

      for J=1:NQ
         DP=GH(J,:)*DELX';
% Calculate corresponding curvature CCURV(J)
         CCURV(J)=2.*(H_H(KLOOP,J)-H_H(KLOOP+1,J)-
GH(J,:)*DELX')/DELXNORM;
      end
   end

%*****RECORD PARAMETERS FOR THE
ITERATION*****************************C

% Write approximation constants to Approx.out
   fprintf(fidA,' Iteration %i \n',KLOOP);
   fprintf(fidA,' ----------\n');
   fprintf(fidA,' X=\n');
   for I=1:N
```

```
      fprintf(fidA,' %12.8f ',X(I));
   end
   fprintf(fidA,'\n F= %15.8e\n',F);
   for I=1:NP
      fprintf(fidA,' C(%i)=%15.8e',I,C(I));
   end
   for I=1:NQ
       fprintf(fidA,' H(%i)=%15.8e',I,H(I));
   end

   fprintf(fidA,' Acurv=%15.8e',ACURV);
   for I=1:NP
      fprintf(fidA,' Bcurv(%i)=%15.8e',I,BCURV(I));
   end
   for I=1:NQ
      fprintf(fidA,' Ccurv(%i)=%15.8e',I,CCURV(I));
   end

% Write solution to file
   if KLOOP==0
      fprintf(fidD,' %4i %+19.12e %i                    ',KLOOP,F,FEASIBLE);
   else
      if RFD~=1.D6
         fprintf(fidD,' %4i %+19.12e %i %9.3e
%9.3e',KLOOP,F,FEASIBLE,RELXNORM,RFD);
      else
         fprintf(fidD,' %4i %+19.12e %i %9.3e
',KLOOP,F,FEASIBLE,RELXNORM);
      end
   end
```

```
   fprintf(fidD,' %+13.6e',X);
   fprintf(fidD,'\n');

% Write solution to screen
   if KLOOP==0
      if N<=MAXX
         fprintf(1,' %4i %+14.7e %i                ',KLOOP,F,FEASIBLE);
         fprintf(1,' %+9.2e',X);
         fprintf(1,'\n');
      else
         fprintf(1,' %4i %+14.7e %i\n',KLOOP,F,FEASIBLE);
      end
    else
      if N<=MAXX
         if RFD~=1.D6&FEASIBLE==1
            fprintf(1,' %4i %+14.7e %i %9.3e
%9.3e',KLOOP,F,FEASIBLE,RELXNORM,RFD);
         else
            fprintf(1,' %4i %+14.7e %i %9.3e
',KLOOP,F,FEASIBLE,RELXNORM);
         end
         fprintf(1,' %+9.2e',X);
         fprintf(1,'\n');
      else
         if RFD~=1.D6&FEASIBLE==1
            fprintf(1,' %4i %+14.7e %i %9.3e
%9.3e\n',KLOOP,F,FEASIBLE,RELXNORM,RFD);
         else
            fprintf(1,' %4i %+14.7e %i %9.3e\n',KLOOP,F,FEASIBLE,RELXNORM);
         end
```

```
      end
   end

% Exit do loop here on final iteration
   if KLOOP==KLOOPMAX|RFD<FTOL|RELXNORM<XTOL
      if KLOOP==KLOOPMAX
         fprintf(1,' Terminated on max number of steps\n');
         fprintf(fidD,' Terminated on max number of steps\n');
      end
      if RFD<FTOL
         fprintf(1,' Terminated on function value\n');
         fprintf(fidD,' Terminated on function value\n');
      end
      if RELXNORM<XTOL
         fprintf(1,' Terminated on step size\n');
         fprintf(fidD,' Terminated on step size\n');
      end
      fprintf(1,'\n');
      fprintf(fidD,'\n');
      break;
   end

%*****SOLVE THE APPROXIMATED
SUBPROBLEM*********************************C

[X,F_A,C_A,H_A]=dqlfopc(X,NP,NQ,F,C,H,GF,GC,GH,ACURV,BCURV,CCURV,
DML...
   ,NL,NU,NLV,NUV,V_LOWER,V_UPPER,XTOL,KLOOP);

% Record solution to approximated problem
```

```
   fprintf(fidA,'Solution of approximated problem:\n');
   fprintf(fidA,'X=\n');
   for I=1:N
      fprintf(fidA,' %12.8f\n',X(I));
   end
   fprintf(fidA,' F_A=%15.8e\n',F_A);
   for I=1:NP+NL+NU+1
      fprintf(fidA,'C_A(%i)=%15.8e\n',I,C_A(I));
   end
   for I=1:NQ
      fprintf(fidA,'H_A(%i)=%15.8e\n',I,H_A(I));
   end

% Increment outer loop counter
   KLOOP=KLOOP+1;
end

% Write final constraint values to file

if NP>0
   fprintf(fidD,' Final inequality constraint function values:\n');
   for I=1:NP
      fprintf(fidD,'  C(%i)=%15.8e\n',I,C(I));
   end
end
if NQ>0
   fprintf(fidD,' Final equality constraint function values:\n');
   for I=1:NQ
      fprintf(fidD,'  H(%i)=%15.8e\n',I,H(I));
```

```
   end
end
if NL>0
   fprintf(fidD,' Final side (lower) constraint function values:\n');
   for I=1:NL
      fprintf(fidD,'  C(X(%i))=%15.8e\n',NLV(I),C_A(NP+I));
   end
end
if NU>0
   fprintf(fidD,' Final side (upper) constraint function values:\n');
   for I=1:NU
      fprintf(fidD,'  C(X(%i))=%15.8e\n',NUV(I),C_A(NP+NL+I));
   end
end

% Write final constraint values to screen
fprintf(1,' Constraint values follow:\n\n')
if NP>0
   fprintf(1,' Final inequality constraint function values:\n');
   for I=1:NP
      fprintf(1,'  C(%i)=%15.8e\n',I,C(I));
   end
end
if NQ>0
   fprintf(1,' Final equality constraint function values:\n');
   for I=1:NQ
      fprintf(1,'  H(%i)=%15.8e\n',I,H(I));
   end
end
if NL>0
```

```
   fprintf(1,' Final side (lower) constraint function values:\n');
   for I=1:NL
      fprintf(1,'  C(X(%i))=%15.8e\n',NLV(I),C_A(NP+I));
   end
end
if NU>0
   fprintf(1,' Final side (upper) constraint function values:\n');
   for I=1:NU
      fprintf(1,'  C(X(%i))=%15.8e\n',NUV(I),C_A(NP+NL+I));
   end
end

% Write history vectors

fprintf(fidH,' %3i%3i%3i%3i%3i%3i\n', KLOOP,N,NP,NL,NU,NQ);
for I=1:KLOOP+1
   fprintf(fidH,' %3i %15.8e',I-1,F_H(I));
   for J=1:N
      fprintf(fidH,' %15.8e',X_H(I,J));
   end
   fprintf(fidH,'\n');
end
if NP>0
   for I=1:KLOOP+1
      fprintf(fidH,' %3i',I-1);
      for J=1:NP
         fprintf(fidH,' %15.8e',C_H(I,J));
      end
      fprintf(fidH,'\n');
   end
```

```
end
if NL>0
   for I=1:KLOOP+1
      fprintf(fidH,' %3i',I-1);
      for J=NP+1:NP+NL
         fprintf(fidH,' %15.8e',C_H(I,J));
      end
      fprintf(fidH,'\n');
   end
end
if NU>0
   for I=1:KLOOP+1
      fprintf(fidH,' %3i',I-1);
      for J=NP+NL+1:NP+NL+NU
         fprintf(fidH,' %15.8e',C_H(I,J));
      end
      fprintf(fidH,'\n');
   end
end
if NQ>0
   for I=1:KLOOP+1
      fprintf(fidH,' %3i',I-1);
      for J=1:NQ
         fprintf(fidH,' %15.8e',H_H(I,J));
      end
      fprintf(fidH,'\n');
   end
end

fclose(fidD);
```

```
fclose(fidH);
fclose(fidA);

if PRNCONST
   histplot;
%    disp('Press a key to continue');
%    pause;
%    close all;
end
toc
```

B-2 FCH.M

```
function [F,C,H]=fch(X);
% Objective and constraint function evaluation for DYNAMIC-Q
%          (USER SPECIFIED)
%
%   synopsis:
%
%      [F,C,H]=fch(X);
%
%   outputs:
%      F  = objective function value
%      C  = vector of inequality constraint functions (1xNP)
%      H  = vector of equality constraint functions (1xNQ)
%
%   inputs:
%      X = design vector (1xN)
%
%                  -----------------
%
% The application of the code is illustrated here for the very simple
% but general example problem (Hock 71):
%
%     minimise  F(X) = X(1)*X(4)*(X(1)+X(2)+X(3))+X(3)
% such that
%              C(X) = 25-X(1)*X(2)*X(3)*X(4) <= 0
%     and
%              H(X) = X(1)^2+X(2)^2+X(3)^2+X(4)^2-40 = 0
%
%    and side constraints
```

```
%
%               1 <= X(I) <= 5 , I=1,2,3,4
%
%   Starting point is (1,5,5,1)
%
%   Solution of this problem is accomplished by:
%      (with FCH and GRADFCH unaltered)
%
%      x0=[1,5,5,1] % Specify starting point
%      lo=[1:4;1,1,1,1]' % Specify lower limits
%      up=[1:4;5,5,5,5]' % Specify upper limits
%      [X,F]=dynq(x0,lo,up); % Solve using Dynamic-Q
%
%   NOTE: This function should return C=[]; H=[]; if these are
%         not defined.
%
%   See also DYNQ and GRADFCH
%

%Objective Function
%Load Design Variables

%Get the Total Heat transfer

F = -LL4{2};

%Inequality Constraints
C(1)=(X(3)/(4*X(1)))-1;
C(2)=1-(2*X(3)/X(1));
C(3)=(X(4)/(4*X(2)))-1;
```

```
C(4)=1-(2*X(4)/X(2));

Volu = 0.05;
%Equality Constraints
H(1)=(X(1)^2*X(3))+(X(2)^2*X(4))-(4*Volu/pi);

% To eliminate error messages
% Do not delete

if ~exist('C')
   C=[];
end
if ~exist('H')
   H=[];
end
```

B-3 GRADFCH.M

```
function [GF,GC,GH]=gradfch(X);
% Objective and constraint function GRADIENT evaluation for DYNAMIC-Q
%          (USER SPECIFIED)
%
%   synopsis:
%
%      [GF,GC,GH]=gradfch(X);
%
%   outputs: Partial derivatives wrt variables X(I) of
%     GF  = objective function (1xN)
%     GC  = inequality constraint functions (NPxN)
%     GH  = equality constraint functions (NQxN)
%
%   inputs:
%      X = design vector (1xN)
%
%    COMPUTE THE GRADIENT VECTORS OF THE OBJECTIVE FUNCTION
F,
%    INEQUALITY CONSTRAINTS C, AND EQUALITY CONSTRAINTS H
%    W.R.T. THE VARIABLES X(I):
%           GF(I),I=1,N
%           GC(J,I), J=1,NP I=1,N
%           GH(J,I), J=1,NQ I=1,N
%
%   NOTE: This function should return GC=[]; GH=[]; if these are
%        not defined.
%
%   See also DYNQ, FCH
```

```
%

% Determine gradients by finite difference
FDFLAG=1;

if FDFLAG
   DELTX=1.D-4;    % Finite difference interval
   [F,C,H]=fch(X);
   N=length(X);
   for I=1:N
      DX=X;
      DX(I)=X(I)+DELTX;
      [F_D,C_D,H_D]=fch(DX);
      GF(I)=(F_D-F)/DELTX;
      if ~isempty(C)
         GC(1,1)=-X(3)/(4*X(1)^2);
         GC(1,2)=0;
         GC(1,3)=1/(4*X(1));
         GC(1,4)=0;
         GC(1,5)=0;
         GC(2,1)=2*X(3)/(X(1)^2);
         GC(2,2)=0;
         GC(2,3)=-2/X(1);
         GC(2,4)=0;
         GC(2,5)=0;
         GC(3,1)=0;
         GC(3,2)=-X(4)/(4*X(2)^2);
         GC(3,3)=0;
         GC(3,4)=1/(4*X(2));
         GC(3,5)=0;
```

```
        GC(4,1)=0;
        GC(4,2)=2*X(4)/(X(2)^2);
        GC(4,3)=0;
        GC(4,4)=-2/X(2);
        GC(4,5)=0;
    end
    if ~isempty(H)
    GH(1,1)=2*X(1)*X(3);
    GH(1,2)=2*X(2)*X(4);
    GH(1,3)=X(1)^2;
    GH(1,4)=X(2)^2;
    GH(1,5)=0;
    end
  end
end

% To eliminate error messages
% Do not erase
if ~exist('GC')
  GC=[];
end
if ~exist('GH')
  GH=[];
end
```

B-4 Execute_Finsim.m

```
%This program initiates DYNQ.M
clear all
clc
close all
x0=[+2.824638e-001 +1.513331e-001 +6.310029e-001 +5.814793e-001 +5.0000e-
002];
lo=[1 0.05
   2 0.05
   5 0.05];
up=[3 0.95
   4 0.95];
dml=0.0005;
xtol=[];
ftol=[];
clim=[];
np=4;
nq=1;
kloop=[];
[X,F] = dynq(x0,lo,up,dml,xtol,ftol,clim,np,nq,kloop);
```